



Influence of the synthesis of Fe-MFI for partial methane oxidation

Thesis submitted in accordance with the requirements of Cardiff University for the degree of Doctor of Philosophy

Kirstie Milne
Cardiff University
2020

Supervisor: Dr Ceri Hammond

Abstract

Iron-containing MFI-type zeolites have been shown to be active catalysts for a range of oxidative transformations. Even though much research has been devoted to these materials in the past, correlations between the choice of zeolite synthesis procedure and catalytic performance are not well explored. Moreover, the impact of catalyst composition on the ultimate catalytic performances of Fe-MFI zeolites is far from understood. However, evidence from zeolite research suggests that these parameters can affect the properties of these materials, which could have implications on catalytic performance. Herein, this thesis aims to better understand the effect of Fe-MFI synthesis and composition on the catalytic performance of these materials for aqueous phase partial methane oxidation.

Aqueous phase partial methane oxidation, which utilises hydrogen peroxide as the oxidant, was chosen as a model reaction for the study of the effect of Fe-MFI hydrothermal synthesis on catalytic performance. Initial work focused on the correlation of the $\text{SiO}_2/\text{Al}_2\text{O}_3$ ratio and Fe content in hydrothermally synthesised catalysts to the catalytic performance of Fe-MFI zeolites for partial methane oxidation. Batch reaction testing was performed at 50 °C to determine turnover frequencies (TOF), and Fe-selective spectroscopic probes, such as DRUV-vis and resonance Raman spectroscopy, were utilised to link the nature of Fe^{3+} speciation with catalytic performance. In addition to this, the effect of each step of Fe-MFI preparation was studied, to determine the extent of Fe^{3+} speciation throughout the different preparation steps. Secondly, the effect of crystallisation time and temperature on the hydrothermal synthesis process were explored, to understand whether crystallisation parameters influenced catalytic performance of partial methane oxidation.

In the later stages of the thesis, a new procedure for the preparation of Fe-MFI zeolites was explored. Typically, Organic Structure Directing Agents (OSDAs) are used during crystallisation of Fe-MFI zeolites, and such compounds are thought to be critical to the success of zeolite crystallisation. Yet, use of OSDAs requires extra processing methods to remove the OSDA prior to catalytic studies, which adds synthetic complexity, produces CO_2 on thermal degradation, and may impact catalytic performance. Furthermore, the presence of the OSDA complicates spectroscopic studies of the synthesised catalyst. In this thesis, an adapted synthesis method, utilising seeding techniques, was developed, resulting in the synthesis of a highly active catalyst for aqueous phase methane oxidation without need of an OSDA.

Acknowledgments

Firstly, I would like to thank the EPSRC and the Catalysis CDT for the funding that allowed me to perform the research laid out in this thesis.

Secondly, I would like to thank Dr Ceri Hammond for his support and guidance throughout my PhD. I would also like to extend my thanks to Dr Giulia Tarantino, for her assistance throughout this project and to Dr Daniele Padovan for his expertise in reactor construction and maintenance. In addition to this, I would like to thank the rest of the Hammond group for peer support and entertainment throughout my PhD period, particularly Guillermo Nicolau.

Finally, I would like to thank both my parents, Lynne and Stuart, for their support, particularly when times were tough. And to Robert Armstrong, who kept me sane, and rather well fed, throughout my PhD, along with providing sage advice about life in academia.

Contents

Chapter 1. Introduction	1
1.1 Zeolites.....	1
1.2. Crystallisation Mechanism of Zeolites.....	5
1.2.1. Mechanism of Zeolite Crystallisation.....	5
1.2.1.1. <i>Synthesis of Zeolites in the Presence of Organic Templates</i>	6
1.2.1.1. <i>Synthesis of Zeolites in the Absence of Organic Templates</i>	8
1.2.2. Tuning of Metal Properties.....	12
1.3. Modification of Zeolites with Transition Metal Ions.....	14
1.3.1. Methods of TMI Modification of Zeolites.....	18
1.3.1.1. <i>Top-down Approaches</i>	18
1.3.1.2. <i>Bottom-up Approaches</i>	20
1.3.1.3. <i>In-situ Observation of Isomorphous Substitution of TMI During Crystallisation</i>	22
1.3.2. Summary.....	24
1.4. Fe-Zeolites for Catalytic Oxidations.....	25
1.4.1. Partial Methane Oxidation.....	27
1.4.1.1. <i>Soluble Methane Monooxygenase (sMMO) Enzymes</i>	29
1.4.2. Design of “ <i>Biomimetic</i> ” Catalysts for Methane Oxidation.....	32
1.4.2.1. <i>Homogeneous Fe-Complexes for Methane Oxidation</i>	33
1.4.2.2. <i>Heterogeneous Fe-Catalysts for Methane Oxidation</i>	33
1.4.2.2.1. <i>Fe-ZSM-5/ N₂O Oxidation Systems</i>	33
1.4.2.2.2. <i>Fe-ZSM-5/ H₂O₂ Oxidation Systems</i>	35
1.5. Thesis Aims.....	38
1.6. References.....	38
Chapter 2. Experimental Procedures	47
2.1. Materials.....	47
2.2. Synthesis of Fe-ZSM-5.....	47
2.2.1. Hydrothermal Synthesis of Fe-ZSM-5.....	47
2.2.2. Seed-assisted Synthesis of Fe-ZSM-5.....	48
2.3. Catalyst Characterisation.....	49
2.3.1. Powder X-Ray Diffraction (<i>p</i> XRD).....	49
2.3.2. N ₂ Physisorption.....	49
2.3.3. Thermogravimetric Analysis (TGA).....	50
2.3.4. Scanning Electron Microscopy (SEM).....	50

2.3.5. Inductively Coupled Plasma Mass Spectrometry (ICP-MS)	50
2.3.6. Magic-Angle Spinning NMR (MAS-NMR)	50
2.3.7. Diffuse Reflectance UV-vis Spectroscopy (DRUV-vis)	51
2.3.8. Resonance Raman Spectroscopy	53
2.4. Fe-ZSM-5 for Partial Methane Oxidation.....	54
2.4.1. Partial Methane Oxidation Catalytic Testing	54
2.4.2. Analytical Techniques	55
2.4.2.1. GC-FID.....	55
2.4.2.2. ¹ H NMR	56
2.4.3. Adapted Testing Protocol for Partial Methane Oxidation	58
2.5. References	59
Chapter 3. Effect of Catalyst Preparation on Fe-speciation in Fe-ZSM-5 for Methane Oxidation and Competing Pathways	61
3.1. Introduction.....	61
3.2. Effect of SiO ₂ /Al ₂ O ₃ ratio on Methane Oxidation and Hydrogen Peroxide Decomposition Activity	63
3.2.1. Hydrothermal Synthesis of 0.1 wt% Fe-ZSM-5	63
3.2.2. Catalytic Performance of 0.1 wt% Fe-ZSM-5_H ⁺	66
3.2.3. Spectroscopic Characterisation of 0.1 wt% Fe-ZSM-5_H ⁺	68
3.3. Effect of Fe loading on Methane Oxidation and Hydrogen Peroxide Decomposition Activity.....	73
3.3.1. Hydrothermal Synthesis of YY wt% Fe-ZSM-5 (42)	73
3.3.2. Catalytic Performance of YY wt% Fe-ZSM-5 (42)_H ⁺	75
3.3.3. Spectroscopic Characterisation of YY wt% Fe-ZSM-5 (42)_H ⁺	76
3.4. Effect of the Preparation of Hydrothermal Prepared Fe-ZSM-5 on Methane Oxidation Activity	82
3.4.1. Preparation of 0.1 wt% Fe-ZSM-5 (XX) for Methane Oxidation	82
3.4.2. Catalytic Performance of 0.1 wt% Fe-ZSM-5 (XX)_ZZ for Methane Oxidation	83
3.5. Conclusions	90
3.6. References	92
Chapter 4. Optimisation of the Hydrothermal Synthesis of Fe-ZSM-5 for Partial Methane Oxidation.....	94
4.1. Introduction.....	94
4.2. Effect of Time on the Rate of Crystallisation of 0.1 wt% Fe-ZSM-5 (42)_AS	96
4.3. Effect of Temperature on the Rate of Crystallisation of 0.1 wt% Fe-ZSM-5 (42)_AS	100
4.4. Effect of Reaction Vessel on Crystallisation of 0.1 wt% Fe-ZSM-5 (42)_AS	103
4.5. Effect of SiO ₂ /Al ₂ O ₃ Ratio on the Rate of Crystallisation of 0.1 wt% Fe-ZSM-5 (42)_AS	108

4.6. Effect of Calcination on 0.1 wt% Fe-ZSM-5 (42) as a Function of Crystallisation Conditions	113
4.7. Conclusions	119
4.8. References	120
Chapter 5. Seed-Assisted Synthesis of Fe-ZSM-5 to Study the Speciation of Fe.....	123
5.1. Introduction.....	123
5.2. Development of Seed-Assisted Synthesis of 0.1 wt% Fe-ZSM-5 (42) for Partial Methane Oxidation	125
5.2.1. Synthesis of the Seed Material for Seed-Assisted Synthesis	126
5.2.2. Synthesis of Seed-Assisted 0.1 wt% Fe-ZSM-5 (42).....	128
5.3. Catalytic Activity in Seed-Assisted 0.1 wt% Fe-ZSM-5.....	138
5.3.1. Reactant Diffusion	138
5.3.2. Changes in Fe ³⁺ Speciation as a Function of Temperature	139
5.3.3. Spectroscopic Evidence for Change in Fe ³⁺ Speciation as a Function of Heat-Treatment Temperature.....	144
5.4. Conclusions	148
5.5. References	149
Chapter 6. Conclusions and Pertaining Challenges.....	152
6.1. Conclusions	152
6.1.1. Chapter 3.....	152
6.1.2. Chapter 4.....	154
6.1.3. Chapter 5.....	156
6.2. Pertaining Challenges.....	157
6.2.1. Optimisation of Fe-ZSM-5.....	157
6.2.2. Optimisation of the Synthesis of Fe-ZSM-5.....	160
6.2.3. Seed-Assisted Synthesis of Fe-ZSM-5	163
6.3. Final Remarks	166
6.4. References	166

Chapter 1. Introduction

1.1. Zeolites

Zeolites are microporous, crystalline aluminosilicates that are made up of a periodic array of corner-sharing TO_4 tetrahedra, where T is typically Si^{4+} or Al^{3+} . These tetrahedra combine to form different size rings (4-10 membered rings), which can combine to form larger rings and cage structures, called secondary building units (SBUs). The SBUs can be arranged in several ways to form uniform arrays of composite building units (CBUs) that make up the zeolite framework. There are many ways in which the CBUs can be arranged resulting in a broad array of potential zeolite frameworks. In fact, over 1000 theoretical zeolite structures have been proposed, which means that great structural diversity is possible.¹ Yet, at present, only 253 zeolite frameworks have been synthesised and classified by the International Zeolite Association (IZA).² Each of these framework types is identified by a unique three-letter code and a few common examples of different zeolite framework types (zeotypes) are shown in Figure 1.³ This broad range of available zeotypes makes various zeolites suited to different chemical applications, such as catalysts,⁴⁻⁹ ion-exchange resins,^{10,11} adsorbents,¹² molecular sieves,¹³⁻¹⁵ and membrane separations.¹⁶⁻¹⁸

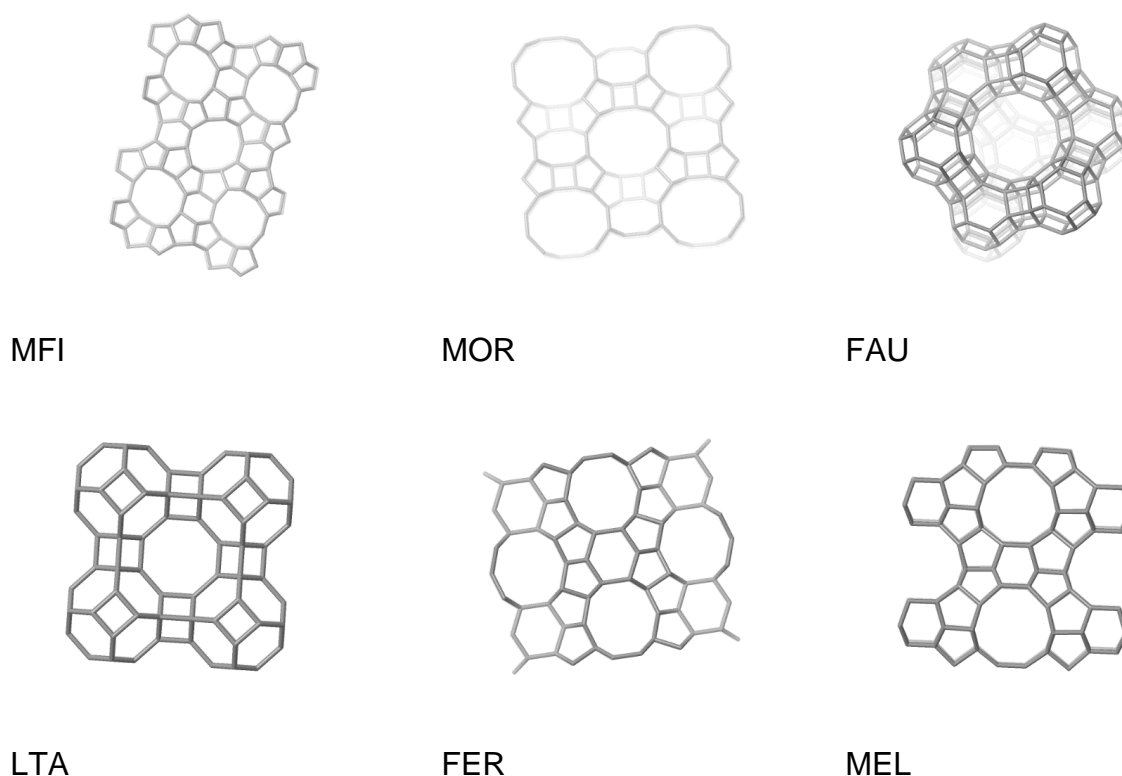


Figure 1 Wireframe models of some common zeolite frameworks. Only the tetrahedral atoms, T, are displayed for clarity. The three letter codes for each framework type is given below the model. As adapted with permission from reference 3. Copyright 2017 International Zeolite Association.

The name “zeolite” derives from the Greek ζέω (zeo) for boil and λίθος (lithos) for stone as it was observed that steam was released when heated to high temperatures. Zeolites can be naturally-occurring or synthetic, although synthetic zeolites are more commonly used within research and industry, as higher phase purity can be achieved through control of the synthesis conditions.¹⁹ Much research has focused on the method of zeolite synthesis and the effect that this has on zeolite properties, which allows them to be optimised for a given application.

The combination of the TO_4 units results in a crystallographic, 3-D network of tetrahedra that forms uniformly sized channels and cavities of molecular dimensions (3 – 15 Å).¹⁹ The arrangement of the channels leads to the formation of micropores, which gives rise to large surface areas (typically several hundred $\text{m}^2 \text{g}^{-1}$) and micropore volumes typically associated with zeolites. This means that zeolites can discriminate between molecules of varying dimensions and geometries, which can impart excellent molecular sieving abilities and makes zeolites suited to molecular separation applications.³⁻⁵ Furthermore, the micropore networks for various zeolite frameworks can be exploited for “shape-selective” reactivity of catalytic processes.²² Preferred reaction products (or transition states) can be sterically favoured within the micropores of the zeolite, leading to the selective formation of the desired products, as demonstrated in Figure 2. For example, this phenomenon is exploited in industrial alkane cracking, where linear isomers are formed preferentially over branched alkanes.⁹ This minimises the amount of processing needed downstream, such as separations, which can be difficult when the products are chemically and physically similar.

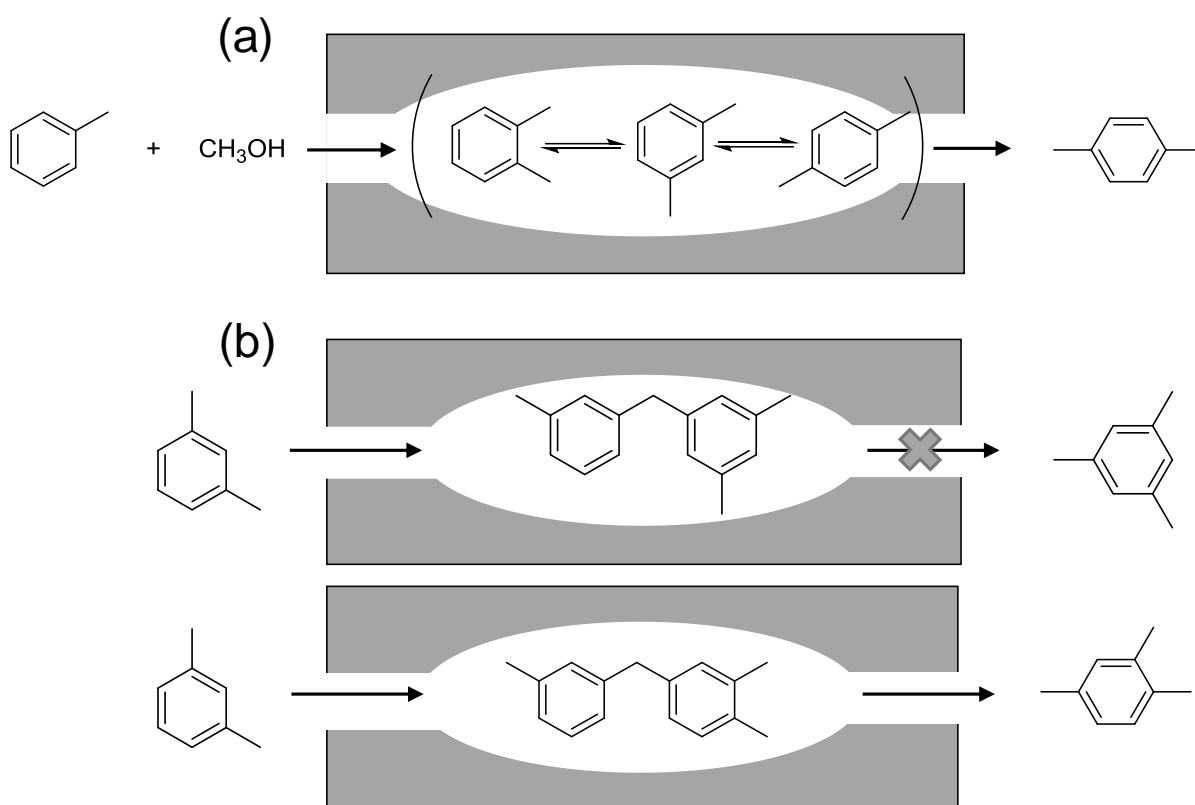


Figure 2 Schematic of shape selective catalysis. (a) Product selectivity, and (b) Transition-state selectivity. Adapted with permission from reference 22. Copyright 1984 Elsevier.

In addition to the micropore structure, the acidity of zeolite frameworks can be modified, which broadens the applications of zeolites. In completely siliceous materials (i.e. $\text{SiO}_2/\text{Al}_2\text{O}_3 = \infty$), the net framework charge is 0. However, substitution of tetravalent Si^{4+} atoms by trivalent Al^{3+} results in the lattice gaining a formal charge of -1. Electroneutrality of the framework can be maintained by uptake of a cation, as shown in Figure 3. When the counter-cation is a proton, a Brønsted acid site is formed, which can affect the performance of the material. For instance, a lower $\text{SiO}_2/\text{Al}_2\text{O}_3$ ratio gives a greater number of Brønsted acid sites in the zeolite lattice. This could affect the acid site density and acid strength of the zeolite,²³ which has an important role in the hydrothermal stability of zeolites. However, according to Löwenstein's rule, $\text{SiO}_2/\text{Al}_2\text{O}_3$ cannot be less than 1, as the arrangement of Al-O-Al is forbidden in zeolitic structures due to repulsive electronic interactions of protons/ counter-cations in proximity within the void space.²⁴ Thus, there is an experimental limit on the number of Al^{3+} (or other trivalent cation) that can be substituted into the framework, potentially restricting Brønsted acid capabilities.

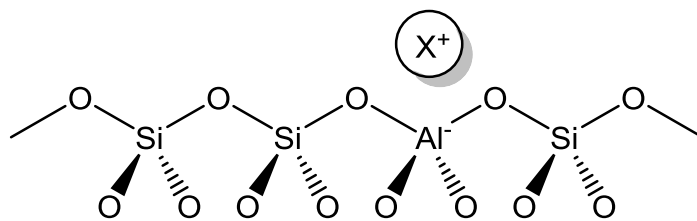


Figure 3 Schematic of the origin of Brønsted acidity from isomorphous substitution of tetraivalent Si⁴⁺ for trivalent Al³⁺, where X⁺ is a cationic species required to balance the negative charge created at the Al (X⁺ = H⁺, Na⁺).

Another key attribute of zeolites is that the chemical and physical properties of the material can be modified, by isomorphous substitution of a framework tetrahedron with a transition or main group metal, for example, P, B, Ga, Ge, Ti, Sn, Fe and Mn.²⁵ This can introduce additional functionality beyond ion-exchange to the zeolite lattice, and allows improved functionality for the zeolite framework. For example, incorporation of Lewis acidic metals into zeolite frameworks forms a solid-Lewis acid catalyst that can promote a variety of organic transformations in place of a conventional homogeneous Lewis acid complex.^{26,27} In addition of exhibiting Brønsted and Lewis acidity, zeolites can be used as bifunctional catalysts, by exploiting the dual Brønsted and Lewis acidity, or can be redox active, by exploiting the redox nature of the substituted T-atom. For instance, Fe and Ti-zeolites have been shown to exhibit redox-properties, and are used in a range of redox transformations.^{14,28–31}

Because of the ability to modify the properties of the zeolite through substitution, modified zeolites are attractive catalysts for a range applications. Discussions of these applications have been put forward in a number of excellent reviews in the relevant areas of oil refinery,^{9,32,33} natural gas conversion,^{34–36} methanol-to-hydrocarbons,³⁷ biomass conversion,^{38–40} selective catalytic reduction of NO_x,⁴¹ and biotechnology.⁴²

Although zeolites are widely employed in oil and gas refinery applications, due to their inherent properties, such shape-selectivity and Brønsted and Lewis acid functionality, the use of zeolites in fine chemical manufacture is less prevalent. This results from an unclear understanding of the nature of the active sites within modified zeolites preventing optimisation of catalyst performance. Advances in the use of molecular modelling and *in-situ* experiments means that the crystallisation process can be studied in more detail and thus lead to the optimisation of the synthesis of zeolites.⁴³ The crystallisation mechanisms and the isomorphous substitution of transition metal ions (TMI) will be explored throughout this chapter and will be used to explore the effect of crystallisation on zeolite properties.

1.2. Crystallisation Mechanism of Zeolites

Zeolites are typically prepared by hydrothermal synthesis, where an (alumino)silicate gel is prepared and then subjected to high temperatures for long periods of time (hours to days) to crystallise the desired zeolite framework. A zeolite gel typically consists of four main components; T-atom precursors (silica source and aluminium source where applicable), an inorganic template/ mineralising agent, a templating agent and solvent. These are mixed to form a gel with a molar composition of $aM_2O: bR_2O: cTO_2: dH_2O$, where M is an alkali metal cation (e.g. Na^+), T is the tetrahedral, framework atom (e.g. Si, Al), R is the organic structural directing agent (OSDA) and the italic letter denotes the molar ratio of each component. Each component is deemed necessary to controlling the output of crystallisation, and variations in the starting materials and ratios can result in different zeotypes being formed. The resulting sol-gel is then crystallised under hydrothermal conditions. In general, this process affords a solid, crystalline product. However, the process is not a continuum as it might seem from the synthesis procedure. Instead, a number of discrete reaction steps occur in a multi-phase solid-gel suspension to afford the crystallised product.⁴⁴

1.2.1. Mechanism of Zeolite Crystallisation

The mechanism of zeolite synthesis has been widely studied and disputed and consequently, a range of crystallisation mechanisms have been proposed.⁴⁴ Studies from the 1970s published by two different authors, have proposed two different theories regarding zeolite crystallisation mechanisms. Breck proposed that zeolite crystallisation proceeds via polymerisation and depolymerisation reactions of (alumino)silicate species that were catalysed by hydroxyl ions in the synthesis mixture.⁴⁵ Another theory was put forward by Zhdanov, who suggested that an equilibrium phase between the amorphous gel and the liquid phase formed during the mixing step that resulted in zeolite nucleation and crystal growth through transfer of aluminosilicate precursor species in the solution phase.⁴⁶ These theories have formed the basis of more modern studies into the crystallisation of zeolites.

It has been suggested that zeolite synthesis is a series of discrete reaction steps that result in the nucleation and growth of a crystalline product with zeolitic structure.⁴³ The precursor species are mixed prior to hydrothermal treatment to homogeneously distribute and equilibrate the gel and solution phases, which can lead to numerous polymerisations and depolymerisation reactions occurring at a given point. These reactions can initiate a chain reaction, which can result in the formation of discrete zeolite nuclei, from which zeolite crystals can grow.⁴³ Yet,

this theory does not take into consideration the impact of chemical and physical variables, such as starting material stoichiometries, time and temperature, can affect the properties of the crystallised product.⁴⁷ Thus, a greater understanding of the growth processes means that the kinetics can be modified to produce a material with the desired crystal size, shape and orientation.

1.2.1.1. *Synthesis of zeolites in the Presence of Organic Templates*

The mechanism of zeolite formation has been investigated by a combination of characterisation techniques. The group of Mintova have identified various silicate precursors in the initial gel phase by ²⁹Si NMR, which formed during the initial hydrolysis of the silica source (typically tetraethyl orthosilicate, TEOS).⁴⁷ It was stipulated that the nature of the precursors formed during the initial stages of zeolite formation could affect the rate of nucleation and subsequently, zeolite crystal growth.⁴⁷ In addition to this, Kirshhock *et al.* suggested that monomeric Si(OH)₄ species could undergo condensation reactions in the solution phase to form oligomeric silicate species within the gel phase.^{48,49} The silicate species were thought to cluster around positively charged cationic organic structural directing agents (OSDA), such as quaternary tetrapropylammonium cation (TPA), to form a silicate-rich shell and TPA-rich core. This process formed a dynamic equilibrium between polymerisation and depolymerisation reactions of the silicate species and template molecules to form MFI-type building units, which could be observed in the crystallised MFI product. This work indicated that the aggregation of such building units as observed by ²⁹Si NMR, led to the desired crystal growth of the zeolite structure. However, it has also been implied that the molar ratio and choice of template can influence the reactions that occur within the gel phase, impacting the distribution of silicate species that form in solution. A study that looked at the effect of OSDA on the distribution of silicate species did not result in the same species being observed by ²⁹Si NMR, instead suggesting that denser silicate species formed.⁵⁰

Further evidence for the interaction of the TPA template with silicate species was reported by Burkett and Davis, using ¹H-²⁹Si CP MAS-NMR to map the interactions between the framework and the OSDA.⁵¹ Interactions between TPA⁺ and the silicalite-1 structure were observed in the amorphous phase and the authors deduced that occlusion of the TPA by the silicate units resulted in the assembly of inorganic-organic composite units, which leads to the crystallisation of MFI framework. This was further supported by later work that reached the same conclusion from the appearance of microporosity in materials that had not undergone full

crystallisation, suggesting that zeolitic units were present within the amorphous structure, but long-range order had not yet developed.⁵²

These conclusions were based on extrapolated observations about the crystallisation mechanism from *ex-situ* characterisation techniques of the initial mixture and final crystallised product. To provide more conclusive evidence about the whole process, *in-situ* spectroscopic techniques were utilised, which were able to process the wide range of scales encountered during zeolite synthesis. For example, X-ray scattering techniques can probe systems that range from sub-nanometre to micron scale, which reflects the change in scale that occurs during the zeolite synthesis mechanism.⁵³ Utilising a combination of ultra-small angle X-Ray scattering (USAXS) and simultaneous small angle and wide-angle scattering (SAXS and WAXS), small primary units (2.8 nm) were detected in the initial mixture, before aggregation of small primary units to form larger particles. Further aggregation of these large particles would result in the formation of zeolite nuclei (5 – 10 nm).⁵³ On addition of further primary units to the nuclei, zeolite crystals were observed that ranged in size from 10 nm to micron scale, depending on the conditions of the gel.⁵³ Through these techniques, it was possible to observe zeolite growth and more research has emerged since to look for further evidence of the growth mechanism.

SAXS studies were used in combination with high-resolution transmission electron microscopy (HRTEM) to study the aging of a silicalite-1 suspension at room temperature.⁵⁴ It was proposed by the authors that MFI crystal growth proceeded via the aggregation of small, secondary SiO₂ nanoparticles (2.4 nm), via a number of intermediate steps, by slowing down the rate of intermediate reaction steps (as shown in Figure 4).⁵⁴ Ostwald-ripening of particles was observed at longer crystallisation times, believed to arise from the addition of a low concentration of monomer units to the crystal aggregate. The study was performed at room temperature, which allowed for direct observation of the intermediate steps. Yet, it may not be representative of crystal growth mechanisms at elevated temperatures at which zeolite syntheses are typically performed. Another study suggested that nucleation occurred by aggregation of smaller particles, as observed by a change in particle size distribution (PSD) during the initial stages of hydrothermal treatment.⁵⁵ This change in PSD coincided with a change in heat distribution, called the “*exo-endo switch time*”, which is the point that crystallisation changes from an exothermic to an endothermic process.³⁷ This indicates that a change in the dominant mechanism occurring within the zeolite synthesis feed.³⁸

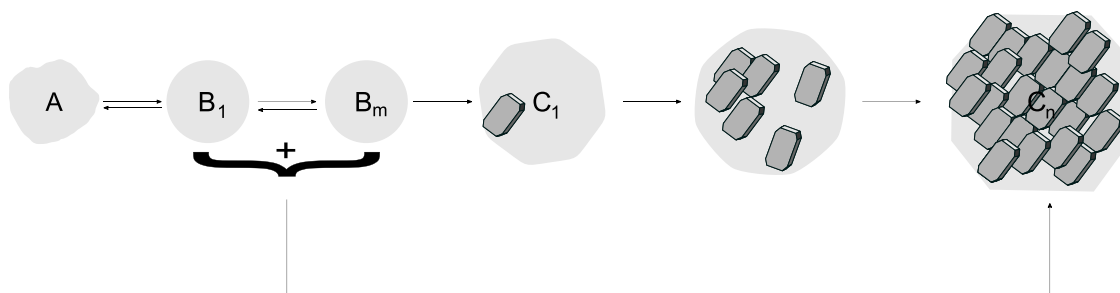


Figure 4 Proposed crystallisation mechanism for silicalite-1 by Tsapatsis *et al.*, where: A is a precursor silicate species; B_m is amorphous silicate nanoparticles (where m indicates the number of nanoparticles in the aggregate); C_1 are silicalite-1 nuclei; C_n are silicalite-1 crystals. Adapted with permission from reference 54. Copyright 2006 Springer Nature.

The crystallisation of zeolites in the presence of an organic templating agent is complex and is thought to proceed by several discrete reaction and growth steps. There is evidence to suggest that an initial dynamic equilibrium of (alumino)silicate species is formed on mixing of the zeolite precursors, and the conditions of this step can affect the rates of the proceeding zeolite crystallisation steps. Thus, the importance of the initial conditions of zeolite have a large effect on the properties of the product material, however, further studies are needed to allow researchers and zeolite synthesis chemists to accurately predict the key properties of the final, crystalline solid, by careful control of the initial conditions. Moreover, advanced and *in-situ* studies should be used to map out the crystallisation mechanisms of a range of zeolite topologies, as it has been shown that this can differ between different structures.

1.2.1.2. Synthesis of Zeolites in the Absence of Organic Templates

The presence of a templating agent, typically tetrapropylammonium hydroxide (TPAOH) for silicalite-1 synthesis, has been shown to favour the formation of MFI crystals.⁵⁴ Yet, on varying the TEOS/TPAOH ratio, it was reported that dense SiO_2 phases were formed when the ratio was low or high.⁵⁰ This observation indicates that the presence of TPAOH template is helpful in achieving kinetically favoured zeolite structures.

It has been shown that zeolite structures can be crystallised in the absence of an OSDA, which has been achieved by replacement of the OSDA with a zeolite seed. Avoiding the use of OSDAs can be beneficial in the large-scale synthesis of zeolites, as OSDAs are expensive and toxic. Furthermore, the synthesised materials require post-synthetic modification to remove the template from the micropore void-spaces and render the catalyst useable, resulting in waste production given that CO_2 and heavy carbon are the by-products of OSDA degradation.⁵⁸

There is precedent for the use of seed-materials in scale-up crystallisation chemistry alongside the use of conventional OSDAs, to reduce crystallisation times and limit the formation of impurity phases.¹⁹ Still, it is thought that the crystallisation mechanism of the seed-assisted approach differs from the of conventional OSDA-mediated approaches.⁵⁹ Generally, it is thought that a seed material can provide an external surface area in which crystal growth can be induced, but the intricacies of the mechanism are less well understood. Reviews into the development of seed-assisted methods for zeolite synthesis have been published and provide an extensive overview of this topic.^{44,59,60}

Early studies into seed-assisted methods could only produce the desired zeolite framework within a narrow margin of conditions, which affected the applicability of these methods.^{61–63} However, these reports showed that seed content and crystallisation temperature could impact on the size of the daughter zeolite material and have implications when considering the design of a material.⁶³

The group of Tang published a series of in-depth reports studying the crystallisation of seed-induced crystallisation of ZSM-5, in the absence of OSDA, to establish the crystallisation mechanism.^{64–66} It was proposed that the seed-assisted crystallisation mechanism proceeded via a “*seed-surface crystallisation*” mechanism (Figure 5), during which amorphous aluminosilicate gel particles were observed to deposit onto the surface of silicalite-1 nanocrystalline seeds by TEM.⁶⁴ Agglomeration of the amorphous phase resulted in partial dissolution of the zeolite seeds and led to the formation of zeolite nuclei. Continual addition of amorphous phase particles to the growing zeolite crystals resulted in zeolite crystal growth.⁶⁶ Also, it was proposed that the crystal properties of the daughter material could be controlled by the size and amount of seed material and control of the gel pH, however, whether this mechanism could be applied to various seed-assisted zeolite syntheses was not explored.⁶⁵ Moreover, this work employed uncalcined seeds, which meant that the occlusion of organic template used in the synthesis of the seed cannot be excluded as a factor influencing the crystallisation mechanism.

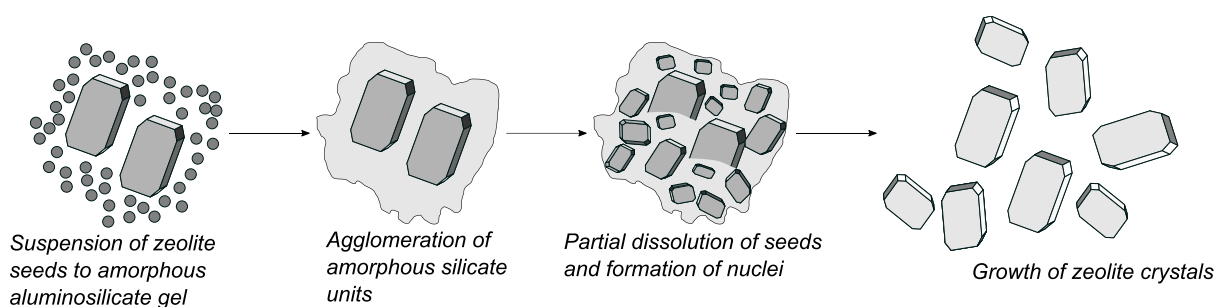


Figure 5 Proposed crystallisation mechanism for seed-assisted of silicalite-1. Adapted with permission from reference 64. Copyright 2010 Elsevier.

To explore the effect of seed preparation, Valtchev *et al.* compared the difference in crystallinity of ZSM-5 when using calcined and uncalcined seeds.⁶³ The daughter zeolite was lower in crystallinity when the seed materials were calcined, suggesting that the calcination of the seeds resulted in aggregation of the crystalline seed particles, which reduced the surface area of the seed crystal and resulted in a smaller area for available for agglomeration of aluminosilicate particles. Yet, the effect of the OSDA within the seed prior to calcination, was not considered, though presence of OSDA might explain why the non-calcined seeds resulted in more crystalline daughter crystals, especially under the harsh hydrothermal conditions used, which could lead to leaching of OSDA in the micropore system of the seeds. The effect of aggregated seeds on material crystallinity was published more recently by Larsen *et al.*, where it was observed that if the seed did not aggregate upon calcination, the crystallinity of the daughter zeolite was not affected.⁶⁷ This observation shows that the preparation of the seed is critical in controlling the particle properties of the daughter material, though it has been demonstrated that microporous zeolites can be made in the absence of OSDA. Development of OSDA-free synthetic routes may lead to possible avenues of research that can study the crystallisation mechanism of zeolites in the absence of OSDA, which can occlude experimental observations, leading to stronger evidence for how zeolites grow in hydrothermal media.

The mechanism driving seed-assisted crystallisation was further elaborated on by the group of Okubo.⁶⁸ In a study on the crystallisation of zeolite beta, it was suggested that zeolite beta-seeds were partially dissolved on contact with the aluminosilicate gel, which resulted in the formation of common composite building units (cCBUs).⁶⁸ Crystal growth occurred through consumption of aluminosilicate species in the amorphous phase to form CBUs until the nutrient supply was exhausted. The international zeolite association structure commission (IZA-SC) database lists 47 known composite building units that make up the 3D structures of known zeolites.³

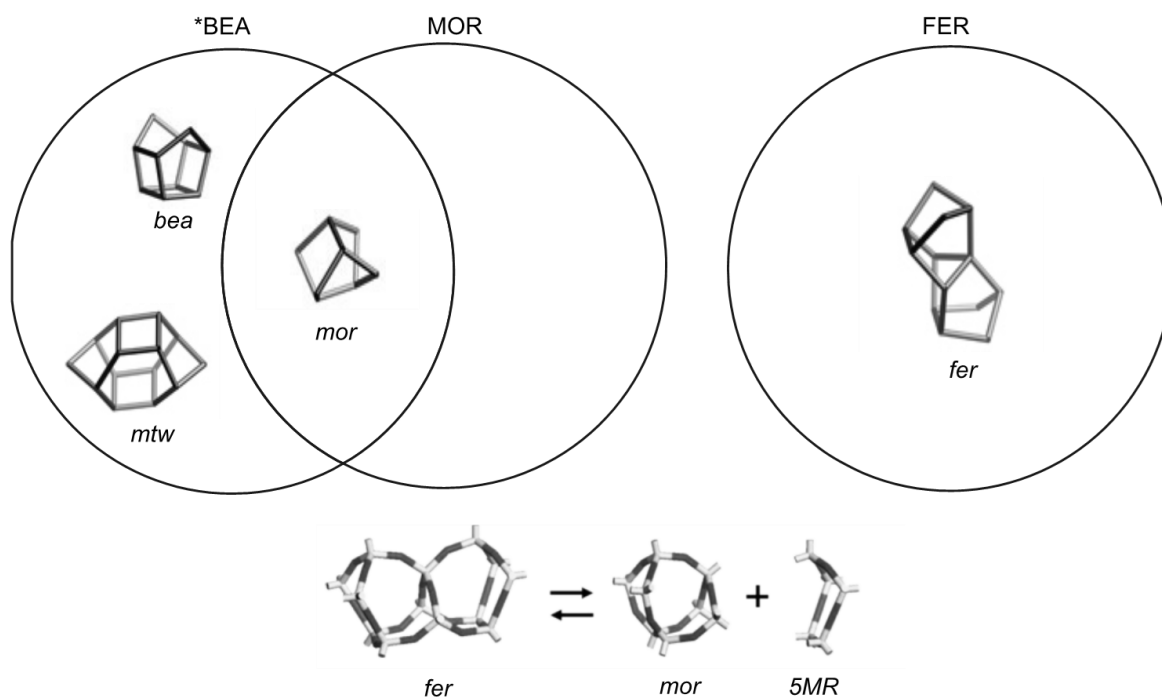


Figure 6 Common composite building units found in *BEA, MOR and FER framework types, which is indicated by the circles. The inset image represents the construction of the *fer* CBU from *mor* and partial 5MR CBUs. Adapted with permission from reference 69. Copyright 2012 American Chemical Society.

Starting from an initial aluminosilicate gel of identical composition, it was proposed that the *mor* CBU was common among MOR, FER and *BEA framework types. It was speculated that the 13T *fer* CBU of FER consisted of 8T *mor* CBU and a 5T fragment, as shown in Figure 6, which explained why this framework could be synthesised from the same gel.⁶⁹ This observation suggested that the common *mor* unit spontaneously formed in the amorphous phase and could be incorporated into either of the three framework types.⁶⁹

To test the above hypothesis, the crystallisation of ZSM-5 and ZSM-11, which both contain the *mor* CBU, from the same starting gels was investigated. Powder X-ray diffraction (*p*XRD) experiments showed that the target framework could be afforded from the initial gel composition, thus the authors proposed that *mor* was a common CBU at certain gel compositions.⁶⁹ Yet, CBUs are theoretical model structures, and were not observed experimentally, thus it could not be concluded that common CBUs were critical for crystallisation of given zeotypes.

Understanding the mechanism of zeolite crystallisation is of importance to the expanding field of zeolite synthesis, to optimise process efficiency in the long run. As summarised above, much experimental work has been carried out, which has been helped by the development of *in-situ* techniques,⁷⁰ although the multiple phases that form during crystallisation still make such

techniques challenging. More recent developments in the study of zeolite crystallisation have employed the use of molecular modelling studies to predict the outcomes of certain conditions and this could be used to direct research into the optimisation and development of zeolite crystallisation processes.⁷¹ These studies can provide complementary data on the zeolite growth mechanisms, for example, it could be used to propose precursor species formed in the gel phase, model condensation and polymerisation reactions that occur in suspension, and study of solvation effects. However, due to the complexity of the zeolite growth process, predictive models can fail, thus more work is required to overcome the challenges of understanding the mechanisms through which zeolite crystallisation can occur to allow for development of novel frameworks and optimised synthesis conditions.

To summarise, zeolite synthesis is a complex process, involving numerous chemical processes to afford the desired zeolite crystal. Moreover, the chemical and physical parameters can affect various particle properties, such as framework type, particle size and morphology of the desired product, so time should be taken to consider the effect of these on the final crystallised product. There remains many questions arising from the current literature, such as the identification of the structures of the precursor species in suspension, and determination of the mechanism of zeolite growth for individual systems, considering the many different variables.⁴³ Modification of zeolites, such as the incorporation of a transition metal ion (TMI) at T-sites via isomorphous substitution can further complicate crystallisation mechanisms, as the substitution of a T atom could alter the crystallisation kinetics and impact upon the particle properties of the crystallised product.²⁵ The synthesis of TMI modified zeolites will be discussed in more detail in the following section.

1.2.2. Tuning of Metal Properties

Crystalline zeolites are made up of numerous crystallographic-defined tetrahedral sites (T-sites, TO_4), the number and type of T-sites is indicative of an individual framework type, which governs the structural characteristics of the zeolite. The characteristics and properties of a zeolite can be further modified through the substitution of Si^{4+} for a trivalent cation, typically Al^{3+} . When this substitution occurs, a delocalised negative charge is created that requires a counter-ion to retain electroneutrality in the framework. It also results in a distortion to the silicate rings, owing to the increase in bond length from 0.163 nm to 0.187 nm that can affect hydrophobicity and structure of the zeolite.⁷²

The effect of adding a trivalent T-atom to the zeolite structure alters the electronic and structural parameters of the zeolite. Furthermore, the precise T-sites where the Al^{3+} substitution

occurs can have major implications on zeolite properties.⁷³ Al³⁺ siting within a zeolite lattice can describe the phenomena of an Al³⁺ atom being located at a distinct T-site in the framework. In high silica zeolites (i.e SiO₂/Al₂O₃ ≥ 8), the siting of Al³⁺ is governed by Löwenstein's rule, which forbids the formation of Al-O-Al linkages within the framework. Such materials are also governed by Takaishi's rule, which dictates that only one Al³⁺ can occupy a 5MR, and Dempsey's rule, where zeolites will tend towards an equal distribution of Al³⁺ across the zeolite matrix.⁷³ There are no experimental reports of synthetic zeolites having a SiO₂/Al₂O ratio less than 1, however density functional theory (DFT) calculations of high alumina CHA and SSZ zeolites have shown that such ratios are feasible in the absence of H₂O, implying that kinetic phenomena can be exploited to overcome Löwenstein's rule.²⁴ The practical limitations of this occurring are highly unlikely though, due to the electronic repulsion that would arise from the counter-balancing protons required to maintain an electroneutral framework. For the purposes of this thesis, the discussion shall focus on the Al³⁺ siting in high silica zeolites and the effect of properties relating to Al³⁺ siting.

Determination of Al³⁺ siting in high silica zeolites can be achieved through a combination of Co titration UV-vis spectroscopy and ²⁹Si MAS-NMR.^{74,75} These methodologies have been shown to be able to distinguish between four distinct Al-O-(SiO)_n-Al sequences:

- single-atom, Al-O-(Si-O)₁-Al sequences could be distinguished by ²⁹Si MAS-NMR.
- Al-O-(Si-O)_{2≤n≤3}-Al, which is indicative of paired Al in a single ring, could be quantified from titration of the negatively charged [AlO₄]⁻ with divalent Co²⁺ ions and this absorbance can be measured by NIR-vis-UV spectroscopy.
- Al-O-(Si-O)_{n≥2}-Al that indicates paired Al located in neighbouring rings and can be quantified by titration with [Co(H₂O)₆]²⁺.
- Al-O-(Si-O)_{n≥2}-Al, where Al are not in close proximity, thus unable to be coordinated to Co²⁺ complexes, and is quantified by subtraction of the other sequences from total [Al].

The siting of Al³⁺ has been shown to be influenced by the positively-charged template ion, which could interact with the negatively charged [AlO₄]⁻ in the aluminosilicate gel and form preferential Al sites.⁷⁵ In the presence of TPA, Al³⁺ was primarily located as paired species within the intersectional cavities of ZSM-5.⁸⁷ It was speculated that during the primary stages of zeolite synthesis, aluminosilicate species formed that were preferentially directed towards the densely charged quaternary ammonium ion, which formed the channel intersections in the crystallised materials.⁷⁵ Changing the template for a small, inorganic cation, such as Na⁺

resulted in a high-distribution of isolated Al atoms, located within the straight and sinusoidal channel walls of ZSM-5, as the channels were not sterically hindered by the presence of a bulky template. Understanding how synthetic parameters affects Al³⁺ siting in different zeolite structures should impart greater control over specific zeolite properties.

The effect of control of Al³⁺ siting was further demonstrated by Tatsumi *et al.*, where it was speculated that ZSM-5 prepared with TPA⁺ only was more selective for the cracking of branched 3-methylpentane, in comparison with straight chain n-hexane.⁷⁶ It was stipulated that the high density of intersectional Al³⁺ led to an increase in Brønsted acid site density at the intersection that was crucial for branched alkane selectivity. A similar effect was observed in the synthesis of H-CHA for methanol dehydration.⁷⁷ The addition of an inorganic cation, such as Na⁺, to the synthesis gel along with tetramethyladamantium hydroxide OSDA, favoured the formation of Al³⁺ pairs, Al-O-(Si-O)₂-Al, in zeolite channels, because a second [AlO₄]⁻ was required to counterbalance the additional positive charge of the sodium cation. The authors demonstrated that close siting of the Al³⁺ pairs and proximal H⁺ sites within H-CHA increased the rate of methanol dehydration by an order of magnitude.⁷⁷

1.3. Modification of zeolites with Transition Metal Ions

The catalytic abilities of zeolites can be enhanced by the addition of transition metal ion (TMIs) species to modify the zeolite properties. As explored in Section 1.1, zeolites are widely employed in a variety of catalytic processes, because the microporous nature allows for reactant/ product selectivity through steric constraints, known as shape selectivity. Furthermore, additional functionality can be introduced through isomorphous substitution of the T atom in the TO₄ tetrahedral group with main group or transition group metal cations, providing electroneutrality of the framework is maintained.

It is believed that TMI-zeolites can bridge the gap between well-defined, homogeneous metal complexes, which have high TOFs and product selectivity. Additionally, solid heterogeneous catalysts combine the advantages of well-defined transition metal catalysts with those of zeolites.²⁷ Furthermore, TMI-zeolites have been labelled as “*biomimetic*”, as the micropore networks of the zeolites can lead to the stabilisation of highly active metal-substrate complexes, responsible for catalytic activity.⁷² This is analogous to the function of enzymes, which are highly selective catalysts, due to “*lock and key*” substrate specificity and also confer “shape selectivity” of desired reaction products due to the shape of the active site.⁷⁸ Enzymatic catalysts are highly efficient catalysts that are active under a narrow range of conditions, yet the use of enzymes in many industrial applications is limited by the difficulty in large scale

production, the expense of growth media and the fragility of the enzymes. On the other hand, zeolites require only a few starting materials to synthesis, and are much more robust, especially under harsh reaction conditions.⁷⁹

Biomimetic zeolites can be prepared through addition of isolated transition metal cations into the zeolite structure, which imparts the desired functionality to the catalyst. The method of transition metal incorporation into the zeolite framework can have a profound impact on the coordination and geometry of the metal species, which impacts on the reactivity of the metal centre. Three potential configuration of metal centres are demonstrated in Figure 7.⁸⁰ The route of metal incorporation is dependent on the method of preparation, with notable methods including:

- Encapsulation of metal clusters within the zeolite framework, resulting in supported metal oxide clusters.
- Post-synthetic methods, such as ion-exchange, impregnation, chemical vapour deposition and ligand exchange, which leads to the formation of isolated and oligomeric metal clusters.
- Isomorphous substitution of framework Si^{4+} for M^{x+} ($x = 4$ or 3), where single ions are substituted into tetrahedral positions within the zeolite framework.

The method used to modify the zeolite affects the dispersion and size of the metal centres, which form within the zeolite, which impacts the chemical and physical properties of the catalyst.

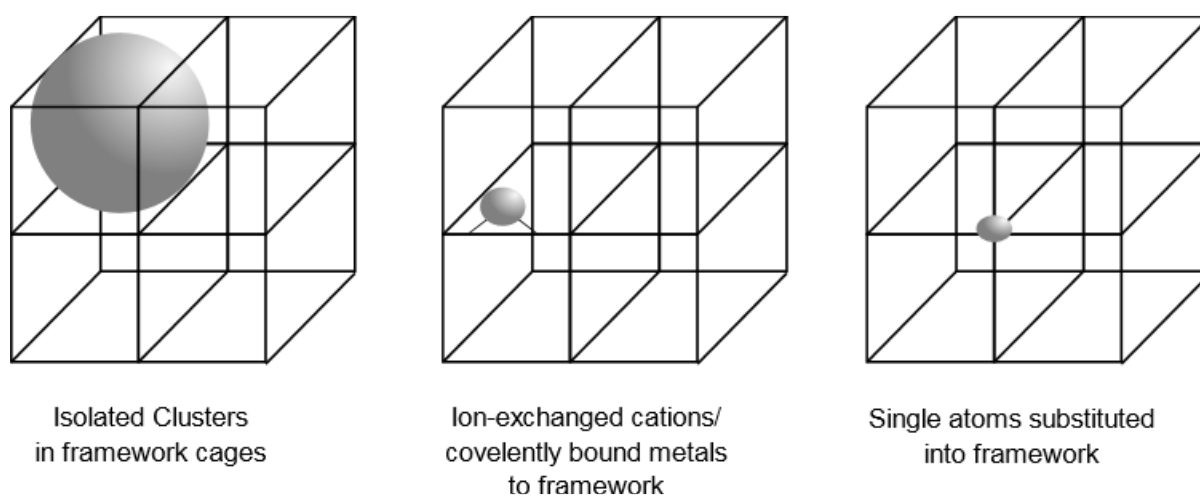
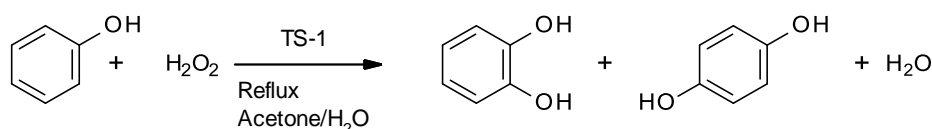


Figure 7 Potential configurations of different TMI modified zeolites. Adapted with permission from reference 80. Copyright 2018 American Chemical Society.

The synthesis of wide variety of TMI modified zeolites has been investigated to determine the effect of preparation on catalytic performance. These include Ti,^{14,81} Fe,^{28,80,82,83} Cu,^{84–87} Sn,^{88–90} Hf,⁹¹ and Mo.⁹² When taken into consideration, these studies emphasise that inclusion of different metal ions can strongly influence the resulting properties of the final crystallised zeolite catalyst. Hence, a variety of processes have been studied including selective oxidations of methane to methanol,^{93–97} benzene to phenol oxidation,^{98–100} Baeyer-Villiger oxidations of ketones,^{101–104} selective catalytic reduction of NO_x,^{105–107} biomass conversion,^{38,103,108,109} and methane dehydroaromatisation^{92,110,111}.

Oxidation reactions of organic functional groups can be promoted using zeolites modified by Cu, Fe or Ti ions.^{14,87,94,99,112–114} Fe and Cu are typically utilised in oxidation of relatively inactive alkanes, such as methane, as these catalysts have been shown to be selective to methanol in a single step at low temperatures (50 °C) by Methane Monooxygenase enzymes, which contain Fe and Cu centres.^{87,96,115,116} It is thought that they work by activating the oxidant (typically N₂O or H₂O₂) to form a highly reactive oxygen species that can activate relatively inactive C-H bonds in CH₄.^{97,112,117,118} This is advantageous to more conventional CH₄ oxidation methods, which involve either high temperatures or highly acidic media, which are not desirable on larger scales. Yet, there are still unresolved issues regarding catalyst turnover and methanol selectivity, which could be resolved by providing further evidence for the structure of the active metal site in these catalysts.

Titanosilicates, such as titanium silicalite-1 (TS-1) have been shown to be effective oxidation catalysts for several industrially relevant organic reactions, including epoxidation,^{119,120} benzene oxidation^{99,121} and *n*-hexene oxidation.¹⁴ TS-1 was identified as an active catalyst for the oxidation of phenol using H₂O₂ as an oxidant, with the *ortho*- and *para*- substituted dihydroxybenzenes the selective reaction products (Equation 1).¹²¹ Over time, the formation of heavy fractions was observed, resulting in catalyst deactivation by coking. The TS-1 catalyst could be regenerated by high temperature removal of the coke and activity was restored.¹²¹

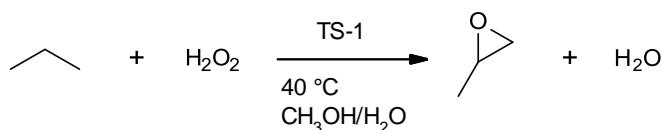


Equation 1 TS-1 catalysed phenol oxidation as reported by Romano *et al.*¹²¹

The authors suggested that yield and selectivity of phenol oxidation was dependant on the purity, crystal size and TiO₂/ SiO₂ ratio, research aimed to develop better synthetic methods to

control the properties of TS-1.^{81,99} A post-synthetic modification was developed by the group of Ungarelli, which utilised an etching agent, NH_4HF_2 to remove extraframework Ti from the zeolite, which would remove spectator Ti species.⁹⁹ Phenol selectivity was increased from 83 to 94 %, the authors stipulated that the post-treatment resulted in changes to the active site that enhanced selectivity to the desired *ortho*- and *para*-dihydroxybenzenes.

Furthermore, TS-1 is a highly active and selective catalyst for propane epoxidation, due to its ability to selectively activate H_2O_2 , thus minimising oxidant loss.¹¹⁹ TS-1 was prepared by hydrothermal methods, substituting Ti into the MFI framework. The catalyst demonstrated remarkable conversion and propylene oxide selectivity (Equation 2). It was proposed that the high activity of TS-1 was due to the unique ability of isolated Ti ions to form an activated hydroperoxyl species within the lattice, though this was not experimentally observed. However, catalyst deactivation was observed over time and regeneration of the catalyst was required to restore initial catalytic performance. Even though regeneration attempts were successful, it limits the applicability of the catalyst on large scales, due to the need to add a high-temperature step to the catalytic process.



Equation 2 TS-1 catalysed epoxidation of propane as reported by Clerici *et al.*¹¹⁹

It is notable from the given examples that modification of a zeolite with transition metal ions is advantageous for several processes. Consideration should be given for each process to the TMI suitable for the application. For example, Fe is prominent in TMI-zeolites for several oxidation reactions,^{28,96,115–117,122,123} thus would make a sensible starting point when choosing a suitable catalyst for oxidation processes. Yet, it has also been suggested that the method of metal incorporation is another key consideration, as the way in which the modified zeolite is prepared can affect the TMI speciation, coordination and geometry of the within the zeolite lattice, which impacts catalytic performance.^{80,82} The next section will explore the methods of TMI incorporation into zeolites and highlight some of the advantages and disadvantages of each method.

1.3.1. Methods of TMI Modification of Zeolites

Transition metals can be incorporated into a zeolite framework either by top-down or bottom-up procedures. The route of incorporation has important implications on the properties and performance of the metal centres in zeolites.

1.3.1.1. Top-down approaches

Top-down approaches to TMI-zeolites involve post-synthetic methods of adding metal precursors to an already synthesised crystalline zeolite. The most common way to prepare TMI-zeolites is by wet-impregnation of the parent zeolite with a metal salt precursor. The zeolite is typically refluxed in an aqueous solution of a metal precursor complex, filtered, dried and then calcined to remove the ligands and afford the TMI-zeolite as shown in Figure 8. Multiple ion-exchanges may be required to reach the full ion-exchange capacity of the zeolite. The cation-exchange capacity of a zeolite is a measure of the number of Bronsted acid sites created from the substitution of Si^{4+} for Al^{3+} , which creates an overall negative charge in the framework. Cations, usually Na^+ during the synthesis step, can retain electroneutrality of the framework, however, this process increases the number of steps required for activation and typically requires an extra, high-temperature step to decompose the ligands of the complexing metal.

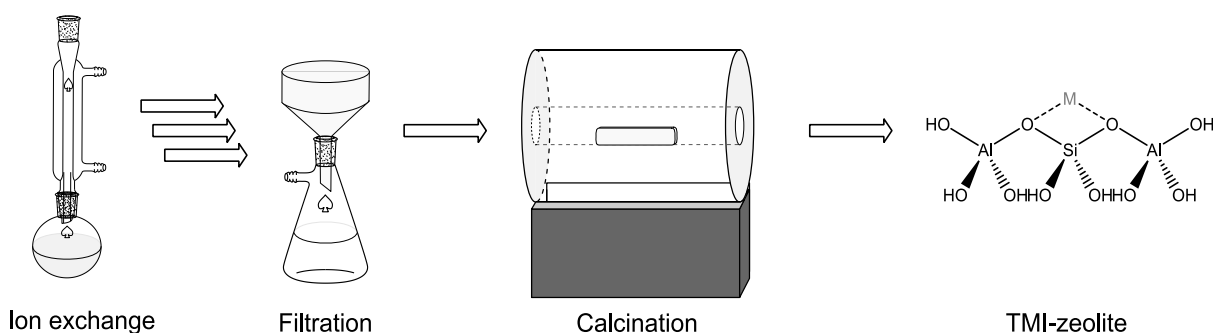


Figure 8 Schematic of wet ion-exchange procedure for preparation of TMI-zeolites.

Due to the simplicity of this method, such materials have been prepared this way throughout the literature. However, metal salt precursors are highly sensitive to pH; too low or too high pH can lead to precipitation of the metal salt, or lead to unwanted side reactions. Moreover, these methods do not exert much control over metal speciation, due to hydration of the metal cations. Hydrated metal cations also have larger ionic radii than non-hydrated metal cations, which can lead to an uneven distribution of metal species within the framework, limited by size constraints of the zeolite pore system. Furthermore, electrostatic attractions between metal cations on the surface of the zeolite can lead to an uneven distribution of metal centres throughout the lattice, which could increase the probability of forming inactive, spectator

species. Spectator species are TMI species that are not thought to be catalytically active, thus formation of spectator species could negatively impact catalytic performance.¹²²

To overcome the issue of using hydrated metal cations, solid-state ion-exchange (SSIE) preparations have been reported as an alternative (Figure 9).¹²² The parent zeolite is ground with a metal precursor salt (e.g. oxides, halides), and the resulting solid-solution is calcined to afford the TMI-zeolite. Upon calcination, the ligands are removed and the metal migrates from the external zeolite surface to the internal zeolite channels to form isolated metal centres, as demonstrated in Figure 10. The preparation of solid Lewis-acid catalysts through SSIE of Sn⁴⁺ and Zr⁴⁺ in zeolite Beta showed enhanced catalytic activity for glyceraldehyde isomerisation compared with Sn- or Zr-beta prepared by wet-ion exchange.¹²² It was suggested that SSIE modification was advantageous, as it allowed for better control of exchange sites and metal site distribution, because the precursor salt was not required in excess and fewer processing steps were required. Fewer processing steps reduces the probability of forming larger metal clusters in the zeolite pore network, leading to poorer catalytic performance. Furthermore, because not all metal salts are water soluble, SSIE can be used to broaden the scope of metal ions that can be incorporated into the zeolite framework.

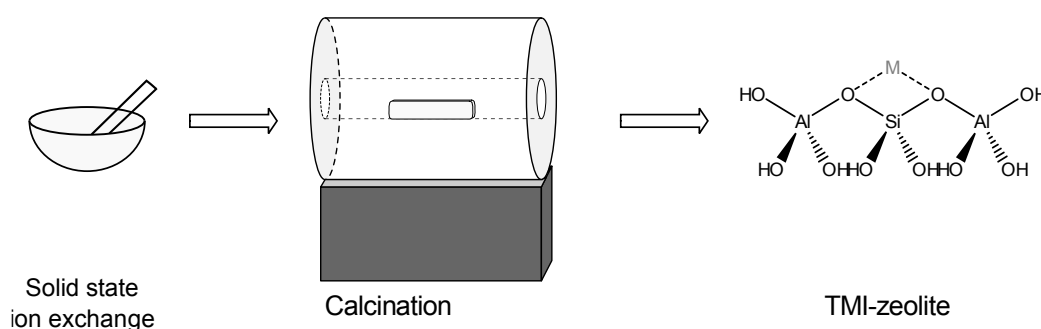


Figure 9 Schematic of solid-state ion-exchange for preparation of TMI-zeolites.

Another top-down approach is chemical vapour deposition (CVD), which utilises volatile and reactive metal salts (e.g. chlorides, alkyls, carbonyls) to deposit the metal on the surface of zeolite channels under anhydrous conditions (Figure 10).¹²⁴ This results in a stoichiometric reaction between Brønsted acid sites of the zeolite and the metal precursor to form an isolated, extra framework metal species. CVD reflects the ambition to design solid-state, single atom catalysts to provide a recoverable, well-defined metal catalyst for industrial application.²⁵ Studies by Gates *et al.* have demonstrated that single atom iridium complexes prepared by CVD were most stable when supported on a zeolite framework, as opposed to an amorphous support. This observation indicates the importance of the framework for the stabilisation of

single-atom metal complexes.¹²⁵ The mechanism of stabilisation could vary between zeolites and the choice of metal, and leads to further questions regarding the stabilisation role of the (alumino)-silicate framework.

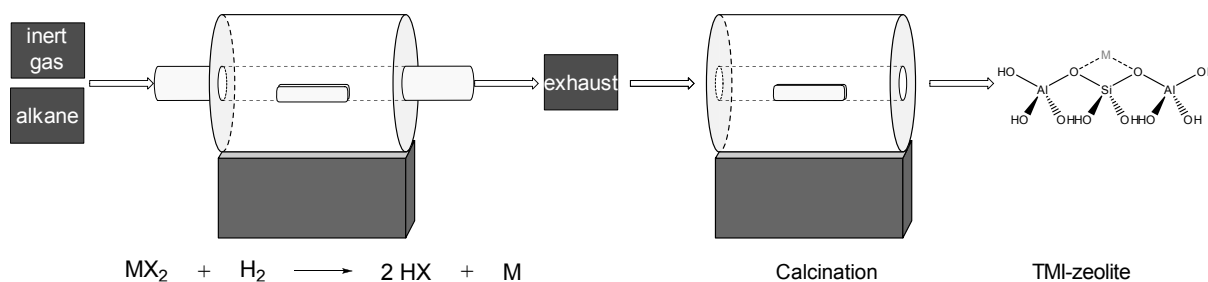


Figure 10 Schematic of chemical vapour deposition for preparation of TMI-zeolites.

Top-down approaches to TMI-zeolites provide facile and cost-effective routes to metal incorporated zeolites, yet, such approaches only afford extra framework metal species that can interact with the surface of the zeolite.²⁵ It is not possible to incorporate other metals into the framework post-zeolite synthesis without the possibility of sacrificing the framework.

1.3.1.2. Bottom-up approaches

To incorporate metals into the framework, metal cations can be introduced to the framework lattice during zeolite crystallisation, as shown in Figure 10. Under hydrothermal conditions, metal cations can substitute Si^{4+} to afford $[\text{SiO-M-OSi}]_n$, where M can be Al, Ga, Ge, Sn, Ti, Fe, Cu (Figure 11).^{25,115} In Section 1.2, the parameters of hydrothermal synthesis, such as gel aging time, crystallisation time and temperature, are shown to have a major impact on the properties of the zeolite, and this is true for TMI-exchanged zeolites. Key parameters also need to be considered in the preparation of metal-substituted frameworks, such as the pH of the solution, the size and charge of the metal cation. The pH can be critical to the formation of the desired metal-zeolite, as the zero-point charge of the metal precursor may prevent it being sufficiently charged for framework incorporation. Yet, zeolites are typically synthesised at high pH, to ensure dissolution of silicate species into the gel, which can be problematic as some metals are most stable at lower pH. At pHs greater than the zero-point charge of a metal complex, inactive metal hydroxide species can form, preventing deposition of cationic metal species within the zeolite lattice. Adjustment of the pH and selection of suitable metal precursors is crucial for the success of bottom-down approaches. Through careful selection of synthesis parameters, isomorphous substitution of TMI during hydrothermal synthesis allows for the formation of well-defined metal species within the zeolite framework that can be harnessed in catalytic processes.⁸⁰

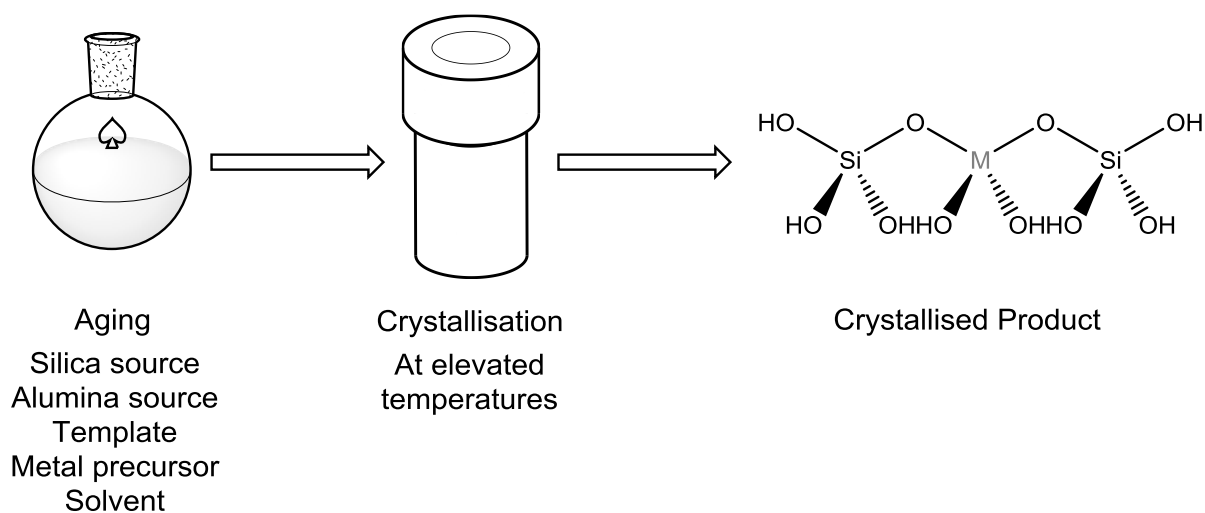


Figure 11 Generalised schematic of preparation of isomorphous substituted TMI-zeolites by hydrothermal methods, where M indicates the substituted metal species in the zeolite framework.

Ti- and Fe-silicates are TMI-zeolites commonly synthesised by isomorphous substitution, as it can prepare isolated TMI species embedded in the MFI framework.^{81,122} The group of Tatsumi demonstrated that TS-1 could be crystallised at $\text{SiO}_2/\text{TiO}_2$ ratios as low as 38, without observation of extra framework or clustered Ti species by DRUV-vis spectroscopy.⁸¹ The absence of extra framework Ti species in these samples resulted in remarkable aromatic oxidation activity compared with catalysts prepared by alternative methods, demonstrating the control of Ti speciation through isomorphous substitution. A tentative mechanism for the isomorphous substitution of Ti^{4+} was proposed by Tatsumi.⁸¹ It was suggested that the addition of base to the initial mixture resulted in the instant formation of a solid-gel phase. Agglomeration of gel-particles lead to the formation of nuclei and onset of crystal growth. As zeolite crystals grew, the solid underwent coalescence and reorganisation of the solid-gel phase, during which time solution-free $\text{Ti}(\text{OH})_4$ species could incorporate into the framework, which was supported by FTIR, SEM and ^{29}Si MAS-NMR. Yet, *ex-situ* methods do not represent real-time processes and observed signals may not be representative of the process as the sample is removed from synthesis conditions, thus are not directly representative of the crystal growth mechanism. The application of *in-situ* spectroscopic methods are needed to represent and model the crystallisation mechanisms that are taking place, but can be difficult to employ under the harsh conditions of hydrothermal zeolite synthesis, and there are only few examples in the literature where *in-situ* studies have been performed, which will be discussed in Section 1.3.1.3.

Hydrothermal synthesis of Fe-silicalite was reported by Berlier *et al.*, where incorporation of Fe into MFI framework was observed post crystallisation, however, further thermal treatment

was needed to activate the material for benzene hydroxylation.¹²² The thermal activation under oxidative conditions, resulted in the extraction of framework trivalent Fe³⁺ species, to form extra framework divalent Fe²⁺, which was observed by FTIR and EXAFS. The coincidence of Fe²⁺ with N₂O activation led the authors to suggest this as the activating species (also known as α -Fe) in benzene hydroxylation.¹²² Compared with Fe-silicalite prepared by top-down approaches, Fe-silicalite prepared by isomorphous substitution and subsequent extraction of framework Fe was observed to produce more active catalysts in oxidation processes, due to lower metal loadings that could be utilised that resulted in the formation of fewer inactive spectator metal species.⁸⁰

Further to this, the substitution of Al into the framework, and the distribution of Al, could have major implications on the tailoring the speciation of transition metal ions in TMI-zeolites.¹²⁶ The speciation of copper, along with the oxidation state of the incorporated Cu, in zeolites can be difficult to qualify, due to the heterogeneous distribution of species formed within a zeolite matrix.⁷² Utilising a combination of DFT calculations and *in-situ* experimental studies, it was shown that different Cu species formed at paired and unpaired Al sites within SSZ-13 during the selective catalytic reduction (SCR) of NO_x with NH₃.¹²⁶ However, changes in speciation were observed under the differing reaction conditions, which may have affected the authors ability to distinguish key Cu species, which could have implications on the design of TMI-zeolites and active-site control could be managed through manipulation synthetic parameters. di Iorio *et al.* reported that crystallisation of H-CHA performed under the same conditions produced materials with varying Al³⁺ pair distributions.⁷⁷ This observation suggests that great caution should be exercised in future studies in the development of synthetic protocols for TMI-zeolites, as small synthetic variations can result in large variations in zeolite properties, which can have an impact on catalyst performance.

1.3.1.3. *In-situ* Observation of Isomorphous Substitution of TMI During Crystallisation

In Section 1.3.1.2, *in-situ* methods were suggesting as a method to better study the substitution of TMIs into zeolite frameworks, which could lead to optimisation of synthetic methods. A paper published by Li *et al.* reported the use of a modified autoclave, with a reinforced viewing window, as pictured in Figure 12, that allowed for *in-situ* resonance Raman observation of the isomorphous substitution of Fe during the crystallisation of Fe-MFI at elevated temperatures.¹²⁷ It was proposed that crystalline Fe-ZSM-5 is formed by aggregation of [Fe(OSi)₄] tetrahedral units and of 5- and 6 membered rings (6MR), characteristic of MFI framework, which form early on in the synthesis. The formation of crystal structure was observed by the disappearance

of amorphous SiO_2 band at 460 cm^{-1} , with increasing intensity of the crystalline SiO_2 vibrational stretch of 5MR at 380 cm^{-1} . Concurrently, the appearance of Fe-O-Si vibrational modes at $520, 1020, 1120$ and 1165 cm^{-1} correlated with the onset of MFI crystal growth. Thus, it was proposed from UV-Raman spectra and supported by HRTEM, that crystallisation proceeded via aggregation of amorphous aluminosilicate particles and Fe tetrahedra in the gel phase, to form Fe-ZSM-5 crystals, as demonstrated in Figure 13.

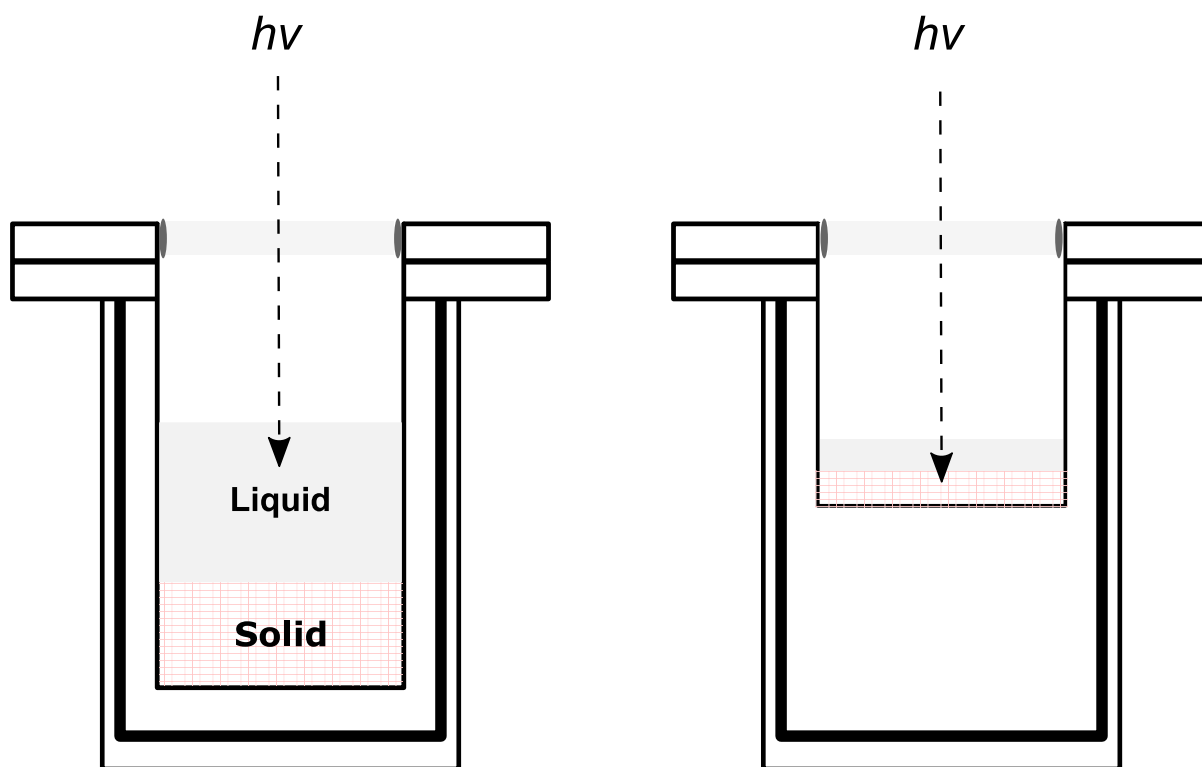


Figure 12 Schematic of the modified autoclaves for *in-situ* observation of incorporation of Fe^{3+} into MFI framework. Left, cell for study of the liquid phase; Right, cell for study of the solid phase. Adapted with permission from reference 127. Copyright 2009 American Chemical Society.

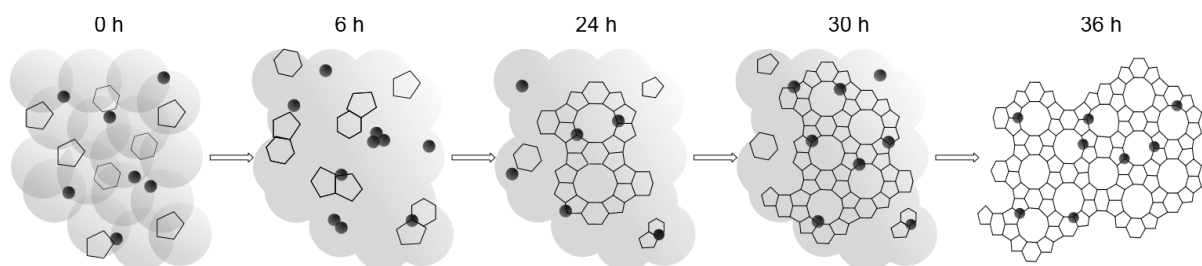


Figure 13 Proposed mechanism by Li *et al.* for isomorphous substitution of Fe^{3+} (represented by black circles) into MFI framework, under hydrothermal conditions. Adapted with permission from reference 128. Copyright 2009 Wiley.

The application of *in-situ* UV-Raman could have a key role in studying the substitution of metal cations under high temperature and pressure conditions, yet, not all metals are Raman active, so different TMI-zeolites may not be able to be studied in this way and alternatives should be pursued. Furthermore, the proposed mechanism for one material may not describe the kinetics of crystallisation of another material. Other techniques should be considered and used alongside Raman studies to measure crystal growth mechanisms of TMI-substitution in zeolite frameworks.

1.3.2. Summary

Many advancements have been made in the design and understanding of dispersed transition-metal species that form on interaction with the zeolite framework for catalytic applications. The method of preparation can have a major impact on the type of species formed and the distribution of species at distinct crystallographic location within the zeolite. Yet, real-time observation of TMI species within a complex zeolitic lattice is complicated, due to the uneven distribution of metal species that can potentially form. Identification of well-dispersed metal centres can be achieved through a combination of DFT modelling studies and advanced metal-selective spectroscopy.⁷² For example, a successful combinatorial approach was reported by di Iorio *et al.*, who utilised DFT studies along with vibrational and absorption spectroscopies, X-ray scattering and titration experiments, to identify various Cu species in SSZ-13.¹²⁶ Further, the development of *in-situ*, and more recently, *operando* studies allow for the study of TMI-zeolites under respective reaction conditions.^{128,129} Ongoing work is focused on the continuing development of more sophisticated techniques to provide a more in-depth understanding of “*synthesis-structure-function*”⁷⁷ relationships and aid in the design of highly active TMI-zeolite catalysts. Moreover, the identification of active metal centres is promising for the development of heterogeneous catalysts with well-defined metal centres, which would be ideal catalysts for chemical synthesis.

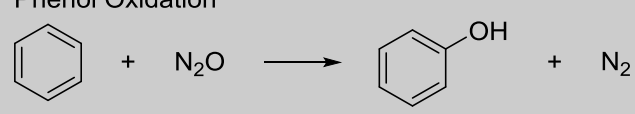
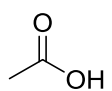
1.4. Fe-Zeolites for Catalytic Oxidations

Among the various reactions catalysed by TMI-zeolites, the partial oxidation of CH₄ is of great interest. This is due to the large economic and environmental benefits of oxidising CH₄ to a more active and more readily transportable compound, such as CH₃OH, in a single step. The use of the correct catalyst and oxidant for this transformation would reduce the energy requirements needed to activate relatively inert CH₄. Thus, a large body of research has been focused on the development of such catalysts, however, issues with selectivity, poor conversion and catalyst stability prevent wide-scale application of direct partial oxidation measures.^{29,36}

Section 1.3 discussed the development and study of transition metal zeolites, and demonstrated that catalyst preparation can impact catalytic performance; thus consideration of catalyst design is critical when optimising catalytic processes. Many different TMIs can be incorporated into various zeolitic framework types and can be tailored to the desired transformation (Table 1, Section 1.3). For example, the use of Fe-substituted zeolites has been extensively covered, and some example reactions are given in Table 2 to demonstrate the wide applicability of Fe-based catalysts. However, there are limited examples of Fe-zeolites utilised in industrial processes, irrespective of the reportedly high levels of catalytic performance. In fact, the only known industrial application of Fe-zeolites is the AlphOx process, which utilises Fe-ZSM-5 as a catalyst for the hydroxylation of benzene to selectively afford phenol, yet the AlphOx process did not make it past the pilot plant stage.¹³⁰ The poor availability of the N₂O oxidant and catalyst deactivation due to formation of coke species in the zeolite micropores were cited as reasons for the lack of commercial success.^{94,131} Moreover, the lack of clear consensus on the nature of the active Fe sites in the Fe-zeolite catalysts may have contributed to the failure of Fe-ZSM-5 as an industrial oxidation catalyst. Even though the recent development of more advanced spectroscopic methods has allowed better observation of active metal sites within the zeolite lattice, there can be many experimental factors that can affect the results.⁷² The formation of inactive spectator Fe species, creates a challenge for identifying and characterising key active species.

Iron catalysts are typically employed in a range of oxidation reactions, owing to a relatively high redox potential (+ 0.77 eV) and ability to readily access various oxidation states; Fe²⁺, Fe³⁺ and Fe⁴⁺ are readily observed. Furthermore, Fe is highly abundant and relatively non-toxic, thus can be considered a “green” metal catalyst, according to Sheldon’s “*Principles of Green Chemistry*”.¹³² The utilisation of greener processes is desirable across all areas of chemistry, to minimise any environmental impact of beneficial chemical technologies. Some desirable transformations, catalysed by Fe-ZSM-5, are given in Table 1.

Table 1 Examples of Fe-ZSM-5 catalysts.

Reaction	References
Phenol Oxidation 	82, 107, 120
Selective Catalytic Reduction of NO _x NO _x + NH ₃ → N ₂ + H ₂ O	89, 90
Partial Methane Oxidation CH ₄ + N ₂ O → CH ₃ OH + N ₂ CH ₄ + H ₂ O ₂ → CH ₃ OH + H ₂ O	80, 81, 100, 101, 106, 107, 123
Ethane Oxidation C ₂ H ₆ + H ₂ O ₂ →  + H ₂ O	97

The use of Fe-zeolite catalysts is reported across a range of industrially relevant oxidation reactions, as listed in Table 1, but, there remains some issues in the use of Fe-ZSM-5 for the reactions listed in Table 1 and the lack on consistent understanding of the active Fe³⁺ species within the zeolite lattice can prevent process improvements and application of Fe-ZSM-5 on a larger scale.^{117,118,133–135} Furthermore, reproducible synthesis of the Fe-zeolite catalyst at large scales, required for industrial processes, is difficult, as small differences in Fe distribution within the zeolite can lead to differences in catalytic performance. On a large scale, differences in performance can result in unpredictable productivity and loss of profits. To alleviate such issues, a greater understanding of the active site and how to consistently produce catalysts with equal Fe distribution is needed.

Another issue with some of the oxidation reactions is the choice of oxidant. N₂O is not readily available, as the main source of N₂O is as a by-product in nitric acid production, so this is limited by demand.¹³¹ This would become economically prohibitive at larger scales, as the oxidant would cost more than the worth of the product. There are no reports of Fe-based catalysts activating molecular oxygen, the ultimate green oxidant, and the need for alternative oxidants is needed.

H₂O₂ is a more readily available oxidant for oxidation processes, and the economics of using H₂O₂ does not outweigh the value of the oxidised products, yet there are issues with selectivity when utilising H₂O₂ in the presence of an Fe-based catalyst.^{97,116} Fe can act as a Fenton's catalyst, meaning H₂O₂ can undergo non-selective decomposition to form hydroxyl radicals,

which initiates a cycle that results in the loss of active oxidant. Establishing methods to reduce hydroxyl radical formation in Fe-ZSM-5 catalysts is crucial for optimising catalytic activity. Furthermore, for utilisation of H₂O₂ as an oxidant in large scale oxidative processes to be viable, the H₂O₂ selectivity (that is, the amount of H₂O₂ that is incorporated into the final products) should be, ideally, 1:1 or 1:2 (reactant: oxidant) for the process to be feasible. Research is ongoing to tune the H₂O₂ selectivity in Fe-zeolite catalysts.^{112,135}

Developing one-step oxidation processes for several key reactions would be critical in developing greener processes. Partial oxidation of CH₄ to form CH₃OH, would be highly beneficial on an industrial scale, due to the large economic and environmental impacts, as will be discussed in Section 1.4.2.

1.4.2. Partial Methane Oxidation

Methane has emerged as a promising alternative to petroleum as an energy source and chemical feedstock, due to the high abundance of CH₄ in natural gas reserves and methane hydrates.¹³⁶ A large percentage of global CH₄ supplies are remotely located, which makes transportation to processing sites, meaning vast quantities of CH₄ cannot be utilised. To address the issue of transporting a gas from remote locations, a facile process for turning CH₄ into a liquid feedstock, such as methanol, CH₃OH, is needed, which can be carried out at the source, without the need for expensive processing and transportation, meaning remotely located CH₄ reserves can be utilised as a potential energy source or feedstock.

Current industrial technologies convert CH₄ into value-added products via the production of synthesis gas by steam reformation of CH₄ (Equation 1) at temperatures > 600 °C, in the presence of a Ni-based catalyst.¹³⁷ The reaction is highly endothermic ($\Delta H_{298\text{ K}} = + 206 \text{ kJ mol}^{-1}$) and relatively high temperatures are required to overcome this barrier and drive the equilibrium towards CO formation. Syngas can then be converted to methanol via hydrogenation of CO (Equation 2), which is an exothermic reaction ($\Delta H_{298\text{ K}} = - 91 \text{ kJ mol}^{-1}$), which utilises Cu-based catalysts at temperatures between 200-300 °C. Yet, step (2) is limited by the thermodynamic equilibrium, which limits CO conversion.¹³⁸



A single-step process is highly difficult due to the high input of energy required to overcome the high bond dissociation energy of CH₄ (C-H_{BDE} = 438.8 kJ mol⁻¹).¹³⁹ Steam-reforming of

CH₄ is an efficient and selective method of activating CH₄, thus allowing valorisation into CH₃OH, higher alkanes, alkenes and aromatics, yet this process is highly energy intensive and temperatures in excess of 500 °C are required. Large capital investments are required to construct and operate such facilities, and consequently, offshore CH₄ processing via syngas is undesirable to investors, due to the technical difficulties and the associated economic impact of carrying out this process. Therefore, it is of interest to develop an active catalyst that can activate and functionalise CH₄ in a single step, which can be selective and is active at relatively low temperatures.

One of the reasons effective CH₄ transformation still eludes researchers is due to the high stability of the C-H bonds.¹³⁹ CH₄ is also a perfectly symmetrical tetrahedron, which allows for delocalisation of occupied and unoccupied molecular orbitals. This effectively stabilises the highest occupied molecular orbitals (HOMO) and destabilises the lowest unoccupied molecular orbitals (LUMO), making CH₄ stable to both electrophilic and nucleophilic attack. Thus, strategies are required that can overcome the high bond dissociation energy at much lower temperatures.

Alternative methods of valorisation have been pursued by many researchers over the past thirty years, owing to the relevance of this topic.³⁶ Some potential routes for CH₄ valorisation are shown in Figure 14.

- partial oxidation, to afford methanol, formic acid and formaldehyde.¹⁴⁰
- oxidative methane coupling to afford higher molecular weight alkenes/ fuels.¹⁴¹
- oxidative carbonylation to afford acetone and acetic acid.¹⁴²
- aromatisation to afford aromatic compounds that are commonly found in bulk-chemical synthesis.¹⁴³

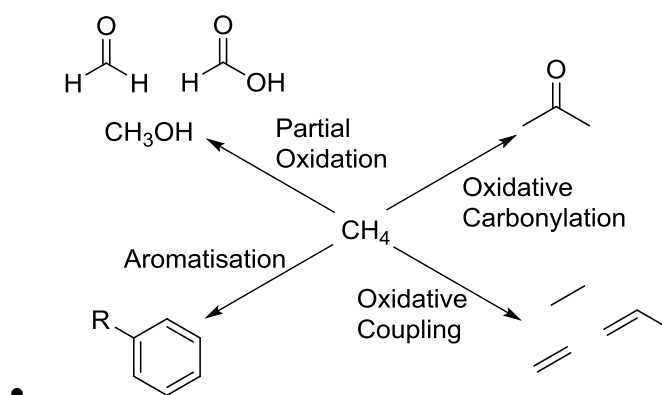


Figure 14 Potential single-step valorisation reactions of CH₄.

However, methods are still lacking the efficiency and selectivity compared to the syngas routes. Moreover, issues of selectivity arise from the stability of CH₄, and the reaction conditions required to activate CH₄, which favour the formation of more energetically stable products, such as CO₂, an environmentally and economically undesirable product. The challenges given need to be resolved to allow technologies to be adopted by industry for ease of CH₄ valorisation. It should be noted that one-step, partial oxidation of CH₄ is not impossible. For example, partial CH₄ oxidation can be performed in nature at ambient temperatures by enzymes found in *Methylococcus capsulatus* (Bath) bacteria,¹⁴⁴ retaining 100 % selectivity to methanol, which has led research groups to explore the design of catalysts that can activate and oxidise CH₄ analogously to these enzymes.

1.4.2.1. Soluble Methane Monooxygenase (sMMO) Enzymes

The advent of biologically-inspired, “*biomimetic*” catalysts has attracted a wealth of research in the past 20 years.⁷⁸ Metalloenzymes demonstrate high substrate specificity, regio- and stereoselectivity and high turnover frequencies, yet can operate at ambient conditions. Furthermore, sMMO can activate molecular O₂, the most environmentally benign oxidant, which would be the ideal oxidant for direct oxidation processes. These features are desirable in the design of selective catalysts, and why chemo-catalysis aspires to enzymatic catalysis. There are three classes of naturally occurring, Fe-containing enzymes: heme, non-heme dinuclear and non-heme mononuclear.⁷⁸ The key to reactivity lies in the ability of each of these active Fe centres to activate molecular oxygen, thus forming an active superoxo species. The superoxo species can gain a proton to form a peroxo species, before cleavage of the O-O bond forms an active, Fe⁴⁺-oxo species, which is able to activate CH₄ under relatively mild conditions.

The existence of a binuclear Fe centre in sMMO was initially observed by UV-absorption, Electron Paramagnetic Resonance (EPR) and Mössbauer studies.^{145, 146} Additional spectroscopic and crystallographic studies have defined a candidate for the active species for O₂ and CH₄ activation.¹⁴⁷ Extended X-ray absorption fine structure analysis (EXAFS) was used to demonstrate that the active Fe-centre in sMMO was a di(μ -oxo) diiron⁴⁺ core.¹⁴⁸ The Fe-Fe distance was calculated to be 2.5 Å, which is relatively short for bridged metal-oxo complexes.^{147,149} Thus, it was speculated that the enzyme possessed a diamond core structure that forced the Fe atoms closer together, forming a highly unstable geometry. This is known as an “*entactic state*”, which is defined as the state of a metal atom, which is modified for a specific function through binding and stabilisation to the enzyme proteins.¹⁵⁰ The di(μ -oxo)

diiron⁴⁺ diamond core structure initially proposed by Que *et al.* was later confirmed by Rosenzweig *et al.* by X-ray crystal structure resolution, as shown in Figure 15.¹⁴⁸

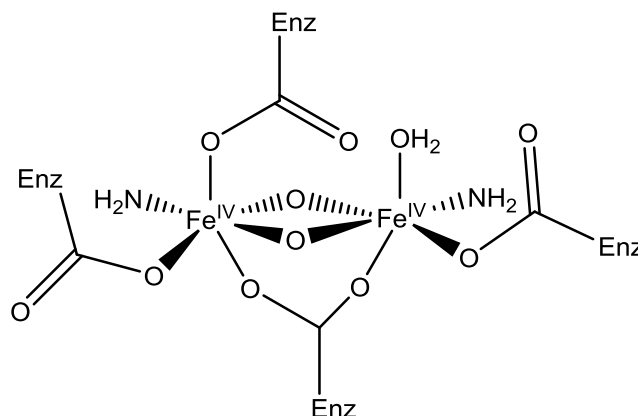


Figure 15 Schematic of dioxo-diiron⁴⁺ centre in soluble methane monooxygenase, where the 'Enz' groups indicate the enzyme proteins. Adapted with permission from reference 148. Copyright 1993 Springer Nature.

A tentative mechanism for sMMO catalysed CH₄ oxidation was proposed by Shu *et al.*¹⁴⁷ In this mechanism (shown in Figure 16), reduced MMOH contained two 5-coordinate Fe centres, each with an open coordination site. This made Fe prone to oxidation by O₂, to form intermediate P that was proposed to be a *cis*- μ -1,2-peroxodiferric centre, which could convert into the high valent, bis- μ -oxodiferryl intermediate Q. Intermediate Q has been shown to contain two antiferromagnetic Fe⁴⁺ centres in close proximity, and has been observed to readily react with CH₄ as the rate-limiting step ($\Delta H = 8.5 \text{ kJ mol}^{-1}$).¹⁵¹ The formation of intermediate Q has been confirmed by vibrational spectroscopy studies, demonstrating the unique structure of the diamond core.¹⁵² Reduction of intermediate Q with CH₄ forms an oxo-bridged diferric intermediate T, which undergoes reduction via NADPH to close the catalytic cycle. To allow the closing of the catalytic cycle, the co-factor NADPH is required to provide the additional 2 electrons. Many attempts have been made to mimic the entatic state of a diiron core within sMMO, as will be discussed in Section 1.4.3, but, the design of chemo-catalysts is not as efficient as that of enzymes, which have evolved to be highly active and selective under desirable conditions.^{72,79} The high CH₃OH selectivity from sMMO is possible due to the evolution of a rigid enzyme structure that can place metal complexes in less than optimal conformations, allowing for more reactive structures. Furthermore, this constrained enzyme structure allows for selective discrimination of substrate/ products to afford only the desired product.

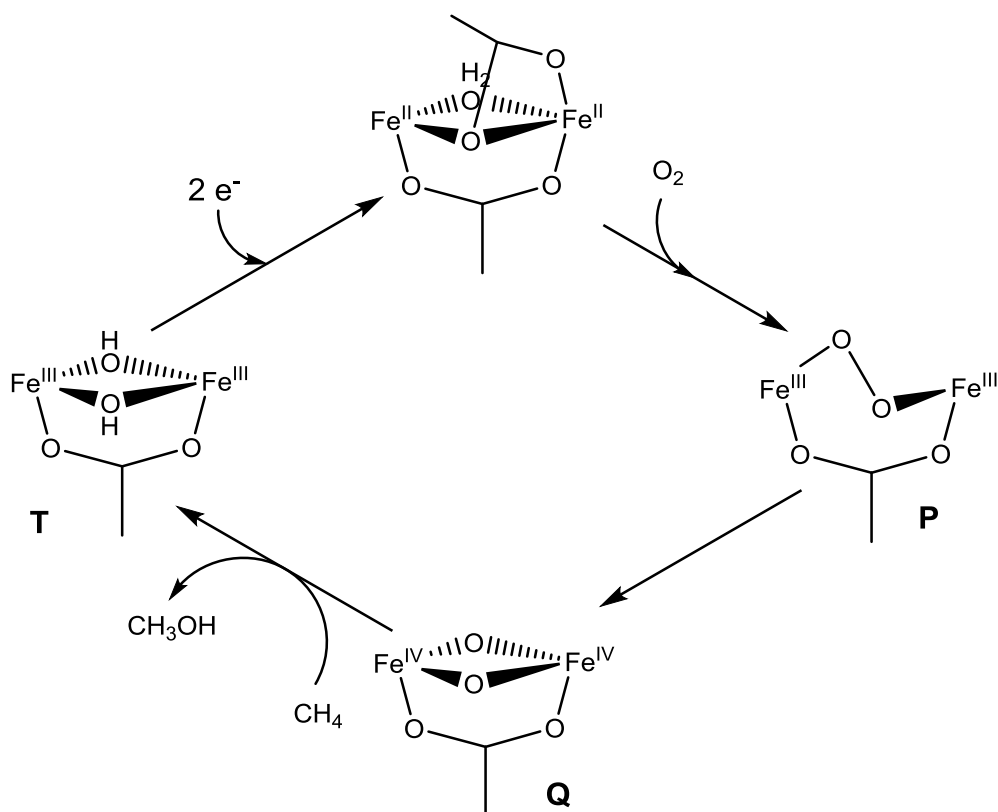


Figure 16 sMMO oxidation pathway of methane, as proposed by Shu *et al.* Adapted with permission from reference 147. Copyright 1997 American Association for the Advancement of Science.

1.4.3. Design of “Biomimetic” Catalysts for Methane Oxidation

Demonstration of the active diiron diamond core in sMMO for CH_4 oxidation has led groups to develop Fe-complexes that mimic the structure of sMMO.¹⁴⁷ There are inherent disadvantages to the use of enzymes for large-scale industrial transformations; enzymes are sensitive to reaction conditions; require co-factors (i.e. NADPH) to complete the catalytic pathway; and are costly to synthesis and maintain.⁷⁹ To alleviate these issues, the development of chemo-catalysts that mimic the highly constrained active-sites observed in enzymes is an interesting prospect. Heterogeneous catalysts offer greater catalyst stability and can be easier to prepare at scale than enzymatic catalysts. Thus, chemo-catalysts that retain high activity and methanol selectivity but are robust and cheaper to synthesise would be desirable for the activation and subsequent oxidation of CH_4 . Literature discussed in this section has shown the sMMO is able to stabilise the active diiron-diamond core due to the geometrical constraints placed on it by the enzymatic framework, forming an “*entactic-state*”.¹⁴⁷ Thus, the use of stabilising ligands that can put Fe complexes in active states similar to that observed in sMMO, should be used to design catalysts for partial oxidation of CH_4 . Examples of various Fe-catalysed partial oxidation of CH_4 are given in Table 2 and discussed in the following sections.

Table 2 Comparison of Fe-based methane oxidation catalysts. ^a Reported selectivity to methanol = (mol MeOH)/(sum mol products)*100. ^b Turnover frequency = (mol product)/(mol Fe)*(unit time). ^c Turnover number = (mol product)/(mol Fe).

Catalyst	Oxidant	T / °C	S _{CH₃OH} / % ^a	TOF / h ⁻¹ ^b	TON ^c	Ref.
sMMO	O ₂ / NADPH	25	100	95	19	153
[Fe ₄ (N ₃ O-L) ₄ (μ-O) ₂] ⁴⁺	H ₂ O ₂	80	62.5	-	24	154
FePc ^t Bu ₄ N	H ₂ O ₂	80	0	-	84.1	155
FePc ^t Bu ₄ N-SiO ₂	H ₂ O ₂	70	0	6	230	156
FeCl ₁₆ Pc/ Na-X	TBHP	25	53.0	9	107	29
Fe-ZSM-5	N ₂ O	>100	100	0	0.25	123
Fe-ZSM-5	H ₂ O ₂	50	18	1139	2200	96

1.4.3.1. Homogeneous Fe-Complexes for Methane Oxidation

The preparation of a supported, diamond-core diiron complex has been demonstrated by Wilkinson.¹⁵⁷ These complexes utilised non-haem ligating groups to stabilise the high-valent di-Fe⁴⁺ core, which was observed by Resonance Raman spectroscopy; a diiron complex, with a shift at 667 cm⁻¹ was assigned to the formation of a di(μ-oxo) diiron⁴⁺ core, which could provide a spectral handle by which to identify diamond-core structures. When these complexes were tested for catalytic activity, using H₂O₂ as the oxidant, negligible TOFs were observed, which indicated that the di-Fe⁴⁺ core was not being stabilised as it is in sMMO. The geometry of the diiron complex was likely different from the enzyme, meaning the catalyst was less accessible to CH₄ and H₂O₂.

The group of Sorokin developed a range of μ-nitrido diiron phthalocyanine complexes as an alternative.¹⁵⁵ The phthalocyanine ligand can mimic the structure of non-heme, mononuclear Fe centres and can activate H₂O₂ to form an active oxygenated species. In comparison to enzyme mediated O₂ activation, H₂O₂ only requires a 2-electron reduction, thus an additional electron source is not required. Compared to the di(μ-oxo) diiron complexes, these complexes were active for CH₄ oxidation, yet CH₃OH was not an observed product.¹⁵⁵ By DFT calculations, it was proposed that Fe=O bonds lengths comparable to those found in intermediate Q of sMMO were present.¹⁵⁸ Supporting these complexes on SiO₂ increased catalytic turnover (TON) over the free metal complex, yet these complexes favoured the formation of formic acid and formaldehyde and CH₃OH was not observed.¹⁵⁶ Another

phthalocyanine complex was reported by Shu *et al.*, where it was demonstrated that an Fe-phthalocyanine complex could be encapsulated within Na-X zeolite. An increase in TON was observed over then homogeneous Fe-phthalocyanine complexes, yet stability of such materials under reaction conditions was not determined.²⁹ Previous research has shown that homogeneous biomimetic Fe-complexes can be synthesised, however poor catalytic activity and selectivity hinders the use of such catalysts (Table 3). Rigid Fe-complexes could be designed that form part of the solid structure itself, thereby addressing issues of catalyst stability and formation of an “*entactic state*”.

1.4.3.2. Heterogeneous Fe-Catalysts for Methane Oxidation

1.4.3.2.1. Fe-ZSM-5/ N₂O Oxidation Systems

The first example of the use of Fe-zeolites as a catalyst for CH₄ oxidation was reported by Panov *et al.*, where it was reported that Fe-ZSM-5 could oxidise CH₄ utilising N₂O as the oxidant.¹⁵⁹ It was speculated by the authors that the active site was an “ α -Fe” species, which was able to activate N₂O to form a highly active, surface bound oxygen species, “ α -O”:



The presence of the α -Fe species was identified as being di-nuclear and in the 2+ oxidation state from Mössbauer studies, which was similar to the structure of sMMO.⁹⁵ It was later proposed by Snyder *et al.* that α -Fe was mono-nuclear Fe²⁺ with square planar geometry that was stabilised by β -6MR.¹¹⁷ It was implied that the β -6MR left an exposed face of the Fe²⁺ core, which could accept an O from N₂O, forming an active M-O species.² Zeolite frameworks with no β -6MRs were found to lack the Fe²⁺ species that was active for N₂O activation, and were found to be inactive.¹¹⁷

Upon formation of the highly active α -O species, CH₄ could be oxidised to afford a surface bound methoxy species:



α -O was proposed to possess a high-spin Fe⁴⁺ core with square pyramidal geometry, the oxygen in the *trans* axial position.¹¹⁷ The effect of the β -6MR enforced an “*entactic*” state on the Fe core; that is, an unstable geometry was observed to be stabilised by a rigid lattice structure, resulting in a highly reactive species and is common in the function of metalloenzymes.¹⁵⁰ A similar species has been predicted for Fe-ZSM-5 by Baerends, which would rationalise the catalytic performance of Fe-ZSM-5 under N₂O oxidation conditions.¹⁶⁰ Based on the above

findings, it has been proposed that Fe-zeolites can exhibit *biomimetic* properties under appropriate conditions, however, this claim remains open to further investigation, as there is still some ambiguity in the true nature of the active Fe site within Fe-zeolites.^{83,117,118}

The observation of α -Fe explains the rapid activation of CH₄ of N₂O at room temperature, though the surface-bound methoxy species is relatively stable and requires an additional step to relinquish CH₃OH. A hydrolysis step is performed at temperatures greater than 200 °C to release a molecule of methanol and regenerate the active, α -Fe site.¹⁶¹ Thus, partial oxidation of CH₄ utilising N₂O as an oxidation in the presence of Fe-ZSM-5, cannot be considered a catalytic cycle. Stoichiometric processes are best avoided to maximise reaction efficiency and atom economy.¹³² Irrespective of the non-catalytic nature of this reaction, much research has focused on the identification of the active α -Fe species.^{83,117,122,133,134,161}

1.4.3.2.2. Fe-ZSM-5/ H₂O₂ Oxidation Systems

To work-around the product desorption issues, Hammond *et al.* proposed the use of hydrothermally prepared Fe-MFI for the oxidation of methane, utilising aqueous H₂O₂ as the oxidant.⁹⁶ Fe-complexes are known to readily activate H₂O₂ to form active oxygenated species, as demonstrated by the works of Sorokin,¹⁵⁶ thus it would seem feasible that an analogous system, utilising biomimetic Fe-zeolites, could activate H₂O₂, too. Reported TOF values for CH₄ oxidation were greater than 14000 h⁻¹, which was greater than any previously reported catalysts (Table 3).⁹⁶ The effect of Fe incorporation was also explored by the authors, suggesting that catalysts prepared via isomorphous substitution were more intrinsically active for CH₄ oxidation than catalysts prepared by top-down approaches, as it allowed for greater control of formation of isolated extra framework centres; post-synthetic incorporations tended towards the formation of oligomeric and clustered spectator species.¹¹⁶ It was proposed from EXAFS and DFT modelling studies that the active metal centre was [Fe₂(μ -OH)₂(OH)₂(H₂O)₂]²⁺, which was like the active Fe⁴⁺²(μ -O)₂ species observed in sMMO.¹⁴⁷ This complex was able to activate H₂O₂ and oxidise methanol and regenerate the active Fe³⁺ centre, thus completing the catalytic cycle (Figure 19). The authors observed that under the reaction conditions, CH₃OH selectivity was poor, with formic acid (HCOOH) being the favoured liquid product.

Mechanistic studies suggested that CH₃OOH was the primary product early in the reaction, before CH₃OOH was reduced to form CH₃OH (Figure 17).⁹⁹ Yet it was observed over-time that moles of CH₃OH decreased at longer reaction times, which occurred with an increase in

thermodynamically favoured products, HCOOH and CO₂.⁹⁶ As Fe³⁺ is known to catalyse the radical decomposition pathway of H₂O₂, *via* a Fenton mechanism, it was stipulated by the authors that radical formation was leading to unselective over-oxidation of the primary products.⁹⁹ Indeed, addition of Cu to the Fe-MFI matrix could suppress formic acid formation by removing ·OH radicals from solution, which was supported by the use of *in-situ* radical scavengers.¹¹² It was also suggested that incorporation of Al into the MFI lattice promoted catalytic performance in Fe-MFI.¹¹⁶ Upon increasing the Al³⁺ content within the lattice, catalytic performance increased. Supporting UV-vis experiments showed that Al³⁺ acted as a “*structural promoter*” of Fe³⁺, which facilitated extraction of framework Fe³⁺ and stabilised isolated extra framework species, even at high activation temperatures (up to 900 °C).

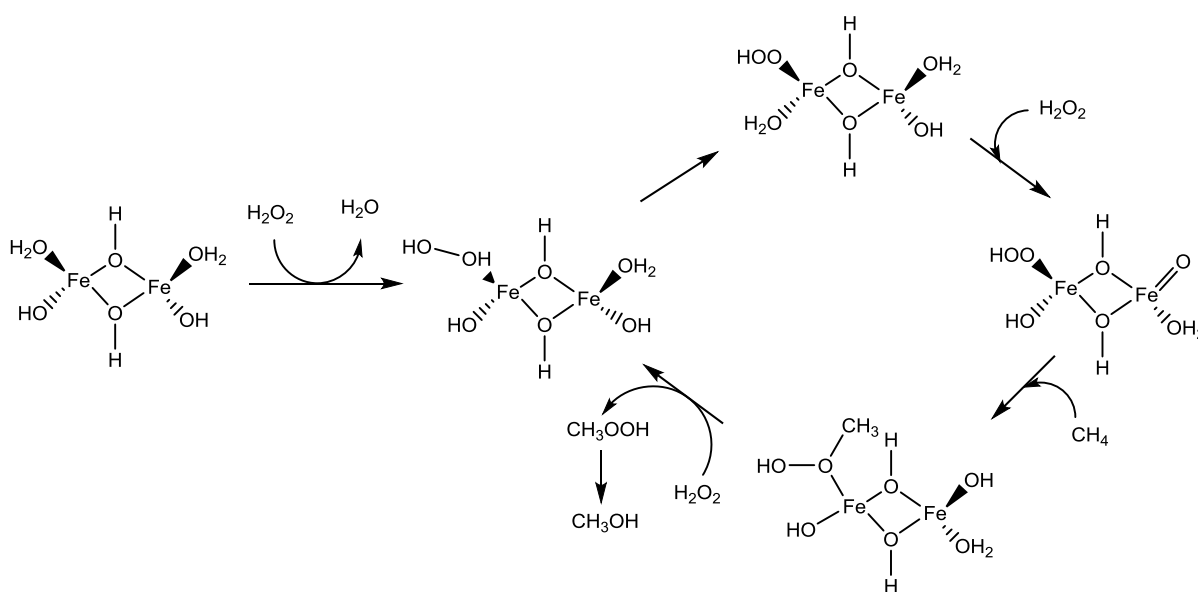


Figure 17 Proposed mechanism for partial methane oxidation with hydrogen peroxide oxidant. Adapted with permission from reference 99. Copyright 2012 Wiley.

Understanding of the key active metal species and catalytic pathways is key to rationalise the design of CH₄ oxidation catalysts, though a representative model of the active Fe³⁺ has yet to be concluded. A tentative [Fe³⁺₂(μ-OH)₂(OH)₂(H₂O)₂]²⁺ species was proposed by Hammond *et al.*, however conclusive evidence of its existence has not been reported thus far.⁹⁶ It was thought that the active Fe-sites in the H₂O₂/Fe-ZSM-5 systems were different to α-Fe site proposed for N₂O/ Fe-ZSM-5 systems, due to initial spectroscopic observations made, although the actual nature of this site has not yet been resolved.¹¹⁶

The onset of catalytic activity is thought to correlate with an increase in the proportion of extra framework Fe³⁺, as observed in DRUV-vis spectra, where the intensity of an absorbance at 280 – 320 nm increases.¹¹⁶ Resonance Raman studies have been used to complement DRUV-vis

data; the lattice to Fe^{3+} transition observed in the DRUV-vis at < 250 nm can be resonance enhanced at 244 nm, where bands attributable to the symmetric and asymmetric stretches of Fe-O-Si have been observed.¹⁶² Further Raman studies stipulate that the Raman shift at 520 cm^{-1} arises from extra framework Fe^{3+} , as this shift disappears following treatment with H_2O_2 , indicating that this Fe species has activated the peroxide to form a Raman inactive species.¹³⁵ Experimental evidence of activated Fe-ZSM-5 for CH_4 oxidation suggest that the active species is extra framework, yet it is difficult to distinguish whether the spectral features of extra framework Fe^{3+} in the DRUV-vis and resonance Raman arise from diiron centres, or a mixture of monomeric, dimeric and polymeric species.

Based on the above findings, Pidko *et al.* modelled Fe-ZSM-5/ H_2O_2 oxidation conditions utilising periodic density functional theory (DFT) calculations to determine the most energetically favoured reaction pathways.¹⁶³ It was concluded that, due to the variety of Fe species possible in the zeolite framework under aqueous conditions, three different C-H activation pathways were participating: Heterolytic, homolytic and Fenton-type pathways (demonstrated in Figure 18). Each of the pathways were calculated to afford methanol following C-H activation and each pathway was dependent on the oxidation and coordination state of the diiron centres.¹⁶³ Low valent Fe species (Fe^{2+} and Fe^{3+}) tended towards the heterolytic and Fenton-type mechanisms, whereas high valent (Fe^{4+}) species favoured the homolytic pathways. The authors did not offer any mechanistic insight on the effect of Al^{3+} siting on the Fe^{3+} speciation that could be implicit in Fe^{3+} speciation within the zeolite and thus activity;⁷⁵ however, this paper does highlight the complexity of these systems and encourages other researchers to combine theoretical studies with computational studies to uncover the nature of the active Fe-species.

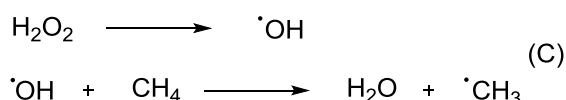
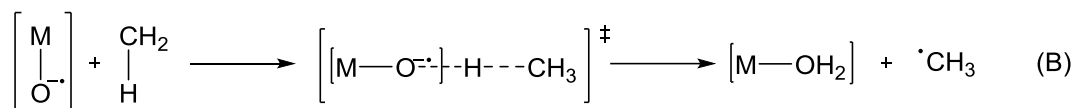
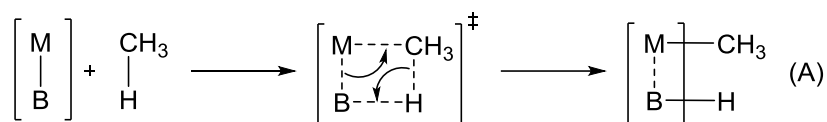


Figure 18 Proposed mechanistic pathways for C-H bond dissociation of CH₄ under aqueous conditions. (A) Heterolytic dissociation; (B) Homolytic dissociation; (C) Fenton-type dissociation. Adapted with permission from reference 163. Copyright 2016 American Chemical Society.

The development of heterogeneous, biomimetic Fe-based catalysts for the direct, partial oxidation of CH₄ is seen as a promising route to forming CH₃OH at low temperatures. The use of Fe-ZSM-5 in an aqueous system, utilising H₂O₂ as the active oxidising species can activate H₂O₂ to form an active oxygen species with which to activate CH₄. Unlike gas phase systems, which use N₂O as an oxidant, the presence of H₂O in the system can readily hydrolyse the methoxy-bound species to afford CH₃OH and close the catalytic cycle; however, there were some limitations with this method that would prevent use at larger scales; low CH₄ conversion and poor CH₃OH selectivity are detrimental to highly productive process.

1.5. Thesis Aims

As highlighted in Section 1.5, Fe-ZSM-5 is an active catalyst for the oxidation of CH₄ under aqueous conditions; however, the nature of the active Fe³⁺ species for this reaction is still under debate.^{116,135,163} It has previously been proposed as a diiron centre from DFT calculations and experimental observations, though there was limited spectral evidence of this proposed species. Iron-selective spectroscopic techniques, such as diffuse reflectance UV and resonance Raman, have been used to provide evidence for an active species.^{96,135} Earlier evidence suggests that isolated, extra framework Fe³⁺ species are the activating species, though molecular modelling studies have suggested that several active Fe³⁺ species may be present in Fe-ZSM-5/ H₂O₂ systems.¹⁶³

The main aims of this thesis are:

- Improve catalytic activity of Fe-ZSM-5 for aqueous phase CH₄ oxidation, by exploring the effect of catalyst composition on the catalytic performance of the reaction.

- Understand the whether there is competition between selective H₂O₂ activation and non-selective H₂O₂ activation. Fe-ZSM-5 can oxidise CH₄ by initially activating H₂O₂ to form an active di-Fe complex capable of reacting with the relatively inert CH₄.
- Identify a possible Fe species that correlates with increases in H₂O₂ decomposition, thus less efficient CH₄ oxidation.
- Develop an understanding of the effect of Fe-ZSM-5 catalyst preparation on Fe³⁺ speciation within the catalyst, and subsequently the effect this has on catalytic performance.

1.6. References

1. W. J. Roth, P. Nachtigall, R. E. Morris, and J. Čejka, *Chem. Rev.*, 2014, 114, 4807 – 4837.
2. L. B. McCusker, D. H. Olson and C. Baerlocher, *Atlas of Zeolite Framework Types*, Elsevier, 2007.
3. C. Baerlocher and L.B. McCusker, Database of Zeolite Structures: <http://www.iza-structure.org/databases/>.
4. A. Corma, M. J. Climent, H. García and J. Primo, *Appl. Catal.*, 1989, 49, 109-123.
5. A. Corma, *J. Catal.*, 2003, 216, 298-312.
6. M. Renz, T. Blasco, A. Corma, V. Fornés, R. Jensen and L. Nemeth, *Chem. - A Eur. J.*, 2002, 8, 4708–4717.
7. A. Primo and H. Garcia, *Chem. Soc. Rev.*, 2014, 43, 7548–7561.
8. G. Bellussi, G. Pazzuconi, C. Perego, G. Girotti and G. Terzoni, *J. Catal.*, 1995, 157, 227–234.
9. E. T. C. Vogt, G. T. Whiting, A. Dutta Chowdhury and B. M. Weckhuysen, *Advances in Catalysis*, 2015, Academic Press Inc., 143 – 314.
10. R. P. Townsend and E. N. Coker, *Studies in Surface Science and Catalysis*, 2001, 467-524.
11. S. Wang and Y. Peng, *Chem. Eng. J.*, 2010, 156, 11-24.
12. K. S. Walton, M. B. Abney and M. D. LeVan, *Microporous Mesoporous Mater.*, 2006, 91, 78-84.
13. J. L. Casci, *Microporous and Mesoporous Materials*, 2005, 82, 217–226.
14. C. Perego, A. Carati, P. Ingallina, M. A. Mantegazza and G. Bellussi, *Appl. Catal. A Gen.*, 2001, 221, 63 – 72.
15. M. Boronat, P. Concepción, A. Corma and M. Renz, *Catal. Today*, 2007, 121, 39–44.
16. J. Gascon, F. Kapteijn, B. Zornoza, V. Sebastián, C. Casado and J. Coronas, *Chem.*

- Mater.*, 2012, 24, 2829-2844.
17. N. Kosinov, J. Gascon, F. Kapteijn and E. J. M. Hensen, *J. Memb. Sci.*, 2016, 499, 65-79.
 18. Y. S. Lin, *Ind. Eng. Chem. Res.*, 2019, 58, 5787 – 5796.
 19. C. S. Cundy and P. A. Cox, *Chem. Rev.*, 2003, 103, 663 – 701.
 20. M. P. M. Nicolau, P. S. Bárcia, J. M. Gallegos, J. A. C. Silva, A. E. Rodrigues and B. Chen, *J. Phys. Chem. C*, 2009, 113, 13173 – 13179.
 21. T. Remy, L. Ma, M. Maes, D. E. de Vos, G. V. Baron and J. F. M. Denayer, *Ind. Eng. Chem. Res.*, 2012, 51, 14824 – 14833.
 22. S. Csicery, *Zeolites*, 1984, 4, 202-213.
 23. S. Auerbach, K. Carrado and P. Dutta, *Handbook of Zeolite Science and Technology*, 2003, CRC Press.
 24. R. E. Fletcher, S. Ling and B. Slater, *Chem. Sci.*, 2017, 8, 7483-7491.
 25. N. Kosinov, C. Liu, E. J. M. Hensen and E. A. Pidko, *Chem. Mater.*, 2018, 30, 3177–3198.
 26. A. Corma and H. Garcíá, *Chem. Rev.*, 2003, 103, 4307 – 4365.
 27. A. Corma, *Catal. Rev.*, 2004, 46, 369 – 417.
 28. A. Ribera, I. W. C. E. Arends, S. De Vries, J. Pérez-Ramírez and R. A. Sheldon, *J. Catal.*, 2000, 195, 287–297.
 29. R. Raja and P. Ratnasamy, *Appl. Catal. A Gen.*, 1997, 158, L7-L15.
 30. R. Gonzalez-Olmos, U. Roland, H. Toufar, F. D. Kopinke and A. Georgi, *Appl. Catal. B Environ.*, 2009, 89, 356-364.
 31. B. Wichtelová, Z. Sobalík and J. Dědeček, *Appl. Catal. B Environ.*, 2003, 41, 97–114.
 32. E. T. C. Vogt and B. M. Weckhuysen, *Chem. Soc. Rev.*, 2015, 44, 7342 – 7370.
 33. V. Blay, B. Louis, R. Miravalles, T. Yokoi, K. A. Peccatiello, M. Clough and B. Yilmaz, *ACS Catal.*, 2017, 7, 6542 – 6566.
 34. A. I. Olivos-Suarez, À. Szécsényi, E. J. M. Hensen, J. Ruiz-Martinez, E. A. Pidko and J. Gascon, *ACS Catal.*, 2016, 6, 2965–2981.
 35. P. Schwach, X. Pan, X. Bao, *Chem. Rev.*, 2017, 117, 8497 – 8520.
 36. C. Hammond, S. Conrad and I. Hermans, *ChemSusChem*, 2012, 5, 1668 – 1686.
 37. V. Van Speybroeck, K. De Wispelaere, J. Van Der Mynsbrugge, M. Vandichel, K. Hemelsoet and M. Waroquier, *Chem. Soc. Rev.*, 2014, 43, 7326 - 7357.
 38. T. Ennaert, J. Van Aelst, J. Dijkmans, R. De Clercq, W. Schutyser, M. Dusselier, D. Verboekend and B. F. Sels, *Chem. Soc. Rev.*, 2016, 45, 584 – 611.

39. C. Hammond, *Studies in Surface Science and Catalysis*, 2017, 177, 567 – 611.
40. F. Su and Y. Guo, *Green Chem.*, 2014, 16, 2934 – 2957.
41. A. M. Beale, F. Gao, I. Lezcano-Gonzalez, C. H. F. Peden and J. Szanyi, *Chem. Soc. Rev.*, 2015, 44, 7371 – 7405.
42. L. Bacakova, M. Vandrovцова, I. Kopova and I. Jirka, *Biomater. Sci.*, 2018, 6, 974 – 989.
43. J. Grand, H. Awala and S. Mintova, *CrysEngComm*, 2016, 18, 650 – 664.
44. C. S. Cundy and P. A. Cox, *Microporous Mesoporous Mater.*, 2005, 82, 1 – 78.
45. D. W. Breck, *Zeolite Molecular Sieves: Structure, Chemistry and Use*, Wiley, New York, 1974.
46. S. P. Zhdanov, *Adv. Chem. Ser.*, 1971, 101, 20.
47. M. Zaarour, B. Dong, I. Naydenova, R. Retoux and S. Mintova, *Microporous Mesoporous Mater.*, 2014, 189, 11–21.
48. C. E. A. Kirschhock, R. Ravishankar, F. Verspeurt, P. J. Grobet, P. A. Jacobs and J. A. Martens, *J. Phys. Chem. B.*, 1999, 103, 4965 – 4971.
49. C. E. A. Kirschhock, S. P. B. Kremer, P. J. Grobet, P. A. Jacobs and J. A. Martens, *J. Phys. Chem. B*, 2002, 106, 4897 – 4900.
50. C. T. G. Knight, S. D. Kinrade, C. E. A. Kirschhock, R. Ravishankar, F. Verspeurt, P. J. Grobet, P. A. Jacobs and J. A. Martens, *J. Phys. Chem. B*, 2002, 106, 3329–3334.
51. S. L. Burkett and M. E. Davis, *J. Phys. Chem.*, 1995, 98, 4647 – 4653.
52. S. L. Burkett and M. E. Davis, *Chem. Mater.*, 1995, 7, 1453 – 1463.
53. P.-P. E. A. de Moor, T. P. M. Beelen, B. U. Komanschek, L. W. Beck, P. Wagner, M. E. Davis and R. A. van Santen, *Chem. - A Eur. J.*, 1999, 5, 2083–2088.
54. T. M. Davis, T. O. Drews, H. Ramanan, C. He, J. Dong, H. Schnablegger, M. A. Katsoulakis, E. Kokkoli, A. V. McCormick, R. L. Penn and M. Tsapatsis, *Nat. Mater.*, 2006, 5, 400–408.
55. B. Tokay, M. Somer, A. Erdem-Şenatalar, F. Schüth and R. W. Thompson, *Microporous Mesoporous Mater.*, 2009, 118, 143–151.
56. S. Yang and A. Navrotsky, *Chem. Mater.*, 2002, 14, 2803 – 2811.
57. S. Yang, A. Navrotsky, D. J. Wesolowski and J. A. Pople, *Chem. Mater.*, 2004, 16, 210 – 219.
58. H. Lee, S. I. Zones and M. E. Davis, *Nature*, 2003, 425, 385 – 388.
59. K. Iyoki, K. Itabashi and T. Okubo, *Microporous Mesoporous Mater.*, 2014, 189, 22 – 30.

60. Y. Wang, Q. Wu, X. Meng and F. S. Xiao, *Engineering*, 2017, 3, 567 – 574.
61. Y. Cheng, L. J. Wang, J. S. Li, Y. C. Yang and X. Y. Sun, *Mater. Lett.*, 2005, 59, 3427 – 3430.
62. Y. Cheng, R. H. Liao, J. S. Li, X. Y. Sun and L. J. Wang, *J. Mater. Process. Technol.*, 2008, 206, 445 – 452.
63. G. Majano, A. Darwiche, S. Mintova and V. Valtchev, *Ind. Eng. Chem. Res.*, 2009, 48, 7084–7091.
64. N. Ren, Z. J. Yang, X. C. Lv, J. Shi, Y. H. Zhang and Y. Tang, *Microporous Mesoporous Mater.*, 2010, 131, 103–114.
65. N. Ren, J. Bronić, B. Subotić, X. C. Lv, Z. J. Yang and Y. Tang, *Microporous Mesoporous Mater.*, 2011, 139, 197–206.
66. N. Ren, J. Bronić, B. Subotić, Y. M. Song, X. C. Lv and Y. Tang, *Microporous Mesoporous Mater.*, 2012, 147, 229–241.
67. M. H. Nada and S. C. Larsen, *Microporous Mesoporous Mater.*, 2017, 239, 444–452.
68. Y. Kamimura, S. Tanahashi, K. Itabashi, A. Sugawara, T. Wakihara, A. Shimojima and T. Okubo, *J. Phys. Chem. C*, 2011, 115, 744–750.
69. K. Itabashi, Y. Kamimura, K. Iyoki, A. Shimojima and T. Okubo, *J. Am. Chem. Soc.*, 2012, 134, 11542–11549.
70. A. Aerts, C. E. A. Kirschhock and J. A. Martens, *Chem. Soc. Rev.*, 2010, 39, 4626–4642.
71. S. M. Auerbach, W. Fan and P. A. Monson, *Int. Rev. Phys. Chem.*, 2015, 34, 35 – 70.
72. B. E. R. Snyder, M. L. Bols, R. A. Schoonheydt, B. F. Sels and E. I. Solomon, *Chem. Rev.*, 2018, 118, 2718–2768.
73. J. Dědeček, Z. Sobalík and B. Wichterlová, *Catal. Rev. - Sci. Eng.*, 2012, **54**, 135–223.
74. S. Sklenak, J. Dědeček, C. Li, B. Wichterlová, V. Gábová, M. Sierka and J. Sauer, *Angew. Chem. Int. Ed.*, 2007, 46, 7286–7289.
75. J. Dedecek, V. Balgová, V. Pashkova, P. Klein and B. Wichterlová, *Chem. Mater.*, 2012, 24, 3231–3239.
76. T. Yokoi, H. Mochizuki, S. Namba, J. N. Kondo and T. Tatsumi, *J. Phys. Chem. C*, 2015, 119, 15303–15315.
77. J. R. Di Iorio, C. T. Nimlos and R. Gounder, *ACS Catal.*, 2017, 7, 6663–6674.
78. L. Que and W. B. Tolman, *Nature*, 2008, 455, 333–340.
79. D. J. Xuereb, J. Dzierzak and R. Raja, *Catal. Today*, 2012, 198, 19–34.
80. A. Zecchina, M. Rivallan, G. Berlier, C. Lamberti and G. Ricchiardi, *Phys. Chem.*

- Chem. Phys.*, 2007, 9, 3483.
81. W. Fan, R. G. Duan, T. Yokoi, P. Wu, Y. Kubota and T. Tatsumi, *J. Am. Chem. Soc.*, 2008, 130, 10150–10164.
 82. M. S. Kumar, M. Schwidder, W. Grünert and A. Brückner, *J. Catal.*, 2004, 227, 384–397.
 83. S. D. Hallaert, M. L. Bols, P. Vanelderen, R. A. Schoonheydt, B. F. Sels and K. Pierloot, *Inorg. Chem.*, 2017, 56, 10681–10690.
 84. U. Deka, I. Lezcano-Gonzalez, B. M. Weckhuysen and A. M. Beale, *ACS Catal.*, 2013, 3, 413 – 427.
 85. B. Ipek and R. F. Lobo, *Chem. Commun.*, 2016, 5, 1668–1686.
 86. M. H. Groothaert, P. J. Smeets, B. F. Sels, P. A. Jacobs and R. A. Schoonheydt, *J. Am. Chem. Soc.*, 2005, 127, 1394-1395.
 87. P. Vanelderen, R. G. Hadt, P. J. Smeets, E. I. Solomon, R. A. Schoonheydt and B. F. Sels, *J. Catal.*, 2011, 284, 157-164.
 88. A. Corma, L. T. Nemeth, M. Renz and S. Valencia, *Nature*, 2001, 412, 423-425.
 89. J. Dijkmans, J. Demol, K. Houthoofd, S. Huang, Y. Pontikes and B. Sels, *J. Catal.*, 2015, 330, 545–557.
 90. P. Wolf, C. Hammond, S. Conrad and I. Hermans, *Dalt. Trans.*, 2014, 43, 4514.
 91. B. Tang, S. Li, W. C. Song, E. C. Yang, X. J. Zhao, N. Guan and L. Li, *ACS Sustain. Chem. Eng.*, 2019, 7, 16329-16343.
 92. Z. R. Ismagilov, E. V. Matus and L. T. Tsikoza, *Energy Environ. Sci.*, 2008, 1, 526 – 541.
 93. E. V. Kondratenko and J. Pérez-Ramírez, *Catal. Today*, 2007, 119, 243–246.
 94. B. R. Wood, J. A. Reimer, A. T. Bell, M. T. Janicke and K. C. Ott, *J. Catal.*, 2004, 225, 300-306.
 95. K. A. Dubkov, N. S. Ovanesyan, A. A. Shteinman, E. V. Starokon and G. I. Panov, *J. Catal.*, 2002, 207, 341 – 352.
 96. C. Hammond, M. M. Forde, M. H. Ab Rahim, A. Thetford, Q. He, R. L. Jenkins, N. Dimitratos, J. a Lopez-Sanchez, N. F. Dummer, D. M. Murphy, A. F. Carley, S. H. Taylor, D. J. Willock, E. E. Stangland, J. Kang, H. Hagen, C. J. Kiely and G. J. Hutchings, *Angew. Chem. Int. Ed.*, 2012, 51, 5129–33.
 97. C. Hammond, R. L. Jenkins, N. Dimitratos, J. A. Lopez-Sanchez, M. H. Ab Rahim, M. M. Forde, A. Thetford, D. M. Murphy, H. Hagen, E. E. Stangland, J. M. Moulijn, S. H. Taylor, D. J. Willock and G. J. Hutchings, *Chem. - A Eur. J.*, 2012, 18, 15735–15745.

98. E. J. M. Hensen, Q. Zhu, R. A. J. Janssen, P. C. M. M. Magusin, P. J. Kooyman and R. A. Van Santen, *J. Catal.*, 2005, 233, 123–135.
99. L. Balducci, D. Bianchi, R. Bortolo, R. D'Aloisio, M. Ricci, R. Tassinari and R. Ungarelli, *Angew. Chem. Int. Ed.*, 2003, 42, 4937–4940.
100. C. Hammond and G. Tarantino, *Catalysts*, 2015, 5, 2309–2323.
101. A. Corma, S. Iborra, M. Mifsud, M. Renz and M. Susarte, *Adv. Synth. Catal.*, 2004, 346, 257–262.
102. C. Hammond, S. Conrad and I. Hermans, *Angew. Chemie Int. Ed.*, 2012, 51, 11736–11739.
103. G. Brink, I. W. C. E. Arends, R. Sheldon, A. Corma and H. Garcia, *Chem. Rev.*, 2002, 102, 4105–4123.
104. K. Yakabi, K. Milne, A. Buchard and C. Hammond, *ChemCatChem*, 2016, 8, 3490–3498.
105. R. Q. Long and R. T. Yang, *J. Am. Chem. Soc.*, 1999, 121, 5595–5596.
106. U. Deka, I. Lezcano-Gonzalez, B. M. Weckhuysen and A. M. Beale, *ACS Catal.*, 2013, 3, 413–427.
107. S. Brandenberger, O. Kröcher, A. Tissler and R. Althoff, *Catal. Rev. - Sci. Eng.*, 2008, 50, 492–531.
108. D. Padovan, S. Tolborg, L. Botti, E. Taarning, I. Sádaba and C. Hammond, *React. Chem. Eng.*, 2018, 3, 155–163.
109. L. Botti, R. Navar, S. Tolborg, J. S. Martinez-Espin, D. Padovan, E. Taarning and C. Hammond, *Top. Catal.*, 2019, 62, 1178–1191.
110. H. Zheng, D. Ma, X. Liu, W. Zhang, X. Han, Y. Xu and X. Bao, *Catal. Letters*, 2006, 111, 111–114.
111. C. Karakaya, S. H. Morejudo, H. Zhu and R. J. Kee, *Ind. Eng. Chem. Res.*, 2016, 55, 9895–9906.
112. C. Hammond, N. Dimitratos, R. L. Jenkins, J. A. Lopez-Sanchez, S. A. Kondrat, M. Hasbi ab Rahim, M. M. Forde, A. Thetford, S. H. Taylor, H. Hagen, E. E. Stangland, J. H. Kang, J. M. Moulijn, D. J. Willock and G. J. Hutchings, *ACS Catal.*, 2013, 3, 689–699.
113. M. M. Forde, R. D. Armstrong, C. Hammond, Q. He, R. L. Jenkins, S. A. Kondrat, N. Dimitratos, J. A. Lopez-Sanchez, S. H. Taylor, D. Willock, C. J. Kiely and G. J. Hutchings, *J. Am. Chem. Soc.*, 2013, 135, 11087–11099.
114. R. V. Prikhod'ko, I. M. Astrelin, M. V Sychev and E. J. M. Hensen, *Russ. J. Appl.*

- Chem.*, 2006, 79, 1115–1121.
115. P. J. Smeets, J. S. Woertink, B. F. Sels, E. I. Solomon and R. A. Schoonheydt, *Inorg. Chem.*, 2010, 49, 3573–3583.
 116. C. Hammond, N. Dimitratos, J. A. Lopez-sanchez, R. L. Jenkins, G. Whiting, S. A. Kondrat, M. Hasbi, M. M. Forde, A. Thetford, H. Hagen, E. E. Stangland, J. M. Moulijn, S. H. Taylor, D. J. Willock and G. J. Hutchings, *ACS Catal.*, 2013, 3, 1835–1844.
 117. B. E. R. Snyder, P. Vanelderen, M. L. Bols, S. D. Hallaert, L. H. Böttger, L. Ungur, K. Pierloot, R. A. Schoonheydt, B. F. Sels and E. I. Solomon, *Nature*, 2016, 536, 317–321.
 118. M. L. Bols, S. D. Hallaert, B. E. R. Snyder, J. Devos, D. Plessers, H. M. Rhoda, M. Dusselier, R. A. Schoonheydt, K. Pierloot, E. I. Solomon and B. F. Sels, *J. Am. Chem. Soc.*, 2018, 140, 12021–12032.
 119. M. G. Clerici, G. Bellussi and U. Romano, *J. Catal.*, 1991, 129, 159–167.
 120. D. Serrano, R. Sanz, P. Pizarro and I. Moreno, *Chem. Commun.*, 2009, 1407.
 121. U. Romano, A. Esposito and F. Maspero, *Stud. Surf. Sci. Cat.*, 1990, 55, 33–41.
 122. G. Berlier, G. Spoto, S. Bordiga, G. Ricchiardi, P. Fisticaro, A. Zecchina, I. Rossetti, E. Selli, L. Forni, E. Giamello and C. Lamberti, *J. Catal.*, 2002, 208, 64–82.
 123. K. A. Dubkov, V. I. Sobolev, E. P. Talsi, M. A. Rodkin, N. H. Watkins, A. A. Shteinman and G. I. Panov, *J. Mol. Catal. A Chem.*, 1997, 123, 155–161.
 124. P. Serp, P. Kalck and R. Feurer, *Chem. Rev.*, 2002, 102, 3085 – 3128.
 125. C. Martinez-Macias, P. Xu, S. J. Hwang, J. Lu, C. Y. Chen, N. D. Browning and B. C. Gates, *ACS Catal.*, 2014, 4, 2662 – 2666.
 126. C. Paolucci, A. A. Parekh, I. Khurana, J. R. Di Iorio, H. Li, J. D. Albarracin Caballero, A. J. Shih, T. Anggara, W. N. Delgass, J. T. Miller, F. H. Ribeiro, R. Gounder and W. F. Schneider, *J. Am. Chem. Soc.*, 2016, 138, 6028–6048.
 127. F. Fan, K. Sun, Z. Feng, H. Xia, B. Han, Y. Lian, P. Ying and C. Li, *Chem. Eur. J.*, 2009, 15, 3268–3276.
 128. B. M. Weckhuysen, *Phys. Chem. Chem. Phys.*, 2003., 5, 4351 – 4360.
 129. A. Chakrabarti, M. E. Ford, D. Gregory, R. Hu, C. J. Keturakis, S. Lwin, Y. Tang, Z. Yang, M. Zhu, M. A. Bañares and I. E. Wachs, *Catal. Today*, 2017, 283, 27 – 53.
 130. P. P. Notté, *Top. Catal.*, 2000, 13, 387–394.
 131. J. Pérez-Ramírez, F. Kapteijn, K. Schöffel and J. A. Moulijn, *Appl. Catal. B Environ.*, 2003, 44, 117–151.

132. R. A. Sheldon, *Chem. Soc. Rev.*, 2012, 41, 1437-1451.
133. K. A. Dubkov, N. S. Ovanesyan, A. A. Shteinman, E. V. Starokon and G. I. Panov, *J. Catal.*, 2002, 207, 341–352.
134. G. D. Pirngruber, P. K. Roy and R. Prins, *Phys. Chem. Chem. Phys.*, 2006, 8, 3939-3950.
135. C. Hammond, I. Hermans and N. Dimitratos, *ChemCatChem*, 2015, 7, 434–440.
136. W. Taifan and J. Baltrusaitis, *Appl. Catal. B Environ.*, 2016, 198, 525–547.
137. O. Vozniuk, N. Tanchoux, J.-M. Millet, S. Albonetti, F. Di Renzo and F. Cavani, in *Studies in Surface Science and Catalysis*, 2019, 281-302.
138. A. De Klerk, in *Future Energy: Improved, Sustainable and Clean Options for our Planet*, 2013, 245-270.
139. B. Ruscic, *J. Phys. Chem. A*, 2015, 119, 7810-7837.
140. P. Tomkins, M. Ranocchiari and J. A. Van Bokhoven, *Acc. Chem. Res.*, 2017, 50, 418–425.
141. A. Galadima and O. Muraza, *J. Ind. Eng. Chem.*, 2015, 37, 1–13.
142. R. A. Periana, D. J. Taube, S. Gamble, H. Taube, T. Satoh and H. Fujii, *Science*, 1998, 280, 560-564.
143. N. Viswanadham, G. Muralidhar and T. S. R. P. Rao, *J. Mol. Catal. A Chem.*, 2004, 223, 269–274.
144. S. Sirajuddin and A. C. Rosenzweig, *Biochemistry*, 2015, 54, 2283–2294.
145. B. G. Fox, W. A. Froland, J. E. Dege and J. D. Lipscomb, *J. Biol. Chem.*, 1989, 264, 10023-10033.
146. R. C. Prince, G. N. George, J. C. Savas, S. P. Cramer and R. N. Patel, *Biochim. Biophys. Acta (BBA)/Protein Struct. Mol.*, 1988, 952, 220-229.
147. L. Shu, J. C. Nesheim, K. Kauffmann, E. Münck, J. D. Lipscomb and L. Que, *Science*, 1997, 275, 515 – 518.
148. J. Sanders-Loehr, W. D. Wheeler, A. K. Shiemke, B. A. Averill and T. M. Loehr, *J. Am. Chem. Soc.*, 1989, 111, 8084–8093.
149. B. L. Vallee and R. J. Williams, *Proc. Natl. Acad. Sci. USA*, 1968, 59, 498 – 505.
150. A. C. Rosenzweig, C. A. Frederick, S. J. Lippard and P. Nordlund, *Nature*, 1993, 366, 537 – 543.
151. E. A. Ambundo, R. A. Friesner and S. J. Lippard, *J. Am. Chem. Soc.*, 2002, 124, 8770-8771.
152. R. Banerjee, Y. Proshlyakov, J. D. Lipscomb and D. A. Proshlyakov, *Nature*, 2015,

- 518, 431–434.
153. J. Colby, D. I. Stirling and H. Dalton, *Biochem. J.*, 1977, 165, 395 – 402.
 154. V. B. Romakh, B. Therrien, G. Süß-Fink and G. B. Shul'pin, *Inorg. Chem.*, 2007, 46, 3166 – 3175.
 155. A. B. Sorokin, E. V. Kudrik and D. Bouchu, *Chem. Commun.*, 2008, 2562 – 2564.
 156. A. B. Sorokin, E. V. Kudrik, L. X. Alvarez, P. Afanasiev, J. M. M. Millet and D. Bouchu, *Catal. Today*, 2010, 157, 149 – 154.
 157. E. C. Wilkinson, Y. Dong, Y. Zang, H. Fujii, R. Fraczkiewicz, G. Fraczkiewicz, R. S. Czernuszewicz and L. Que, *J. Am. Chem. Soc.*, 1998, 120, 955 – 962.
 158. C. Colomban, E. V. Kudrik, V. Briois, J. C. Shwarbrick, A. B. Sorokin and P. Afanasiev, *Inorg. Chem.*, 2014, 53, 11517 – 11530.
 159. G. I. Panov, V. I. Sobolev, K. A. Dubkov and A. S. Kharitonov, *Stud. Surf. Sci. Catal.*, 1996, 101 A, 493 – 502.
 160. A. Rosa, G. Ricciardi and E. J. Baerends, *Inorg. Chem.*, 2010, 49, 3866 – 3880.
 161. M. V. Parfenov, E. V. Starokon, L. V. Pirutko and G. I. Panov, *J. Catal.*, 2014, 318, 14–21.
 162. K. Sun, F. Fan, H. Xia, Z. Feng, W. Li and C. Li, *J. Phys. Chem. C*, 2008, 112, 16036–16041.
 163. Á. Szécsényi, G. Li, J. Gascon and E. A. Pidko, *ACS Catal.*, 2018, 8, 7961–7972.

Chapter 2. Experimental Procedures

2.1. Materials

All chemicals were used as received unless otherwise stated:

Tetraethyl orthosilicate, TEOS ($\geq 99\%$, GC grade, Sigma Aldrich).

Tetrapropylammonium hydroxide, TPAOH (1.0 M in H₂O, Sigma Aldrich).

Iron (III) nitrate nonahydrate, Fe(NO₃)₃·9H₂O ($\geq 99.999\%$ trace metal basis, Sigma Aldrich).

Oxalic acid, C₂H₂O₄, (Sigma Aldrich).

Sodium aluminate, NaAlO₂, (technical, anhydrous, 50 – 56 % Al₂O₃, 37 – 45 % Na₂O, Sigma Aldrich).

Ammonium nitrate, NH₄NO₃, (Sigma Aldrich).

Sodium hydroxide, NaOH, (pellet form, analytical grade, Fisher Chemical).

Ethanol, CH₃CH₂OH, (absolute, Sigma Aldrich).

Hydrogen peroxide aqueous solution, H₂O₂ (50 wt % in H₂O (with stabiliser), Sigma Aldrich).

Methane, CH₄ (Research grade, 99.999 %, BOC gases).

2.2. Synthesis of Fe-ZSM-5

2.2.1. Hydrothermal Synthesis of Fe-ZSM-5 (HT_YY wt% Fe-ZSM-5 (XX))

Hydrothermal synthesis of YY wt% Fe-ZSM-5 (XX), where YY denotes the weight percent loading of Fe and XX denotes the SiO₂/Al₂O₃ ratio of the zeolite, was performed following a procedure reported initially by Hammond *et al.*¹ A typical procedure for 0.1 wt% Fe-ZSM-5 (SiO₂/Al₂O₃ = 42) is provided below.

An aqueous solution of 1.0 M TPAOH (15.0g, 15.4 mmol) was added to a clean, borosilicate round bottom flask and stirred. To this, TEOS (10.24 g, 49.4 mmol) was added dropwise at room temperature. After addition, the solution was heated to 60 °C and aged for 2 h at a stirring rate of 600 rpm. Concurrently, an aqueous solution of Fe(NO₃)₃·9H₂O (29.4 mg, 0.073 mmol) and oxalic acid (30.4 mg, 0.25 mmol) in 5 mL of deionised (DI) H₂O was stirred at room temperature for 2 h, to afford Fe₂(oxalate)₃. The Fe₂(oxalate)₃ solution was then added dropwise to the aged silicate gel and the resulting solution was left to homogenise at 60 °C for 30 min. An aqueous solution of NaAlO₂ (0.1934 g, 2.4 mmol) was prepared in 5 mL DI H₂O and then added dropwise to the homogenised solution dropwise. The resulting aluminosilicate gel, with a molar ratio of 1 SiO₂: 0.048 Al₂O₃: 0.0147 Fe₂O₃: 3.21 TPA: 24.7 H₂O, was left to age for 16 h at 60 °C to hydrolyse the ethanol present from the silica source.

The aged gel was transferred to a PTFE lined stainless-steel autoclave and placed into a pre-heated oven at 175 °C. The gel was left to crystallise for 120 h, before the autoclave was cooled to room temperature. The solid product was recovered by filtration and washed with 2 L DI H₂O. The recovered white, crystalline solid was dried in an oven at 80 °C for 16 h, to afford the synthesised form of the catalyst (containing TPA OSDA).

The synthesised form of the catalyst was calcined at 550 °C (1 °C min⁻¹, 5 h N₂ plus 3 h air) to remove TPA from the pores of the catalyst. The TPA-free catalyst was then ion-exchanged under reflux in a 1.0 M solution of aqueous NH₄NO₃ (30 mL g⁻¹ catalyst) three times at 100 °C for 8 h, prior to activation at 550 °C for 3 h in static air to afford the proton form of the catalyst.

According to the above procedure, analogous zeolites containing different quantities of Fe and Al were prepared. The masses of NaAlO₂, Fe(NO₃)₃·9H₂O, oxalic acid were adjusted, as appropriate, to achieve the required molar ratio.

2.2.2. Seed-assisted Synthesis of Fe-ZSM-5 (SA_YY wt% Fe-ZSM-5 (XX))

The seed material employed during this synthesis was first synthesised according to the procedure described in section 2.3.1. The seed material was calcined at 550 °C under N₂ for 5 h and air for 3 h to remove the TPA OSDA for use as the seed material.

The seed-assisted catalyst material was subsequently prepared according to the following procedure. NaAlO₂ (0.193 g, 2.4 mmol) was dissolved in DI H₂O (27.6 g, 1533 mmol) and stirred at room temperature. To this, 1.0 M NaOH aqueous solution (2.4 mL, 2.4 mmol) was added dropwise to adjust the pH (measured by pH probe) of the solution to pH = 12.2, which was equivalent to the pH of the silicate suspension formed after addition of TPAOH to TEOS in the preparation of the seed material. Once the pH had stabilised at pH = 12.2, TEOS (10.2 g, 49.4 mmol) was added dropwise to the initial solution. The resulting suspension was homogenised for 2 h at 60 °C to form a clear suspension. Concurrently, a solution of Fe(NO₃)₃·9H₂O (29.4 mg, 0.076 mmol) and oxalic acid (30.4 mg, 0.25 mmol) in 5 mL DI water was prepared by stirring at room temperature, and this solution was subsequently added dropwise to the synthesis gel after two hours aging. The pH of the solution fell to pH = 9.8, and the resulting aluminosilicate gel, with a molar ratio of 1 SiO₂: 0.024 Al₂O₃: 0.0147 Fe₂O₃: 0.067 Na₂O: 39.4 H₂O, was left to age for 16 h at 60 °C.

Meanwhile, a seed solution was prepared by suspending 1.0 wt % (of total mass of silica in the gel, 29.4 mg) of calcined 0.1 wt% Fe-ZSM-5 (42) in 1.0 mL EtOH and this solution was sonicated for 5 min at room temperature. The suspension was added to the aged aluminosilicate

gel before the mixture was transferred to a PTFE lined stainless steel autoclave, which was then placed in a pre-heated oven at 200 °C for 168 h. The autoclave was cooled to room temperature and the resulting material was separated from the slurry by centrifugation (3 x 4000 rpm for 15 min). After each centrifuge cycle, the remaining solid was rinsed with 45 mL DI H₂O and the solid resuspended, before centrifuging. The afforded solid was collected from the centrifuge tubes and dried in an oven at 80 °C to remove residual H₂O, to afford the synthesised seed-assisted material. Some of the parameters of the synthesis, such as temperature and time of crystallisation, were varied throughout the study.

2.3. Catalyst Characterisation

2.3.1. Powder X-Ray Diffraction (pXRD)

Powder X-Ray diffraction (pXRD) was performed using a PANalytical X'PertPRO X-Ray diffractometer using a CuK_α X-Ray source (40 kV and 40 mA). Samples were ground to a fine powder and packed uniformly into the sample holder. Diffraction patterns were recorded between 5 – 60° 2θ at a step size of 0.017°. Diffraction patterns of the samples were matched to the simulated zeolite patterns reported by Treacy *et al.*²

Relative crystallinity of the samples was calculated following an ASTM International method for determining the relative crystallinity of zeolites with MFI framework type.³ Relative crystallinity was determined by integration of the area under the peaks between 2θ = 22.5 – 25° and calculated according to the Relative Crystallinity equation:

$$\text{Relative Crystallinity, RC (\%)} = \frac{\text{Area } 22.5\text{--}25^\circ 2\theta \text{ of sample}}{\text{Area } 22.5\text{--}25^\circ 2\theta \text{ of reference}} \times 100$$

2.3.2. N₂ physisorption

N₂ physisorption measurements were performed using a Quantachrome Autosorb iQ. Approximately 50 mg of sample were weighed into tared 9 mm glass ampoules. The weighed samples were then degassed at 350 °C for 6 h (1 °C min⁻¹). N₂ adsorption/desorption isotherms were then generated at 77 K (55 adsorption points/ 40 desorption points). Apparent surface area (SA_{app}) was determined using a modified Brunauer-Emmett-Teller (BET) equation:⁴

$$\frac{1}{X\left[\left(\frac{P_0}{P}\right) - 1\right]} = \frac{1}{X_m C} + \frac{C - 1}{X_m C} \cdot \left(\frac{P}{P_0}\right)$$

Where X_m is the monolayer; X is the number of gas molecules adsorbed; P/P_0 is the relative partial pressure, and; C is a physical constant. Surface area of solids can be determined by plotting (P/P_0) vs. $1/X[(P_0/P)-1]$ in the partial pressure range of 0.05 – 0.35. Due to the

microporous nature of zeolites, C values in this range results in a negative (non-physical) number, thus, to adjust for this, the partial pressure range is reduced by a factor of ten to determine the SA_{app} .

Total pore volume (pV_{micro}) was determined using nonlocal density functional theory (NLDFT) methods, against a kernel file of N_2 adsorption/ desorption on silica at 77 K using Quantachrome software.

2.3.3. Thermogravimetric analysis (TGA)

Thermogravimetric analysis (TGA) was performed using a PerkinElmer STA 6000. A small amount of sample (30 mg) was added to a tared ceramic crucible and carefully placed on the instrument. The crucible was heated up to 700 °C (1 °C min⁻¹) in an atmosphere of N_2 (60 mL min⁻¹) before cooling down to room temperature after the analysis. Samples were evaluated by monitoring the mass of the sample in the crucible as a function of the furnace temperature and was plotted as the % mass loss. The first derivative (mg min⁻¹) of the mass loss curve was found using the derivative function with the Pyris software.

2.3.4. Scanning Electron Microscopy (SEM)

Scanning Electron Microscopy (SEM) was performed using a Hitachi benchtop SEM TM3030Plus. Samples were loaded onto a Carbon background and focused using 15 kV electron beam and mixed scattering was used to capture SEM images. SEM images were recorded at a range of magnifications to determine particle morphology.

2.3.5. Inductively Coupled Plasma Mass-Spectrometry (ICP-MS)

ICP-MS analysis was performed using an Agilent 7300. Approximately 50 mg of sample was weighed into a volumetric flask. HF (0.5 mL) was added to the flask to dissolve the sample. Following digestion, unreacted HF was quenched using Boric acid and the solution was diluted using 5% HNO_3 and H_2O . The digested samples were submitted and the element weight% was calculated against calibrated standards.

2.3.6. Magic-Angle spinning NMR (MAS-NMR)

The coordination state and geometry of Al^{3+} within the zeolite lattice can be determined from the chemical shift, δ , which is a measure of the degree of shielding experienced by the Al nucleus in different coordination states and geometries.¹⁷⁸ Typically, isomorphous substituted Al^{3+} in the zeolite framework forms tetrahedral species that can be observed by the presence of $\delta = 60$ ppm, whereas octahedral, extra framework Al^{3+} is characterised by a peak at $\delta = 0$ ppm, as demonstrated in Figure 1.

^{27}Al and ^{29}Si Magic Angle Spinning nuclear magnetic resonance spectroscopy (MAS NMR) was performed using a Bruker Avance III 400 MHz solid-state spectrometer. Samples were ground in agate pestle and mortar to ensure samples were homogeneous and the sample was packed into a 4 mm zirconia rotor prior to analysis. The samples were spun at a spinning rate of 10 MHz for all nuclei.

^{27}Al single-pulse MAS NMR spectra were recorded at a Larmor frequency of 104 MHz and referenced to $\text{Al}(\text{H}_2\text{O})_6^+$ at $\delta = 0$ ppm. The signals were fitted with a Gaussian model to find the area of the peaks using Origin software.

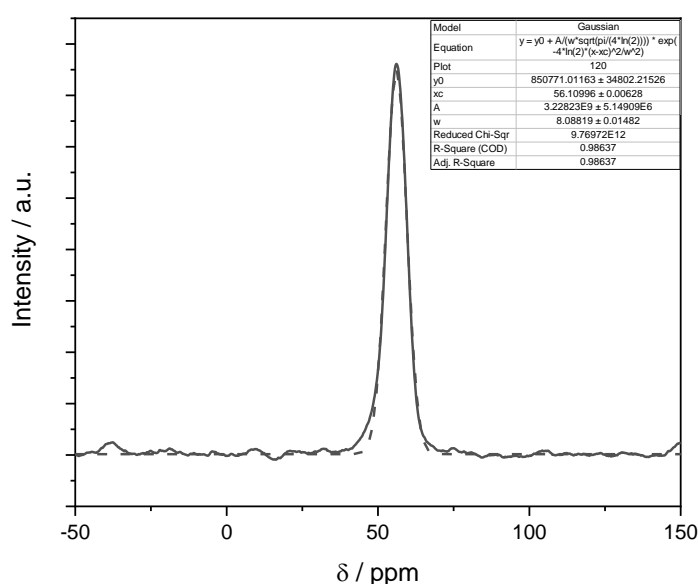


Figure 1 Example ^{27}Al MAS-NMR spectrum of 0.1 wt% Fe-ZSM-5(42) with Gaussian fit.

^{29}Si single-pulse MAS-NMR spectra were recorded at a Larmor frequency of 79 MHz and the spectra were referenced to tetramethylsilane (TMS) at $\delta = 0$ ppm.

2.3.7. Diffuse Reflectance UV-vis spectroscopy (DRUV-vis)

DRUV-vis spectroscopy is a useful tool that can determine the relative distribution of Fe within the zeolite matrix by measuring the absorbance of the ligand-to-metal charge transfer (LMCT) bands of a given absorbing species. DRUV-vis spectroscopy can be used to identify the coordination and geometry of Fe^{3+} within the zeolite framework.⁵⁻⁸ Absorptions arise from LMCT bands of the Si-O ligands to the Fe^{3+} centres, which give information on the coordination and environment of the Fe^{3+} centre. The absorbance maxima, λ , that arise from different LMCT bands within Fe-MFI are reported in Table 1 and Figure 1. Additionally, d-d

transitions associated with the oxidation state of the Fe³⁺ centre can be measured by DRUV-vis; however, these are difficult to observe, as the extinction coefficient (ϵ) of d-d transitions is < 1 . In contrast, the ϵ of LMCT is 2 to 3 times greater in magnitude, so they obscure the absorbances of the d-d transitions.⁹ Herein, the d-d transitions will not be considered due to their weakly absorbing nature.

Table 1 List of LMCT bands observable by DRUV-vis spectroscopy of Fe-ZSM-5.²²⁻²⁵

λ_n	λ / nm	Fe speciation
1	200-250	Tetrahedrally coordinated Fe ³⁺
2	250-350	Extra framework Fe ³⁺
3	350-450	Oligomeric Fe
4	>450	Bulk Fe _x O _y species

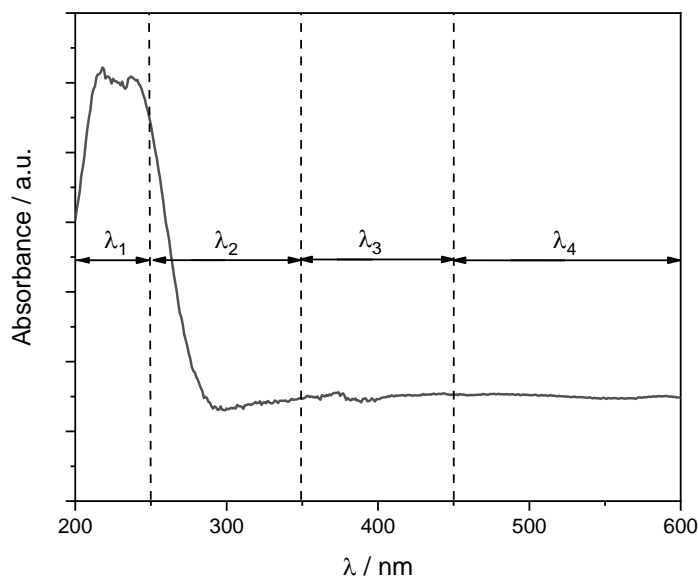


Figure 2 Example DRUV-vis spectrum of 0.1 wt% Fe-ZSM-5 (42)_AS, showing the Fe³⁺ LMCT bands that are described in Table 2.

Diffuse Reflectance Ultra-Violet-visible spectroscopy (DRUV-vis) was recorded using an Agilent Cary 4000. The background was determined using BaSO₄, a non-absorbing solid. Samples were packed into sample holders, which were placed in a diffuse reflectance cell (Harrick Mantis cell). The samples were irradiated between 800 – 200 nm, at a scan rate of 200 nm min⁻¹ and the spectra recorded in absorbance mode. The BaSO₄ background spectra was

recorded, and this was subtracted from each of the raw sample spectra to remove the background signal.

To determine the relative proportions of the Fe³⁺ species within the samples, the area under the curve for each of the sub-regions (as defined in Table 1) were calculated. The relative proportion was given as:

$$\text{Relative proportion } \lambda_n = \frac{\text{area under curve } \lambda_n}{\text{total area under curve}}$$

This gave a qualitative comparison of the distribution of Fe³⁺ species within the samples.

2.3.8. Resonance Raman spectroscopy

Resonance Raman spectroscopy can be used to probe the region of interest by selecting a laser of the desired wavelength range that closely matches the energy transition.¹⁰⁻¹² If the energy of the transition closely matches the energy of the laser, the intensity of the Raman shift will be enhanced.¹¹ This can be used to identify and differentiate between distinct species within the complex zeolitic matrix and used in combination with DRUV-vis spectroscopy to identify potential active species for partial CH₄ oxidation.

To determine a suitable laser, Raman spectra of 0.1 wt% Fe-silicalite-1 were recorded at 266, 325 and 785 nm to determine the correct laser wavelength that could selectively enhance Fe species within Fe-ZSM-5 samples (Figure 2). Silicalite-1 samples were chosen, as framework Al can cause excessive fluorescence at longer wavelengths, thus an Al-free sample should avoid this issue.

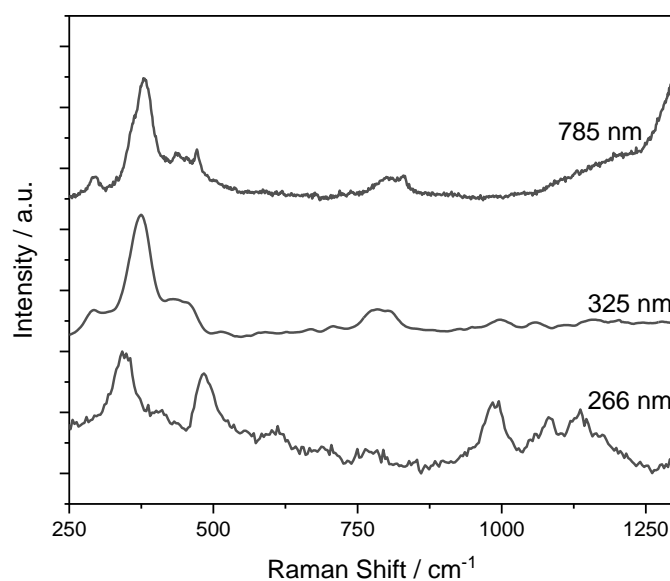


Figure 3 Raman Spectra of 0.1 wt% Fe-ZSM-5 (42)_H⁺ at various laser wavelengths.

In Figure 3, a broad feature, centred at 380 cm^{-1} , was observed at all three laser wavelengths, which is thought to arise from the presence of symmetrical Si-O-Si vibrations in 5MRs that are typical of MFI.²⁸ However, a broad band, centred at 520 cm^{-1} , and three bands at 1020 , 1120 and 1165 cm^{-1} were observed in the spectra at 266 nm . Much less intense bands at similar Raman shifts can be observed in the 325 nm spectrum, although there is an absence of these bands at 785 nm . The lack of spectral features at 785 nm indicates that the bands at $520 - 1165\text{ cm}^{-1}$ are associated with Fe^{3+} species absorbing at lower wavelengths, which correlates with the large absorptions observed at $200 - 300\text{ nm}$ in the DRUV-Vis spectrum (Figure 1). To explore the effect of $\text{SiO}_2/\text{Al}_2\text{O}_3$ on the distribution of Fe-species formed, resonance-Raman was used to determine the relative intensities of the Fe^{3+} vibrations in 0.1 wt% Fe-ZSM-5 (XX)_H⁺.

Raman spectroscopy was recorded at multiple laser wavelengths. 266 and 785 nm spectra were recorded using a Renishaw confocal inVia Raman microscope. Each of the samples were irradiated at 100% of the laser power, which was 25 mW for the 266 nm laser and 300 mW for the 765 nm laser. Samples were not damaged at relatively high power due to the stability of the inorganic samples. Typically, spectral acquisitions were $4\text{ s} \times 128$, to minimise signal to noise (S/N) ratio in the spectra, but to limit the time of each acquisition. The vibrational modes of the MFI SiO_4 bonds acted as an internal reference, and the spectra were normalised to the intensities of the bands at 380 and 800 cm^{-1} . This allowed for comparison of the intensities of

the Fe bands at 520, 1020, 1120 and 1170 cm^{-1} , by determining the relative intensity, defined as:

$$\text{Relative Intensity, RI} = \frac{\text{Intensity of Raman shift at } x \text{ cm}^{-1}}{\text{Intensity of Raman shift at } 380 \text{ cm}^{-1}}$$

Additionally, 325 nm Raman spectra were recorded using a Jobin-Yvon-Horiba confocal Raman microscope with a CCD detector, based at the University of Liverpool. Samples were irradiated at 100% laser power (20 mW) and spectral acquisitions were collected at 1 s x 20. The spectra were normalised to the internal SiO_2 bands at 380 and 800 cm^{-1} to allow for comparison of the Fe^{3+} bands in the region of the spectra at 1000 – 1200 cm^{-1} .

2.4. Fe-ZSM-5 for Methane Oxidation

2.4.1. Partial Methane Oxidation Catalytic Testing

The partial oxidation of CH_4 using Fe-MFI as a catalyst was evaluated using a 50 mL Parr mini reactor. In a typical reaction, a sample of an Fe-MFI catalyst (the mass of which was dependant on the nominal Fe wt % loading of the catalyst, so that 2.4 mmol Fe was utilised per run) was added to a borosilicate glass liner, which was then charged with an aqueous solution of H_2O_2 (10mL, 0.5 M, 5.0 mmol). The reactor vessel was sealed and secured and then purged three times with CH_4 (10 bar) to remove atmospheric gases from the reactor that could interfere with the integrity of the data. The reactor was then charged with CH_4 (10 bar) and the vessel was heated to 50 $^\circ\text{C}$ under a slow rate of stirring (150 rpm). When the reactor reached the temperature set-point (50 $^\circ\text{C}$), the stirring was increased to 1500 rpm and the timer was started, and this point was considered t_0 . After 15 min reaction time, the reaction was quenched using an ice bath to 20 $^\circ\text{C}$. Once the reactor had reached 20 $^\circ\text{C}$, the gaseous contents (CO_2) of the reactor were collected in a Tedlar gasbag. The liquid and solid phases were collected and then separated by centrifuge, so that the aqueous phase could be collected for quantification of the H_2O soluble products, CH_3OH , CH_3OOH and HCOOH . Turnover frequency (TOF) was calculated to determine the productivity of the catalysts:

$$\text{Turnover frequency, TOF (h}^{-1}\text{)} = \frac{\text{(total mol oxygenated products formed)}}{\text{(mol Fe)(time)}}$$

Product selectivity was determined to show the selectivity to desired products:

$$\text{Selectivity, } S_{\text{prod}} (\%) = \frac{\text{(mol of product)}}{\text{(total mol product)}} \times 100$$

2.4.2. Analytic Techniques

2.4.2.1. GC-FID

Gaseous products were analysed by GC-FID (gas chromatography) on a Varian 450 GC, fitted with a CP-Sil 5CB capillary column (50 m x 0.32 mm) and a methaniser unit. A calibration curve was calculated using calibrated C₁ commercial standards (Figure 4).

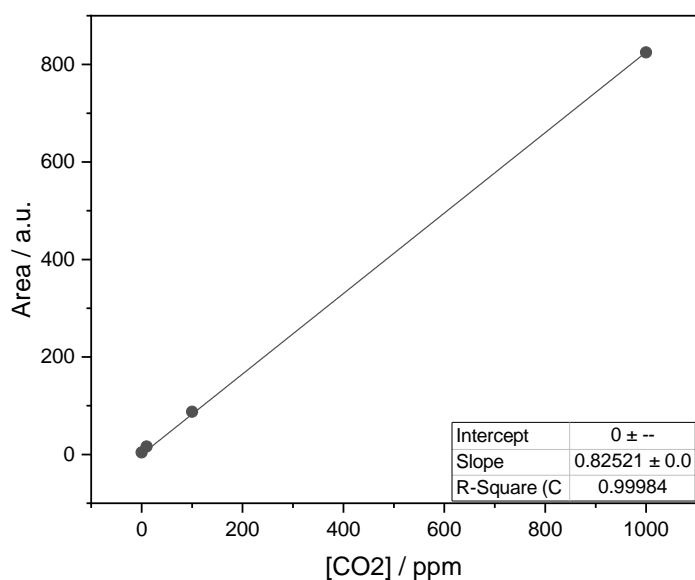


Figure 4 Calibration curve of CO₂ performed by GC-FID against calibration standards.

2.4.2.2. ¹H NMR

Liquid-phase products were analysed by quantitative ¹H NMR spectroscopy on a Bruker 500 MHz Ultra-shield NMR spectrometer. ¹H spectra were recorded at a frequency of 500.13 MHz. Calibration curves for methanol (MeOH) and formic acid (HCOOH) were performed against a 1 % TMS in CDCl₃ internal standard that was sealed in a glass ampoule and placed inside the NMR-tube.

In a standard analysis, 0.7 mL of centrifuged reaction sample was added to an NMR tube along with 0.1 mL of D₂O and the calibrated glass ampoule internal standard containing TMS in CDCl₃. A solvent suppression program was run to suppress the large H₂O signal at $\delta = 5.4$ ppm that would otherwise broaden the less intense product peaks. The chemical shifts (δ) were reported as parts per million (ppm) relative to the TMS internal standard at 0 ppm; MeOH (s, $\delta = 3.4$ ppm), MeOOH (s, $\delta = 3.8$ ppm) and HCOOH (s, $\delta = 8.4$ ppm). The MeOOH peak agreed with previous data reported by Süß-Fink *et al.*¹³ Quantification of products was calculated relative to the integral of the product shift relative to the integral of TMS at 0 ppm

(the integral value was set at 1.00). The calibration curves for MeOH (Figure 5) and HCOOH (Figure 6) are provided below for reference. A calibration curve for methyl hydroperoxide (MeOOH) was not performed, due to the poor stability of the compound. It was assumed that as a methyl group ($\text{CH}_3\text{-R}$), the calibration curve of MeOH would provide a suitable calibration curve for MeOOH. Thus, MeOOH was quantified against MeOH.

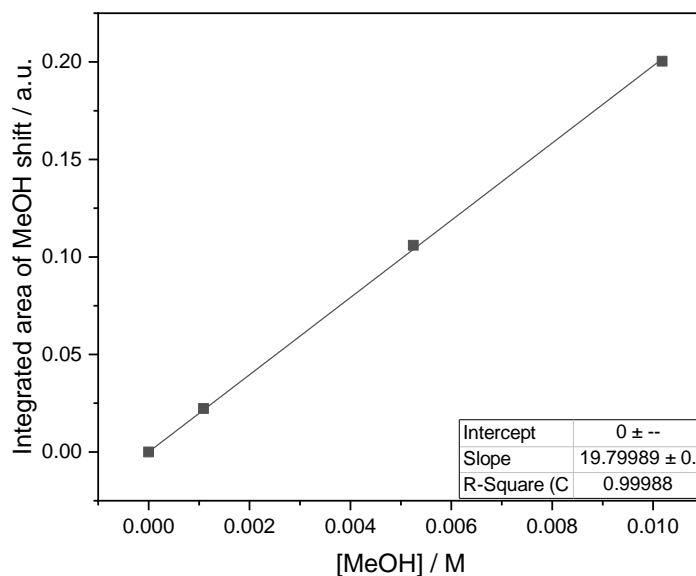


Figure 5 Calibration curve of $\text{MeOH}_{(\text{aq})}$. Integrated area of MeOH peak (at 3.4 ppm) is relative to integrated area of TMS internal standard (at 0 ppm).

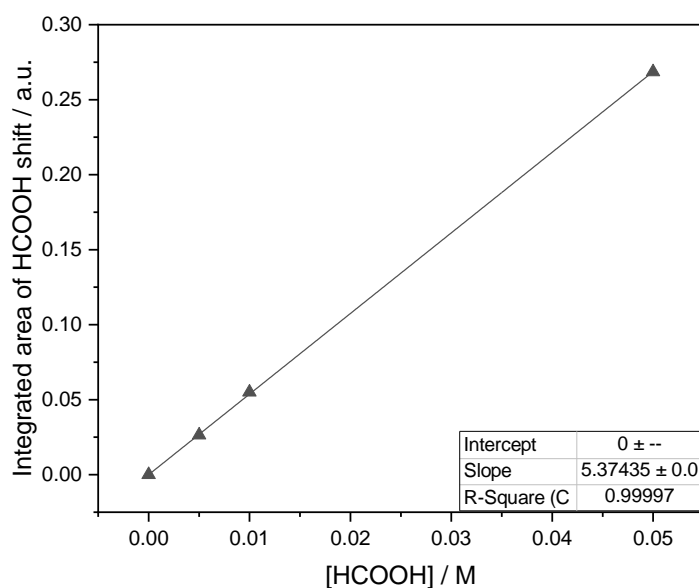
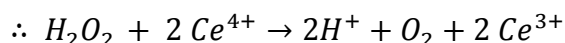
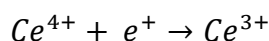
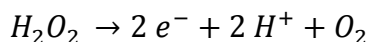


Figure 6 Calibration curve of $\text{HCOOH}_{(\text{aq})}$. Integrated area of HCOOH peak (at 3.8 ppm) is relative to integrated area of TMS internal standard (at 0 ppm).

The conversion of H_2O_2 during the reaction was calculated using $\text{Ce}(\text{SO}_4)_2$ redox titration, as described below:



A 0.1 mL reaction aliquot was taken from the centrifuged reaction mixture and added to 2 mL of DI H_2O along with 5 drops of 1 w/v % H_2SO_4 and ferroin indicator, which turns from red to colourless at the endpoint. The solution was titrated against a 8×10^{-3} M aqueous solution of $\text{Ce}(\text{SO}_4)_2$ to determine the number of moles consumed during the reaction, as per the stoichiometric equation below:

$$[\text{H}_2\text{O}_2] = \frac{(V_{\text{Ce}^{4+}})([\text{Ce}^{4+}])}{2(V_{\text{sol}})}$$

Where $V_{\text{Ce}^{4+}}$ is the volume of $\text{Ce}(\text{SO}_4)_2$ solution added to the solution, $[\text{Ce}^{4+}]$ is the concentration of the standard $\text{Ce}(\text{SO}_4)_2$ solution and V_{sol} is the volume of reaction aliquot (typically, it is assumed the density of the aliquot = 1 g dm^{-3} due to it being an aqueous solution, and the $V_{\text{sol}} = m_{\text{sol}}$).

2.4.3. Adapted Testing Protocol for Partial CH₄ Oxidation

For the seed assisted catalyst testing, an adapted testing protocol was developed to determine the catalytic performance of the catalytic materials. The adapted testing protocol was performed as follows: the catalyst sample (mass of the catalyst was dependant on the wt % loading of the catalyst, so that 2.4 mmol Fe was consistently used) was weighed out and added to the borosilicate glass liner, followed by a charge of DI H₂O (8 mL, 0.44 mol). The reactor was sealed and purged three times with N₂ to remove atmospheric gases. The reactor was heated to the set point (50 °C) under stirring (1500 rpm). Once the reactor had reached the set point, a solution of 50 wt % H₂O₂ was delivered to the reactor (via an inlet valve) using a PTFE HPLC pump at a rate of 1.0 mL min⁻¹ for 2 min, thus preparing a H₂O₂ aqueous solution (0.5 M, 5.0 mmol) *in-situ*. Following addition of H₂O₂, the reactor was charged with CH₄ (10.0 bar) and the timer started (t₀). The reaction was left to run at 50 °C for 15 min (unless stated otherwise), after which the stirring was stopped, and the reactor placed in an ice-bath to rapidly cool the reactor < 20 °C. Once the reactor had cooled down, the gaseous phase was collected in a Tedlar gas sampling bag, and the gas phase was quantified by GC-FID. The remaining slurry was separated by centrifuge and the liquid phase was quantified by ¹H NMR.

1.1. References

1. C. Hammond, M. M. Forde, M. H. Ab Rahim, A. Thetford, Q. He, R. L. Jenkins, N. Dimitratos, J. a Lopez-Sanchez, N. F. Dummer, D. M. Murphy, A. F. Carley, S. H. Taylor, D. J. Willock, E. E. Stangland, J. Kang, H. Hagen, C. J. Kiely and G. J. Hutchings, *Angew. Chem. Int. Ed. Engl.*, 2012, 51, 5129–33.
2. M. M. J. Treacy and J. B. Higgins, *Collection of Simulated XRD Powder Patterns for Zeolites*, Elsevier, 2007.
3. ASTM, 2015, **01**, 6–9.
4. M. Thommes, *Chemie-Ingenieur-Technik*, 2010, 82, 1059–1073.
5. S. Bordiga, R. Buzzoni, F. Geobaldo, C. Lamberti, E. Giamello, A. Zecchina, G. Leofanti, G. Petrini, G. Tozzola and G. Vlaic, *J. Catal.*, 1996, 158, 486-501.
6. M. S. Kumar, M. Schwidder, W. Grünert and A. Brückner, *J. Catal.*, 2004, 227, 384–397.
7. J. Pérez-Ramírez, J. C. Groen, A. Brückner, M. S. Kumar, U. Bentrup, M. N. Debbagh and L. A. Villaescusa, *J. Catal.*, 2005, 232, 318–334.
8. G. D. Pirngruber, P. K. Roy and R. Prins, *Phys. Chem. Chem. Phys.*, 2006, 8, 3939–3950.

9. A. Zecchina, M. Rivallan, G. Berlier, C. Lamberti and G. Ricchiardi, *Phys. Chem. Chem. Phys.*, 2007, 9, 3483–3499.
10. K. Sun, F. Fan, H. Xia, Z. Feng, W. Li and C. Li, *J. Phys. Chem. C*, 2008, 112, 16036–16041.
11. S. Jin, Z. Feng, F. Fan and C. Li, *Catal. Letters*, 2015, 145, 468–481.
12. C. Hammond, I. Hermans and N. Dimitratos, *ChemCatChem*, 2015, 7, 434–440.
13. G. Süss-Fink, G. V. Nizova, S. Stanislas and G. B. Shul'Pin, *J. Mol. Catal. A Chem.*, 1998, 130, 163-1

Chapter 3. Effect of Catalyst Preparation on Fe-Speciation in Fe-ZSM-5 for Methane Oxidation and Competing Pathways

3.1. Introduction

In Chapter 1, the synthesis and application of Fe-ZSM-5 was discussed in detail. One of the reactions catalysed by this material is partial methane oxidation to produce methanol. This is seen as a more energy-efficient and atom economic way to functionalise methane into a more reactive precursor molecule (methanol).¹ Early studies were performed in the gas phase and utilised N₂O as an oxygen source (Equation 1).²⁻⁷



In this case, it was shown that the catalyst mediates the selective formation of a surface bound methoxy (-OCH₃) species. However, methanol remains bound to the active Fe-site under the reaction conditions and requires an additional washing step at elevated temperature to hydrolyse the methoxy group from the catalytic site to afford methanol.⁵ Consequently, this process cannot be considered a closed catalytic cycle and is considered a stoichiometric process. The poor atom efficiency and extra energy required to regenerate the active site makes such a process undesirable for large-scale conversion of methane under these conditions. Yet this work demonstrated the ability of Fe-ZSM-5 to activate oxygen donors, which in turn can activate methane.

Considering the ability of Fe-ZSM-5 to activate oxygen donors, Hammond *et al.* considered the use of hydrogen peroxide as the oxygen donor (Equation 2).⁸

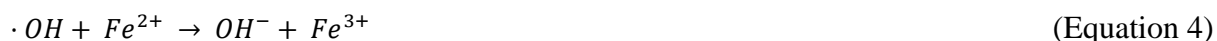


The advantage of using H₂O₂ as the oxidant over N₂O is that, under aqueous conditions, methanol is readily desorbed from the catalyst, without apparent destruction of the active site, meaning turnover numbers (TON) greater than 1 can be achieved.⁹ Furthermore, Fe-ZSM-5 was able to achieve high turnover-frequencies (TOF > 14 000 h⁻¹) at relatively low temperatures (50 °C), which was more similar to the ambient conditions that soluble methane monooxygenase (sMMO) is able to activate CH₄ under (*cf.* Chapter 1 for more discussion of sMMO).^{10,11} It was surmised through experimental observations and DFT calculations that the active site in H₂O₂ mediated CH₄ oxidation was different to the α-Fe species that activates

N₂O.⁸ It was proposed that the active species for aqueous phase methane oxidation is a binuclear, extra framework Fe³⁺ species, [Fe₂(μ₂-OH)₂(=O)(OH)(OOH)(H₂O)]²⁺,⁸ though this assignment is not yet conclusive and further studies are required.

In previous studies, it was suggested that substitution of the framework Si⁴⁺ with Al³⁺ could promote the catalytic activity of Fe-ZSM-5 for aqueous phase methane oxidation, despite the Fe-free ZSM-5 analogues being shown to be inactive for the same reaction.¹² Diffuse-Reflectance Ultra-Violet-Visible (DRUV-vis) spectroscopy suggests that the active, extra framework Fe³⁺ species is formed more readily upon addition of Al³⁺ to the zeolite lattice.¹³ Formation of extra framework Fe³⁺ has been shown to be a result of the co-presence of tetrahedral Al³⁺ within the MFI framework, which may aid the extraction of framework Fe³⁺ to afford extra framework species.¹² However, it might be thought that Al³⁺ can stabilise isolated Fe³⁺ sites in the zeolite pores, preventing further agglomeration into larger, inactive bulk species.^{12,14} Even though the reported turnover frequencies (TOFs) for these catalysts were greater for methane oxidation, the nature of the active site in both cases was not made clear. It was not certain whether framework Al³⁺, or the formation of Brønsted acid sites associated with substitution with Al³⁺, also contribute to the improved performance. Moreover, the role of these factors in terms of interaction with the oxidant is also not yet clear. As such, the optimal concentration and ratio of Fe³⁺ and Al³⁺ for methane oxidation performance has yet to be identified.

It is also crucial to realise that the presence of Fe³⁺ within the catalyst can increase the likelihood of inefficient H₂O₂ decomposition through a Fenton-type mechanism (Equations 3-6).^{15,16}



This would reduce the oxidant efficiency of the system, thus making it a less desirable approach for methane oxidation. Furthermore, the formation of hydroxyl radicals can lead to unselective oxidation of CH₄ and CH₃OH, resulting in undesirable higher oxygenation products such as formic acid, HCOOH and carbon dioxide, CO₂. Hence, it is essential to gain a better understanding of how different aspects of the catalyst, such as elemental composition and catalyst preparation, affect the rate of both reaction pathways.¹⁷

Accordingly, this chapter will investigate the effect of catalyst composition and further, the effect of catalyst activation, on the performance of Fe-ZSM-5 for both methane hydroxylation and H₂O₂ decomposition. By identifying trends between the two reaction pathways, it may be possible to identify an Fe site responsible for promoting oxidant decomposition. Moreover, the role of these parameters on the nature of the Fe speciation present in the catalyst will also be studied by DRUV-Vis and resonance Raman spectroscopy to identify spectral features that relate to partial oxidation reaction trends. The aim is to identify the optimal catalyst for achieving high oxidation activity and H₂O₂ efficiency during aqueous phase methane oxidation.

3.2. Effect of SiO₂/ Al₂O₃ Ratio on Methane Oxidation and Hydrogen Peroxide Decomposition Activity

3.2.1. Hydrothermal Synthesis of 0.1 weight % Fe-ZSM-5

Catalysts were prepared under hydrothermal conditions, as reported by Hammond *et al.*⁸ A series of samples were prepared with varying SiO₂/Al₂O₃ ratio (from ∞ to 42), by varying the amount of Al precursor added to the synthesis gel, whilst maintaining the Fe³⁺ loading of each of the catalysts at 0.1 wt%. The catalysts are denoted as 0.1 wt% Fe-ZSM-5 (XX)_ZZ throughout the text, where XX denotes the SiO₂/Al₂O₃ ratio and ZZ denotes the catalyst form (i.e. AS for the as-synthesised form, Na⁺ for the sodium form, NH₄⁺ for the ammonium ion-exchanged form and H⁺ for proton form). An aluminosilicate gel, containing an organic template (tetrapropylammonium hydroxide, TPAOH) and a Fe precursor (Fe₂(oxalate)₃) was aged for 16 h at 60 °C. This affords a gel with the molar composition: 1 SiO₂: *x* Al₂O₃: 0.0147 Fe₂O₃: 3.21 TPA: 24.7 H₂O, where *x* indicates the desired molar ratio of Al₂O₃. The resulting gel was crystallised in a PTFE-lined stainless-steel autoclave at 175 °C for 120 h to afford a white slurry. The synthesised materials were separated by filtration and dried at 80 °C to afford 0.1 wt% Fe-ZSM-5_AS, which contained the TPA template encapsulated within the micropores. To remove the OSDA, the AS form was calcined at 550 °C to afford the Na⁺ form of the catalyst. To removal residual Na cations, the Na⁺ form underwent ion-exchange with ammonium nitrate solution to afford the NH₄⁺ form of the catalyst. The final stage required thermal degradation of the NH₄ cation to afford the proton form, H⁺, which was assigned as the active catalyst for partial oxidation of methane.¹²

To ensure that crystalline MFI had been synthesised under the above conditions, the samples were analysed by powder X-ray diffraction (*p*XRD), which are shown in Figure 1. MFI crystalline phases were observed for each of the synthesised catalysts from the presence of diffraction peaks at 2θ = 7 – 8° and 22.5 – 25°, with no impurity phases observed.¹⁸ Pore

volumes and apparent surface areas were below the values expected for microporous MFI (Table 1), suggesting that the OSDA might be present in the pore network.¹⁹

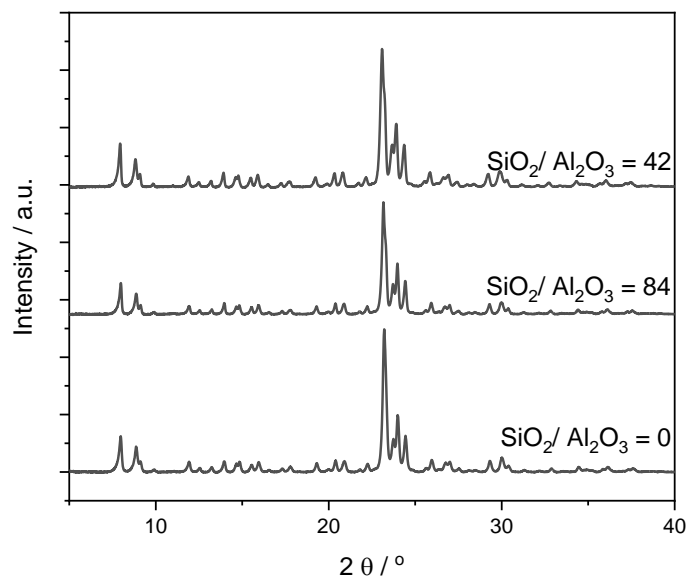


Figure 1 pXRD diffractogram of synthesised 0.1 wt % Fe-ZSM-5 (XX)_AS, where XX denotes the SiO₂/Al₂O₃ ratio of the sample.

Table 1 N₂ physisorption data (at 77 K) of 0.1 wt % Fe-ZSM-5 (45) before and after calcination at 550 °C. ^a Apparent surface area (SA_{app}) was calculated from the modified BET equation applied in the region 0.005 ≤ p₀ ≤ 0.05. ^b Micropore volume (V_{micro}) was calculated from NLDFT methods against a kernel file of N₂ absorption/ desorption of silica at 77 K.

Catalyst	SA _{app} ^a / m ² g ⁻¹	V _{micro} ^b / cc g ⁻¹
0.1 wt % Fe-ZSM-5 (42)_AS	33.4	0.032
0.1 wt % Fe-ZSM-5 (42)_Na ⁺	399.4	0.192

To confirm the presence of OSDA within the structure, thermogravimetric analysis (TGA) was used to detect the presence of TPA in the MFI framework, by measuring the % mass loss over a temperature ramp from 25 to 700 °C, under a flow of N₂. At 400 °C, a 10 % mass loss was observed in 0.1 wt % Fe-ZSM-5 (42)_AS, which was thought to be due to the decomposition of TPA in the sample (Figure 2). Subsequently, to ensure full removal of OSDA from each of the synthesised catalysts, the samples were calcined at 550 °C. Following calcination, an expansion of micropore dimensions indicated that the reduced pore volume of the as-

synthesised catalysts was due to the presence of TPA OSDA trapped within the micropore network.

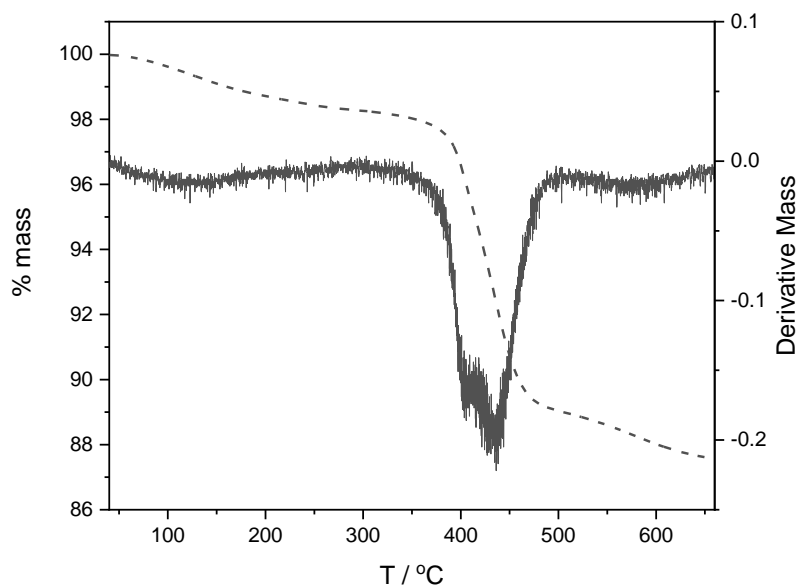


Figure 2 Thermogravimetric curve (dashed line) and derivative (solid line) of 0.1 wt% Fe-ZSM-5 (42)_AS.

To show that Fe^{3+} had been incorporated into the framework following hydrothermal synthesis, DRUV-vis measurements of the synthesised materials were made and shown in Figure 3. There is a broad absorption in each of the spectra at 200 – 250 nm that corresponds to the LMCT of tetrahedral, framework Fe^{3+} . No absorbances can be seen at wavelengths greater than 300 nm that implies that the Fe has fully been incorporated into the framework.²²⁻²⁵ After confirming that the Fe^{3+} was substituted into the framework following hydrothermal synthesis at 175 °C, without the formation of extra framework species, the samples were activated for CH_4 oxidation. This afforded the proton form, H^+ , of the catalyst, which has previously been suggested to be the active form of Fe-ZSM-5 for CH_4 oxidation.⁸

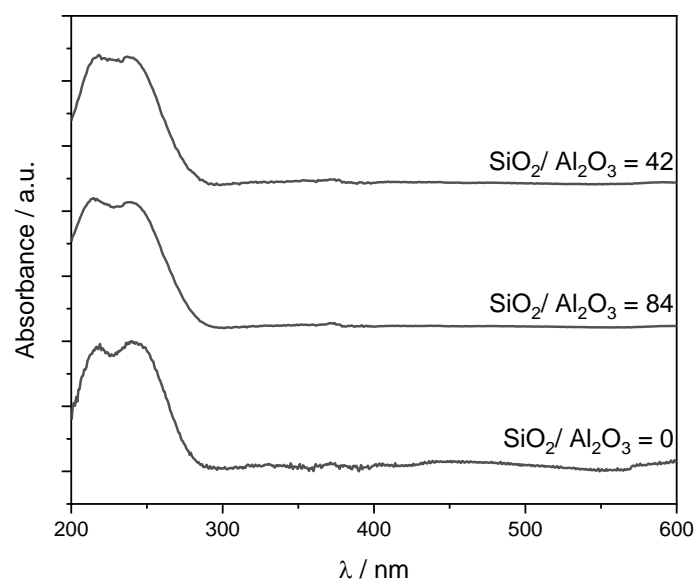


Figure 3 DRUV-vis spectra of 0.1 wt% Fe-ZSM-5 (XX)_{AS}, where XX denotes the SiO₂/Al₂O₃ ratio.

3.2.2. Catalytic Performance of 0.1 wt% Fe-ZSM-5 (XX)_H⁺

As discussed above, the addition of Al³⁺ into the matrix of Fe-MFI is reported to increase the activity of the catalyst for methane oxidation.^{12,20} However, the optimal concentrations of Fe³⁺ and Al³⁺ for catalytic CH₄ oxidation performance have not yet been identified. Al³⁺ is thought to play a key role in the activation and stabilisation of active Fe species.¹² Moreover, increasing the Al³⁺ content leads to an increase in the number of Bronsted acid sites in the zeolite, which may influence the competing reaction.²¹ Thus, it is important to gain an understanding into how the Fe speciation is having an effect, to better direct catalyst design in the future.

To investigate the effect of SiO₂/Al₂O₃ ratio on catalytic activity of CH₄ and H₂O₂ decomposition, a range of catalysts possessing equivalent Fe³⁺ content, but varying SiO₂/Al₂O₃ ratios were prepared by hydrothermal synthesis. The samples were tested under partial CH₄ oxidation conditions previously reported by Hammond *et al.*⁸ Reactions were performed in a high-pressure, stirred tank batch reactor, which were pre-loaded with the catalyst, oxidant, solvent and reactant. To normalise the amount of reaction products at different Fe loadings, the catalytic activity of the samples was determined as turnover frequency (TOF), i.e. the (number of moles of total oxygenated products)/((mol Fe)*(unit time)). Experimental error was determined by performing the reaction with 0.1 wt % Fe-ZSM-5(42)_H⁺ three times to determine an average TOF value and standard deviation. An error of 6.4 % was determined and applied to each of the reported results. Errors for each set of samples (at various SiO₂/Al₂O₃

ratios) should have been made in hindsight, to account for differences in TOF due to differences with the catalysts.

The TOF values were plotted in Figure 4 as a function of Al^{3+} loading. The rate of CH_4 oxidation increased with increasing Al^{3+} loading, which indicates that Al^{3+} has a role to play in the catalytic performance of Fe-ZSM-5. To determine whether Al^{3+} was an active component within the oxidation pathway, an Fe-free sample of the catalyst (at $\text{SiO}_2/\text{Al}_2\text{O}_3 = 42$) was tested under partial CH_4 oxidation conditions. The observed sum of oxygenated products as a function of Fe content of the catalyst are shown in Figure 5. In the absence of Fe, a relatively low number of oxygenated products were observed, indicating that Al^{3+} does not play an active role in CH_4 oxidation.

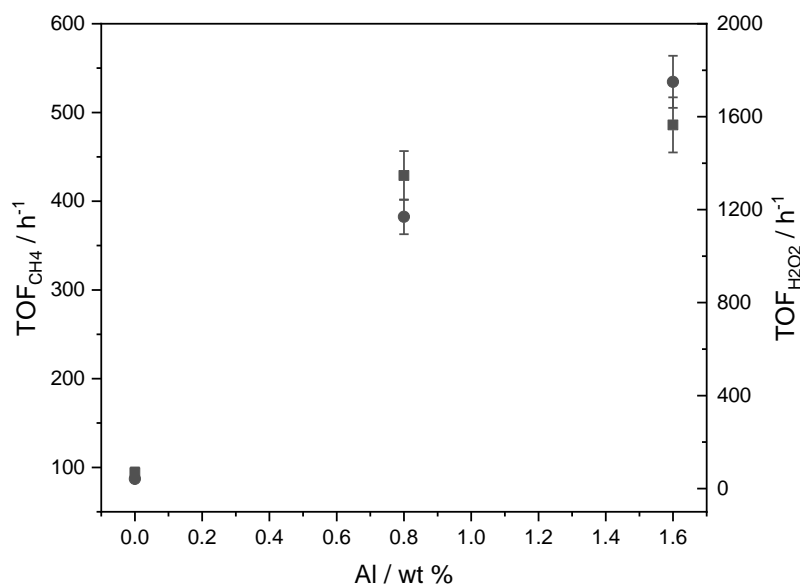


Figure 4 Left x-axis (squares), methane oxidation activity (reported as TOF values) of 0.1 wt% Fe-ZSM-5 (XX)_H⁺ as a function of Al^{3+} loading. Right x-axis (circles), hydrogen peroxide decomposition (reported as TOF values) of 0.1 wt% Fe-ZSM-5 (XX)_H⁺ as a function of Al^{3+} loading. Error bars are set at 6.4 %.

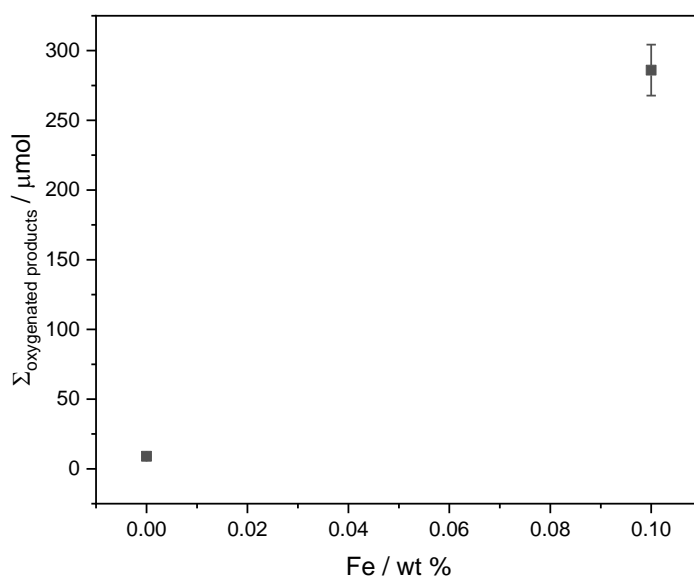


Figure 5 Sum of oxygenated products versus Fe wt% loading of Fe-ZSM-5 (42)_H⁺. Error bars at 6.4 %.

Concurrently, the catalysts were tested for the decomposition of H₂O₂ in the absence of a hydrocarbon substrate, so that interaction with the alkane would not affect H₂O₂ decomposition. The catalytic activity was plotted as a TOF value ((mol H₂O₂ consumed)/(mol Fe)*(unit time)). In Figure 4, the activity observed for the catalysts increases with increasing Al³⁺ content (lower SiO₂/Al₂O₃ ratio), potentially suggesting that activation of H₂O₂ occurs prior to reaction with CH₄ to afford CH₃OOH and CH₃OH. This is consistent with a previously reported reaction mechanism, where the catalytic cycle is initially started by activation by of H₂O₂.^{8,9}

3.2.3. Spectroscopic Characterisation of 0.1 wt% Fe-ZSM-5 (XX)_H⁺

3.2.3.1. DRUV-vis Spectroscopy

To identify how the quantity of Al³⁺ impacts the activity of the catalyst, it is important to identify changes in Fe³⁺ speciation as a function of SiO₂/Al₂O₃ ratio after calcination, ion-exchange and final activation at 550 °C to afford the protonated catalyst. DRUV-vis was used to analyse the absorbances of LMCT bands of different Fe³⁺ species (as described in Chapter 2, Section 2.2.6). Following activation of the catalysts at 550 °C, a shift in absorbance maxima was observed on addition of Al³⁺ to the framework (Figure 6). To probe the differences further, the DRUV-vis spectra of the areas of the four sub-regions were found by determining the area under the curve by integration of the sub-band areas (Figure 7). Caution must be taken when interpreting the data in this way, as there may be overlapping of the various sub-bands that may

occur due to uncertainty in the ϵ values of the various Fe species, which can make full quantification challenging. Nevertheless, the areas of the sub-bands can be utilised as a semi-quantitative method to determine an approximate contribution from each of the Fe species within a framework, thus allowing a qualitative comparison of different samples.¹² Upon integration of the sub-band areas, a reduction in the proportion of framework Fe^{3+} ($\lambda < 250$ nm) upon activation at 550 °C was observed in samples that contained a higher proportion of Al^{3+} . A subsequent increase in extra framework Fe^{3+} species ($\lambda = 250 - 350$ nm) was observed in samples that contained more Al^{3+} .

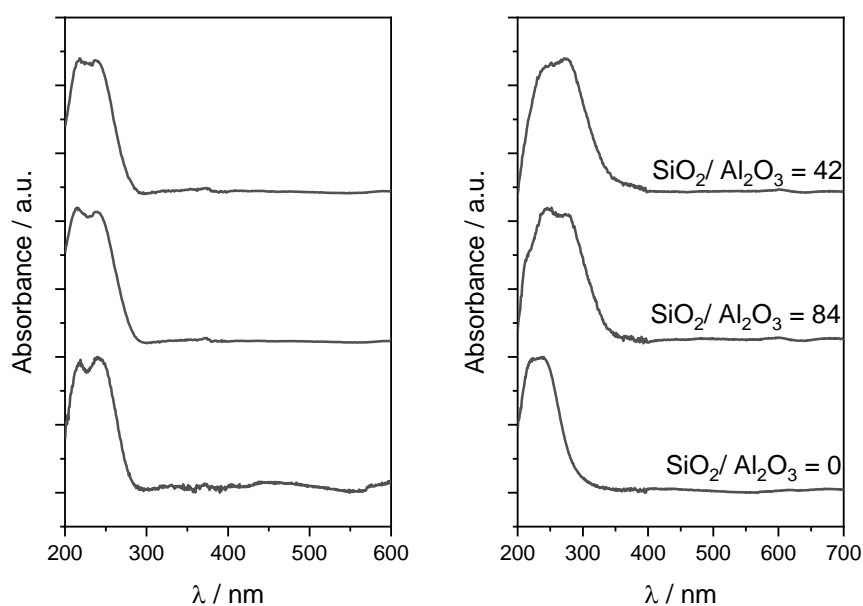


Figure 6 Left; DRUV-Vis of 0.1 wt % Fe-ZSM-5 (XX)_AS. Right; DRUV-vis spectra of 0.1 wt % Fe-ZSM-5 (XX)_H⁺, where XX denotes the $\text{SiO}_2/\text{Al}_2\text{O}_3$ ratio.

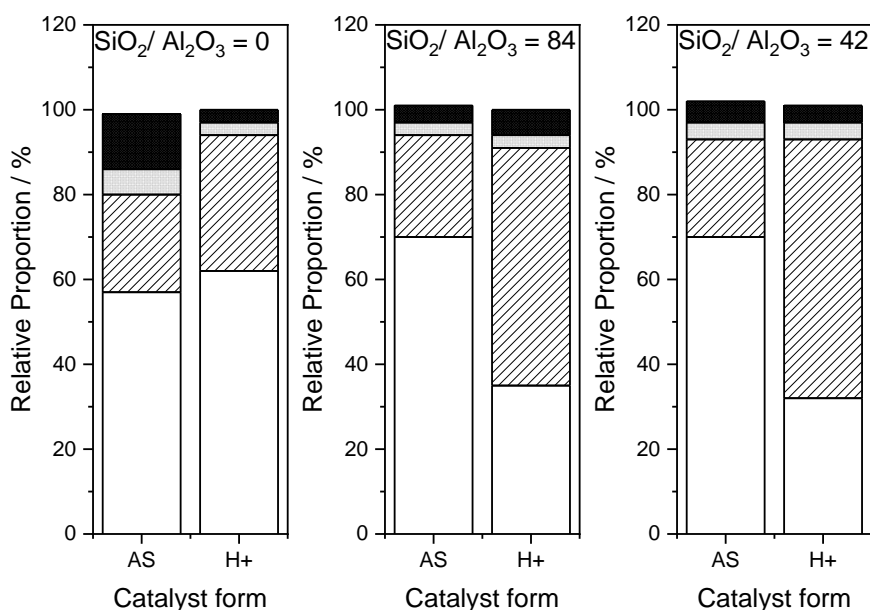


Figure 7 Relative proportion of sub-bands of DRUV-vis spectra of 0.1 wt % Fe-ZSM-5 (XX)_ZZ as a function of catalyst form, where XX denotes the SiO₂/Al₂O₃ ratio. Z denotes the catalyst form; AS, as synthesised; H⁺, proton form. The different sub-bands are; blank, λ₁; stripes, λ₂; grey, λ₃, and; black, λ₄.

In the Al-free 0.1 wt% Fe-Silicalite-1, a small change in distribution of framework Fe³⁺ (λ₁) was observed following the activation to the H⁺ form. Yet, the relative proportion of extra framework Fe³⁺ (λ₂) increases, whilst a reduction in the distribution of λ₃ and λ₄ was observed following thermal activation. The loss of oligomeric Fe clusters following activation of the catalyst indicates that these species were removed during the various treatment steps. When Al³⁺ was incorporated into the MFI lattice, an increase in relative proportion of λ₂ species was observed following catalyst activation. A higher proportion of extra framework Fe³⁺ species can be linked to increased TOF values shown in Figure 5, suggesting that Al³⁺ facilitates the formation of active, extra framework Fe³⁺ species. A 5 % difference between the relative proportion of λ₂ in 0.1 wt% Fe-ZSM-5 (42)_H⁺ and 0.1 wt % Fe-ZSM-5 (84)_H⁺, however, the difference in TOF between the two catalysts was calculated as 25 %. The difference in observations suggests that there may be subtle differences in the nature of the extra framework Fe that cannot be detected the DRUV-vis, and alternative Fe-probes should be used to determine any differences

3.2.3.2. Resonance Raman Spectroscopy

It has been previously discussed that DRUV-vis alone is not enough to distinguish between specific Fe sites, for example isolated and oligomeric Fe³⁺, monomer, dimers and trimers are thought to absorb in the region 250-350 nm.^{12,22} However, the most active samples possessed

a much larger fraction of species absorbing in this region, thus further investigation into these bands is required. As discussed in Chapter 2, resonance Raman spectroscopy can be used to selectively enhance signals from Fe³⁺ species that absorb in the UV region, thus different Fe³⁺ species can be distinguished.^{23,24}

The resonance Raman spectra of 0.1 wt % Fe-ZSM-5 (XX)_H⁺ at 266 nm are shown in Figure 8. Silicalite-1 was provided as a reference of the Si-O-Si vibrations typical of MFI ring structure.²⁷ Two additional bands at 380 and 800 cm⁻¹ can be assigned as the SiO₂ vibrations within the 5-membered rings of the MFI framework, and can be used in parallel with *p*XRD patterns to identify the zeolitic phase of the material. Given the non-resonant nature of the bands associated with the MFI lattice, all further spectra were normalised to the SiO₂ vibrations at $\bar{\nu} = 380$ and 800 cm⁻¹, allowing direct comparison of the intensities of the Fe bands. Five bands can be observed at 520, 650, 1020, 1120 and 1165 cm⁻¹ in the Raman spectra of 0.1 wt % Fe-ZSM-5 (XX) that are not observed in the Silicalite-1 reference spectrum. Thus, these bands were attributed to the presence of Fe³⁺ within the zeolite matrix. It was proposed by the group of Li that each of these bands arise from vibrations of tetrahedral, framework [Fe(OSi)₄] species.^{25,26} However, their work only focused on hydrothermally prepared Fe-ZSM-5 prior to post-synthetic modification (e.g. calcination, ion-exchange), therefore does not consider any changes that might occur to the Fe speciation during post-synthetic processing. As seen in the DRUV-vis spectra of hydrothermally synthesised 0.1 wt % Fe-ZSM-5 (Figure 4), an additional, extra framework Fe species can be observed ($\lambda > 300$ nm). Thus contributions from these species in the resonance Raman spectra cannot be discounted.²⁷

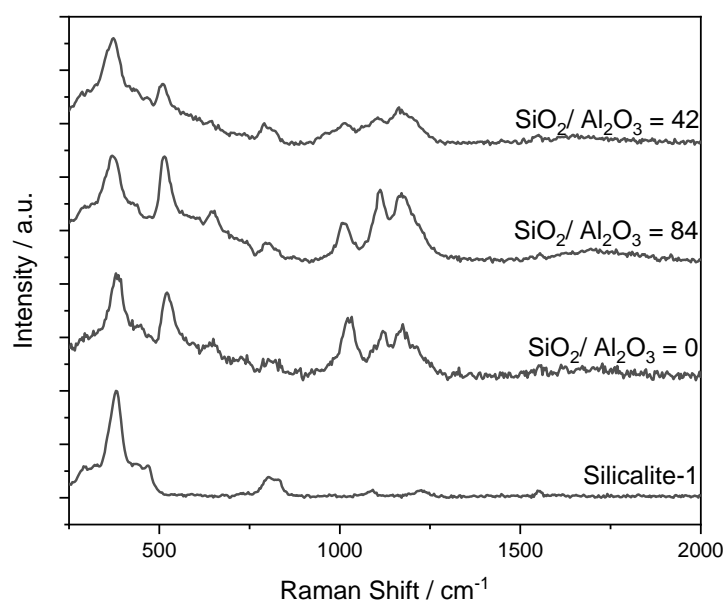


Figure 8 Resonance Raman ($\lambda = 266$ nm) spectra of 0.1 wt % Fe-ZSM-5 (XX)_H⁺, where XX denotes the SiO₂/Al₂O₃ ratio. A Fe-free silicalite-1_H⁺ spectrum is provided as a SiO₂ reference.

Table 2 Relative intensities of Raman-active features of 0.1 wt % Fe-ZSM-5 (XX)_H⁺ as calculated from the ratio of the intensity of the Raman band and the intensity of the Si-O-Si stretch at 380 cm⁻¹, as determined from the resonance Raman spectra (266 nm).

SiO ₂ /Al ₂ O ₃	520 cm ⁻¹	650 cm ⁻¹	1020 cm ⁻¹	1120 cm ⁻¹	1165 cm ⁻¹
0	0.764	0.388	0.593	0.449	0.473
42	0.556	0.186	0.199	0.258	0.342
84	0.992	0.465	0.372	0.681	0.619

To compare differences in the contributions from the bands at 520, 650, 1020, 1120 and 1165 cm⁻¹ in 0.1 wt % Fe-ZSM-5 (XX)_H⁺ samples, the relative intensities (RI) of the bands were calculated (relative to the SiO₂ band at 380 cm⁻¹). The RIs are provided in Table 2. A difference in the band intensity can be observed at the different SiO₂/Al₂O₃ ratios. In particular, the RI are generally lower as the Al content of the catalyst increases. This contradicts what has previously been observed by Li *et al.*, who implied that these bands correspond to framework Fe species, [Fe(OSi)₄].^{25,26} When the DRUV-vis and resonance Raman spectra are considered together, it appears that the decrease in relative intensity might result from a decrease in framework Fe³⁺ ($\lambda = 200$ -250 nm) and an increase in extra framework and oligomeric Fe³⁺ species ($\lambda = 250$ – 350 nm) present in the structure.

Herein, it has been demonstrated that the presence of structural Al^{3+} within the MFI lattice is crucial for promoting CH_4 partial oxidation activity, which is in line with previous observations. However, Al^{3+} itself is not thought to be involved in the catalytic pathway, as there was low catalytic activity reported for the Fe-free ZSM-5 catalyst (Figure 5).^{12,20} Furthermore, the rate of H_2O_2 decomposition, a competing reaction pathway in aqueous phase CH_4 oxidation, increases with increasing Al^{3+} content. The similar trends for both pathways supports earlier mechanistic studies that suggest that activation of H_2O_2 occurs prior to C-H activation and the activated peroxide species can either oxidise CH_4 , or undergo a disproportionation reaction to afford H_2O and O_2 (Equation 3).⁸ The addition of Al^{3+} into the zeolite framework increases the number of Brønsted acid sites, which may be implicit in the decomposition of H_2O_2 . However, as shown in Figure 5, relatively low TOFs were reported for the decomposition of H_2O_2 in the Al-free analogue Fe-silicalite-1, and the rate of partial CH_4 oxidation increased on addition of Al^{3+} to the framework. Incorporation of Al^{3+} into the MFI lattice suggests that there is limited effect of the Brønsted acid sites on decomposition of H_2O_2 , but implies another mechanism is dominant in this reaction pathway.

3.3. Effect of Fe Loading on Methane Oxidation and Hydrogen Peroxide Decomposition

3.3.1. Synthesis of YY wt % Fe-ZSM-5 (42)

In the previous section, it was found that greater Al^{3+} content was able to promote catalytic rates during CH_4 oxidation. As the Al^{3+} content increases, so does the number of ion-exchange sites within the catalyst. It has been suggested there is an optimal balance between the concentration of Fe^{3+} and the number of exchange sites; this could be exploited, then an optimally active catalyst for methane oxidation could be developed.¹² In Section 3.2, 0.1 wt% Fe-ZSM-5 with a $\text{SiO}_2/\text{Al}_2\text{O}_3$ ratio of 42 is the most active for methane oxidation. To investigate the effect of Fe loading on catalytic performance, a range of samples were prepared by hydrothermal synthesis, with varying amounts of Fe-precursor added to the synthesis gel prior to crystallisation at 175 °C for 120 h. The synthesised catalysts are denoted as YY wt% Fe-ZSM-5 (42), where YY denotes the nominal loading of Fe, for example 0.1 wt% Fe-ZSM-5 (42)_{H⁺}. The crystalline structure of the material was confirmed by *p*XRD, where characteristic crystalline MFI diffraction peaks were identified at $2\theta = 7-8^\circ$ and $22.5-25^\circ$, as shown in Figure 9.¹⁸ No other crystal phases were observed at different Fe loadings, demonstrating that the hydrothermal synthesis was comparable at different Fe loadings.

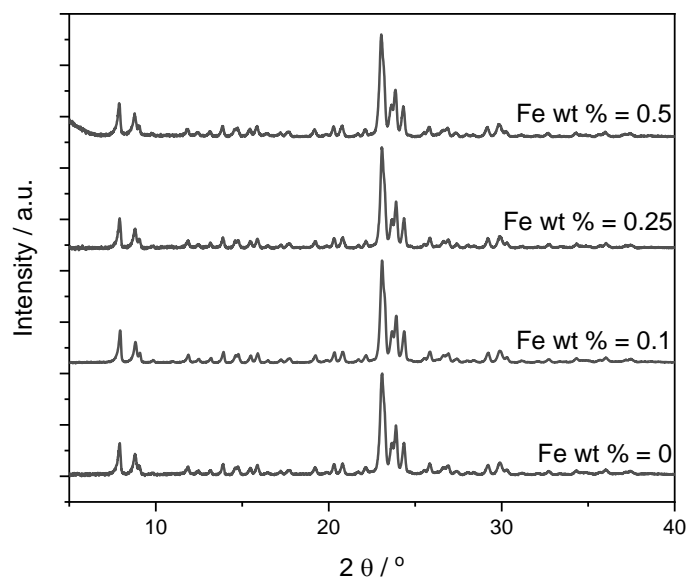


Figure 9 *p*XRD patterns of synthesised YY wt% Fe-ZSM-5 (42), crystallised at 175 °C for 120 h, where YY denotes the Fe wt% loading.

The isomorphous substitution of Fe³⁺ into the MFI framework, following hydrothermal synthesis, was determined by DRUV-vis spectroscopy and the data is shown in Figure 10. The DRUV-vis spectra plotted in Figure 10 show that a large proportion of Fe was substituted into the framework in each of the synthesised samples, however, an additional absorption band could be observed at 250 -350 nm in 0.5 wt% Fe-ZSM-5 (42)_AS. This suggests that at greater Fe loadings, not all the Fe³⁺ is fully incorporated into the framework, possibly due to an excess in Fe³⁺ that exceeds the exchange capacity of the catalyst. As such, the as-synthesised samples are not equivalent at various Fe loadings, which should be taken into consideration when comparing the catalysts throughout this section. The synthesised catalysts were then activated by calcination to remove the template, ion-exchange and final thermal activation at 550 °C to afford the H⁺ form of the materials, which were subsequently characterised and tested.

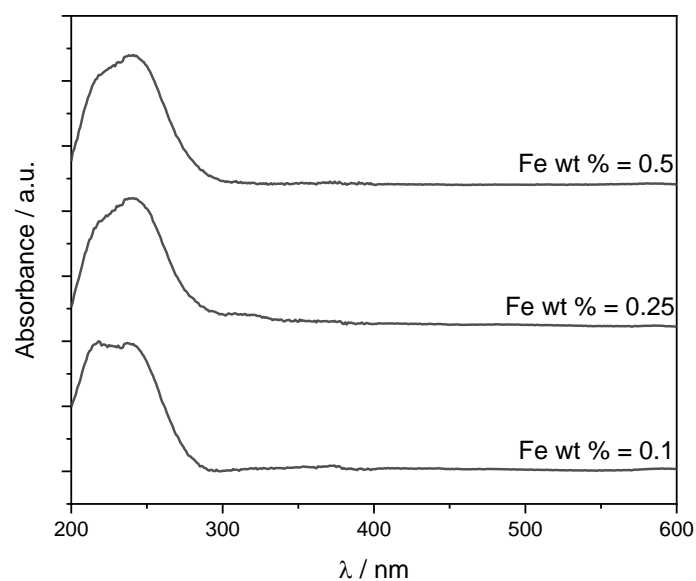


Figure 10 DRUV-vis of synthesised YY wt% Fe-ZSM-5 (42) where YY denotes the Fe wt% loading.

3.3.2. Catalytic Performance of YY wt% Fe-ZSM-5 (42)_{H⁺}

The catalytic activity of YY wt% Fe-ZSM-5 (42) for CH₄ oxidation and competing H₂O₂ decomposition reaction are plotted in Figure 11. As shown in Figure 5, the Fe-free analogue produced relatively low quantities of oxygenated product following reaction, indicating the essential role of Fe in the sample. Yet, on addition of 0.1 wt% Fe to the ZSM-5 framework, an increase in the quantity of oxygenated products was observed, implicating Fe in catalytic activity. At 0.1 wt% Fe content, the reported TOF, used as a measure of catalytic performance, is 487 h⁻¹. Upon increasing the Fe³⁺ loading to 0.25 wt%, the TOF was reported as 352 h⁻¹ and the observed value at 0.5 wt% Fe loading was 358 h⁻¹ (both are within the calculated error of 6.4% for the reaction). Overall, TOF decreased by approximately 25% in the range of 0.1 – 0.5 wt% Fe in the MFI catalysts. As the TOF is normalised to the moles of Fe in the catalyst, catalysts with a relatively high Fe content were determined to be less intrinsically active than at lower nominal Fe loadings. Furthermore, the activity of both CH₄ oxidation and H₂O₂ decomposition reactions decreased in a similar trend, which agrees with the observation provided in Section 3.2 that the activation of the H₂O₂ oxidant by the Fe-MFI catalyst occurs prior to CH₄ oxidation step.

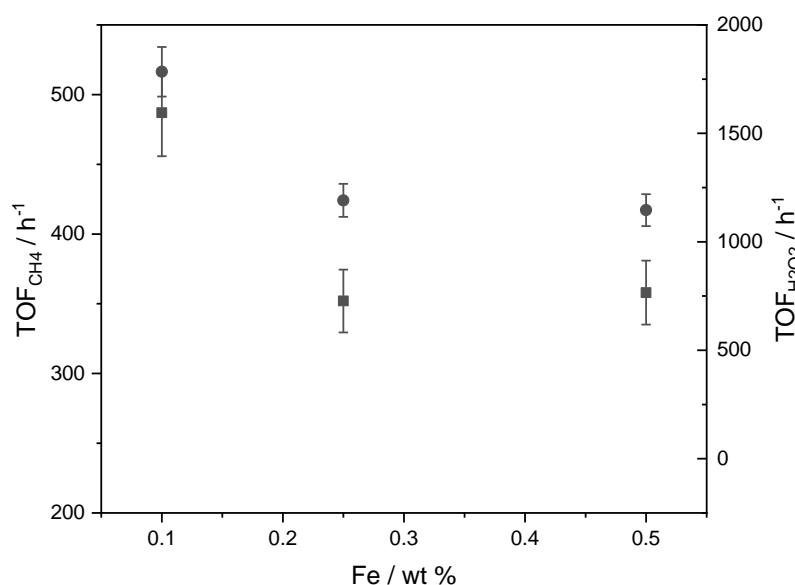


Figure 11 Left: x-axis (squares), methane oxidation activity (reported as TOF values) of YY wt% Fe-ZSM-5 (42)_H⁺ as a function of Fe loading. Right: x-axis (circles), hydrogen peroxide decomposition (reported as TOF values) of YY wt% Fe-ZSM-5 (42)_H⁺ as a function of Fe loading. Error bars are set at 6.4%.

3.3.2. Spectroscopic Characterisation of YY wt% Fe-ZSM-5 (42)_H⁺

3.3.2.1. DRUV-vis Characterisation

The DRUV-vis spectra of the activated YY wt% Fe-ZSM-5 (42)_H⁺ are shown in Figure 12. The areas of the sub-regions were integrated to give a generalised population of Fe³⁺ species throughout the catalyst.¹²⁻¹⁵ Following activation, there is a clear change in Fe³⁺ distribution from framework positions to extra framework Fe³⁺, which is thought to be a result of destabilisation of framework Fe³⁺ species.¹² Upon further increasing the nominal Fe³⁺ loading to 0.5 wt%, there is a large increase in the relative proportion of oligomeric and bulk oxidic species, which can be observed by the increase in absorbance bands of oligomeric Fe (λ_3) and bulk Fe oxide species (λ_4). The changes of Fe³⁺ speciation that occur due to catalyst activation are shown in Figure 13, after the relative area under the curve of the each of the sub-bands was calculated from the spectra shown in Figure 12. Following activation of the samples, the distribution of extra framework Fe³⁺ (λ_2) appears to increase, suggesting that the subsequent treatments leads to the formation of active, extra framework Fe³⁺ species. Further, additional bands are observed in the DRUV-vis spectra of 0.5 wt% Fe-ZSM-5(42)_H⁺ at 350 and 500 nm, correlating to . As the catalyst at higher Fe loading is less intrinsically active for partial CH₄ oxidation, it can be assumed that such species are inactive for CH₄ oxidation. It should be noted that an increase in the relative proportion of λ_3 and λ_4 was not seen in 0.25 wt% Fe-ZSM-

5(42)_H⁺, even though there is no observed difference in TOF value between the two samples at different Fe loadings. Thus, higher Fe loadings lead to formation of inactive, oligomeric and oxidic Fe species. Furthermore, catalytic activity can drop at higher loadings due to the formation of extra framework species that absorb in a similar region to those correlated with catalytic activity. It has been noted that several overlapping Fe³⁺ species can absorb in the range 250 – 300 nm.²⁷ By not being able to distinguish between distinct Fe³⁺ species within the lattice, it is not yet possible to demonstrate why these catalysts are more active at lower Fe loadings.

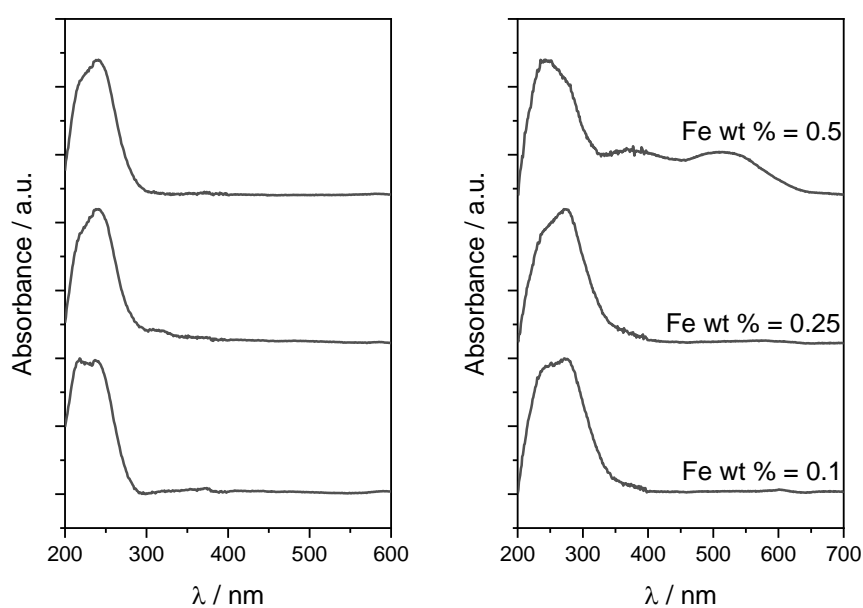


Figure 12 Left; DRUV-vis of synthesised YY wt% Fe-ZSM-5 (42), where YY denotes the Fe wt% loading. Right; DRUV-vis spectra of YY t % Fe-ZSM-5 (42) after calcination, ion-exchange and thermal activation to afford the H⁺ form.

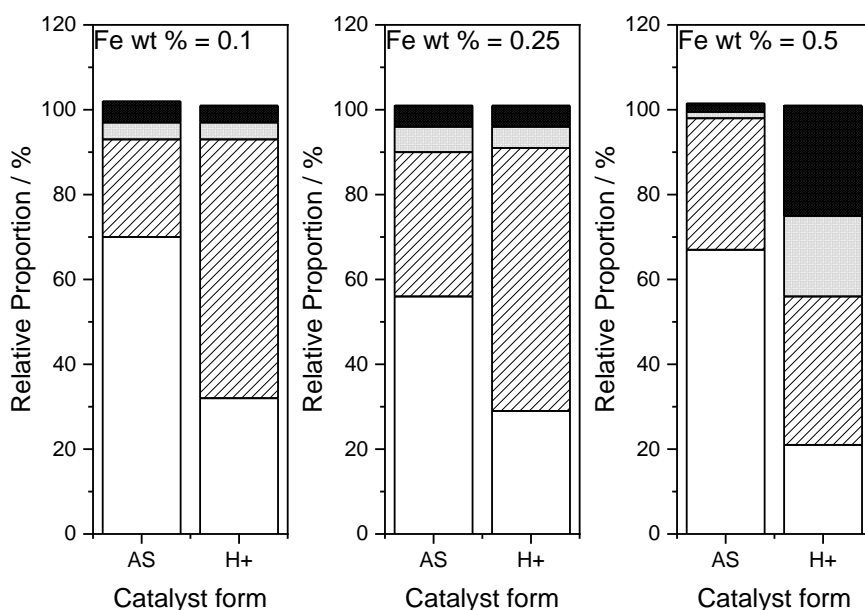


Figure 13 Relative proportion of sub-bands of DRUV-vis spectra of YY wt% Fe-ZSM-5 (42), as a function of catalyst form, where YY denotes the Fe wt % loading. The different sub-bands are; white, λ_1 ; stripes, λ_2 ; grey, λ_3 , and; black, λ_4 .

3.3.2.2. Resonance Raman Characterisation of YY wt% Fe-ZSM-5 (42)_{H⁺}

To complement the observations made in the DRUV-vis spectra, Raman measurements were taken at 266 nm of the activated samples at different Fe loadings (Figure 14). In the Fe-free analogue, only the normal Raman vibrations of the symmetric and asymmetric Si-O-Si vibrational modes in the 5MR of MFI are observed at $\bar{\nu} = 380$ and 800 cm^{-1} , respectively.²⁸ These bands were also observed in the Fe-containing analogues, which confirms the crystalline structure of the MFI framework has been conserved after consecutive treatments. A further five resonance features are observed at $\tilde{\nu} = 520, 650, 1020, 1120$ and 1165 cm^{-1} . The intensity of each of these bands was calculated relative to the SiO₂ stretch at 380 cm^{-1} , and were normalised by the number of moles of Fe to determine the relative intensity of each of the features.

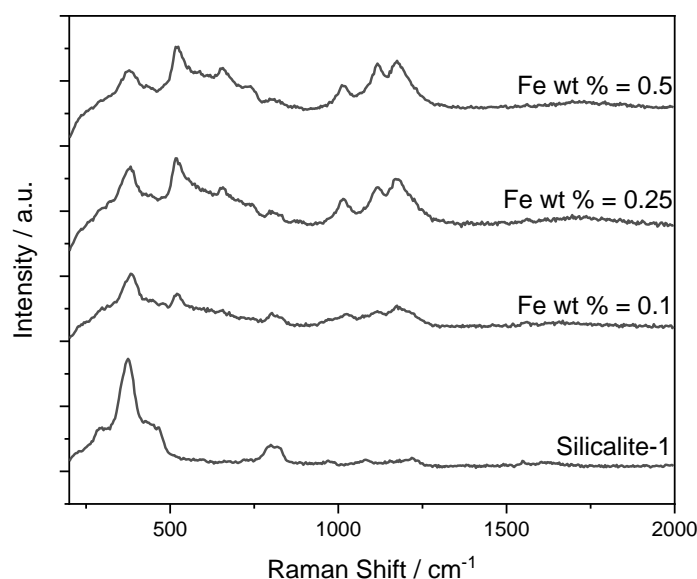


Figure 14 Resonance Raman ($\lambda = 266$ nm) of YY wt% Fe-ZSM-5 (42)_H⁺, where YY denotes the Fe wt% loading. Silicalite-1 is provided for reference.

Table 3 Relative intensities of Raman-active features of YY wt% Fe-ZSM-5 (42)_H⁺ as calculated from the ratio of the intensity of the Raman band and the intensity of the Si-O-Si stretch at 380 cm⁻¹, as determined from the resonance Raman spectra (266 nm).

Fe wt%	520 cm ⁻¹	1020 cm ⁻¹	1120 cm ⁻¹	1170 cm ⁻¹
0.1	0.556	0.199	0.258	0.342
0.25	0.483	0.167	0.254	0.316
0.5	0.334	0.110	0.228	0.255

All the features associated with Fe³⁺ appear to increase in intensity on increase of the nominal Fe loading. When the absolute intensity is normalised to the nominal number of moles of Fe in the samples, the relative intensity of each of the bands decreases as Fe³⁺ content increases, as shown in Table 3. When correlated to the TOF values shown in Figure 11, a decrease in TOF value corresponds to a reduction in the intensity of the Raman bands. Li *et Al.* has assigned the bands at 520, 1020, 1120 and 1165 cm⁻¹ in the resonance Raman spectra of Fe-MFI to tetrahedral [Fe(OSi₄)] units in the MFI framework; the results demonstrated here support Li's observation. The decrease in the relative intensities of framework Fe³⁺ also correlates with the decreasing relative proportion of framework Fe³⁺ species seen in the DRUV-vis spectra (Figure 12) observed at higher Fe loadings. Additionally, a band was observed at 650 cm⁻¹ in 0.25 wt% Fe-ZSM-5 (42)_H⁺, which increased in absolute intensity at 0.5 wt% Fe loading. This band has

not previously been reported for Fe-ZSM-5, however, the DRUV-vis spectra suggests that oligomeric Fe species form at higher Fe loadings. Modelling studies should be performed to support experimental observations and predict possible structures for extra framework oligomeric species.

The samples were further studied using a 325 nm wavelength laser. This wavelength is closer in energy to the species absorbing at 280 - 320 nm observed in the DRUV-vis (Figure 12), so may provide additional information on Fe³⁺ speciation of extra framework species.^{25,26,29} A longer wavelength laser better matches the energy of the electronic transition of the LCMT bands of extra framework Fe species (*cf.* Chapter 2, Section 2.2.6), thus can be used to further explore Fe³⁺ species at 300-350 nm.

In Figure 15, which compares the Raman spectra of 0.1 wt% Fe-ZSM-5(42)_H⁺ at 266 and 325 nm, a shift in the peak positions of the Fe-relevant bands, indicating the presence of different Raman active Fe³⁺ features within the MFI framework. The shifts of the bands at 520 and 1165 cm⁻¹ are independent of the laser wavelength and can be assumed to arise from the same species that absorbs at a wavelength between 266 and 325 nm. In the Raman spectra recorded at 325 nm, the Raman shifts of two peaks at 1000 and 1080 cm⁻¹ had shifted to a lower wavenumber compared to the spectra recorded at 266 nm (1020 and 1120 cm⁻¹ respectively). The change in the frequency of the peak suggests that a different species is enhanced at 325 nm. Furthermore, the peak intensities of each of the bands is lower at 325 nm, which suggests that the Fe³⁺ species that give rise to these bands absorb at higher energies than 325 nm, thus are not as strongly resonance enhanced. When comparing the spectra of the various samples at 325 nm (Figure 16), the absolute intensity of the bands at 520, 1000, 1080 and 1165 cm⁻¹ is greater at higher Fe loading, but this could be due to the increased Fe³⁺ content within the sample.

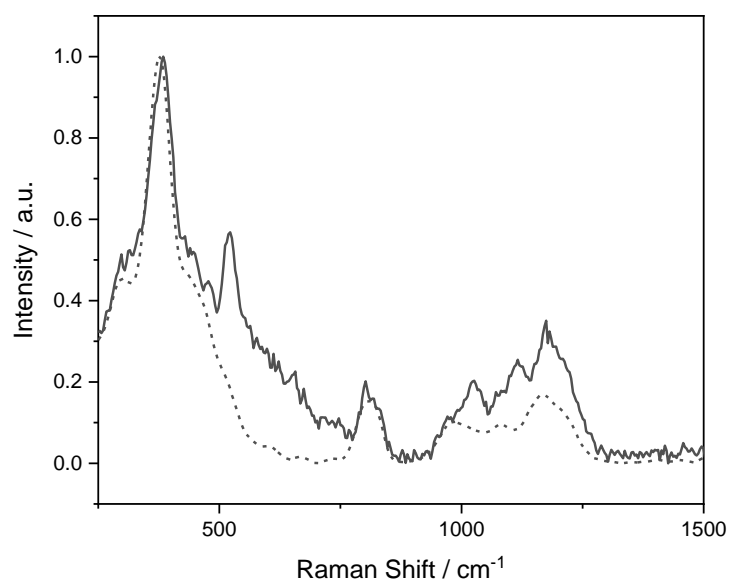


Figure 15 Comparison of the resonance Raman of 0.1 wt% Fe-ZSM-5 (42)_H⁺ at 266 nm (bold line) and 325 nm (dashed line).

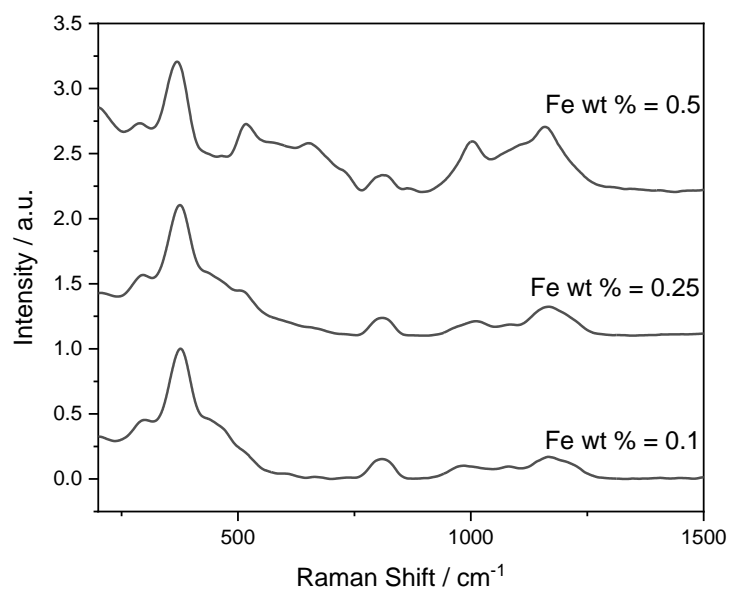


Figure 16 Resonance Raman ($\lambda = 325$ nm) of YY wt% Fe-ZSM-5 (42)_H⁺, where YY denotes Fe wt% loading.

In conclusion, it has been shown by TOF determination that low loadings of Fe³⁺ are pivotal for the synthesis of an active catalyst for CH₄ oxidation. At loadings greater than 0.25 wt %, intrinsic activity fell, which was correlated with a decrease in framework and extra framework Fe³⁺ species. These changes could be observed by semi-quantitative DRUV-vis, where relative

populations of Fe species absorbing at high energies (< 300 nm) falls as the Fe content of the samples increased. The reduction in the relative proportion of framework Fe^{3+} species was further observed by the loss of relative intensity of Fe-resonant bands observed in resonance Raman spectroscopy. However, identification of an active Fe^{3+} species was not achieved using resonance Raman technique, as the relative intensity of each the Fe^{3+} features decreased in line with catalytic activity. Observation of an active species in the Raman spectra would correlate to an increase in relative intensity of Raman bands in the most active catalyst. Identification of a tangible active species would be crucial to developing an active catalyst for partial CH_4 oxidation and designing syntheses to avoid formation of inactive species. Furthermore, the addition of higher loadings of Fe to the framework results in the formation of clustered Fe oxides after thermal activation of the catalysts. The formation of such species may be a result of the formation of a large proportion of inactive, spectator species. It has been proposed that such species do not participate in the CH_4 oxidation pathway.¹²

3.4. Effect of the Preparation of Hydrothermally Prepared Fe-ZSM-5 on Methane Oxidation Activity

3.4.1. Preparation of 0.1 wt% Fe-ZSM-5 (XX) for CH_4 Oxidation

The catalysts synthesised in the above sections were prepared in a series of steps to afford the active proton form of the catalyst. These catalysts were prepared by hydrothermal methods as reported by Prikhod'ko *et al.* and later modified by Hammond *et al.*, where an aluminosilicate gel with the addition of an iron salt precursor is placed under hydrothermal conditions in the presence of an organic structural directing agent (OSDA) to crystallise the desired MFI framework.³⁰ The hydrothermal synthesis affords a synthesised form of the catalyst that is then activated by a series of steps, as described in Chapter 2, Section 2.1, to afford the H^+ form of the catalyst.^{12,20} Throughout the activation steps, it has been suggested that extraction of framework substituted Fe^{3+} to extra framework positions can occur, which can be seen in the DRUV-vis spectra of the AS and H^+ forms of the catalyst (Section 3.2 and 3.3). However, intermediate steps are performed between these two forms that are not as well understood, and it is possible that extraction of framework Fe^{3+} occurs prior to the final thermal activation step. Earlier studies by the group of Hutchings has provided evidence that early extraction of Fe^{3+} occurs, as it has been shown that some of the intermediate forms exhibit oxidation activity.¹²

To better understand the changes that Fe-ZSM-5 undergoes during post-synthetic treatments, the investigation was expanded to explore the effect of each stage of the preparation of 0.1 wt% Fe-ZSM-5. Various forms of 0.1 wt% Fe-ZSM-5 (XX)_{ZZ} at two different $\text{SiO}_2/\text{Al}_2\text{O}_3$ ratios

(where XX = 42 or 84 and ZZ = AS, Na⁺, NH₄⁺ or H⁺) were prepared by hydrothermal synthesis, as described in Chapter 2, Section 2.1. A small amount (circa. 500 mg) was recovered at each stage of the sample preparation to characterise and test the materials under reported conditions (Chapter 2, Section 2.3).

3.4.2. Catalytic Performance of 0.1 wt% Fe-ZSM-5 (XX)_ZZ

To establish whether each form of the catalyst was active for CH₄ oxidation, samples generated from each step of the synthesis procedure were tested under CH₄ oxidation conditions (as described early in Chapter 3) and the CH₄ oxidation TOF values were plotted in Figure 17. Both as-synthesised forms of the catalysts are inactive for CH₄ oxidation, though following calcination, catalytic activity was observed. The catalyst at higher Al³⁺ content was more active following calcination to remove the OSDA.

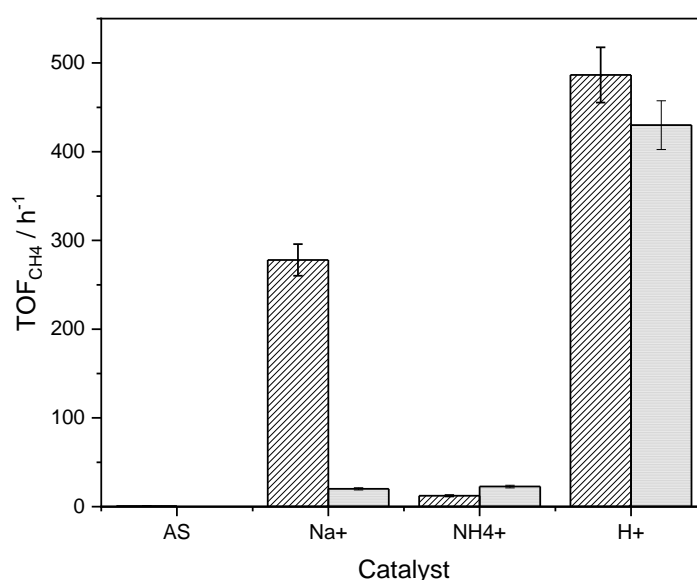


Figure 17 Methane hydroxylation activity (reported as TOF values) as a function of catalyst form. Stripes, 0.1 wt% Fe-ZSM-5 (42)_ZZ; Dots, 0.1 wt% Fe-ZSM-5 (84)_ZZ. ZZ denotes the catalyst form (AS, Na⁺, NH₄⁺ and H⁺). Error bars set at 6.4%.

The observation that the Na⁺-form of Fe-MFI could be active for partial CH₄ oxidation was intriguing and could lead to a reduction in the number of post-synthetic steps required to produce an active catalyst, thus improving catalyst production output and productivity. Moreover, by requiring fewer processing steps, the probability of altering other aspects of the catalyst, such as structure, can be reduced. The reason for the onset of activity is unknown, though it would be important to understand the cause of activity, as this might provide some crucial insight into the evolution of active Fe³⁺ species within the zeolite matrix.

Following ion-exchange in NH_4NO_3 , a decrease in the activity was observed in sample 0.1 wt% Fe-ZSM-5 (42) $_{\text{NH}_4^+}$, whereas no change was observed in 0.1 wt% Fe-ZSM-5 (84) $_{\text{NH}_4^+}$. It is not clear why the catalyst deactivates following ion exchange, especially as Hammond *et al.* have reported that the ammonium form of 0.5 wt% Fe-ZSM-5 (84) was relatively active for CH_4 oxidation, though the difference in Fe content might be significant.¹² Another theory for the poor activity of the NH_4^+ forms could be that the ion-exchange resulted in exchange of extra framework Fe^{3+} along with Na^+ , thus the sample is losing active Fe^{3+} species. The loss of Fe from the samples was not investigated, though elemental analysis of the ion-exchange filtrate by microwave plasma atomic emission spectroscopy (MP-AES) could validate this, along with ICP-OES of the solid sample.

The proton forms for both samples were the most active samples for partial CH_4 oxidation and it is possible that a greater proportion of Fe^{3+} has been extracted from framework positions after subsequent heat treatments. Further characterisation of the Fe^{3+} speciation will be explored further in Section 2.4.3 to correlate changes in Fe speciation with catalytic trends reported in Figure 17. To explain the observed catalytic activity trends, particularly following calcination, the synthesised and calcined samples were studied spectroscopically to observe any differences in the Fe^{3+} speciation between the samples.

3.4.3. Hydrothermally Synthesised 0.1 wt % Fe-ZSM-5

The plot of activity versus catalyst form shown in Figure 18 shows that 0.1 wt % Fe-ZSM-5 $_{\text{AS}}$ is inactive, regardless of the $\text{SiO}_2/\text{Al}_2\text{O}_3$ ratio. There are two possibilities for this; mass diffusion is restricted in the pore network due to presence of TPA^+ , or activation of active sites has not occurred. To rule out the former possibility, N_2 physisorption measurements were made to determine the surface area and micropore volume of the samples. As stated in Section 3.2, the micropore void spaces of the synthesised sample are significantly reduced due to the presence of TPA^+ within the micropores, which restricts reactant diffusion and prevent access to the active sites. To remove TPA^+ , the samples were calcined at 550 °C, which resulted in an increase in V_{micro} and apparent surface area, as shown previously in Table 1. When the Na^+ samples were tested for CH_4 oxidation activity, there was an observed increase in catalytic activity, which could be explained by the increase in micropore volume that would result in increased reactant diffusion. However, the TOF value of 0.1 wt% Fe-ZSM-5 (42) $_{\text{Na}^+}$ is 15 times greater than that of 0.1 wt% Fe-ZSM-5 (84) $_{\text{Na}^+}$, which indicates that the onset of catalytic activity is not as straightforward as removal of TPA from the zeolite micropores. To

understand whether the presence of TPA prevents catalytic activity, a novel OSDA-free synthesis of Fe-ZSM-5 was developed and discussed in Chapter 5.

The activity measurements of the Na⁺-forms of the catalysts suggests that there is a difference in the distribution of Fe³⁺ species that occurs during the calcination step. To assess if the difference in performance arises from different changes to the Fe³⁺ species during heat treatment, Fe-selective spectroscopy was utilised to determine any relative population changes before and after calcination. DRUV-vis spectroscopy was used to observe LMCT bands of Fe³⁺, which are indicative of the coordination environment of Fe³⁺.²⁹ The spectra of both the AS and Na⁺ forms of the two samples are shown in Figure 18 and the spectra were integrated to determine an approximate distribution of the Fe³⁺ species that are shown in Table 4.

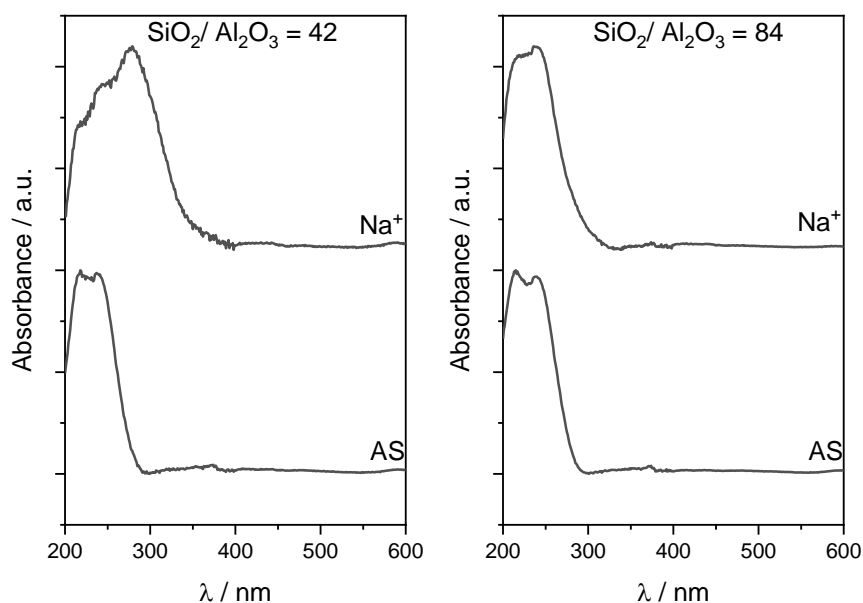


Figure 18 Left: DRUV-vis of 0.1 wt% Fe-ZSM-5 (42)_ZZ. Right; DRUV-vis spectra of 0.1 wt% Fe-ZSM-5 (84)_ZZ. Where ZZ denotes the catalyst form.

Table 4 Quantification of Fe species in 0.1 wt% Fe-ZSM-5 (XX)_ZZ, where ZZ denotes the catalyst form, calculated from integrated DRUV-vis spectra.

Sample	λ_1	λ_2	λ_3	λ_4
0.1 wt% Fe-ZSM-5 (42)_AS	70	22	3.8	4.5
0.1 wt% Fe-ZSM-5 (42)_Na ⁺	30	62	4.3	4.1
0.1 wt% Fe-ZSM-5 (84)_AS	70	24	3.0	3.9
0.1 wt% Fe-ZSM-5 (84)_Na ⁺	62	30	3.3	4.5

The DRUV-vis spectra for the synthesised samples shown in Figure 18 are similar and are in good agreement with Fe^{3+} being substituted into the framework after crystallisation. However, following calcination at 550 °C, a distinct difference between the two spectra can be observed; a shift to a lower energy maximum was observed in the more active sample. The shift to a lower energy is indicative of the formation of accessible, extra framework species during high temperature calcination at low $\text{SiO}_2/\text{Al}_2\text{O}_3$. Integration of the sub-bands in the spectra of 0.1 wt% Fe-ZSM-5 (84) $_{\text{Na}^+}$ suggests that there is a minor loss of the tetrahedral Fe^{3+} following heat treatment and there is an equivalent increase in the percentage of extra framework Fe^{3+} forming. However, a significant shift in the distribution of species in 0.1 wt% Fe-ZSM-5 (42) $_{\text{Na}^+}$ following calcination at 550 °C was observed. Following integration of the area under the curve of the UV regions, the proportion of extra framework Fe^{3+} (λ_2) increases by 40% whilst the proportion of framework Fe^{3+} (λ_1) decreases by an equivalent percentage. When the relative proportions of the sub-bands λ_1 and λ_2 are plotted against CH_4 oxidation TOF values (Figure 19), it appears that the increase in catalytic activity correlates with an increase in extra framework Fe^{3+} and simultaneous decrease in framework species.

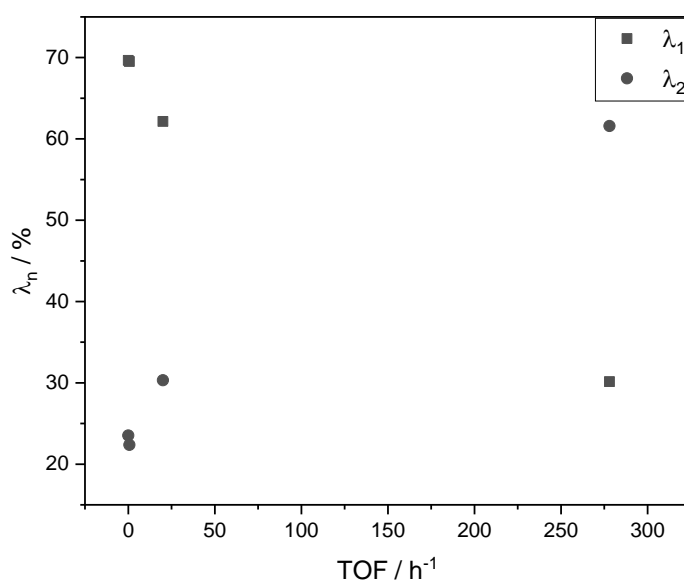


Figure 19 Relative proportion of λ_1 (squares) and λ_2 (circles) as a function of CH_4 partial oxidation activity (reported as TOF values) of 0.1 wt% Fe-ZSM-5 (42) $_{\text{Na}^+}$ and 0.1 wt% Fe-ZSM-5 (84) $_{\text{Na}^+}$.

3.4.4. Resonance Raman to Determine Changes in Fe³⁺ Speciation during Calcination

To complement the data acquired in the DRUV-vis, resonance Raman spectroscopy was used to distinguish between individual Fe³⁺ species that absorb between 200 and 300 nm.^{23,24} The spectra of the samples before and after calcination were recorded at 266 nm and shown in Figure 20. Characteristic bands of Si-O-Si stretching modes of MFI are observed at $\bar{\nu} = 380$ and 800 cm^{-1} , which confirms that the correct zeolite structure has formed during crystallisation.²⁸ Additionally, there is an intense feature at $\bar{\nu} = 1500\text{ cm}^{-1}$ in the AS samples that arises from the presence of TPA cations within the zeolite pores.²⁸ Following treatment, the shift associated with TPA is reduced in intensity, indicating that the OSDA has been removed, which is consistent with N₂ physisorption data (Table 1) and TGA data (Figure 3).

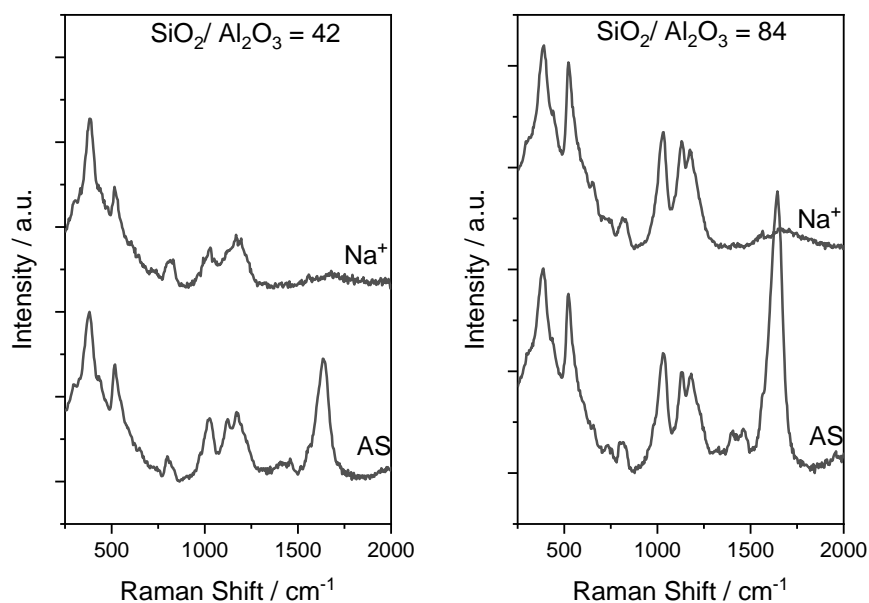


Figure 20 Left; Resonance Raman ($\lambda = 266\text{ nm}$) spectra of 0.1 wt% Fe-ZSM-5 (42)_ZZ. Right; Resonance Raman ($\lambda = 266\text{ nm}$) spectra of 0.1 wt% Fe-ZSM-5 (84)_ZZ, where ZZ denotes the catalyst form.

Table 5 Quantification of Fe bands in 0.1 wt% Fe-ZSM-5 (XX)_ZZ, where ZZ denotes the catalyst form, calculated from integrated resonance Raman ($\lambda = 266$ nm) spectra. ^a Values calculated as the ratio of I_R / I_{380} .

Sample	520 cm^{-1}	1020 cm^{-1}	1080 cm^{-1}	1166 cm^{-1}
0.1 Fe-ZSM-5 (42)_AS	0.693	0.378	0.361	0.415
0.1 Fe-ZSM-5 (42)_Na ⁺	0.615	0.237	0.228	0.295
0.1 Fe-ZSM-5 (84)_AS	0.876	0.563	0.492	0.470
0.1 Fe-ZSM-5 (84)_Na ⁺	0.922	0.559	0.527	0.491

To understand whether changes to the intensities of Fe³⁺ bands occur post-calcination, the relative intensities of the bands at $\bar{\nu} = 520, 1020, 1120$ and 1170 cm^{-1} were calculated (relative to Si-O-Si vibrational mode at 380 cm^{-1}) and given in Table 5. Little change was observed in the relative intensities of the Fe³⁺ stretch at SiO₂/Al₂O₃ = 84 following calcination, which correlates with the lack of new absorbance maxima in the DRUV-vis (Figure 18). The lack of change in the Fe signals in the Raman spectrum suggests that at lower Al³⁺ content, the tetrahedral [Fe(OSi)₄] species are not destabilised following the initial heat treatment.^{25,26} The Raman spectra of 0.1 wt% Fe-ZSM-5 (42) shows that there is a decrease in the relative intensities of the Fe³⁺ bands following calcination. The change in relative intensity supports the theory demonstrated by the DRUV-vis spectra in Figure 18 that framework Fe³⁺ species are destabilised during the initial heat-treatment, which leads to the formation of extra framework Fe³⁺. The decrease in framework Fe vibrations in the resonance Raman spectrum correlates to the observed catalytic activity of 0.1 wt % Fe-ZSM-5 (42)_Na⁺. However, identification of a band in the spectra at 266 nm related to an active species was not achieved, as there were no apparent increases in relative intensities of the Fe³⁺ bands.

As the absorbances of the proposed active species are observed at longer wavelengths (250-350 nm), the laser wavelength was increased to 325 nm to better observe changes in the λ_2 region.²⁹ A comparison of 0.1 wt% Fe-ZSM-5 (42)_Na⁺ at two wavelengths are shown in Figure 21 to show the distinction between the two samples. The band at 520 cm^{-1} has previously been assigned to framework Fe³⁺ and was only observed in the Raman spectrum at 266 nm, which implies that this band is only resonance at this wavelength.^{25,26} The bands between 1000 and 1165 cm^{-1} can be observed in the spectra at both laser wavelengths, although at a reduced intensity at 325 nm. The reduction in relative intensity at 325 nm implies that the species which

corresponds to the stretching modes between 1000 – 1165 cm^{-1} are no longer resonance enhanced at 325 nm.

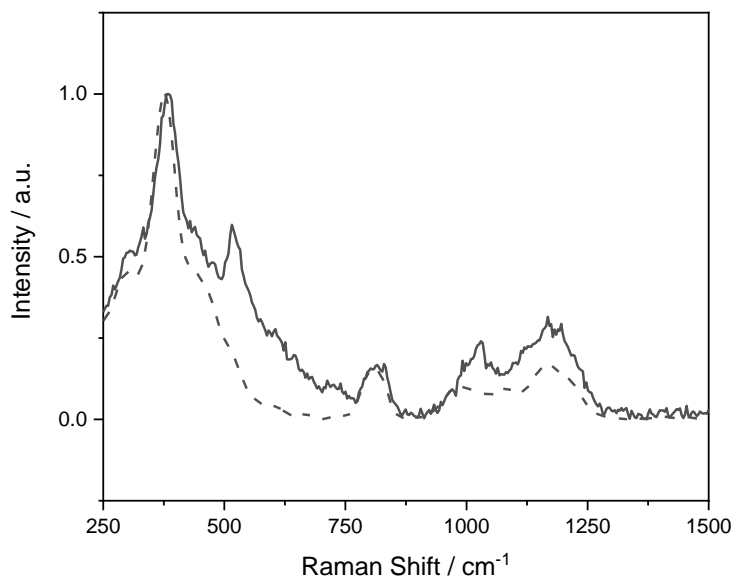


Figure 21 Resonance Raman spectroscopy of 0.1 wt% Fe-ZSM-5 (42) $_{\text{Na}^+}$ at two different wavelengths; solid line, 266 nm, and dashed line, 325 nm.

The Raman spectra of the samples are shown in Figure 22 to demonstrate the change in Fe^{3+} speciation following calcination of the AS form. However, clear identification of the bands at 1000 – 1165 cm^{-1} in the AS catalysts was not possible, due to significant fluorescence at longer wavelengths caused by the TPA^+ template in the pores of the synthesised material.²⁸ Following TPA^+ removal, these bands become more distinguished, but it was not possible to compare changes in intensity before and after calcination at 325 nm. However, a few differences in the spectra of 0.1 wt% Fe-ZSM-5 (42) $_{\text{Na}^+}$ and 0.1 wt% Fe-ZSM-5 (84) $_{\text{Na}^+}$ could be observed in the region 980 – 1170 cm^{-1} following calcination at 550 °C. The relative intensities of the Raman bands at 325 nm of the Na^+ form samples are given in Table 6. A minor difference in the intensity of the band at 980 cm^{-1} can be observed, which suggests that the species arising from this band does not contribute to CH_4 oxidation activity, as the lack of change in intensity does not correlate with the change in catalytic activity. However, there is an increase in relative intensity of the bands at 1080 and 1166 cm^{-1} in the more active sample (0.1 wt% Fe-ZSM-5 (42) $_{\text{Na}^+}$), which was more noticeable in the band at 1166 cm^{-1} . A similar trend was observed in the Raman spectra at $\lambda = 325$ nm of YY wt% Fe-ZSM-5 (42) $_{\text{H}^+}$ (Figure 16) in that the intensity of the $\bar{\nu} = 1170$ cm^{-1} band was greatest in the most active catalyst.

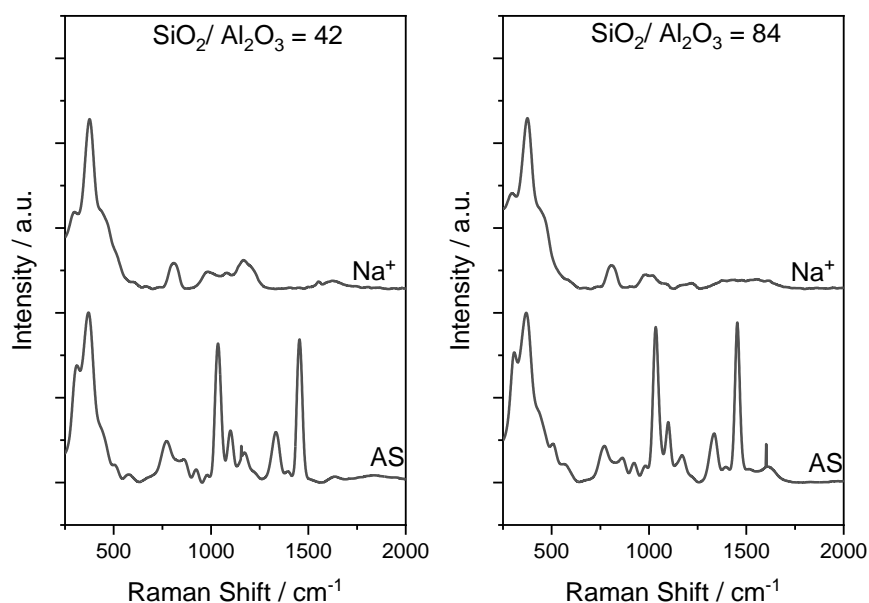


Figure 22 Left; Resonance Raman ($\lambda = 325$ nm) spectra of 0.1 wt% Fe-ZSM-5 (42)_ZZ. Right; Resonance Raman ($\lambda = 325$ nm) spectra of 0.1 wt% Fe-ZSM-5 (84)_ZZ, where ZZ denotes the catalyst form.

Table 6 Quantification of Fe bands the resonance Raman spectra of 0.1 wt% Fe-ZSM-5 (XX)_Na⁺ calculated from integrated resonance Raman ($\lambda = 325$ nm) spectra. Values calculated as the ratio of I_R/I_{380} .

SiO ₂ /Al ₂ O ₃	980 cm ⁻¹	1080 cm ⁻¹	1166 cm ⁻¹
42	0.094	0.089	0.17
84	0.078	0.028	0.033

Such trends indicate that an active Fe³⁺ species can be determined by Raman spectroscopy by tailoring the wavelength of the laser to match the energy of the Fe transitions. Further work would be needed to verify these observations. This study has shown that a change in Fe³⁺ speciation occurs during the initial calcination step at 550 °C. However, this change was only observed at SiO₂/Al₂O₃ = 42. The effect of SiO₂/Al₂O₃ ratio on the extraction of framework Fe³⁺ should be further investigated to better understand the supporting role the Al has in Fe-ZSM-5 catalysts for CH₄ partial oxidation.

3.5. Conclusions

It has been shown in this Chapter that Fe³⁺ is necessary for catalytic activity and Al³⁺, although not explicitly active for this reaction, can promote the formation of an active Fe³⁺ species. Literature studies have implied that the active species is a binuclear, extra framework Fe³⁺ and

the work reported here supports the theory that the active species is located outside of the zeolite framework.⁸ DRUV-vis and resonance Raman spectra show that the Al^{3+} within the MFI framework facilitates the extraction of the active Fe^{3+} species. Furthermore, the catalysts are more intrinsically active for methane oxidation at lower loadings of Fe^{3+} , as at higher loadings, the propensity to form inactive, clustered species is greater.

Catalytic rates of the competing H_2O_2 decomposition pathway were shown to follow the same trends as CH_4 oxidation upon addition of Fe^{3+} to the framework. This agrees with previous mechanistic studies where a diiron centre is initially activated by interaction with H_2O_2 , before undergoing reaction with CH_4 to afford the methyl hydroperoxide species.⁸ The activated hydroxy species could decompose to afford water and oxygen, reducing the oxidant efficiency; however, as activation of the oxidant is thought to precede both CH_4 oxidation and H_2O_2 decomposition, it was not possible to selectively reduce the rate of the side-reaction. To demonstrate whether H_2O_2 decomposition is radical induced, radical scavenger studies should be performed to eliminate radical contributions in each of the reaction pathways; radical formation could also participate in partial CH_4 oxidation. Furthermore, alternative oxidants should be considered that could prevent oxidant decompositions from occurring, however this would require further mechanistic understanding of oxidant activation by the active Fe sites.

Initially, it was assumed that Fe-ZSM-5 was activated via several post-synthetic steps to afford a protonated form of the catalyst. Yet, Section 3.4 shows that Fe-ZSM-5 is active following the initial calcination step that is required to remove the TPA OSDA from the micropores of the catalyst. Activation of Fe-ZSM-5 was only observed at lower $\text{SiO}_2/\text{Al}_2\text{O}_3$ ratios, the sample 0.1 wt% Fe-ZSM-5 (42) $_{\text{Na}^+}$ was substantially more active than 0.1 wt% Fe-ZSM-5 (84) $_{\text{Na}^+}$ for partial CH_4 oxidation following calcination,. Activation of samples with higher Al^{3+} content implies that Al^{3+} in the MFI framework affects the Fe^{3+} speciation, leading to the stipulation that Al^{3+} is crucial in the activation of the active Fe^{3+} species in Fe-ZSM-5., Catalytic tests demonstrated that Al^{3+} was not active for partial CH_4 oxidation in the absence of Fe^{3+} , indicating that Al^{3+} is not participating in the catalytic cycle. The presence of the organic template in the as-synthesised samples means that the catalytic activity of Fe-ZSM-5 cannot conclusively be caused by a change in Fe^{3+} speciation that occurs during calcination; the onset of catalytic activity may be a result of improved mass diffusion within the catalysts. To rectify this, Chapter 5 discusses the development of a template free Fe-ZSM-5 analogue to investigate whether catalytic activity is a result in a change in Fe^{3+} speciation, and not differences in reactant diffusion.

3.6. References

1. C. Hammond, S. Conrad and I. Hermans, *ChemSusChem*, 2012, 5, 1668-1686.
2. K. A. Dubkov, V. I. Sobolev, E. P. Talsi, M. A. Rodkin, N. H. Watkins, A. A. Shteinman and G. I. Panov, *J. Mol. Catal. A Chem.*, 1997, 123, 155-161.
3. G. Berlier, G. Spoto, S. Bordiga, S. Ricchiardi, P. Fisicaro, A. Zecchina, I. Rossetti, E. Selli, L. Forni, E. Giamello and C. Lamberti, *J. Catal.*, 2002, 208, 64-82.
4. K. A. Dubkov, N. S. Ovanesyan, A. A. Shteinman, E. V. Starokon and G. I. Panov, *J. Catal.*, 2002, 207, 341-352.
5. B. R. Wood, J. A. Reimer, A. T. Bell, M. T. Janicke and K. C. Ott, *J. Catal.*, 2004, 225, 300-306.
6. J. Pérez-Ramírez, F. Kapteijn, J. C. Groen, A. Doménech, G. Mul and J. A. Moulijn, *J. Catal.*, 2003, 214, 33-45.
7. M. V. Parfenov, E. V. Starokon, L. V. Pirutko and G. I. Panov, *J. Catal.*, 2014, 318, 14-21.
8. C. Hammond, M. M. Forde, M. H. Ab Rahim, A. Thetford, Q. He, R. L. Jenkins, N. Dimitratos, J. a Lopez-Sanchez, N. F. Dummer, D. M. Murphy, A. F. Carley, S. H. Taylor, D. J. Willock, E. E. Stangland, J. Kang, H. Hagen, C. J. Kiely and G. J. Hutchings, *Angew. Chem. Int. Ed.*, 2012, 51, 5129-33.
9. C. Hammond, R. L. Jenkins, N. Dimitratos, J. A. Lopez-Sanchez, M. H. Ab Rahim, M. M. Forde, A. Thetford, D. M. Murphy, H. Hagen, E. E. Stangland, J. M. Moulijn, S. H. Taylor, D. J. Willock and G. J. Hutchings, *Chem. - A Eur. J.*, 2012, 18, 15735-15745.
10. S. Sirajuddin and A. C. Rosenzweig, *Biochemistry*, 2015, 54, 2283-2294.
11. R. Banerjee, Y. Proshlyakov, J. D. Lipscomb and D. A. Proshlyakov, *Nature*, 2015, 518, 431-434.
12. C. Hammond, N. Dimitratos, J. A. Lopez-Sanchez, R. L. Jenkins, G. Whiting, S. A. Kondrat, M. Hasbi, M. M. Forde, A. Thetford, H. Hagen, E. E. Stangland, J. M. Moulijn, S. H. Taylor, D. J. Willock and G. J. Hutchings, *ACS Catal.*, 2013, 3, 1835-1844.
13. J. Pérez-Ramírez, J. C. Groen, A. Brückner, M. S. Kumar, U. Bentrup, M. N. Debbagh and L. A. Villaescusa, *J. Catal.*, 2005, 232, 318-334.
14. E. A. Pidko, E. J. M. Hensen and R. A. van Santen, *Proc. R. Soc. A*, 2012, 46, 2070-2086.

15. R. Gonzalez-Olmos, F. Holzer, F. D. Kopinke and A. Georgi, *Appl. Catal. A. Gen.*, 2011, 398, 44-53.
16. Á. Szécsényi, G. Li, J. Gascon and E. A. Pidko, *ACS Catal.*, 2018, 8, 7961-7972.
17. A. Zecchina, M. Rivallan, G. Berlier, C. Lamberti and G. Ricchiardi, *Phys. Chem. Chem. Phys.*, 2007, 9, 3483-3499.
18. M. M. J. Treacy and J. B. Higgins, *Collection of Simulated XRD Powder Patterns for Zeolites*, 2007, Elsevier.
19. W. Song, R. E. Justice, C. A. Jones, V. H. Grassian and S. C. Larsen, *Langmuir*, 2004, 20, 8301-8306.
20. C. Hammond, N. Dimitratos, R. L. Jenkins, J. A. Lopez-Sanchez, S. A. Kondrat, M. H. ab Rahim, M. M. Forde, A. Thetford, S. H. Taylor, H. Hagen, E. E. Stangland, J. H. Kang, J. M. Moulijn, D. J. Willock and G. J. Hutchings, *ACS Catal.*, 2013, 3, 689-699.
21. T. Yashima, Y. Kobayashi, T. Komatsu and S. Namba, *Stud. Surf. Sci. Catal.*, 1993, 75, 1689-1692.
22. G. D. Pirngruber, P. K. Roy and R. Prins, *Phys. Chem. Chem. Phys.*, 2006, 8, 3939-3950.
23. Y. Yu, G. Xiong, C. Li and F. S. Xiao, *Micro Meso Mater.*, 2001, **46**, 23-34.
24. F. Fan, Z. Feng and C. Li, *Acc. Chem. Res.*, 2010, 43, 378-387.
25. K. Sun, F. Fan, H. Xia, Z. Feng, W. Li and C. Li, *J. Phys. Chem. C*, 2008, 112, 16036-16041.
26. F. Fan, K. Sun, Z. Feng, H. Xia, B. Han and Y. Lian, *Chem. Eur. J.*, 2009, 15, 3268-3276.
27. C. Hammond, I. Hermans and N. Dimitratos, *ChemCatChem*, 2015, 7, 434-440.
28. P. K. Dutta and M. Puri, *J. Phys. Chem.*, 1987, 91, 4329-4333.
29. M. S. Kumar, M. Schwidder, W. Grünert and A. Brückner, *J. Catal.*, 2004, 227, 384-397.
30. R. V. Prikhod'ko, I. M. Astrelin, M. V Sychev and E. J. M. Hensen, *Russ. J. Appl. Chem.*, 2006, 79, 1115-1121.

Chapter 4. Optimisation of the Hydrothermal Synthesis of Fe-ZSM-5 for Partial Methane Oxidation

4.1. Introduction

In Chapter 3, it was demonstrated that the composition of Fe-ZSM-5 catalysts for aqueous phase partial-methane oxidation was critical for optimising catalytic performance. Lower SiO₂/Al₂O₃ ratios promoted catalytic activity, even though it was shown that Al³⁺ was not involved directly in CH₄ oxidation. Instead of being active in the catalytic mechanism, it was stipulated that Al³⁺ has a role as a structural promoter of the active Fe³⁺ sites. DRUV-vis and resonance Raman spectroscopy were used to demonstrate that at higher Al³⁺ loadings, a higher proportion of extra framework Fe³⁺ was present in the structure. It was also demonstrated that partial CH₄ oxidation and H₂O₂ decomposition were affected by the proportion of active Fe³⁺ species equally, which suggested that the two reaction pathways are not parallel and occur sequentially. As a H₂O₂ selective Fe³⁺ species was not determined, an oxidant selectivity problem may limit the efficacy of Fe-ZSM-5 catalysts for partial CH₄ oxidation. Other aspects of the catalyst design, other than composition, could affect performance of the catalyst, and should be further investigated.^{1,2}

For example, in Chapter 1, the effect of the method of synthesis of Fe-ZSM-5 was presented, along with the effect of Fe³⁺ speciation on catalytic performance.^{1,3} Isomorphous substitution of Fe³⁺, where an Fe³⁺ precursor is added to an aluminosilicate precursor gel, and the zeolite is crystallised via hydrothermal methods, is associated with isolated Fe³⁺ situated in tetrahedral positions in the zeolite lattice.⁴ Post-synthetic routes, such as chemical vapour deposition (CVD), favour the formation of oligomeric and extra-framework Fe³⁺.⁵ The method of Fe³⁺ incorporation can influence the catalytic performance of the material, as supported by the observation that the catalytic performance of CH₄ partial oxidation in the aqueous phase, utilising H₂O₂ as the oxidant, is greater for Fe-ZSM-5 catalysts prepared by isomorphous.^{4,6-8} Accordingly, opportunities to improve catalyst performance by modifying the synthesis approach appear to be relevant.

Despite the catalyst's efficacy, synthesis by hydrothermal procedure is time-consuming and requires multiple steps to afford an activated catalyst.^{4,6-8} Using the procedure reported by Prikhod'ko *et al.*,⁴ and later adapted by Hammond *et al.*,⁶ it took 11 days from the initial

preparation of the hydrogel to the final heat treatment to afford the active, protonated form of the catalyst.⁸ Efforts to improve the synthesis, both from an activity perspective and a productivity perspective, are necessary.

Towards this aim, partial CH₄ oxidation performance were preliminarily explored at different stages of Fe-ZSM-5 preparation in Chapter 3 and the results are re-shown in Figure 1 for reference.

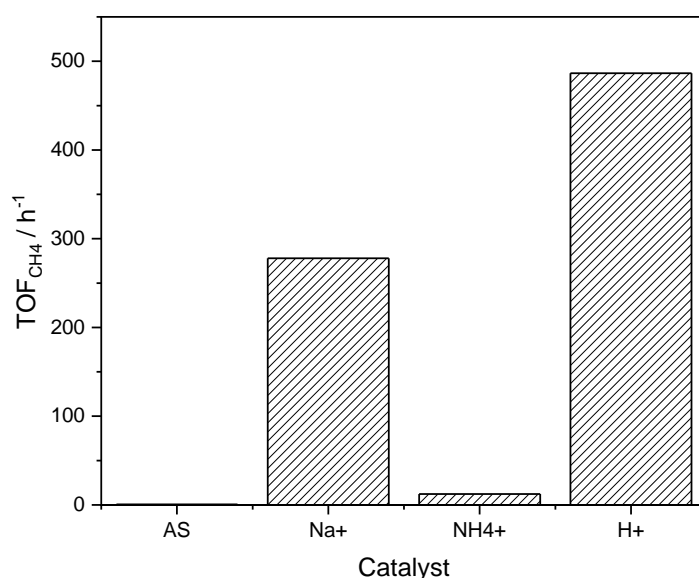


Figure 1 Partial methane oxidation activity (TOF) of 0.1 wt% Fe-ZSM-5 (42) as a function of catalyst preparation (taken from Chapter 3).

Even though the catalyst are most active for partial CH₄ oxidation following the final heat-treatment at 550 °C, the catalyst was relatively active following the initial calcination step performed to remove the template from the pores of the catalyst. On this observation, the time required to prepare an active catalyst could be reduced by 4 days (a reduction of a third), making preparation of such catalysts for large-scale application seem more viable due to higher production output. However, the longest stage the hydrothermal synthesis of Fe-ZSM-5 preparation is the crystallisation step, which is currently 5 days long. Long synthesis times are unattractive for large scale operations due to increased costs and lower productivity. If synthesis times could be reduced without affecting the catalyst performance, this could make the use of active Fe-ZSM-5 more feasible at large scales.

In each of the catalysts tested in Chapter 3, and in previous literature, crystallisation of Fe-ZSM-5 was performed at 175 °C for 120 h.⁶⁻⁸ To understand whether the synthesis of Fe-ZSM-

5 could be shortened, the effect of the crystallisation conditions should be understood. Accordingly, this chapter presents a study of the effect of crystallisation time on the performance of the synthesised Fe-ZSM-5 catalysts.

A benchmark catalyst, from which to compare the performance of the catalysts as a function of crystallisation conditions, was chosen based on the findings reported in Chapter 3. The catalysts in Chapter 3 were synthesised under hydrothermal conditions at 175 °C for 120 h. The optimal catalyst composition was 0.1 wt% Fe containing ZSM-5, with a SiO₂/Al₂O₃ molar ratio of 42. The outlined catalyst was chosen as the benchmark catalyst for further study. Using *p*XRD, N₂ physisorption and MAS NMR measurements, structural features of the synthesised catalysts under various crystallisation conditions will be compared. Furthermore, to determine the effect of the crystallisation on the incorporation and speciation of the active site, Fe³⁺ spectroscopic methods, such as DRUV-vis and resonance Raman will be utilised.^{5,9,10} Following calcination of the synthesised catalysts, a correlation between the varying crystallisation parameters and catalyst performance can be made, which is crucial for understanding how the changes in crystallisation parameters effect the catalyst and whether it is comparable in activity. Evidence that the crystallisation times of Fe-ZSM-5 for catalytic applications can be reduced will make Fe-ZSM-5 a more viable option on an industrial scale.^{11,12}

4.2. Effect of time on rate of crystallisation of 0.1 wt% Fe-ZSM-5 (42)_AS

According to the protocols benchmarked in the literature, the crystallisation of Fe-ZSM-5 under hydrothermal conditions occurs over a period of 120 h.⁶ Accordingly, to improve the favourability of the catalyst for methane oxidation, the length of time required to synthesis a fully crystalline sample of Fe-ZSM-5 was first explored.¹³ A number of synthesis gels were prepared in an analogous manner, each of which was prepared on a 49.4 mmol of SiO₂ scale. Each hydrogel was prepared with a molar ratio of 1 SiO₂: 0.024 Al₂O₃: 0.00147 Fe₂O₃: 0.306 TPAOH: 24.7 H₂O.⁶ After aging each gel at 60 °C for 16 hours, the gels were transferred to a PTFE-lined autoclave and placed into an oven pre-heated at 175 °C. The length of time the gels were in the oven was varied from 120 h to 6 h. Following the desired crystallisation time (t), the as synthesised (AS) form of the catalyst was afforded. Throughout this chapter, the catalysts will use the following notation for brevity: HT_XXX_YY_ZZ (where HT indicates the catalyst was made hydrothermally; XXX is the temperature of crystallisation; YY is the time of crystallisation; ZZ is the form of the catalyst). Under this nomenclature, the benchmarked material that has been crystallised for 120 h at 175 °C would be HT_175_120_AS.

To determine the crystal phases and the crystallinity of the samples that form under hydrothermal conditions, *p*XRD patterns were recorded. The onset of MFI crystal growth can be observed in the AS samples by the formation of characteristic peaks at $2\theta = 6-7^\circ$ and $2\theta = 22.5-25^\circ$.^{14,15} In Figure 2, the MFI crystal phase is present in each of the catalysts, however, it is difficult to observe any differences between the synthesised materials from the diffraction patterns alone. Relative crystallinity was determined by integration of the area under the peaks between $2\theta = 22.5 - 25^\circ$ and calculated according to Equation 1:¹⁶

$$\text{Relative crystallinity} = \frac{A_x}{A_R} \quad (1)$$

where A_x = integrated peak area of the measured sample; and A_R = integrated peak area of the reference sample (the seed material was used as the reference). On integration of the crystalline region, the relative crystallinities were plotted as a function of crystallisation time at 175°C (Figure 2). An error of 1.0% was calculated by repeating the *p*XRD analysis of the samples three times, and the integrated area was averaged for the three experiments.

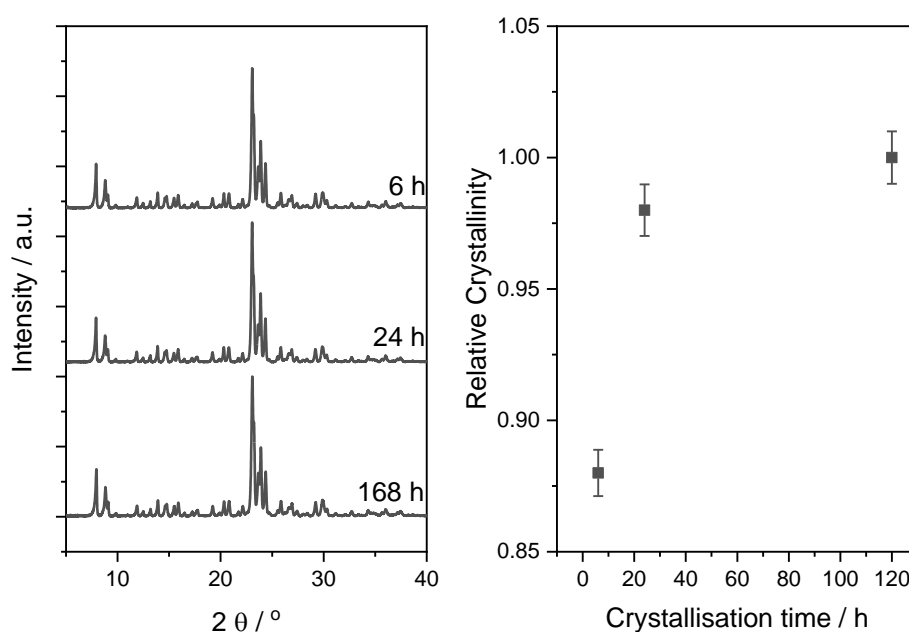


Figure 2 Left; *p*XRD diffraction patterns of 0.1 wt% Fe-ZSM-5 (42)_AS as a function of crystallisation time at 175°C . Right; Relative crystallinity of 0.1 wt% Fe-ZSM-5 (42)_AS as a function of crystallisation time at 175°C . Relative crystallinity was calculated as the (integrated area at $22.5 - 25^\circ 2\theta$ of sample)/ (integrated area of reference). Error bars were calculated at 1.0%.

Characteristic MFI diffraction peaks can be seen in the *p*XRD pattern of HT_175_6_AS, and no further diffraction peaks were observed, indicating that selective crystallisation of the MFI

phase has occurred in as little as 6 h at 175 °C. The relative crystallinity (relative to the benchmark sample) was 0.86, which increased as the crystallisation time increased to 120 h (Figure 2). These findings suggest that 6 h is sufficient time to afford a relatively crystalline sample of 0.1 wt% Fe-ZSM-5 (42).

Although crystallinity is important, it does not account for the effect of crystallisation time on the isomorphous substitution of Al^{3+} and Fe^{3+} into the framework, which is crucial for catalytic activity.⁶⁻⁸ Additional spectroscopic techniques were employed to determine the incorporation of both Al^{3+} and Fe^{3+} into the MFI lattice as a function of crystallisation time. ^{27}Al MAS NMR was used to determine the coordination and oxidation state of Al^{3+} within the zeolite lattice. It has been suggested that the distribution and coordination of Al^{3+} within the MFI lattice can be affected by the crystallisation process, which consequently influences catalytic performance.¹⁷

In Figure 3, no peak exists at 0 ppm, which is characteristic of octahedral Al^{3+} , indicating that no extra framework Al^{3+} is present, which suggests that at reduced crystallisation times, Al^{3+} is fully incorporated into the framework.¹⁷ Furthermore, a peak at 55 ppm corresponds to the presence of tetrahedrally coordinated Al^{3+} within the MFI framework.^{17,18} The signals were fitted as Gaussian peaks and integrated to compare differences in the tetrahedral Al^{3+} signal, as shown in Table 1. The tetrahedral signal was greatest in HT_175_6_AS, which might not be expected for the least crystalline sample. However, it should be taken into consideration that Fe^{3+} is paramagnetic, which could affect the intensity resonance of the Al^{3+} nucleus. The unpaired electron can create a local magnetic field that shields the ^{27}Al resonance, resulting in less intense resonances in the ^{27}Al NMR.¹⁹ As the tetrahedral Al^{3+} signal is greatest in HT_175_6_AS, the increase in NMR signal intensity might suggest that at shorter crystallisation times, less Fe^{3+} is incorporated into the lattice, thus less shielding of the Al^{3+} tetrahedra is occurring.

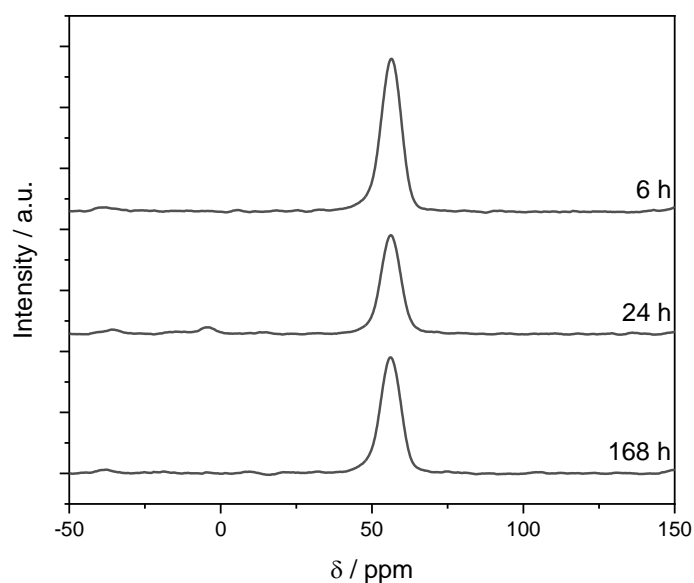


Figure 3 ^{27}Al single pulse MAS-NMR spectra of 0.1 wt% Fe-ZSM-5(42)_AS as a function of crystallisation time at 175 °C.

Table 1 Integrated area of tetrahedral Al^{3+} peaks from ^{27}Al MAS NMR spectra as a function of crystallisation time at 175 °C

Time / h	Integrated area δ 55 ppm
120	3.84476×10^8
24	3.25934×10^8
6	5.06611×10^8

To gain more conclusive evidence regarding the incorporation of Fe^{3+} into the zeolite beyond the indirect evidence gained from ^{27}Al MAS NMR, Diffuse reflectance UV-vis (DRUV-vis) spectroscopy was used to observe the incorporation of Fe^{3+} into the MFI framework. Isomorphous substitution of Fe^{3+} into the framework is pivotal for catalytic activity, though it might be expected that incomplete incorporation of Fe^{3+} might occur at reduced contact times.⁶⁻⁸ Thus, how crystallisation time effects the incorporation of Fe^{3+} into the zeolite matrix can be observed.

The DRUV-vis spectra of each of the as synthesised samples is given in Figure 4. In each of the spectra, there are strong absorbances observed at 220 and 240 nm, which are believed to arise from the presence of tetrahedrally coordinated Fe^{3+} . Additionally, a feature at 320 nm is observed in the spectrum of HT_175_6_AS that was not observed at longer synthesis times.

From Table 1, the maximum at 320 nm can be attributed to isolated and oligomeric Fe^{3+} species located externally to the zeolite framework (anchored to the SiO_4 network, but not substituted), as discussed in Chapter 2.⁵ The formation of oligomeric Fe^{3+} species would suggest that at reduced synthesis times, there is insufficient energy for full isomorphous substitution of Fe^{3+} .

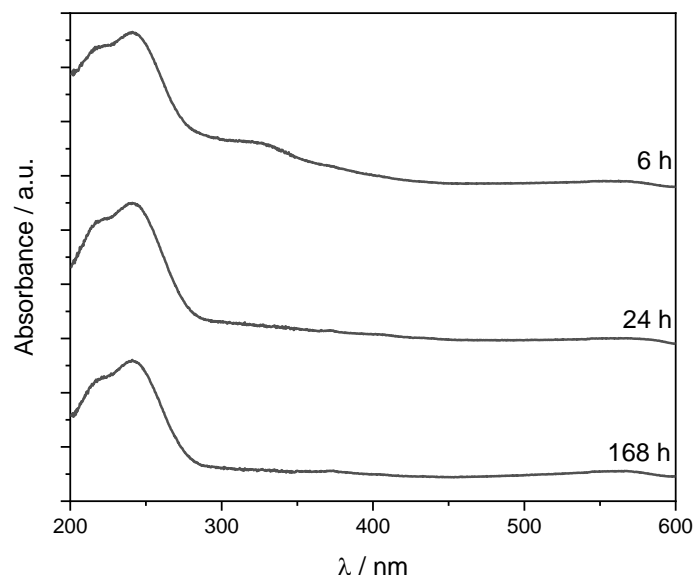


Figure 4 DRUV-vis spectra of 0.1 wt %Fe-ZSM-5(42)_AS as a function of crystallisation time at 175 °C.

From the evidence presented above, there is a link between crystallisation time and Fe-ZSM-5 crystal formation and Fe^{3+} substitution. After 6 h crystallisation, crystalline MFI phases are observed in the *p*XRD, although there is 12% less crystallinity present in the material relative to HT_175_120_AS. Moreover, Al^{3+} was fully substituted into the tetrahedral positions in 6 h, as observed by MAS NMR. However, it was observed that substitution of Fe^{3+} , the active species for methane oxidation, was incomplete following crystallisation at 6 h, which suggests that longer times are required to synthesis Fe-ZSM-5 for methane oxidation.

4.3. Effect of Temperature on the Rate of Crystallisation of 0.1 wt% Fe-ZSM-5 (42)_AS

In the previous section, reducing the synthesis time of 0.1 wt% Fe-ZSM-5 (42) had a minor effect on crystallinity and the degree of Al^{3+} incorporation, but there was DRUV-vis evidence to suggest that substitution of Fe^{3+} was impacted at reduced crystallisation times. As crystallisation is a kinetically controlled process, the rate of crystallisation could be increased by an increase in crystallisation temperature.²⁰ To determine the effect of increasing the

crystallisation temperature on the degree of crystallinity and metal incorporation, two samples of 0.1 wt% Fe-ZSM-5 (42) were made at a constant contact time of 6 h. However, it is important to note that the internal temperature of the gel was not measured, and nominal temperatures given were used.

The catalysts were prepared as described in Section 4.2, though the oven temperature was set at either 175 or 200 °C. Characteristic crystal peaks of zeolite with MFI structure was observed for both samples (Figure 5).¹⁵ The relative crystallinities of the AS materials were calculated from Equation 1 and plotted as a function of the oven temperature. Increasing the temperature to 200 °C resulted in a sample with a relative crystallinity of 1.01, however this was within the calculated 1.0% error of the sample synthesised at 175 °C. The temperature was not increased beyond than 200 °C as fully crystallinity had been achieved, and higher temperatures can result in degradation of the OSDA (pure TPAOH decomposes at 250 °C, but decomposition temperature can be affected by environment).²¹

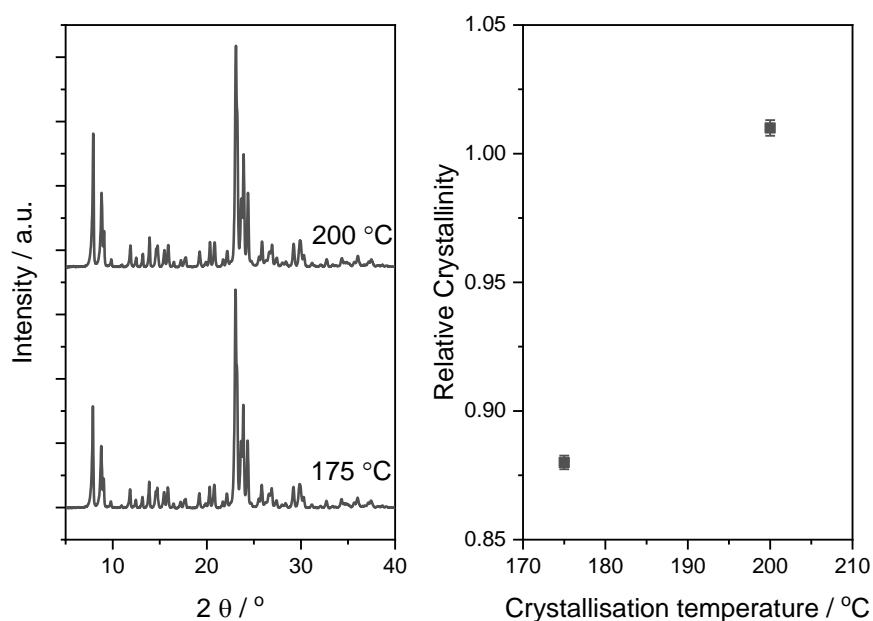


Figure 5 Left; pXRD diffraction patterns of 0.1 wt% Fe-ZSM-5 (42)_AS as a function of crystallisation temperature at 6 h. Right; Relative crystallinity of 0.1 wt% Fe-ZSM-5 (42)_AS as a function of crystallisation temperature at 6 h. Relative crystallinity was calculated as the (integrated area at 22.5 – 25 ° 2 θ of sample)/ (integrated area of reference). Error bars were calculated at 1.0 %.

To prove that substitution of Al³⁺ into tetrahedral positions was unaffected by the increase in temperature, ²⁷Al MAS-NMR experiments were also run. Only the resonance at 55 ppm was observed in the spectrum of both samples (Figure 6), indicating that the change in temperature did not result in changes to the Al³⁺ coordination.¹⁷ A decrease in signal area was calculated

for HT_200_6_AS, which agrees with the previous observation that, at higher temperatures, a greater proportion of Fe^{3+} is incorporated into the MFI framework.¹⁸

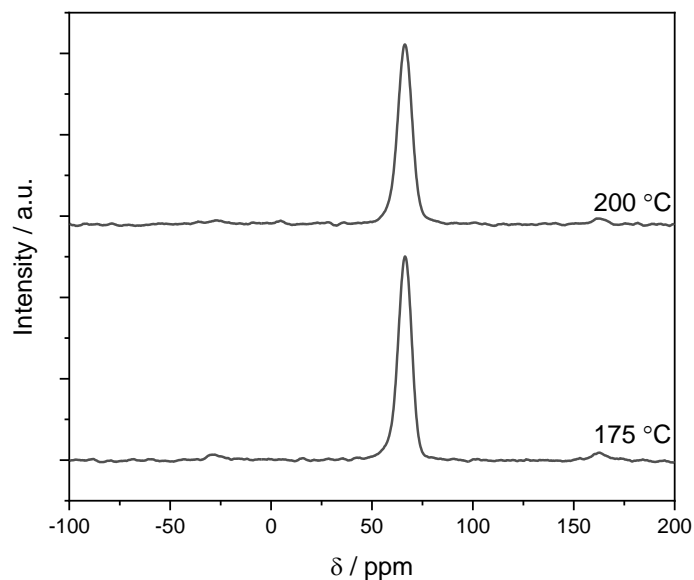


Figure 6 ^{27}Al single pulse MAS-NMR spectra of 0.1 wt% Fe-ZSM-5(42)_AS as a function of crystallisation temperature at 6 h.

In Chapter 3, Fe^{3+} is shown as crucial for catalytic activity. To determine whether the change in crystallisation results in changes to Fe^{3+} incorporation, DRUV-vis spectroscopy was utilised to observe Fe^{3+} within the samples (Figure 7). Crystallisation for 6 h at 175 °C was insufficient for complete substitution of Fe^{3+} into the MFI framework, as a secondary maximum is seen at 320 nm, which is suggestive of extra framework and oligomeric Fe^{3+} species forming. At elevated temperatures, the maximum at 320 nm was not observed, indicating that a large proportion of the Fe^{3+} is located primarily within the framework. Thus, at elevated temperatures, the extent of Fe^{3+} substitution into the framework increases.²²

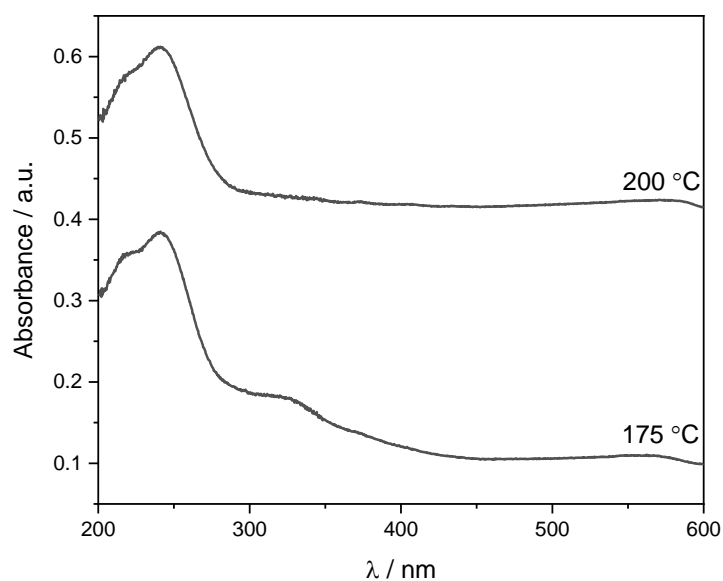


Figure 7 DRUV-vis spectra of 0.1 wt% Fe-ZSM-5(42)_AS as a function of crystallisation temperature at 6 h.

On consideration of the data collected on the as-synthesised samples, at two different temperatures, the time scale of the synthesis can be readily reduced from 120 h to 6 h, without affecting the crystallinity of the sample. Further, DRUV-vis spectra show that Fe^{3+} is fully incorporated into the MFI, which is thought to be critical in forming an active catalyst for methane oxidation.

4.4. Effect of Reaction Vessel on Crystallisation of synthesised 0.1 wt% Fe-ZSM-5 (42)

In the previous section, the time of crystallisation of 0.1 wt% Fe-ZSM-5 (42) was reduced from 120 h to 6 h by increasing the crystallisation temperature to 200 °C, without changing isomorphous substitution of Fe^{3+} . A consideration to further facilitate rapid zeolite synthesis would be to consider the type of vessel used to crystallise the material. Typically, stainless-steel pressure vessels are employed to perform batch synthesis, which are designed to withstand the high, autogenous pressures created under hydrothermal conditions.²³ The vessels are constructed with thick steel walls to contain the elevated pressure produced under hydrothermal conditions. Furthermore, the gel is contained within a PTFE liner, to prevent corrosion of the stainless-steel surface, which results in a temperature lag between the heating medium and the synthesis gel.²³ For the onset of crystallisation to commence, heat transfer limitations must be overcome, and this results in extended synthesis times. The effect of synthesis vessel on crystallisation time was explored by Liu *et al.* by comparing the rate of crystallisation of

silicalite-1 in a standard batch autoclave and stainless steel (SS) tubular reactors.²⁰ It was reported that fully crystalline silicalite-1 could be synthesised in minutes when performed in SS tubing, whereas it took more than 90 minutes to achieve the same material in the autoclave. This suggests that the effects of thermal lag can be negated by switching the synthesis vessel to stainless steel tubing and should reduce overall crystallisation times.

Based on the literature observation, the crystallisation of 0.1 wt% Fe-ZSM-5 (42) was carried out in SS tubular reactors.²⁰ A tube diameter of 3/8" was chosen, as the working volume would be suitable for the lengths of tubing that would fit into the available heating medium. The synthesis gel was made as described above (*cf.* section 4.2) and transferred to Swagelok 3/8" tubing. The tubes were sealed and placed in a pre-heated oven at 175 °C, as it was thought that the better heat transfer would allow for the use of lower crystallisation temperatures. The tubes were removed at the desired time and the resulting slurry was separated by centrifugation, washed with DI water and dried at 80 °C for 16 h. For clarity, the samples made by this method use the notation TB_XXX_YY_ZZ, where TB indicates that the samples were made within SS tubing; XXX is the temperature; YY is the crystallisation time; ZZ is the catalyst form. For example, a sample crystallised in SS tubing for 4 h at 175 °C would be TB_175_4_AS.

The diffraction patterns of the samples crystallised at 175 °C in SS tubing for various lengths of time are shown in in Figure 8. The benchmark material (HT_175_120_AS) is shown to provide a reference of the MFI diffraction pattern.¹⁵ After 1 h crystallisation time, a broad peak centred at $2\theta = 23.8^\circ$ is observed that arises from amorphous SiO₂, which demonstrates that 1 h is insufficient for crystallisation. Characteristic MFI crystal peaks appear in after 2 h at 175 °C, and the intensity of the peaks at $2\theta = 22.5 - 25^\circ$ increases with increasing crystallisation time. Continuation of crystal growth with an increase in time can be seen by plotting the relative crystallinity values (calculated from Equation 1, using HT_175_120_AS as the reference). An error for all samples was determined to be 0.3 %, after determining the average and standard deviation from three replicate *p*XRD measurements. In sample TB_175_2_AS, the relative crystallinity was determined to be 0.70, which suggests that amorphous aluminosilicate particles are present in the sample.¹³ An increase in relative crystallinity up to 4 h crystallisation was observed, at which point, a fully crystalline material is afforded (RC = 1.1) and the crystallinity remains unchanged past this time. The increase in relative crystallinity over the reference sample indicates that the improvement in heat transfer results in faster crystallisation, and that the samples crystallised in autoclaves are not 100% crystalline, as previously thought. The increase in crystallinity with time is consistent with a previously proposed zeolite

crystallisation mechanism, where the formation of a bulk amorphous phase proceeds the formation of defined crystal phases.¹⁸

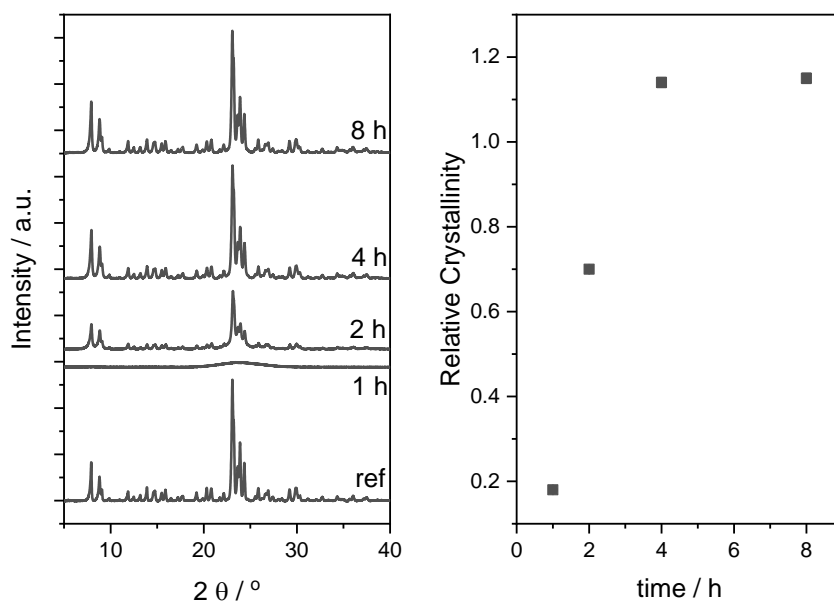


Figure 8 Left: pXRD pattern of 0.1 wt% Fe-ZSM-5 (42)_AS crystallised at 175 °C in 3/8" SS tubing as a function of crystallisation time. A fully crystalline material (120 h, 175 °C, in an autoclave) is provided as a reference. Right: Relative crystallinity of as synthesised 0.1 wt% Fe-ZSM-5 (42) crystallised at 175 °C in 3/8" 316 SS tubing as a function of crystallisation. Relative crystallinity was calculated as the (integrated area at 22.5 – 25 ° of sample)/ (integrated area of HT_175_120_AS). Error bars were calculated at 0.3 %.

There is a clear increase in crystallinity at increased crystallisation times, which might affect the co-ordination of Al^{3+} into the MFI lattice. Each of the ^{27}Al MAS-NMR spectra shown in Figure 9 shows a single signal at 55 ppm that can be assigned to tetrahedral Al^{3+} .¹⁷ Thus, it is probable that the formation of tetrahedral Al^{3+} occurs during the initial mixing step. No signals are observed at 0 ppm, indicating that there is no octahedral Al present in any of the samples. The area of the tetrahedral signal does decrease with increasing contact time, though this might be explained by more Fe being coordinated into the zeolite framework.¹⁹

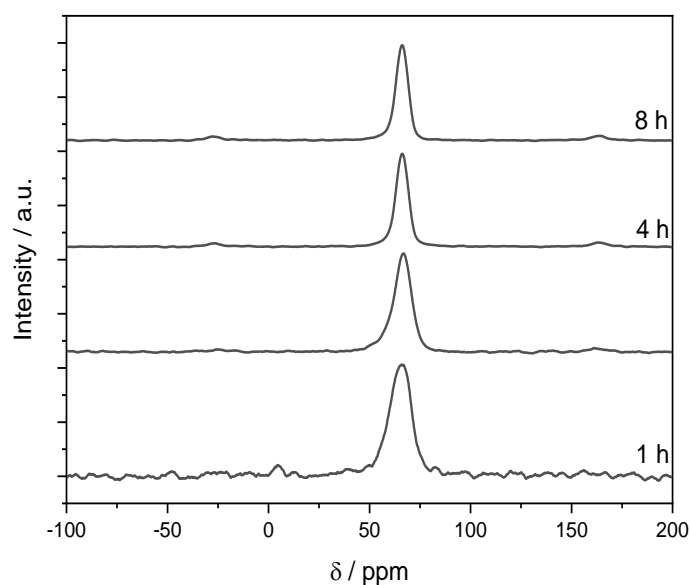


Figure 9 Single pulse ^{27}Al MAS NMR of 0.1 wt% Fe-ZSM-5 (42)_AS crystallised at 175 °C in 3/8" SS tubing as a function of crystallisation time.

The extent of MFI lattice formation can be observed by ^{29}Si MAS NMR. ^{29}Si atoms are sensitive to the surrounding environment, which can give structural information about the material. Typically, 4 silanol species are found in solid silicate materials, with an increase in crystallinity corresponding to an increase in connectivity. The increase in connectivity leads to increased shielding experienced by the ^{29}Si atom, thus signals are shifted upfield (in chemical shift) relative to tetramethylsilane (TMS) standard at 0 ppm.²⁴ The observable shifts correspond to Q^n species, where $n = 1, 2, 3, 4$, and the value of n indicates the connectivity of Si atoms in $[\text{Si}(\text{OSi})_n(\text{OH})_{4-n}]$; the higher the n value, the greater the connectivity.²⁵ Deconvoluting of the ^{29}Si MAS-NMR spectra into sub-bands, correlating to different Q^n species, the relative concentration can be determined, which can give information on the crystal structure of the sample. Q^n bands were observed at $\delta = -87$ (Q^1), -95 (Q^2), -99 (Q^3) and -103 (Q^4) and Gaussian peaks were fitted to the ^{29}Si MAS NMR spectra of each sample.^{24,25}

The deconvoluted ^{29}Si MAS NMR spectra are shown in Figure 10. As relative crystallinity increases, the relative proportion of Q^4 atoms increases, because as the MFI crystallites grow, the number Si-O-Si bonds increases and the interaction with the TPA cation decreases (seen by the decrease in the relative proportion of Q^3).¹⁸

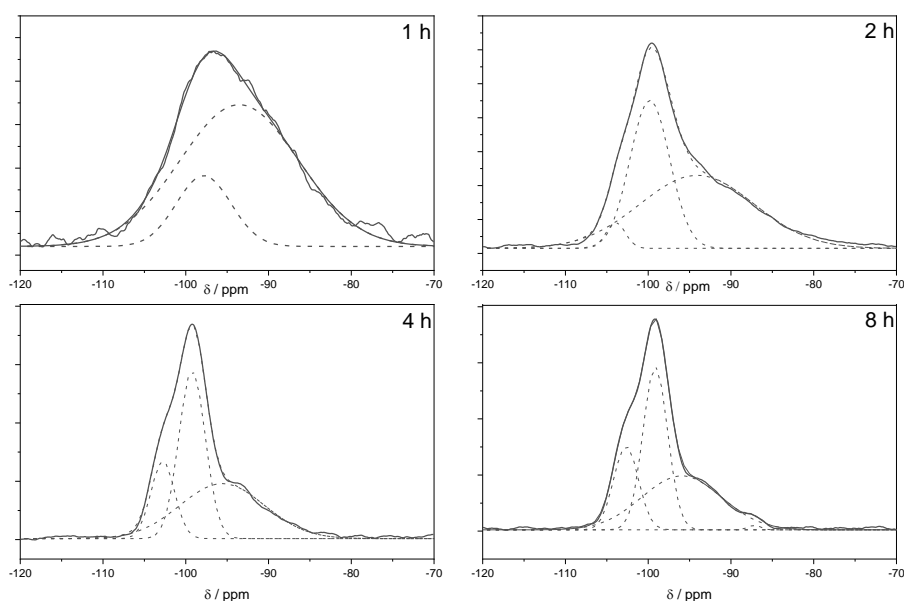


Figure 10 Single pulse ^{29}Si MAS NMR of 0.1 wt% Fe-ZSM-5 (42)_AS crystallised at 175 °C in 3/8" SS tubing as a function of crystallisation time.

Table 2 Quantification of ^{27}Al and ^{29}Si (Q^n) calculated from deconvoluted ^{29}Si MAS NMR spectrum as a function of crystallisation time in 0.1 wt% Fe-ZSM-5 (42) crystallised in 3/8 " SS tubing.

Catalyst	T_d peak / area	Q^1 / %	Q^2 / %	Q^3 / %	Q^4 / %	Q^3 / Q^4
TB_175_1_AS	5.81509×10^9	0	81.3	18.7	0	-
TB_175_2_AS	4.02265×10^9	0	40.0	56.7	3.40	16.7
TB_175_4_AS	2.71684×10^9	0	42.5	40.7	16.8	2.4
TB_175_8_AS	2.72492×10^9	0.60	41.2	38.4	19.9	1.9

To understand whether the incorporation of Fe^{3+} had been affected by the reduction in synthesis time, DRUV-vis was used. Earlier in this chapter, during autoclave synthesis, incomplete incorporation of Fe^{3+} into the MFI lattice was proposed. A broad peak at 320 nm was observed in sample HT_175_6_AS (Figure 11), which suggested that longer contact times would be crucial for the complete incorporation of Fe^{3+} into the lattice. Using the characteristic LMCT bands of Fe^{3+} observed in DRUV-vis spectra (Chapter 2),⁵ the speciation of Fe^{3+} as a function of crystallisation time of the samples crystallised at 175 °C within SS tubing can be qualified. The DRUV-vis spectra in Figure 11 show that each of the catalysts has characteristic absorbances of tetrahedrally coordinated Fe^{3+} at 220 and 260 nm.⁵ There is a broadening of the signal in TB_175_1h, which is indicative of incomplete substitution of Fe^{3+} and may be related to the low crystallinity of the sample. However, the relative proportion of Fe^{3+} located within

the framework increases after 2 h, which seems to contradict the observation previously made in Section 4.2, where incomplete Fe^{3+} was observed at lower crystallisation times, even though the samples were more crystalline. The absence of a heating-lag period may then affect the rate in which Fe^{3+} can incorporate into the structure, hence the differences in incorporation in the two different types of vessel. A way to determine whether there was free Fe^{3+} in the synthesis liquor would have been to run DRUV-vis spectroscopy of the liquor, but this experiment was not performed due to disposal of the filtrate post-crystallisation. Analysis of the wash liquor would have allowed for the determination of the differences in non-incorporated Fe^{3+} from the two different vessels, to further support the initial observations.

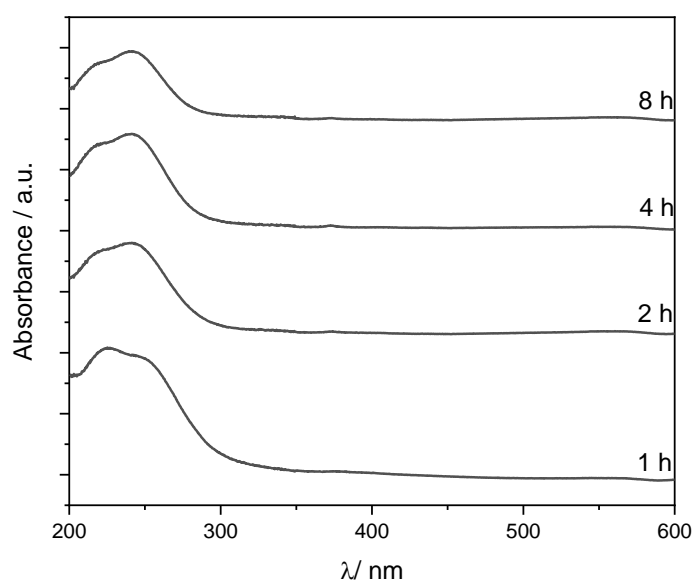


Figure 11 DRUV-vis spectrum of 0.1 wt% Fe-ZSM-5 (42)_AS crystallised at 175 °C in 3/8" SS tubing as a function of crystallisation time.

Herein, the synthesis of a fully crystalline sample of 0.1 wt% Fe-ZSM-5 (42) in 4 h at 175 °C has been shown by changing the synthesis vessel to stainless-steel tubing. Furthermore, the reduction in crystallisation time did not affect the substitution of Fe into the framework, as full coordination of Fe^{3+} into tetrahedral positions was observed by DRUV-vis spectroscopy.

4.5. Effect of $\text{SiO}_2/\text{Al}_2\text{O}_3$ Ratio on the Rate of Crystallisation of Synthesised 0.1 wt% Fe-ZSM-5

The time of crystallisation of Fe-ZSM-5 affects the relative crystallisation and Fe^{3+} coordination in the synthesised samples. Early work by Persson *et al.* has suggested that, at increased Al content, the rate of crystal growth rate is reduced.²⁶ For example, Al^{3+} can form

$\text{Al}(\text{OH})_n$ in the gel phase that decreases the number of free Al^{3+} in the solution. Hydroxide ions are thought to catalyse various dissolution processes within the hydrogel. By increasing the Al content, OH^- is consumed and the rates of nucleation altered.²⁷ Without altering the number of OH^- in solution, varying the $\text{SiO}_2/\text{Al}_2\text{O}_3$ ratio can influence the rate of crystallisation. Hence, it is important to explore the effect of zeolite composition on the rate of Fe-ZSM-5 crystallisation.

To investigate, gels were prepared with a molar ratio of 1 SiO_2 : x Al_2O_3 : 0.00147 Fe_2O_3 : 0.306 TPAOH: 24.7 H_2O , where x was varied. After homogenisation at 60 °C for 16 h, the gels were transferred to 3/8" SS tubing and placed in a pre-heated oven at 175 °C. The resulting slurry was separated by centrifuge and washed to afford the AS form of the catalyst. The notation TB_175_XX_YY_ZZ is used for brevity, where XX is the length of crystallisation; YY is the $\text{SiO}_2/\text{Al}_2\text{O}_3$ ratio and; ZZ is the form of the catalyst. Two $\text{SiO}_2/\text{Al}_2\text{O}_3$ ratios were chosen to investigate: 84 and ∞ (Al free), where x in the gel stoichiometry is 0.024 and 0 respectively. It is worth noting that after 16 h homogenisation in both gels, the synthesis gel remained clear, which was unlike the gel of 0.1 wt% Fe-ZSM-5 (42), where the homogenised gel was cloudy. The molar ratio of SiO_2 and Al_2O_3 has been suggested to lead to the formation of amorphous aluminosilicate particles that are visible, leading to the formation of a cloudy suspension.¹³

In comparison to samples with $\text{SiO}_2/\text{Al}_2\text{O}_3 = 42$ (Figure 8), characteristic MFI diffraction peaks were observed after 1 h at 175 °C when $\text{SiO}_2/\text{Al}_2\text{O}_3 = 84$ (Figure 12) and full crystallinity is observed after 2 h. Halving the Al content of the initial aluminosilicate gel, the time required to crystallise Fe-ZSM-5 is halved. To test if Al^{3+} was affecting the rate of MFI crystallisation, 0.1 wt % Fe-silicalite-1 ($\text{SiO}_2/\text{Al}_2\text{O}_3 = \infty$) was prepared by hydrothermal methods within 3/8" SS tubing. In Figure 13, the rate of crystallisation of 0.1-Fe-silicalite-1 ($\text{SiO}_2/\text{Al}_2\text{O}_3 = \infty$) increases by a factor of 2; a fully crystalline sample is synthesised in 1 h. Therefore, it can be proposed that the addition of Al^{3+} precursors into the hydrogel can be proposed to retard the rate at which ZSM-5 crystallites form.²² The state of the precursors which form in the initial gel may also affect the rate of crystallisation. A study on the precursors formed in solution (²⁷Al and ²⁹Si NMR experiments and dynamic light scattering (DLS)) would give some insight into the mechanistic reasons of these findings.²⁸⁻³⁰

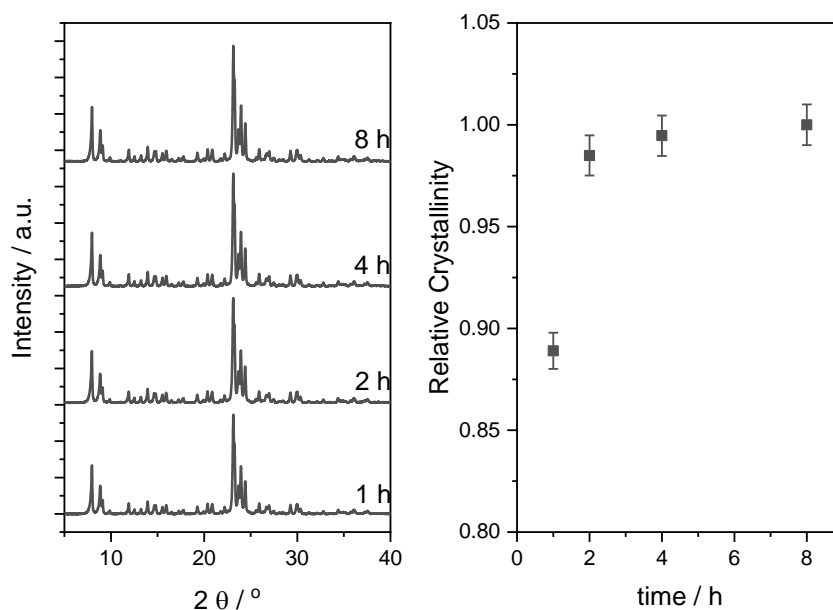


Figure 12 Left: *p*XRD pattern of as synthesised 0.1 wt% Fe-ZSM-5 (84) crystallised at 175 °C in 3/8" 316 SS tubing as a function of crystallisation time. Right: Relative crystallinity of as synthesised 0.1 wt% Fe-ZSM-5 (84) crystallised at 175 °C. Relative crystallinity was calculated as the (integrated area at 22.5 – 25 ° 2 θ of sample)/ (integrated area of HT_175_120_AS). Error bars were calculated at 1.0%.

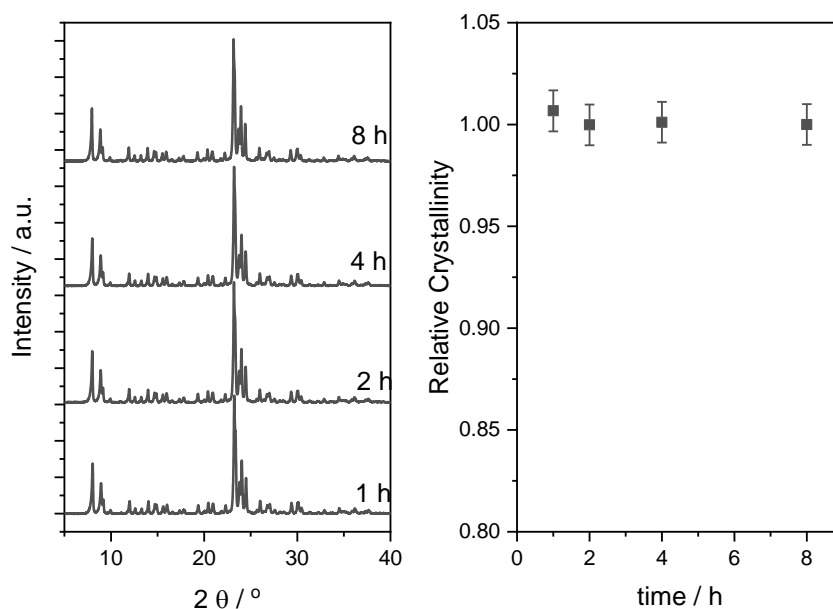


Figure 13 Left: *p*XRD pattern of as synthesised 0.1 wt% Fe-Silicalite-1 crystallised at 175 °C in 3/8" 316 SS tubing as a function of crystallisation time. Right: Relative crystallinity of as synthesised 0.1 wt% Fe-Silicalite-1 crystallised at 175 °C in 3/8" 316 SS tubing as a function of crystallisation. Relative

crystallinity was calculated as the (integrated area at 22.5 – 25 ° of sample)/ (integrated area of HT_175_120_AS). Error bars were calculated at 1.0 %.

To observe whether the changing ratio affects the extent of Fe³⁺ incorporation into the zeolite, DRUV-vis spectroscopy was used.⁵ The DRUV-vis of the AS catalysts of both 0.1 wt% Fe-ZSM-5 (84) and 0.1 wt % Fe-silicalite-1 have two maxima at < 250 nm (Figures 14 and 15 respectively). This shows that all the Fe³⁺ is present within the lattice even at lower contact times and the rate of incorporation of Fe³⁺ is not affected by the SiO₂/Al₂O₃ ratio.

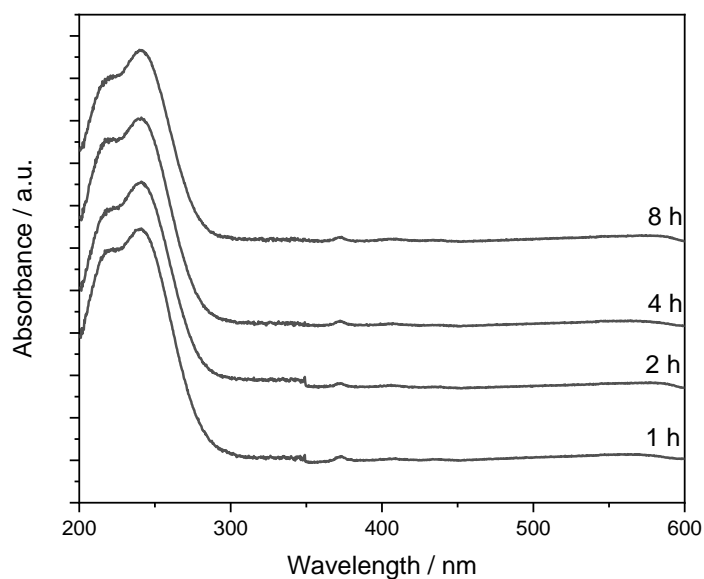


Figure 14 DRUV-vis of 0.1 wt% Fe-ZSM-5 (84)_AS crystallised at 175 °C in 3/8" 316 SS tubing as a function of crystallisation time.

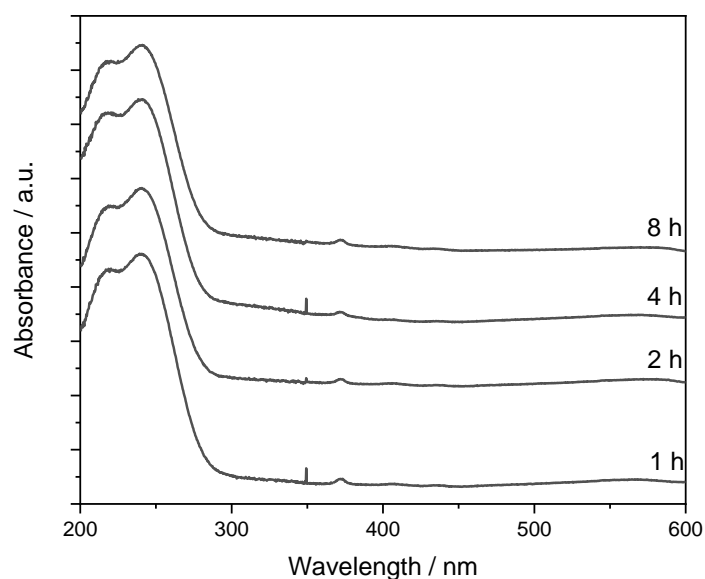


Figure 15 DRUV-vis of 0.1 wt% Fe-silicalite-1_AS crystallised at 175 °C in 3/8" 316 SS tubing as a function of crystallisation time.

Figure 16 plots the calculated RC of the samples at the different Al^{3+} contents as a function of time; the time where a RC of 1 is reached reduces at lower Al^{3+} content. Thus, it can be concluded that the addition of Al^{3+} into the zeolite framework retards the nucleation and crystal growth rates of Fe-ZSM-5. An increase in Al^{3+} content is thought to result in the consumption of OH^- ions in the gel suspension, which can affect the equilibrium of aluminosilicate species in the gel. Also, isomorphous substitution of Al^{3+} into the zeolite framework in the liquid phase slows the rate of crystal growth.³¹ Through modification of the $\text{SiO}_2/\text{Al}_2\text{O}_3$ ratio, it is possible to increase the crystal growth rate of Fe-ZSM-5. As the catalyst is *most* active at greater Al^{3+} (*cf.* Chapter 3), there is a benefit to maintaining a minimum amount of Al^{3+} .

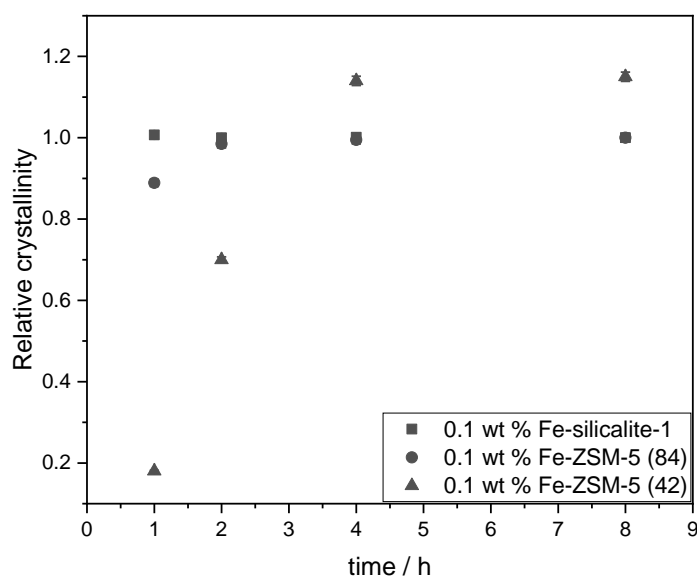


Figure 16 Relative crystallinity of 0.1 wt% Fe-MFI at different $\text{SiO}_2/\text{Al}_2\text{O}_3$ ratios, as a function of crystallisation time at 175 °C. The relative crystallinities were calculated from the area of the diffraction peak at $2\theta = 22.5 - 25^\circ$ and are relative to sample crystallised for 8 h in each series.

4.6. Effect of Calcination on 0.1 wt% Fe-ZSM-5 (42) as a Function of Crystallisation Conditions

In the above sections, the discussion has focused on the effect of crystallisation conditions on the outcome of the as-synthesised (AS) materials. The synthesis time can be greatly reduced by switching the crystallisation vessel to a thin-walled stainless steel tubing. However, in Chapter 3, it was shown that the as synthesised (AS) form of the catalyst was inactive for methane oxidation (Figure 1).

To establish whether these newly synthesised catalysts are suitable for catalytic application, the catalysts were subjected to calcination conditions to remove the OSDA from the void spaces of the zeolite lattice. As demonstrated in Chapter 3, calcination is able to extract Fe^{3+} from the zeolite framework, to occupy extra framework positions at low $\text{SiO}_2/\text{Al}_2\text{O}_3$ ratios; extra framework Fe^{3+} has been stipulated to be the active species for partial CH_4 oxidation.⁸ To determine the viability of the reduced crystallisation time for hydrothermal synthesis, the samples were tested for catalytic reactivity, using partial CH_4 oxidation as a model reaction, as described in Chapter 2. The Na^+ forms of the catalyst were tested for catalytic performance, as well as analysed using DRUV-vis and resonance Raman spectroscopy to identify differences in Fe^{3+} speciation as a function of crystallisation conditions.^{5,9}

Three samples, with SiO₂/Al₂O₃ ratio of 42, were chosen to investigate the effect of crystallisation time on partial CH₄ oxidation activity, as Chapter 3 demonstrated that the Na⁺ form of Fe-ZSM-5 was active post-calcination. Three samples, prepared by different methods, were chosen to study; HT_175_120_AS was the benchmark catalyst; HT_200_6_AS was chosen as it was structurally comparable to the benchmark catalyst, as was TB_175_4_AS, in that the relative crystallinity was 1.0 and Fe³⁺ was demonstrated to be fully incorporated into framework positions in the DRUV-vis spectra. The chosen samples were calcined at 550 °C at a rate of 1 °C min⁻¹ under an atmosphere of N₂ (5 h) and flowing air (3 h) to afford the Na⁺ samples.⁸ Choosing parent samples that are comparable in the synthesised form eliminates any issues that may arise from choosing different parent samples. *p*XRD patterns were recorded for the calcined materials to observe that there were no other crystal phases formed following calcination.

To observe changes in the pore network before and after calcination, N₂ physisorption measurements of the catalysts were taken. The surface areas of the AS materials, calculated by a modified BET equation, were low for MFI.³² Pore volumes are also relatively low (Table 3), due to the void spaces of the catalysts are inaccessible due to the presence of TPA cations, preventing the transport of N₂.³² From this observation, the surface area of the AS samples can be assumed as equivalent to the external surface area (*S_{ext}*) of Fe-ZSM-5.³³ Following calcination at 550 °C, there was an increase in the apparent surface area and total pore volumes of the TPA materials consistent with values for crystalline ZSM-5.³⁴ The increase in *S_{ext}* corresponds to the removal of TPA cations from the void spaces and would allow transport of reactants to access the active sites located within the zeolite pores. However, there is quite a large difference in the calculated apparent surface areas of the Na⁺ samples (Table 3). The sample crystallised in the tubular reactors (TB_175_6_Na⁺) has a lower surface area and pore volume than either of the materials synthesised via more conventional, hydrothermal methods that suggest that the differences in crystallisation conditions results in differences in crystal size and pore structure.

Table 3 N₂ physisorption data recorded at 77 K of 0.1 wt % Fe-ZSM-5 (42) crystallised for 6 h at various temperatures. ^aCalculated as the apparent BET surface area of the AS catalyst; ^bCalculated as the apparent BET surface area of the Na⁺ catalyst; ^cS_{int} = S_{tot} - S_{ext}; ^dCalculated using NLDFT methods.

Catalyst	S _{ext} ^a / m ² g ⁻¹	S _{tot} ^b / m ² g ⁻¹	S _{int} ^c / m ² g ⁻¹	PV _{micro} (AS) ^d / cc g ⁻¹	PV _{micro} (TPA) ^d / cc g ⁻¹
HT_175_120_Na ⁺	33.4	399.4	366	0.032	0.192
HT_200_6_Na ⁺	24.7	432.4	407.7	0.020	0.200
TB_175_4_Na ⁺	45.0	181.9	136.9	0.068	0.136

The change in Fe³⁺ speciation that occurs during the calcination step is crucial for the onset of catalytic activity, as was seen in Chapter 3. The DRUV-vis spectra shown in Figure 17 shows that there was a change in the distribution of Fe³⁺ species following calcination of the synthesised samples. A shift to lower energy can be observed following calcination, with a new maximum observed at 320 nm in samples HT_175_120_Na⁺ and TB_200_6_Na⁺. Each of the sub bands were deconvoluted and semi-quantitative analysis of the proportion of Fe³⁺ species within each of the catalysts are given in Table 4.

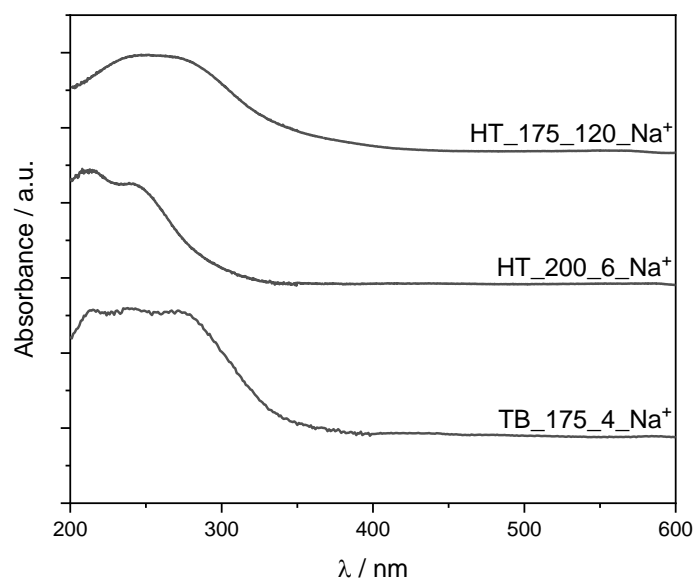


Figure 17 DRUV-vis of 0.1 wt% Fe-ZSM-5 (42) following calcination at 550 °C as a form of catalyst preparation.

Table 4 Quantification of Fe³⁺ species in 0.1 wt% Fe-ZSM-5 (42)_Na⁺ as a function of crystallisation conditions, calculated from deconvoluted sub-bands in the DRUV-vis spectra.

Catalyst	λ_1 / %	λ_2 / %	λ_3 / %	λ_4 / %
HT_175_120_Na ⁺	39.7	52.4	3.43	4.51
HT_200_6_Na ⁺	60.3	31.9	2.07	5.71
TB_175_4_Na ⁺	32.3	58.2	7.00	2.76

Though, there are differences in the intensity of the new maximum, which could indicate that there are differences that occur to the speciation of the Fe³⁺ as a result of the different crystallisation conditions, which only become apparent following calcination at 550 °C. The broadest shift occurs in the sample prepared within the tubular reactors that may indicate that incorporation of Fe³⁺ at shorter crystallisation times results in Fe³⁺ that can be more readily extracted from the framework.

The changes in Fe³⁺ speciation after calcination was further investigated by resonance Raman spectroscopy.^{9,10,33} Stretching frequencies, that arise from ν_s (Si-O-Si) modes situated within the five-membered rings (5MR) of the MFI framework, were observed at 380 and 800 cm⁻¹ in the resonance Raman spectra of each of the samples (Figure 17).³⁵ This indicates that each of the catalysts are crystalline and possess the MFI framework, which agrees with the *p*XRD diffraction patterns of these samples (shown in Figures 2, 5 and 8). Additional to the MFI bands, a band centred at $\bar{\nu} = 520$ cm⁻¹ was observed in each of the spectra, along with bands observed at $\bar{\nu} = 1020$, 1120 and 1170 cm⁻¹.^{9,10} These have previously been assigned as tetrahedral, framework-bound Fe³⁺ species, [Fe(OSiO₃)₄], which was observed to decrease in intensity when the intensity of the λ_2 band in the DRUV-vis spectra increased in intensity following calcination in Chapter 2.⁹ In each of the Raman spectra shown in Figure 18, the intensity of the bands at 520, 1020, 1120 and 1170 cm⁻¹ are not that intense, suggesting that framework Fe³⁺ have been destabilised following calcination. Comparison with the Raman spectra of the synthesised samples would have been more insightful to make a true comparison in the change of the Raman band intensities. Yet, as demonstrated in Chapter 3, the presence of TPA⁺ in the zeolite lattice leads to overlapping with the relevant Fe³⁺ bands, thus it can be difficult to directly compare the intensity to the Fe³⁺. Additionally, resonance Raman spectra at 325 nm could have been recorded, as there did appear to be some differences in the bands that were resonance enhanced at lower laser energy. However, due to the fact measurements were recorded at an external facility, it was not possible to collect the data for this thesis.

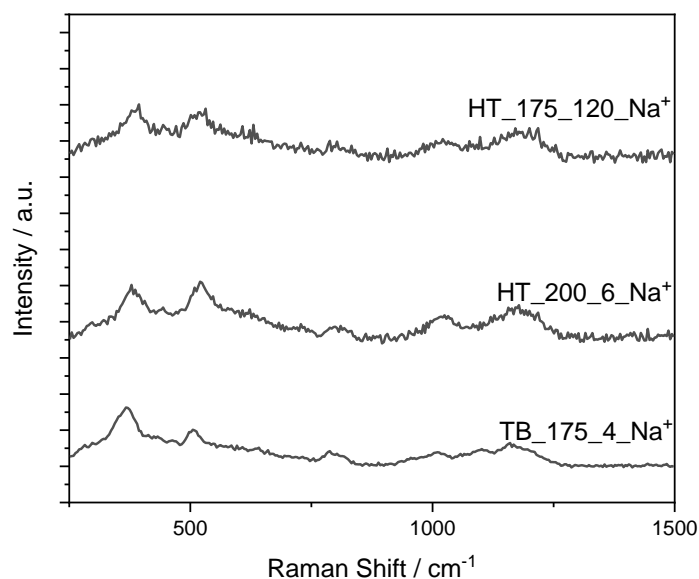


Figure 18 Resonance Raman ($\lambda = 266$ nm) spectra of 0.1 wt % Fe-ZSM-5 (42) following calcination at 550 °C as a form of catalyst preparation.

To compare the catalytic performance of the calcined materials, thus validating whether reduction in crystallisation time is feasible, the catalysts were evaluated for partial CH_4 oxidation activity. As reported in Chapter 3, the AS form of the catalyst was inactive and were not tested here, as the inactivity was not expected to change. The TOF were calculated after 15 minutes under reaction conditions. TOF were plotted as a function of crystallisation conditions are shown in Figure 19. The two samples prepared by conventional hydrothermal conditions (denoted “HT”) were comparably active, yet this does not correlate to the previous observation made from the DRUV-vis spectra. From the DRUV-vis (Figure 17), the relative proportion of extra framework (λ_2) Fe^{3+} species in the benchmark catalyst was 1.63 times greater than HT_200_6_Na⁺. The difference in relative proportion of extra framework Fe^{3+} species contradicts the observations made in Chapter 3, where it was stipulated that a higher proportion of extra framework Fe^{3+} species corresponded to an increase in catalytic activity. Other aspects of the materials, then, must influence overall catalytic performance, such as Al^{3+} siting within the framework.¹⁷

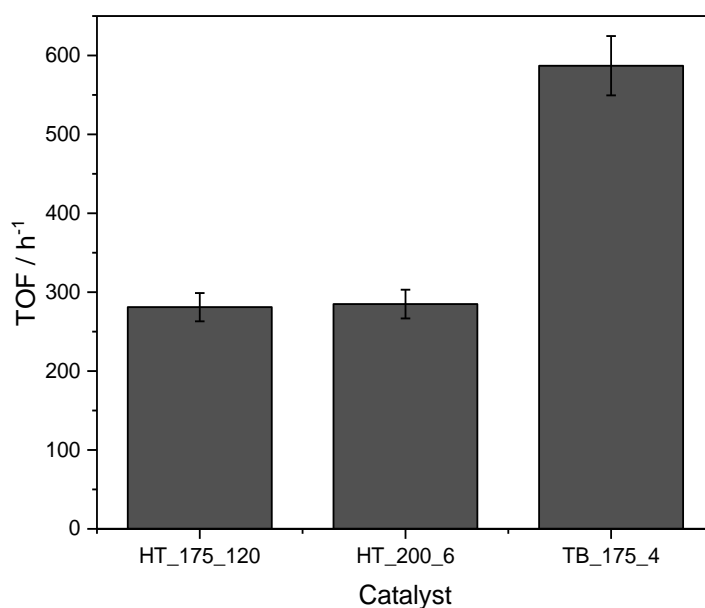


Figure 19 Catalytic activity (TOF = (mol product formed)/(mol Fe)*(unit time)) of 0.1 wt% Fe-ZSM-5 (42)_{Na}⁺ as a function of the synthesis method of the catalyst. Reaction conditions: 135 mg catalyst, 10 mL 0.5 M H₂O₂ (aq), 10.0 bar CH₄, 50 °C, 15 min, 1500 rpm. Aqueous phase products (CH₃OH, CH₃OOH and HCOOH) were quantified by ¹H NMR and gas phase products (CO₂) were quantified by GC-FID, against calibrated standards. Error bars were calculated at 6.4 % from repeat measurements of the benchmark catalyst (HT_175_120_{Na}⁺).

The calculated TOF for TB_175_4_{Na}⁺ was approximately double the TOF of the benchmark sample, even though there is only a 6 % difference in the relative proportion of λ₂ species between the two samples (Figure 17). Because semi-quantification of DRUV-vis spectra cannot be considered an accurate method for determining the actual percentages of Fe³⁺ species within the structure, it should be considered that the relative proportion of extra framework Fe³⁺ species in both HT_175_120_{Na}⁺ and TB_175_4_{Na}⁺ can be considered equivalent. These observations contradict the conclusions in Chapter 3; the relative proportion of λ₂ (extra framework Fe³⁺ species) corresponds to the relative catalytic activity. The results reported here, however, suggest that additional contributing factors affect the catalytic activity of Fe-ZSM-5 for partial CH₄ oxidation. Differences in zeolite preparation methods can lead to differences in particle size, actual Fe³⁺ and Al³⁺ loading of the catalysts and the siting of Al³⁺ within the MFI framework.¹³ Furthermore, there are evident differences in the appearance of each of the DRUV-vis spectra of the samples (Figure 17), which suggests that there are several different extra framework Fe³⁺ species that can form within the structure, dependant on the length of crystallisation. Additional spectroscopic methods could be employed, such as Mössbauer, which can provide additional information on the speciation of Fe³⁺ within the zeolite matrix.³⁶

It can be concluded from the work performed in this section that reducing the crystallisation time from 120 h to 4 h can afford an even more active catalyst for partial CH₄ oxidation. Yet, it is not clear why this increase in activity was observed, thus additional studies should be performed that can identify trends that can explain the increase in catalytic performance, even though the catalysts appear structurally similar from the characterisation performed herein.

4.7. Conclusion

Herein, it has been shown that the hydrothermal synthesis of 0.1 wt% Fe-ZSM-5 (42) can be performed with lower crystallisation times than previously thought, to afford a structurally comparable catalyst. Increasing the temperature of the crystallisation step from 175 to 200 °C reduces crystallisation time from 120 h to 6 h, without loss of crystal structure. DRUV-vis spectroscopy demonstrates that Fe³⁺ was fully incorporated into the MFI framework and ²⁷Al MAS NMR demonstrated that the Al³⁺ was also incorporated into the framework. The overall crystallisation time could be reduced to 4 h at 175 °C by changing the crystallisation vessel from a thick-walled SS autoclave to a thin-walled 3/8" SS tubing. The rate of crystallisation could be improved due to the reduction in heating time, which can be caused by poor heat transfer. The time to reach the desired internal temperature within the SS tubing was reduced. Reducing vessel-wall thickness resulted in a fully crystalline material in 4 h, as shown by *p*XRD. MAS NMR and DRUV-vis were used to demonstrate that Al³⁺ and Fe³⁺ were fully incorporated into the MFI framework following synthesis. The rate of crystallisation is affected by the Al³⁺ content within the initial aluminosilicate gel. Fully crystalline samples of 0.1 wt% Fe-silicalite-1 were afforded when synthesised within 3/8" SS tubing, and 0.1 wt% Fe-ZSM-5 (84) produced a fully crystalline sample in as little as 2 h at 175 °C. These results could suggest that substitution of framework SiO₄ species with Al³⁺ is a slower process than the formation of the MFI crystal structure. It would be interesting to determine whether the differences in crystallisation time has affected the extent of crystallisation by performing elemental analyses on the sample, to determine whether all the Al precursor had been incorporated into the catalyst structure.

As this work was performed to demonstrate whether comparable active catalysts for partial CH₄ oxidation could be prepared in less time than 120 h, it was necessary to test the catalysts under CH₄ oxidation catalysts, following calcination to remove the TPA template from the pores. The three chosen catalysts (HT_175_120_Na⁺, HT_200_6_Na⁺ and TB_175_4_Na⁺) were all shown to be active for partial CH₄ oxidation. Discrepancies were observed in the TOFs and the relative proportion of Fe³⁺ species observed by DRUV-vis. Relative to the benchmark

catalyst, HT_200_6_Na⁺ was comparatively active for CH₄ oxidation, whereas TB_175_4_Na⁺ was twice as active for CH₄ oxidation. The relative proportion of extra framework Fe³⁺ species, as observed in the DRUV-vis spectra, did not correlate with catalytic activity trends, which contradicts the stipulation made in Chapter 3. The relative proportion of extra framework species in the DRUV-vis spectra were proportional to the relative catalytic rate. The differences observed in the samples, however, suggests that there are additional factors to Fe³⁺ speciation that can affect the rate of partial CH₄ oxidation. To better understand the impact of synthesis method on catalytic performance, the catalysts should be studied for differences in particle and crystal size, which could result from the different crystallisation times, and the effect of particle size may affect the accessibility of the active sites of each of the catalysts to reactants. Additionally, there may be subtle differences in the nature of the extra framework Fe³⁺ species that form under different synthesis conditions.

4.8. References

1. A. Zecchina, M. Rivallan, G. Berlier, C. Lamberti and G. Ricchiardi, *Phys. Chem. Chem. Phys.*, 2007, 9, 3483–3499.
2. N. Kosinov, C. Liu, E. J. M. Hensen and E. A. Pidko, *Chem. Mater.*, 2018, 30, 3177 – 3198.
3. G. Berlier, G. Spoto, S. Bordiga, G. Ricchiardi, P. Fisticaro, A. Zecchina, I. Rossetti, E. Selli, L. Forni, E. Giamello and C. Lamberti, *J. Catal.*, 2002, 208, 64–82.
4. R. V. Prikhod'ko, I. M. Astrelin, M. V Sychev and E. J. M. Hensen, *Russ. J. Appl. Chem.*, 2006, 79, 1115-1121.
5. M. S. Kumar, M. Schwidder, W. Grünert and A. Brückner, *J. Catal.*, 2004, 227, 384–397.
6. C. Hammond, M. M. Forde, M. H. Ab Rahim, A. Thetford, Q. He, R. L. Jenkins, N. Dimitratos, J. a Lopez-Sanchez, N. F. Dummer, D. M. Murphy, A. F. Carley, S. H. Taylor, D. J. Willock, E. E. Stangland, J. Kang, H. Hagen, C. J. Kiely and G. J. Hutchings, *Angew. Chem. Int. Ed.*, 2012, 51, 5129–33.
7. C. Hammond, R. L. Jenkins, N. Dimitratos, J. A. Lopez-Sanchez, M. H. Ab Rahim, M. M. Forde, A. Thetford, D. M. Murphy, H. Hagen, E. E. Stangland, J. M. Moulijn, S. H. Taylor, D. J. Willock and G. J. Hutchings, *Chem. - A Eur. J.*, 2012, 18, 15735–15745.
8. C. Hammond, N. Dimitratos, J. A. Lopez-Sanchez, R. L. Jenkins, G. Whiting, S. A. Kondrat, M. Hasbi, M. M. Forde, A. Thetford, H. Hagen, E. E. Stangland, J. M. Moulijn, S. H. Taylor, D. J. Willock and G. J. Hutchings, *ACS Catal.*, 2013, 3, 1835–1844.
9. K. Sun, F. Fan, H. Xia, Z. Feng, W. Li and C. Li, *J. Phys. Chem. C*, 2008, 112, 16036–16041.

10. C. Hammond, I. Hermans and N. Dimitratos, *ChemCatChem*, 2015, 7, 434–440.
11. J. L. Casci, *Microporous Mesoporous Mater.*, 2005, 82, 217-226.
12. P.P Notté, *Top. Catal.*, 2000, 13, 387-394.
13. J. Grand, H. Awala, S. Mintova, *CrysEngComm.*, 2016, 18, 650-664.
14. van Koningsveld, H. van Bekkum and J. C. Jansen, *Acta Crystallogr. Sect. B Struct. Sci.*, 1987, 43, 127–132.
15. M. M. J. Treacy and J. B. Higgins, *Collection of Simulated XRD Powder Patterns for Zeolites*, Elsevier, 2007.
16. ASTM, 2015, 0.1, 6-9.
17. J. Dedecek, V. Balgová, V. Pashkova, P. Klein and B. Wichterlová, *Chem. Mater.*, 2012, 24, 3231–3239.
18. R. van Grieken, J. L. Sotelo, J. M. Menéndez and J. A. Melero, *Micro Meso Mater.*, 2000, 39, 135-147.
19. P. Marturano, L. Drozdová, A. Kogelbauer and R. Prins, *J. Catal.*, 2000, 192, 236–247.
20. Z. Liu, T. Wakihara, C. Anand, S. H. Keoh, D. Nishioka, Y. Hotta, T. Matsuo, T. Takewaki and T. Okubo, *Micro Meso Mater.*, 2016, 223, 140–144.
21. M. Briend, A. Lamy, M. J. Peltre, P. P. Man and D. Barthomeuf, *Zeolites*, 1993, 13, 201-211.
22. P. J. Smeets, J. S. Woertink, B. F. Sels, E. I. Solomon and R. A. Schoonheydt, *Inorg. Chem.*, 2010, 49, 3573–3583.
23. V. P. Valtchev, A-C. Faust and J. Lézervant, *Micro Meso Mater.*, 2004, 68, 91-95.
24. G. Engelhardt, *Stud. Surf. Sci. Catal.*, 1989, 52, 151-162.
25. S. L. Burkett and M. E. Davis, *J. Phys. Chem.*, 1994, 98, 4647–4653.
26. A. E. Persson, B. J. Schoeman, J. Sterte and J. E. Otterstedt, *Zeolites*, 1995, 15, 611-619.
27. K. J. Chao, T. C. Tasi, M. S. Chen and I. Wang, *J. Chem. Soc. Faraday Trans. 1 Phys. Chem. Condens. Phases*, 1981, 77, 547-555.
28. C. E. A. Kirschhock, R. Ravishankar, F. Verspeurt, P. J. Grobet, P. A. Jacobs and J. A. Martens, *J. Phys. Chem. B*, 1999, 103, 4965-4971.
29. C. E. A. Kirschhock, S. P. B. Kremer, P. J. Grobet, P. A. Jacobs and J. A. Martens, *J. Phys. Chem. B*, 2002, 106, 4897-4900.
30. T. P. Caremans, B. Loppinet, L. R. A. Follens, T. S. Van Erp, J. Vermant, B. Goderis, C. E. A. Kirschhock, J. A. Martens and A. Aerts, *Chem. Mater.*, 2010, 22, 3619-3629.
31. E. G. Derouane, S. Determerie, Z. Gabelica and N. Blom, *Appl. Catal.*, 1981, 1, 201-224.

32. M. Zaarour, B. Dong, I. Naydenova, R. Retoux and S. Mintova, *Micro Meso Mat.*, 2014, 189, 11-21.
33. S. Jin, Z. Feng, F. Fan and C. Li, *Catal. Lett.*, 2015, 145, 468–481.
34. G. Majano, A. Darwiche, S. Mintova and V. Valtchev, *Ind. Eng. Chem. Res.*, 2009, 48, 7084-7091.
35. P. K. Dutta and M. Puri, *J. Phys. Chem.*, 1987, 91, 4329–4333.
36. B. E. R. Snyder, M. L. Bols, R. A. Schoonheydt, B. F. Sels and E. I. Solomon, *Chem. Rev.*, 2018, 118, 2718–2768.

Chapter 5. Seed-Assisted Synthesis of Fe-ZSM-5 to Study the Speciation of Fe

5.1 Introduction

In Chapter 3, Fe-ZSM-5 is shown as active for methane oxidation following the initial calcination step required to thermally decompose the organic structural directing agent (OSDA) within the zeolite micropores, provided the Al content was high enough to facilitate the extraction of Fe^{3+} from framework positions (Figure 1). Yet, the synthesised form of the catalyst that contained OSDA was relatively inactive for this reaction irrespective of the $\text{SiO}_2/\text{Al}_2\text{O}_3$ ratio. Due to presence of organic material within the synthesised material, it was not possible to determine the onset in catalytic activity. Two possibilities could account for the onset of catalytic ability; a change in Fe^{3+} speciation during the high-temperature calcination; or, because the OSDA restricted access to internally located active sites. Diffusion of CH_4 and H_2O_2 into the MFI pores could be limited in the as-synthesised (denoted as AS) form of the catalyst, as the void-free space is filled with the tetrapropylammonium (TPA) cation that has a diameter of 4.4 Å. As the pore dimensions of MFI are approximately 5-6 Å,¹ there is limited free space within the MFI micropores for reactant diffusion to occur, thus preventing access of CH_4 and H_2O_2 to active sites potentially located within the micropores. DRUV-vis spectra reported in Chapter 3 suggested that there was a change in the distribution of Fe^{3+} species following the initial calcination step at 550 °C. This suggested that Fe^{3+} speciation does change as a result of high temperature calcination and removal of the OSDA.² Furthermore, due to the presence of OSDA in the synthesised catalyst, it was not possible to conclusively state that catalytic activity was a result of a change in Fe^{3+} speciation following calcination.

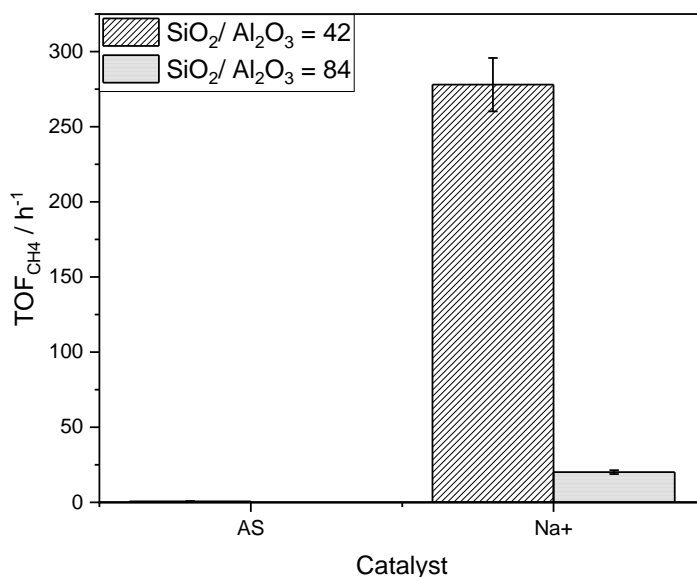


Figure 1 Partial CH₄ oxidation activity, reported as TOF, as a function of catalyst form. Error bars were calculated as 6.4 % and were found as an average of 3 replicate reactions.

To investigate the onset of catalytic activity in Fe-ZSM-5 for CH₄ oxidation, a non-invasive route was needed to afford a template-free form of the catalyst, that did not result in Fe-speciation changes within the zeolite. Various methods for non-invasive OSDA removal were considered.³⁻⁵ For example, the use of an oxidising agent, such as O₃, can break down the template at lower temperatures.³ The use of reversible, building block templates that have been shown to be readily broken down within the pores of zeolites, leaving the zeolite framework intact.^{4,5} However, these methods introduce additional variables that may result in a change in Fe³⁺ speciation. After considering the literature, the design and synthesis of Fe-ZSM-5 in the absence of an OSDA was reasoned to be possible. Various methods for OSDA-free zeolite synthesis procedures have been reported, however, the effect that such methods have on the isomorphous substitution of Fe³⁺ and other transition metal ions has been less well studied. The possibility to synthesise an OSDA-free zeolite, where the pores would not be restricted by the presence of organic material, would allow for a study on the onset of catalytic activity within Fe-ZSM-5 more conclusively than with the previously reported work (*cf.* Chapter 3 for further discussion).

5.2 Development of Seed-Assisted Synthesis of 0.1 wt% Fe-ZSM-5 (42) for Partial Methane Oxidation

Conventional hydrothermal preparations typically utilise quaternary ammonium salts, such as tetrapropylammonium hydroxide (TPAOH), to facilitate the formation of the desired crystalline zeolite topology.⁶ High-temperature calcination is the most common method used to remove the template, though this can lead to aggregation of the zeolite crystals that decreases the surface area of the material. Furthermore, the removal of OSDA through calcination leads to the formation of unwanted by-products, such as CO₂ and coke, which are environmentally destructive and can affect catalyst performance.⁷ Moreover, use and subsequent decomposition of OSDAs adds additional economic burden to the synthesis. Thus, a reliable synthetic pathway that omits the use of organic templates would be economically and environmentally advantageous.

In recent years, the use of zeolites as ‘seed materials’ to enable formation of the desired zeolite framework in lieu of an OSDA has come into focus, due to the versatility of zeolites and their use in a variety of applications.^{5,8-10} Zeolite seeds contain the framework structure of the desired material, and provide a large surface area to drive nucleation and crystal growth of the zeolite. The use of seeding in zeolite crystallisation has been beneficial in large-scale zeolite synthesis because seeds can increase the rate of crystallisation by reducing the need to form discrete zeolite nuclei, suppress the formation of unwanted phases, and exert greater control on crystallite size whilst avoiding the use of tetraalkylammonium salts.¹¹⁻¹³

Many studies have been published that have focused on the development and characterisation of seed-induced zeolite synthesis. A seed-assisted crystallisation of nanocrystalline ZSM-5 with a narrow particle size distribution (PSD) was realised by the group of Valtchev.¹⁴ To achieve the desired nanocrystal diameter (20 nm), a seed suspension was prepared and added to a parent aluminosilicate gel to favour the aggregation of ZSM-5 nuclei instead of larger crystals. A fully crystalline ZSM-5 product was afforded in 3 h at 170 °C with 3 wt % seeds used. The authors claimed that this route was TPA-free, as shown by thermogravimetric analysis (TGA) profiles; however, TPA was used in the preparation of the seed suspension and was not removed prior to addition to the aluminosilicate gel, thus this mechanism was not truly seed-assisted, and that presence of the OSDA in the seed may have aided crystallisation. Another seed-assisted route was proposed by Larsen *et al.*, who utilised calcined ZSM-5 seeds to crystallise nanocrystalline ZSM-5 in 24 h at 165 °C.¹⁵ This work demonstrated that several

variables in the gel preparation, such as pH, stoichiometry, seed size and mass of added seed were critical in controlling the crystallisation of pure, crystalline MFI.

None of these previous reports considered the incorporation of transition metal cations to the zeolite framework, even though their inclusion in the synthesis gel can impact the crystallisation processes.¹⁶ Further, metal-substituted zeolites are important catalysts in many industrially relevant transformations, as discussed in Chapter 1. It is therefore of interest to develop a seed-assisted synthesis of Fe-substituted ZSM-5 that contains equivalent metal centres distributed throughout the zeolite lattice.¹⁷ A seeded approach to the synthesis of Fe-ZSM-5 was reported by the group of Li to allow *in-situ* Raman monitoring of the incorporation of Fe³⁺ into the MFI framework during hydrothermal synthesis.^{18,19} The work suggested that the formation of tetrahedral [Fe(OSi)₄] species occurred early on in the crystallisation. However, the samples were not tested for catalytic activity and the impact of the Fe³⁺ speciation on catalytic performance was not determined. As shown in Chapter 3, it is possible that Fe-ZSM-5 is catalytically inactive prior to high temperature treatment. Thus, it is important to understand and observe why the catalysts become active as a function of heat treatment.

With this insight, a seed-assisted methodology for Fe-ZSM-5 was developed using a method adapted from Larsen, that incorporates a low Fe loading (0.1 wt%) into the zeolite lattice.¹⁵ The new catalysts were characterised by *p*XRD, N₂ physisorption, SEM, ²⁷Al MAS-NMR, TGA, DRUV-vis, and resonance Raman spectroscopy to determine the crystal phases and extent of Fe³⁺ incorporation into the crystalline zeolite lattice.

5.2.1 Synthesis of the Seed Material for Seed-Assisted Synthesis

A seed material can be used in place of an OSDA in which the silicate and aluminate species are able to nucleate and grow to afford the desired zeolite crystals. Zeolite seeds were prepared by conventional hydrothermal methods, as described in Chapter 3, at 175 °C for 120 h to afford crystalline 0.1 wt% Fe-ZSM-5 (42)_AS.²⁰ The longer crystallisation time was used for the development of a seed-assisted method as this work preceded the work reported in Chapter 4. Throughout the text, the seed material will be denoted as HT_0.1 wt% Fe-ZSM-5 (42)_ZZ, where HT shows that the material was prepared by hydrothermal methods and ZZ denotes the catalyst form (AS = as synthesised; Na⁺ = Na⁺, post calcination; NH₄⁺ = ammonium form; H⁺ = proton form). The seed was calcined at 550 °C in flowing N₂ to remove the OSDA prior to use as the seed, as the presence of OSDA in the seed impacts upon the nucleation and crystallisation. Thus, it would not be possible to determine whether crystallisation occurred

due to the seed or because the OSDA was promoting crystallisation of the daughter zeolite material.

The crystallinity and zeolite topology of the synthesised seed material were confirmed by *p*XRD, which showed diffraction peaks typical of MFI (Figure 2). No impurity phases or amorphous material was identified, which indicates that the MFI seed is 100% pure.²¹ From the Scanning Electron Microscopy (SEM) image, shown in Figure 3, the average particle size of the calcined seed is determined to be 3 μm . It has previously been suggested by Larsen *et al.* that smaller particles provide a greater surface area from which zeolite crystallite growth can occur.¹⁵ Thus, the particle size of the seed material might impact on the structural properties of the synthesised daughter material.

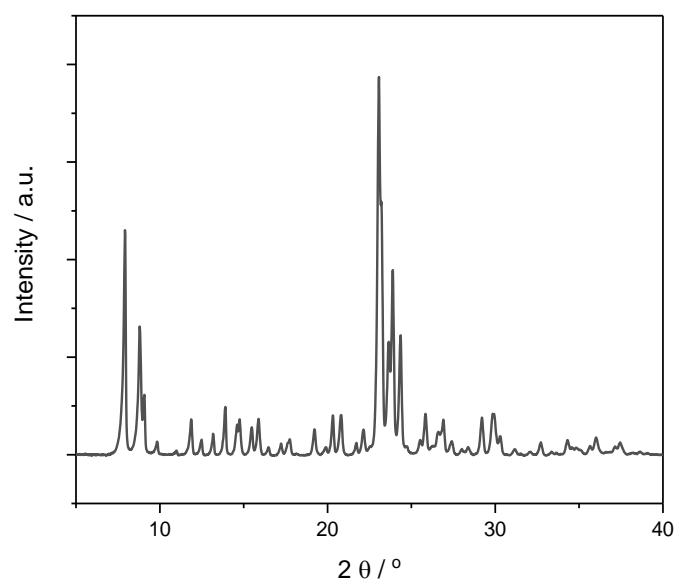


Figure 2 *p*XRD diffractogram of HT 0.1 wt% Fe-ZSM-5 (42)_{Na}⁺ seed material.

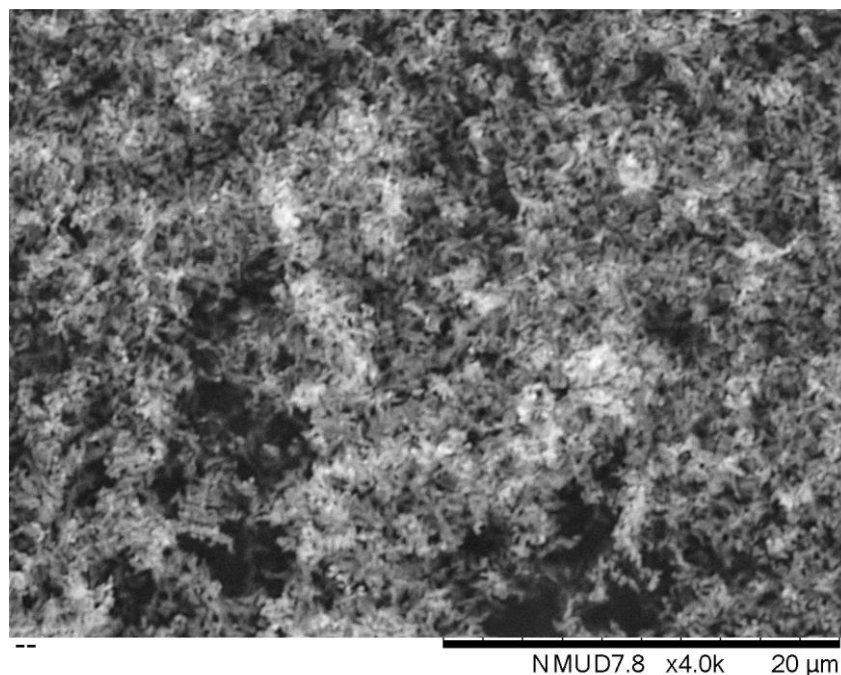


Figure 3 SEM image of HT_0.1 wt %Fe-ZSM-5 (42)_Na⁺ seed. Image was taken at x 4 k magnification.

5.2.2 Synthesis of Seed-Assisted 0.1 wt% Fe-ZSM-5 (42)

Using the parameters reported by Larsen *et al.*, the following methodology was investigated for the synthesis of 0.1 wt% Fe-ZSM-5 (42) in the absence of OSDA.¹⁵ A gel with the molar ratio 1 SiO₂: 0.024 Al₂O₃: 0.067 Na₂O: 0.0147 Fe₂O₃: 39.4 H₂O was prepared as follows; 0.193 g of NaAlO₂ (2.4 mmol) was dissolved in 27.6 mL di-ionised H₂O (1533 mmol) and 2.44 mL of 1.0 M NaOH (2.44 mmol) was added dropwise to bring the pH of the solution to 12.0. To this, TEOS (10.2 g, 49.4 mmol) was added dropwise and the resulting mixture was aged for 2 h at 60 °C. Concurrently, a solution of Fe(NO₃)₃·9H₂O (29.4 mg, 0.076 mmol) and oxalic acid (30.4 mg, 0.25 mmol) in 5 mL DI H₂O was prepared and then added dropwise to the suspension after 2 h. The mixture was homogenised for 16 h at 60 °C. Following aging, 1 wt % (of SiO₂ mass, 29.7 mg) of calcined HT_0.1 wt % Fe-ZSM-5 seeds were dissolved in 1.0 mL EtOH by sonication and added to the gel and stirred. The gel was transferred to a PTFE-lined stainless-steel autoclave and placed into a pre-heated oven at 200 °C for 168 h. A white slurry was afforded, and the crystalline solid was washed with deionised water and separated by centrifugation to afford the AS form of the catalyst.

Initial attempts to crystallise Fe-ZSM-5 at these experimental conditions resulted in the formation of amorphous SiO₂ that was observed by the appearance of a broad diffraction peak in the *p*XRD pattern of the synthesised material. Larsen *et al.* indicated that equilibration of the aluminosilicate precursor species could not be reached when the pH of the gel was not

ideal.¹⁵ Recording the pH of the gel after the addition of NaOH showed that the pH was less than 12, thus it is possible that the gel was not basic enough for formation of key precursor aluminosilicate species. For reference, the recorded pH of conventional HT_0.1 wt% Fe-ZSM-5 (42) was 12. To adjust the gel pH to that of the conventional synthesis, 1.0 M NaOH was titrated in until the pH was adjusted and stabilised at pH 12. Following titration of the NaOH solution to the aluminosilicate gel, the gel was crystallised at 200 °C for 168 h. Harsh conditions were chosen to drive crystallisation to completion. The synthesised material exhibited characteristic MFI diffraction peaks, as shown in Figure 4 (a diffraction pattern of the seed, HT_0.1 wt% Fe-ZSM-5 (42)_Na⁺, is provided for reference of the MFI framework topology).²¹ For all seed-assisted syntheses performed after this investigation, NaOH was added by titration to adjust the pH of the gel to 12.

The *p*XRD patterns of the hydrothermally prepared seed and seed-assisted prepared Fe-ZSM-5 are shown in Figure 4, which demonstrates that both samples possess typical MFI crystal diffraction peaks following crystallisation. The addition of the seed material into the aluminosilicate gel was able to propagate MFI crystal growth from the aluminosilicate gel. To understand whether crystal growth was promoted by the addition of seed or was spontaneous under the reaction conditions, a control sample was synthesised to determine whether MFI crystal structure could be afforded in the absence of template or seed. The aluminosilicate gel was prepared as described above, but addition of the seed was omitted prior to crystallisation at 200 °C. A white solid was afforded, but, a broad peak, centred around 22 ° 2 θ , is observed in the *p*XRD diffraction pattern, indicating poor crystallinity of the sample (Figure 5). Ill-defined diffraction peaks at 22.5 – 25.0 ° 2 θ can be seen in the control sample, which suggests slow crystal growth in the absence of seed and the extent of crystallisation was hugely increased following addition of seed to the aluminosilicate gel.

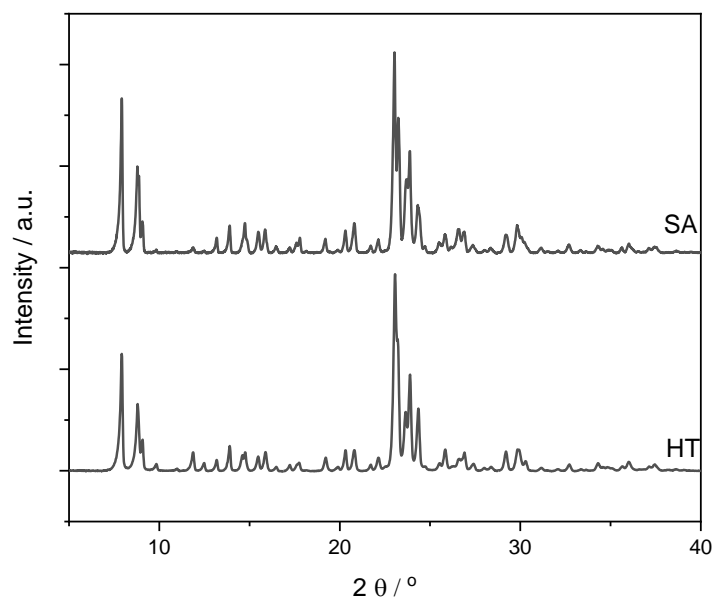


Figure 4 pXRD diffractogram of HT_0.1 wt% Fe-ZSM-5 (42)_Na⁺ and SA_0.1 wt% Fe-ZSM-5 (42)_AS.

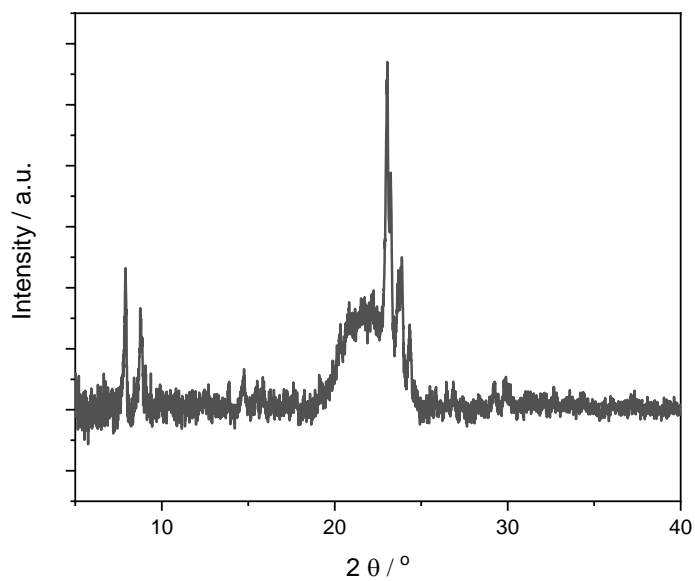


Figure 5 pXRD diffraction pattern of 0.1 wt% Fe-ZSM-5 (42)_AS synthesised in the absence of OSDA or seed at 200 °C for 168 h.

After establishing a protocol for the seed-assisted synthesis of 0.1 wt % Fe-ZSM-5, the rate of crystallisation was determined by varying the time of crystallisation at 200 °C. To determine the crystallinity of the synthesised (AS) samples, the AS forms of the catalysts were

characterised by *p*XRD to determine the crystallinity (relative to the sample crystallised for 168 h at 200 °C) and sample phase purity.

The *p*XRD diffraction patterns of the synthesised seed-assisted materials are shown in Figure 6, which show that the characteristic MFI diffraction peaks at 6-7 ° 2 θ and 22.5 – 25 ° 2 θ are present in each of the materials prepared by seed-assisted methods.²¹ There is a discernible difference in the integrated area of the diffraction peaks of the sample crystallised for 24 h, relative to the sample crystallised for 168 h at 200 °C.

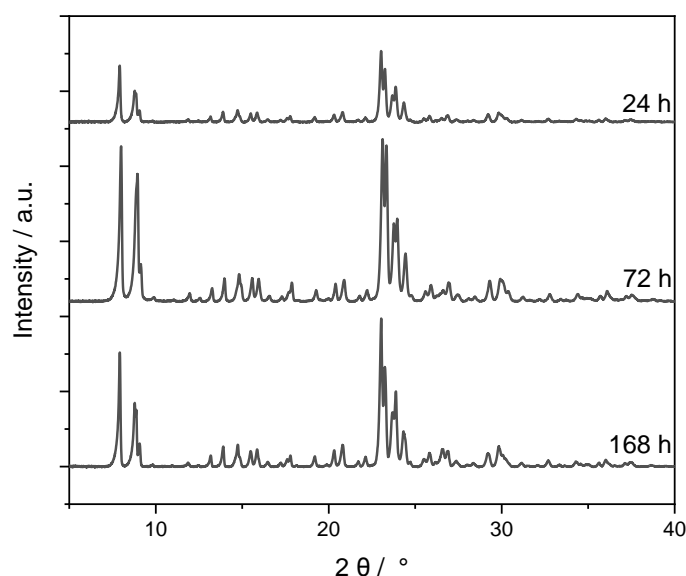


Figure 6 *p*XRD patterns of SA_0.1 wt% Fe-ZSM-5 (42)_AS crystallised for *x* h at 200 °C, where *x* is the length of crystallisation.

On integration of the peaks at 22.5-25 ° 2 θ , the area of the sample crystallised for 24 h is diminished by 43%, relative to the area of SA_0.1 Fe-ZSM-5 (45) crystallised for 168 h. The reduction in peak area suggests that 24 h is insufficient time for crystal growth and crystallisation is incomplete. In Chapter 4, 6 h at 200 °C was sufficient for complete crystallisation of the MFI framework, however, the seed-assisted material was not fully crystalline after 24 h. This suggests that the new, seed-assisted procedure crystallises at a much slower rate than that of the conventional preparation. It is possible that the ODSA can promote both the rate of zeolite crystal growth and substitution of metal cations in the zeolite lattice. Incomplete crystallisation at shorter time frames was also evident in the mother liquor of the 24 h sample following crystallisation; a cloudy white solution was collected after centrifugation, which was indicative of unreacted aluminosilicate particles.²² A clearer mother liquor was

observed at longer crystallisation times due to the aluminosilicate particles being incorporated into the growing zeolite crystal. To support this theory, elemental analysis of the mother liquor should be made to show that unreacted aluminosilicate units are left post crystallisation.

An increase in the relative crystallinity is observed after 72 h, relative to the sample at 168 h. The cause of the increase is uncertain. Large experimental error associated with *p*XRD method; parameters such as sample preparation, amount of sample used and packing of sample on the *p*XRD sample holder can affect the line-width of diffraction peaks. Moreover, other crystallisation parameters may have impacted the samples, and optimisation of the method is needed to better understand the system. Longer crystallisation times may not be necessary for full crystallisation of the MFI framework. Furthermore, longer crystallisation times may result in the formation of more thermodynamically stable phases, such as quartz.¹⁵ The presence of impurity phases would not be suitable for the formation of an active catalyst. The *p*XRD does not take the incorporation of Fe³⁺ ions into the MFI framework into account, thus the success of the new synthetic method cannot be determined from crystallinity measurements alone.

The size and morphology of the seed-assisted samples were determined using SEM and the images are displayed in Figure 7. The morphology of the crystal particles in the seed-assisted materials is noticeably different from that of the seed material shown in Figure 3. The SEM image of HT_0.1 wt% Fe-ZSM-5 (42)_Na⁺ suggests that the seed crystals have a cubic-type morphology. The seed-assisted particles form needle-like aggregates. Furthermore, the seed-assisted particles are several times larger than that of the seed material (3 μm). Difference in the particle morphology indicates that the seed-assisted crystallisation mechanism differs from the conventional hydrothermal synthesis mechanism. It is possible that the zeolite crystal growth propagates from aggregates of the calcined seed material suspended within the aluminosilicate gel.²³

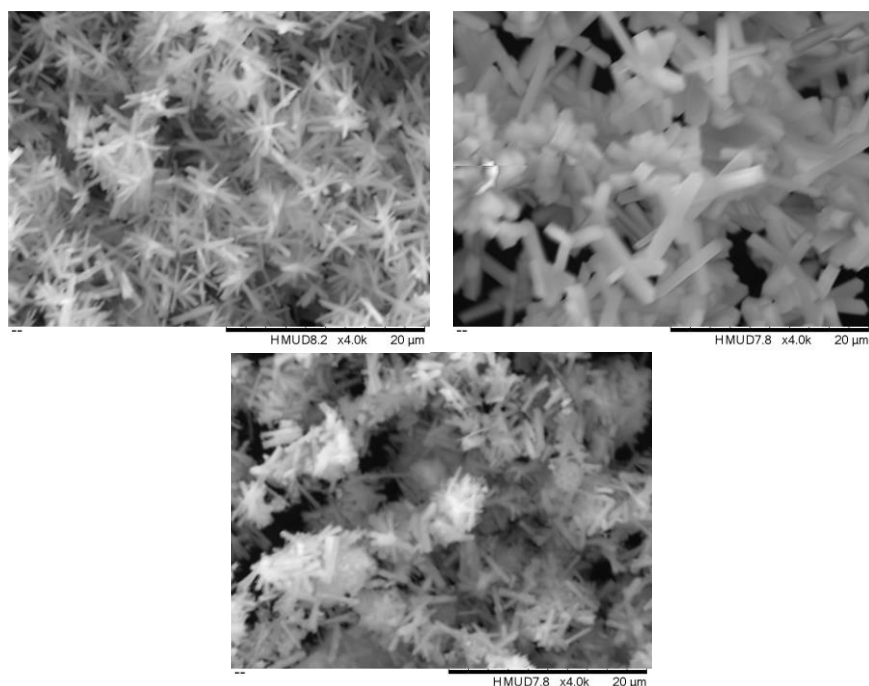


Figure 7 SEM images of SA_0.1 wt %Fe-ZSM-5 (42)_AS crystallised at 200 °C for x h. Top left, 168 h; top right, 72 h, and; bottom, 24 h. Images were taken at x 4000 magnification.

To quantify the amount of Fe and Al in the parent sample crystallised for 168 h (prior to heat treatment), inductively coupled plasma-mass spectrometry (ICP-MS) was performed. Three replicate measurements were made to determine the error and reliability of the method. In Table 1, the average wt% Fe in the sample is 0.1173%, which is slightly above the nominal value of 0.1%. The error across the 3 replicates is 3.8 %, which is acceptable. The nominal loading of Al within the parent sample is 1.5 wt%, yet the average value calculated from ICP-MS analysis is 1.3181%, though the error is calculated to be 27.3%. An error of 27.3% is quite high, thus it was decided that the data recorded by ICP-MS was not accurate enough to use to compare the actual composition of the samples prepared at different times.

Table 1 ICP-MS data of SA_0.1 wt% Fe-ZSM-5 (42)_AS. The errors were calculated from the 3 replicate values.

Replicate	Fe wt%	Al wt%	Na wt%
1	0.1196	1.5791	1.2646
2	0.1123	0.9072	1.0937
3	0.1201	1.4680	0.6457
Average	0.1173	1.3181	1.0013
Error / %	3.8	27.3	31.9

The above techniques focus on the determination of the crystal properties of the samples, and not the substitution of T-sites for Al^{3+} or Fe^{3+} . From the conclusions in Chapter 2, both Fe^{3+} and Al^{3+} are shown as essential for good catalytic performance in Fe-ZSM-5. If the incorporation of either cation was affected by the adapted crystallisation conditions, then the seed-assisted synthesis would not be viable for partial CH_4 oxidation.

^{27}Al MAS NMR was used to show the substitution of Al^{3+} into the MFI framework.²⁴ Figure 8 shows the Al MAS NMR spectrum of the seed-assisted samples and the seed reference. A singlet peak at -66 ppm is observed in the spectrum of the seed, corresponding to tetrahedral, framework Al^{3+} species. Singlet peaks are observed in the ^{27}Al MAS NMR spectra of the seed-assisted samples; however, the peak is shifted upfield to -70 ppm. The change in peak position of the tetrahedral unit could be caused by the shielding effect of the paramagnetic Fe^{3+} in the sample. For the purpose of confirming the presence of isomorphous substituted tetrahedral Al^{3+} , the shift is not of concern, however, this would affect quantitative studies. Furthermore, from the MAS NMR spectra, no other Al^{3+} species can be observed in the samples crystallised for 168 and 72 h. There is a shoulder on the peak at -70 ppm in the 24 h sample, which indicates the incomplete crystallisation observed in the *p*XRD pattern (Figure 6).²⁵

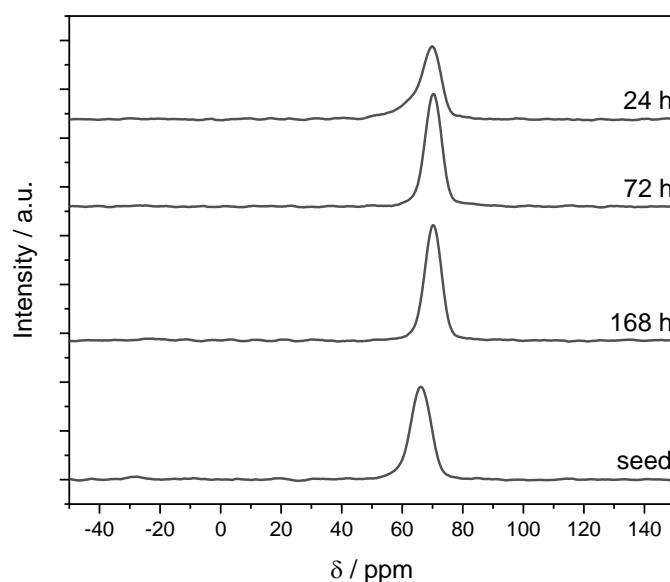


Figure 8 ^{27}Al MAS-NMR Single Pulse experiments of synthesised SA_0.1 w % Fe-ZSM-5 (42) at 210 $^{\circ}\text{C}$ for x h, where x indicates the crystallisation time. HT_0.1 wt% Fe-ZSM-5 (42)_ Na^+ , is provided as a reference.

To determine the speciation of Fe^{3+} within the zeolite lattice, DRUV-vis spectroscopy was used to give a relative distribution of the Fe^{3+} species found at different coordination geometries and environments within the zeolite from the energy of the absorption of the ligand to metal charge transfer bands (LMCT).^{26,27} In the conventional hydrothermal synthesis, approximately 70 % of the Fe absorbed in the region between 200 to 250 nm, which was indicative of tetrahedral, framework $[\text{Fe}(\text{OSi})_4]$ species post synthesis. The remaining species existed as isolated and oligomeric extra framework Fe^{3+} species, as evidenced by the absorptions between 250 and 350 nm.

In Figure 9, the DRUV-vis spectra of the synthesised seed-assisted catalysts are shown along with the spectrum of the hydrothermally prepared HT_0.1 wt% Fe-ZSM-5 (42)_{Na⁺} seed material, which was used to compare the relative Fe^{3+} speciation within the catalysts. Relative to the seed, the samples synthesised for 168 and 72 h are comparable to the Fe^{3+} distribution in the seed material. However, the sample synthesised for 24 h exhibited an additional absorbance at 350 nm, which is indicative of oligomeric Fe^{3+} species. The observation of oligomeric Fe^{3+} species would suggest that the Fe^{3+} has not been fully incorporated into the framework at shorter synthesis times. Incomplete crystallisation of the 24 h sample was also indicated in the *p*XRD pattern (Figure 6), and the DRUV-vis spectra supports this observation.

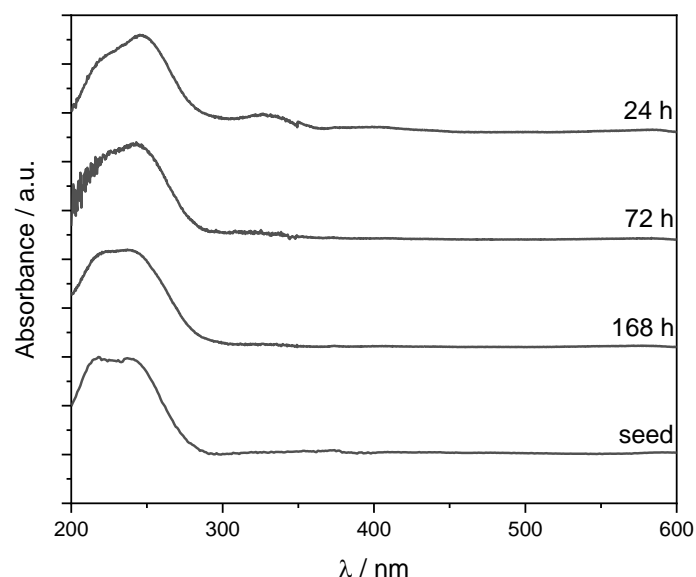


Figure 9 DRUV-vis of synthesised 0.1 wt% Fe-ZSM-5 (42) at 210 °C for *x* h, where *x* indicates the crystallisation time. The seed material, HT_0.1 wt% Fe-ZSM-5 (42)_{Na⁺}, is provided as a reference.

Due to the overlapping of absorption maxima of similar Fe³⁺ species, it can be difficult to differentiate between subtly different species from DRUV-vis spectra alone. The high energy region of the DRUV-vis spectra can be probed selectively using resonance Raman spectroscopy.^{18,28} A laser with wavelength of 266 nm was selected to analyse the synthesised, seed-assisted samples to determine the relative distribution of Fe³⁺ species in the synthesised samples. In Figure 10, a prominent band at $\bar{\nu} = 1600 \text{ cm}^{-1}$ in the spectrum of HT_0.1 wt% Fe-ZSM-5 (42)_AS can be observed that is absent in the spectra of the seed-assisted samples. This is characteristic of C-H vibrations from the TPA cation and indicates the absence of organic material in the samples prepared by seed-assisted methods.²⁹

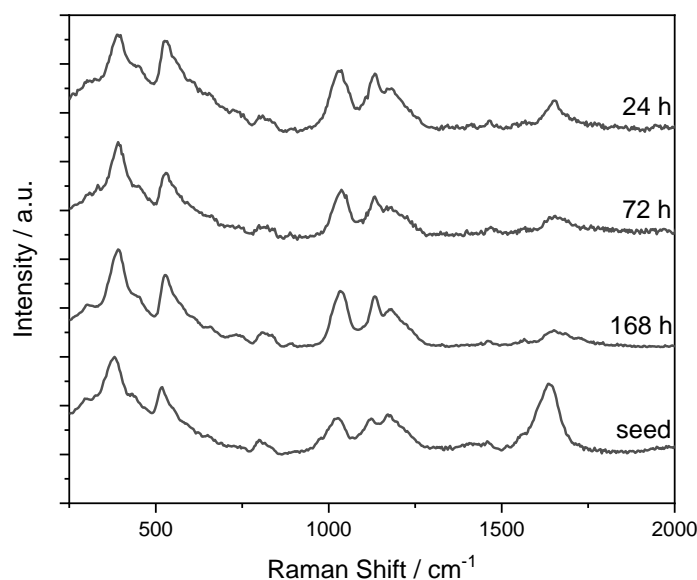


Figure 10 Resonance Raman ($\lambda = 266 \text{ nm}$) of synthesised 0.1 wt% Fe-ZSM-5 (42) at 210 °C for $x \text{ h}$, where x indicates the crystallisation time. The seed material, HT_0.1 wt% Fe-ZSM-5 (42)_Na⁺, is provided as a reference.

Table 2 Relative intensities of Raman-active features of synthesised 0.1 wt% Fe-ZSM-5 (45)_AS, prepared by seed assisted method at 200 °C as a function of crystallisation time, as calculated from the ratio of I_R / I_{380} determined from the resonance Raman spectra (266 nm).

Crystallisation t / h	520 cm^{-1}	1020 cm^{-1}	1120 cm^{-1}	1165 cm^{-1}
168	0.74	0.57	0.52	0.52
72	0.67	0.49	0.44	0.33
24	0.94	0.62	0.60	0.45
Seed	0.69	0.38	0.36	0.42

Furthermore, a large band centred at $\bar{\nu} = 380 \text{ cm}^{-1}$ and a small broad feature at 800 cm^{-1} arise from stretching vibrational modes of Si-O-Si of the 5-membered rings (5MR) in crystalline MFI.²⁹ Resonant features are observed in each of the samples at $\bar{\nu} = 520, 1020, 1120$ and 1165 cm^{-1} that have previously been assigned as various vibrational modes of framework Fe^{3+} .¹⁸ The relative intensities of these stretching frequencies were calculated relative to the intensity of the $\bar{\nu} = 380 \text{ cm}^{-1}$ band to determine the extent of Fe^{3+} speciation after crystallisation, and the RI values given in Table 2. Interestingly, the relative intensity of the Fe resonant features of SA_0.1 wt% Fe-ZSM-5 (42)_24h are greater than those at longer crystallisation times, yet the relative proportion of framework species, observed in the DRUV-vis spectrum, is lower in the 24 h sample. Evidence suggests that the intensity of the Si-O-Si stretch at 380 cm^{-1} correlates to the size of the silicate rings in the framework and this can be related to relative crystallinity of the sample that was calculated from *p*XRD patterns.³⁰ As the sample spectra were normalised to the feature at 380 cm^{-1} , it is possible that the RIs of the Fe^{3+} bands could be affected. Therefore, quantification of the resonance Raman spectra is not without limitations, which should be taken into consideration when comparing samples of differing crystallinity. It should be noted that, when the relative crystallinity is 1.0, the relative intensities of the Fe^{3+} Raman bands can be used to approximate the distribution of Fe^{3+} species in each sample. For example, the samples in Chapter 3 were assumed to be fully crystalline, thus it was possible to compare the relative intensities of the Fe^{3+} bands.

The trend of the RI values of the 168 and 72 h samples are in agreement with the data from the DRUV-vis, as the RI of framework species in the SA_0.1 wt% Fe-ZSM-5 (42)_168h reflects the absorbance of λ_1 . From the data gathered from the AS samples, the AS sample crystallised for 168 h at $200 \text{ }^\circ\text{C}$ was comparable to the seed material prior to calcination, which indicates that Fe^{3+} has been successfully incorporated into the framework. It cannot be concluded from comparable DRUV-vis spectra alone whether the seed-assisted catalysts are comparatively active for CH_4 oxidation and catalytic testing of the samples are needed for comparison. Yet, a synthetic procedure that omits the use of an OSDA to form a crystalline MFI structure, with isomorphous substituted Fe^{3+} , has been shown.¹⁵

5.3 Catalytic Activity in Seed-Assisted 0.1 wt% Fe-ZSM-5

5.3.1 Reactant Diffusion

In Chapter 3, the conventionally synthesised Fe-ZSM-5 was inactive for CH₄ oxidation prior to post-synthetic modifications. Though, there is uncertainty whether this is because of diffusion limitations, due to the presence of TPA cations in the micropore network preventing access to internally located active sites, or whether the application of high temperatures used to remove TPA⁺ results in a change in Fe³⁺ speciation. There was spectral evidence in Chapter 3 that suggested that the onset of partial CH₄ oxidation activity was due to the extraction of framework Fe³⁺ to extra framework positions, however the presence of TPA⁺ in the AS material meant that diffusion limitations could not be ruled out. Thus, the development of a novel, OSDA-free synthesis of Fe-ZSM-5 allows study of the onset of catalytic activity in these catalysts for partial CH₄ oxidation following high-temperature treatment. Through better understanding of how the active Fe³⁺ site forms, more efficient catalysts can be designed.

To eliminate mass diffusion limitations in the seed-assisted catalysts, TGA and N₂ physisorption measurements were made to establish that the seed-assisted materials are free of organic molecules in the pore networks. The TGA curves of hydrothermally synthesised Fe-ZSM-5 and seed-assisted Fe-ZSM-5 are shown in Figure 11. The TGA curves are plotted separately to account for the differences in scale. At 100-300 °C. in HT_0.1 wt% Fe-ZSM-5 (42)_AS_120h, 2% of mass loss occurs, which corresponds to the desorption of H₂O. A smaller mass loss is observed in the same temperature region for the seed-assisted sample (0.02%). The differences in water content arise from differences in hydration of the sample that occur over time.³¹ A greater mass loss (10%) is observed at 400 - 460 °C in the hydrothermally prepared sample, which represents the loss of the TPA⁺ from the zeolite micropores. An equivalent mass loss was not observed in the seed-assisted analogue (Figure 11). Furthermore, N₂ physisorption data (Table 3) showed that the apparent surface area (SA_{app}) and pore volume of HT_0.1 wt % Fe-ZSM-5 (42)_AS_120h is 33.4 m g⁻¹ and 0.032 cc g⁻¹ respectively. These values were lower than expected for a microporous zeolite, and the percentage mass loss corresponds to the loss of TPA template. The SA_{app} and pore volumes are far greater in the synthesised SA_0.1 wt % Fe-ZSM-5 (42)_AS_168h, which indicates that the micropores are free of OSDA and that reactant diffusion within the seed-assisted samples would not be limited by mass-diffusion.

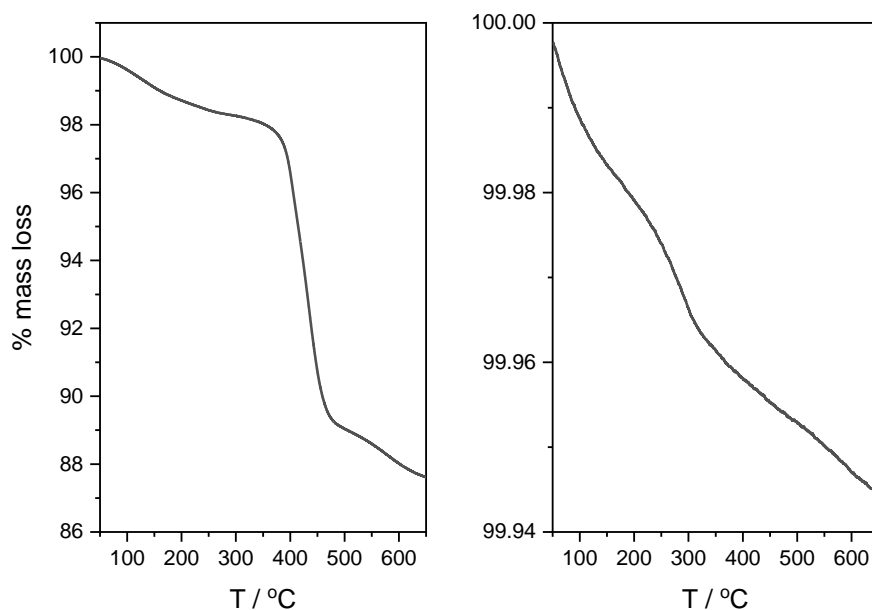


Figure 11 Left; TGA curve of HT_0.1 wt% Fe-ZSM-5 (42)_AS. Right; TGA curve of SA_0.1 wt % Fe-ZSM-5 (42)_AS_168 h. Samples were heated from 50 °C to 650 °C under an atmosphere of air.

Table 3 N₂ physisorption data of 0.1 wt% Fe-ZSM-5 (42)_AS prepared by hydrothermal synthesis and seed-assisted methods. ^a Surface area was calculated from the BET equation that was modified to account for the microporous nature of the samples. ^b Micropore volume was calculated from NLDFT kernel file at 77 K.

Catalyst	SA_{app}^a / m² g⁻¹	Micropore volume^b / cc g⁻¹
HT_0.1 wt% Fe-ZSM-5 (42)_AS_120h	33.4	0.032
SA_0.1 wt% Fe-ZSM-5 (42)_AS_168h	329.1	0.147

The low mass loss observed in the TGA and the larger micropore volume calculated for the seed-assisted sample indicates that mass diffusion restrictions are not a limiting factor in partial CH₄ oxidation. The next section will correlate catalytic activity with the preparation of the catalyst.

5.3.2. Changes in Fe³⁺ Speciation as a Function of Temperature

As discussed in the previous section, mass diffusion limitations, due to presence of OSDA, were eliminated. In the absence of OSDA, the as synthesised catalysts can be tested for partial CH₄ oxidation activity to study whether the change in Fe³⁺ speciation as a function of

temperature affects catalytic performance. Synthesised seed-assisted materials were subjected to various temperatures for 2 h in static air, to afford SA_0.1 wt% Fe-ZSM-5 (42)_ZZ, where ZZ denotes the temperature of the heat-treatment. The sample crystallised for 168 h was chosen as the parent sample to eliminate differences in the starting material. Also, this work preceded the optimisation work performed above, so it was not known that the 72 h sample was more crystalline. As the seed-assisted samples did not contain any OSDA, as indicated by the TGA in Figure 11, longer heat treatment times were not deemed to be necessary. The samples were tested for partial CH₄ oxidation following an alternative testing protocol. The desired mass of catalyst (2.4 mmol Fe) was weighed into a borosilicate liner and concurrently charged with 8 mL DI H₂O. The liner was placed in the reactor vessel and the reactor sealed and then purged three times with N₂ to remove atmospheric gases from the vessel. The reactor was heated to 50 °C at a stirring rate of 1500 rpm. Once the reactor has reached the temperature set point, a HPLC pump was utilised to deliver 50 wt % H₂O₂ directly into the reactor vessel at a rate of 2 mL min⁻¹ for 1 min. Afterwards, the reactor was charged with CH₄ (10 bar) and the reaction was started. After 15 min, the stirring was stopped, and the reactor was left to cool in an ice-bath to < 20 °C over a period of 15 min. The gas phase was recovered and gaseous products (CO₂) quantified by GC-FID, and the liquid products (CH₃OH, CH₃OOH, HCOOH) were quantified by ¹H NMR, against calibrated standards.

Figure 12 shows the effect of heat treatment temperature of the seed assisted samples on the catalytic performance of partial CH₄ oxidation. Prior to subjecting the sample to heat treatment, the AS form of the catalyst was relatively inactive (TOF = 2 h⁻¹). A small amount of CH₃OH and CH₃OOH were observed by ¹H NMR, so the sample is not completely inactive and some of the Fe³⁺ must be present as extra framework species. The DRUV-vis spectra of the AS samples (Figure 9) does show a proportion of species in the extra framework position. Following heat treatment of the samples, the TOF increases. At 550 °C, there is an increase in catalytic performance of 76 h⁻¹. Further increasing the heat treatment temperature up to 900 °C results in a 7-fold increase in TOF to 551 h⁻¹. The increase in TOF indicates that increasing the temperature of sample heat treatment results in an increase in catalytic activity. The increase in activity suggests that higher temperatures are necessary to activate the catalysts; however, the selectivity to the desired product, CH₃OH, decreased at higher heat treatment temperatures. A plot of the sum of oxygenated products (CH₃OH, CH₃OOH, HCOOH and CO₂) versus selectivity to kinetic oxidation products (CH₃OOH and CH₃OH) is plotted in Figure 13. This plot shows that, as the total μmol of oxygenated products increases, the selectivity towards the

desired products decreases. HCOOH and CO₂ are thermodynamically more favourable products, thus the equilibrium will be shifted in favour of their formation at higher yields of product.³²

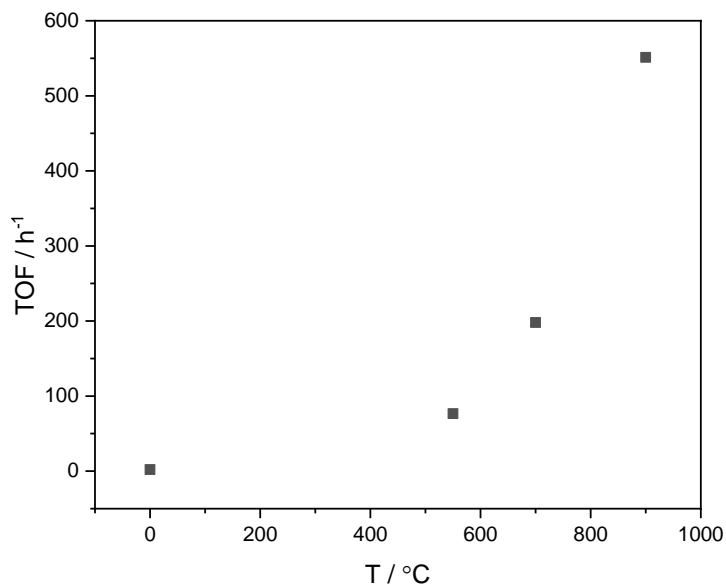


Figure 12 Catalytic performance of SA_0.1 wt % Fe-ZSM-5 (42) as a function of heat treatment temperature. Heat treatments were performed at the set temperature for 2 h. Catalytic performance is reported as TOF.

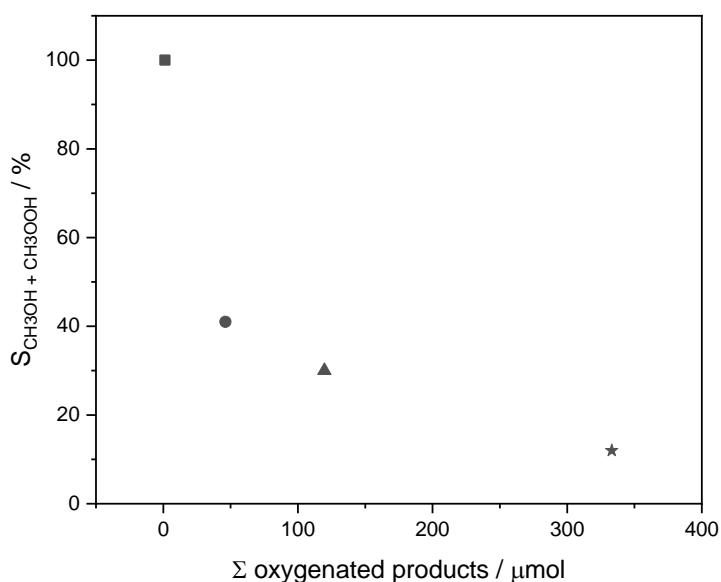


Figure 13 Selectivity to CH₃OH + CH₃OOH (primary oxidation products) versus sum of the oxygenated products. The symbols indicate the temperature of the heat treatment of SA_0.1 wt% Fe-ZSM-5 (42); Square, no heat treatment; Circle, 550 °C; Triangle, 700 °C, and; Star, 900 °C.

To determine whether the reaction was heterogeneously catalysed by the seed-assisted catalysts, a hot-filtration study of SA_0.1 wt% Fe-ZSM-5 (42) catalysed partial CH₄ oxidation was performed.³³ Hot-filtration experiments can provide information on whether or not the catalyst leaches active components under the reaction conditions, thus it is possible to determine whether the reaction is heterogeneously catalysed, or metal has leached out of the catalyst and homogeneous catalysis is occurring.

The reaction was performed as described in Section 5.4, and the sample SA_0.1 wt% Fe-ZSM-5 (42)_550 was used to perform the hot filtration study. After 5 minutes, the stirring was stopped, and the reactor was left to cool to < 20 °C. The reaction was cooled down to prevent accidental release of volatile products at higher temperatures, which would compromise the integrity of the results. The reaction mixture was filtered to remove the catalyst from the reaction mixture and the aqueous component was returned to the reactor and heated back up to 50 °C and charged with CH₄ (10 bar). The reaction was left to run for a further 10 minutes with agitation. The gas phase products was quantified by GC-FID and the aqueous phase was determined by ¹H NMR, against calibrated standards. The error was calculated as 5,7 % from repeating the 15 minute reaction three times and calculating the average and standard deviation. A time-online profile for the hot-filtration study, and a standard minute reaction, is shown in Figure 14. After 5 minutes online, the sum of oxygenated products was 40 μmol of product in both reaction profiles. The reaction continued when the catalyst was not removed from the reaction; however, when the catalyst was filtered out of the reaction mixture, the sum of oxygenated products did not increase once the aqueous phase was returned to the reactor following filtration of the solid catalyst. As the measured amount of product did not increase after filtration, it can be concluded that the reaction is heterogeneously catalysed. Even though homogenous reaction was ruled out, it cannot be stated whether the catalyst was leached under the reaction conditions, as no elemental analysis of the reaction mixture was performed. Understanding whether the catalyst leaches under reaction conditions would help predict the stability of the catalyst over time.

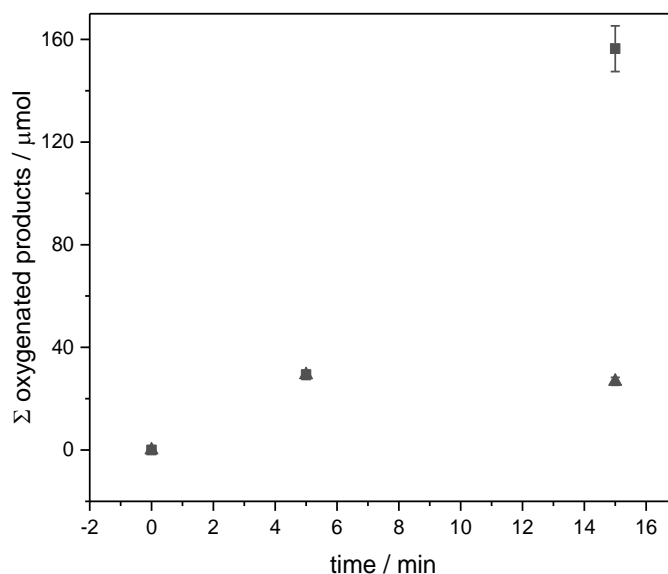


Figure 14 Time-online experiment of methane oxidation at 50 °C, with SA_0.1 wt % Fe-ZSM-5 (42)_550 (squares) and SA_0.1 wt % Fe-ZSM-5 (42)_550 hot-filtration experiment (triangles). Reaction conditions: T = 50 °C, stirring = 1500 rpm, 135 mg catalyst, 10 bar CH₄, 0.5 M H₂O₂, 10 mL H₂O. Liquid phase products were quantified by ¹H NMR and gas phase products quantified by GC-FID. Error bars were calculated from the error from 3 replicate experiments and were calculated at 5.7 %.

Here, it has been shown that SA_0.1 wt % Fe-ZSM-5 (42)_AS is inactive for methane oxidation, even when the reactants are free to diffuse within the catalyst, thus it can be concluded that activation of the framework Fe³⁺ species is required. To understand the differences in activity and selectivity trends of the samples heat-treated at different temperatures, various spectroscopic methods were employed to determine differences in Fe³⁺ speciation that might indicate a primary active species for CH₄ oxidation.

5.3.3. Spectroscopic Evidence for Change in Fe³⁺-Speciation as a Function of Heat-Treatment Temperature

To rationalise the change in catalytic performance that was observed upon increasing the temperature of heat treatment, Fe selective spectroscopic techniques were used. The DRUV-vis spectra of the heat-treated seed-assisted samples are plotted in Figure 15.

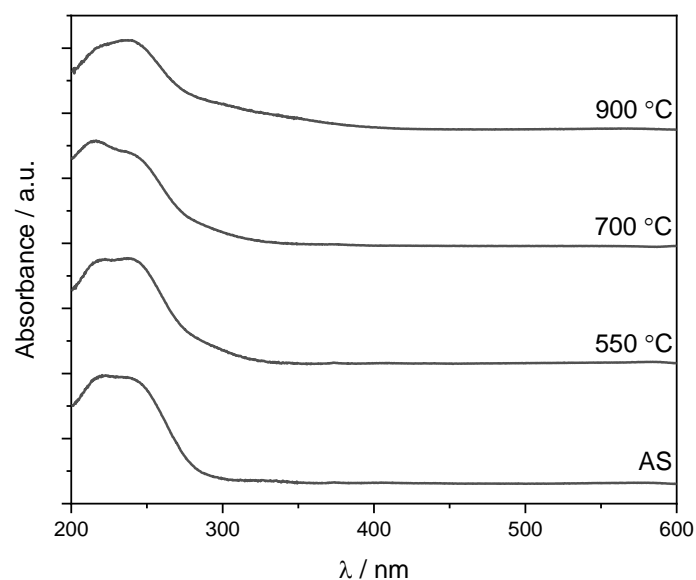


Figure 15 DRUV-vis of SA_0.1 wt% Fe-ZSM-5 (42)_ZZ, where ZZ denotes the temperature of heat-treatment. The AS sample is provided as a reference.

Following heat treatment at 550 °C, a red-shift was observed, with the maximum at 300 nm increasing in intensity. This suggests that the extraction of framework Fe³⁺ occurs after the samples were exposed to elevated temperatures. At 900 °C, an additional absorbance, with a maximum at 350 nm that was not observed following heat treatment at 550 and 700 °C. The absorbance at 350 nm has been attributed to the presence of clustered and oligomeric Fe³⁺ species that lie in the void-spaces of the MFI pore network.^{26,27,34} As the 350 nm peak is not observed in the other samples, it is feasible to correlate the appearance of this feature with poor selectivity to the desired reaction product.

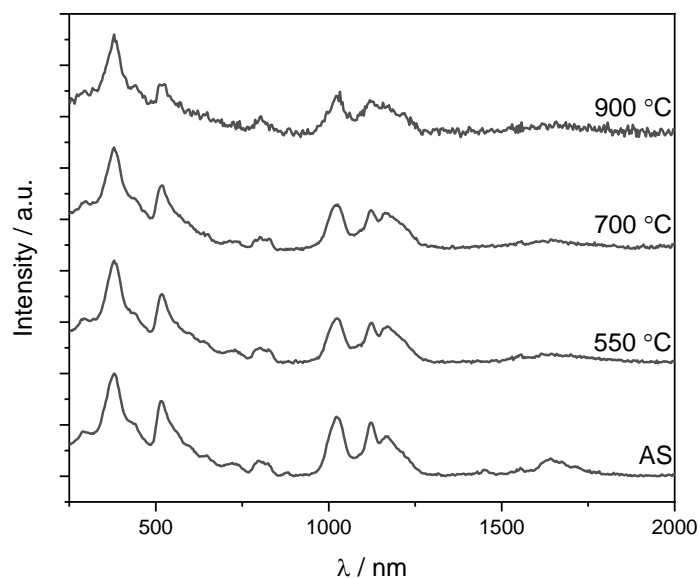


Figure 16 Resonance Raman spectra ($\lambda = 266$ nm) of SA_0.1 wt % Fe-ZSM-5 (42)_ZZ, where ZZ denotes the temperature of heat-treatment. The AS sample is provided as a reference.

Additional information on the extent of changes in Fe^{3+} was provided by utilising Resonance Raman at two different laser wavelengths to probe the high-energy absorbances of the Fe^{3+} species.^{18,28} In Figure 16 ($\lambda = 266$ nm), bands arising from symmetrical vibrations of 5- and 6MR rings in the MFI framework type were observed in each of the samples both before and after heat-treatment, which could indicate that the framework is stable following high temperature treatment.²⁹ When the temperature of heat treatment increased, the band centred at 520 cm^{-1} , which has previously been assigned to a symmetric Fe-O-Si stretch, decreases in relative intensity, when compared to the AS sample. It has previously been thought that the stretch at 520 cm^{-1} correlates to framework Fe^{3+} , thus the decrease in relative intensity in more active samples is consistent with this statement.¹⁸ Further, the decrease in Raman band intensity at 520 cm^{-1} correlates with the decrease in the λ_1 absorbance maximum observed in the DRUV-vis spectra, shown in Figure 15.

Table 4 Relative intensities of Raman active bands in SA_0.1 wt% Fe-ZSM-5 (42)_ZZ, where ZZ denotes the temperature of heat treatment, as calculated from the ratio of I_R/I_{380} determined from the resonance Raman spectra (266 nm). The AS sample is provided as a reference.

Temperature (°C)	520 cm ⁻¹	1020 cm ⁻¹	1120 cm ⁻¹	1165 cm ⁻¹
550	0.67	0.44	0.39	0.36
700	0.63	0.45	0.38	0.36
900	0.50	0.40	0.35	0.30
AS	0.74	0.57	0.52	0.38

Furthermore, the observed decrease in relative intensity of the 520 cm⁻¹ stretch correlates with the increase in catalytic activity at higher heat treatment temperatures.¹⁸ Consistent with observations made on resonance Raman in previous chapters, it would seem that the resonance enhanced feature at 520 cm⁻¹ arises from the presence of tetrahedral [Fe(OSi)₄] units in the MFI framework.²⁸ Further decreases in the RI of the Raman bands at 1020, 1120 and 1165 cm⁻¹, which have been assigned as asymmetric stretches of framework Fe³⁺ species,¹⁸ are seen in the heat-treated samples (Table 4). The decrease in relative intensity of framework Fe³⁺ species in the resonance Raman are again consistent with observations made from the DRUV-vis spectra (Figure 15).²⁷ Similar observations were made in Chapter 3, where the initial calcination step of the hydrothermally synthesised samples to remove ODSA resulted in a decrease in relative intensities seen in the Raman spectra at 266 nm, of the resonance-enhanced bands at 520, 1020, 1120 and 1165 cm⁻¹.

The heat-treated seed-assisted samples were additionally analysed by Raman spectroscopy, using a laser with a wavelength of 325 nm. It was previously observed in Chapter 2 that many of the Raman-active Fe³⁺ features were no longer resonance-enhanced at longer wavelengths, as the energy of the transition no longer aligned with the energy of the laser. Thus, the intensity of the bands, relative to the Si-O-Si stretches at 380 and 800 cm⁻¹ is reduced. The Raman spectra shown in Figure 17 demonstrates the loss of the feature at $\bar{\nu} = 520$ cm⁻¹ in the spectra at 325 nm, which was very intense in the 266 nm spectrum. As the stretching frequency associated with this shift is believed to arise from tetrahedral, framework species, absorbing at < 250 nm, the energy of the transition no longer matches the wavelength of the laser and no resonant effects can be observed. Comparison of the Raman spectra at two wavelengths shows a difference in the absolute peak positions, indicating that different Raman active Fe³⁺ species

can be observed. This suggests that the nature of the absorbing species in Fe-MFI is more complex than initially thought.³⁴

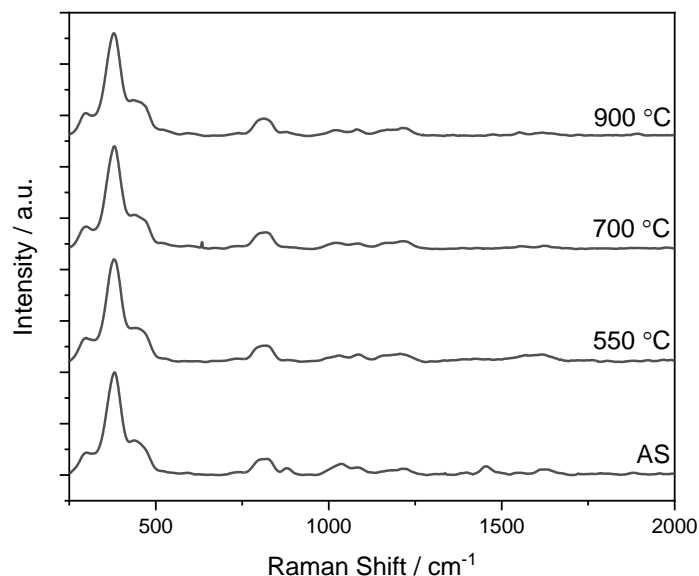


Figure 17 Resonance Raman spectra ($\lambda = 325$ nm) of SA_0.1 wt% Fe-ZSM-5 (42)_ZZ, where ZZ denotes the temperature of heat-treatment. The AS sample is provided as a reference.

Table 5 Relative intensities of Raman active bands in SA_0.1 wt% Fe-ZSM-5 (42)_ZZ, where ZZ denotes the temperature of heat treatment, as calculated from the ratio of I_R / I_{380} determined from the resonance Raman spectra (325 nm).

Temperature (°C)	1020 cm^{-1}	1081 cm^{-1}	1166 cm^{-1}	1211 cm^{-1}
550	0.062	0.071	0.064	0.077
700	0.061	0.054	0.058	0.076
900	0.057	0.064	0.055	0.076
AS	0.111	0.076	0.037	0.061

The relative intensity of the Fe-bands in the Raman spectra at 325 nm were calculated relative to the $\bar{\nu}$ Si-O-Si stretch and given in Table 5. The relative intensity of the shifts at 1020 and 1081 cm^{-1} decreases with temperature, which correlates with the observed trend from the 266 nm Raman spectra. Therefore, it can be assumed that these features are related to framework Fe^{3+} ; however, as heat treatment temperature increases, the bands at 1166 and 1211 cm^{-1} also increase in intensity. The bands at 1166 and 1211 cm^{-1} suggests that a new species is observed

at 325 nm, which may relate to the observed catalytic activity in the different samples. As seen in Figure 15, the proportion of oligomeric species increases after heat treatment at 900 °C, thus the bands observed in the 325 nm Raman spectra may relate to that. Further, the wavelength of the absorbance in the DRUV-vis is approximately 350 nm, which is closer in energy to the 325 nm laser. As discussed in Chapter 3, resonance enhancement of Raman signals is related to the size (ΔE) of the electronic transition of the species and the wavelength of the laser, thus it is feasible these species are better observed when using a longer wavelength laser. More conclusive evidence should be gathered to better characterise the active feature in ZSM-5 and molecular modelling studies should be used to determine a theoretical structure for the species that are resonant at 1081 and 1211 cm^{-1} .¹⁸ Even though the Raman observations were not conclusive to the identification of an active species, the spectra suggests that temperatures greater than 550 °C are required to activate isomorphously substituted Fe-ZSM-5, when made by seed-assisted methods, for partial CH_4 oxidation. Further, the results discussed here indicates that the speciation of active species Fe^{3+} for CH_4 oxidation is quite complex. The appearance of two additional bands at 1166 and 1211 cm^{-1} in the Raman spectra at 325 nm, which correlate with an increase in catalytic activity, could be related to extra framework species that are structurally distinct from one another.

5.4. Conclusion

Herein, it has been shown that Fe-ZSM-5 can be synthesised in the absence of tetrapropylammonium hydroxide by using seeding techniques.¹⁵ The presence of seed material was deemed necessary, as amorphous silica was afforded in the absence of seed and template in the initial aluminosilicate gel. The crystallinity of the seed-assisted materials was confirmed by *p*XRD and isomorphous substitution of Al^{3+} and Fe^{3+} was demonstrated by ²⁷Al MAS NMR and DRUV-vis and resonance Raman spectroscopy. Unfortunately, the rate of crystallisation was slower than that of the hydrothermal Fe-ZSM-5 synthesis, even at increased crystallisation temperature, and few optimisation studies were performed to develop the seed-assisted material, and further refinements should be made by performing additional experiments. For example, it is not known how the particle size of the seed material affects the crystallinity, size and morphology of the Fe-ZSM-5 daughter materials and should be studied to understand the relationship between the seed and the seed-assisted material.¹⁰

Furthermore, it has been demonstrated that SA_0.1 wt% Fe-ZSM-5 (42), in the absence of a heat treatment step, is inactive for partial CH_4 oxidation. Surface area and pore volume

measurements showed that the synthesised form of the seed-assisted material had no residual OSDA within the micropores of the synthesised, seed-assisted samples, yet the synthesised samples were inactive for methane oxidation. To investigate the effect of the heat-treatment on Fe-speciation, a study of the heat treatment step at various temperatures was performed. It was observed by DRUV-vis and resonance Raman spectroscopy that Fe³⁺ speciation within the MFI framework changed as a function heat-treatment temperature. The greater the temperature, the greater the proportion of extra framework Fe³⁺ species were observed, which has been attributed to increased catalytic activity for methane oxidation.¹⁸ The observation was supported by catalytic testing of the seed-assisted samples under methane oxidation conditions, where the proportion of extra framework species correlated to an increase in TOF. An increase in heat treatment temperature resulted in poorer methanol selectivity. At temperatures greater than 700 °C, the proportion of oligomeric Fe³⁺ clusters and Fe oxides increased, as observed by DRUV-vis spectroscopy, relative to the amount of extra framework Fe³⁺ that might correlate to the decrease in selectivity to methanol. The formation of Fe oxides could lead to unselective formation of hydroxyl radicals that would lead to over-oxidation of oxidation products.³⁵ To confirm the theory, radical scavenger experiments should be run, to eliminate the possibility of unselective radical processes occurring in the reaction solution. *In-situ* DRUV-vis spectroscopic studies during the heat treatment of Fe-ZSM-5 catalyst activation should be performed to record *in-situ* monitoring of the change of Fe³⁺ speciation as a function of heat treatment temperature, which would allow the heat treatment temperature to be controlled to maximise catalytic activity and methanol selectivity of the catalysts.

5.5. References

1. E. M. Flanigen, J. M. Bennett, R. W. Grose, J. P. Cohen, R. L. Patton, R. M. Kirchner and J. V. Smith, *Nature*, 1978, 271, 512-516.
2. S. Jin, Z. Feng, F. Fan and C. Li, *Catal. Letters*, 2015, 145, 468–481.
3. J. Kuhn, J. Gascon, J. Gross and F. Kapteijn, *Micro Meso Mater.*, 2009, 120, 12-18.
4. H. Lee, S. I. Zones and M. E. Davis, *Nature*, 2003, 425, 385-388.
5. S. Goel, S. I. Zones and E. Iglesia, *Chem. Mater.*, 2015, 27, 2056–2066.
6. E. G. Derouane, S. Determmerie, Z. Gabelica and N. Blom, *Appl. Catal.*, 1981, 1, 201-224.
7. M. E. Davis, *Chem. Mater.*, 2014, 26, 239-345.
8. C. S. Cundy and P. A. Cox, *Chem. Rev.*, 2003, 103, 663–701.
9. J. Grand, H. Awala and S. Mintova, *CrystEngComm*, 2016, 18, 650–664.

10. K. Iyoki, K. Itabashi and T. Okubo, *Micro Meso Mater.*, 2014, 189, 22–30.
11. R. D. Edelman, D. V. Kudalkar, T. Ong, J. Warzywoda and R. W. Thompson, *Zeolites*, 1989, 9, 496-502.
12. K. Suzuki and T. Hayakawa, *Micro Meso Mater.*, 2005, 77, 131-137.
13. G. Reding, T. Mäurer and B. Kraushaar-Czarnetzki, *Micro Meso Mater.*, 2003, 57, 83-92.
14. G. Majano, A. Darwiche, S. Mintova and V. Valtchev, *Ind. Eng. Chem. Res.*, 2009, 48, 7084–7091.
15. M. H. Nada and S. C. Larsen, *Micro Meso Mater.*, 2017, 239, 444–452.
16. N. Kosinov, C. Liu, E. J. M. Hensen and E. A. Pidko, *Chem. Mater.*, 2018, 30, 3177–3198.
17. A. Zecchina, M. Rivallan, G. Berlier, C. Lamberti and G. Ricchiardi, *Phys. Chem. Chem. Phys.*, 2007, 9, 3483–3499.
18. K. Sun, F. Fan, H. Xia, Z. Feng, W. Li and C. Li, *J. Phys. Chem. C*, 2008, 112, 16036–16041.
19. F. Fan, Z. Feng and C. Li, *Acc. Chem. Res.*, 2010, 43, 378-387.
20. C. Hammond, M. M. Forde, M. H. Ab Rahim, A. Thetford, Q. He, R. L. Jenkins, N. Dimitratos, J. a Lopez-Sanchez, N. F. Dummer, D. M. Murphy, A. F. Carley, S. H. Taylor, D. J. Willock, E. E. Stangland, J. Kang, H. Hagen, C. J. Kiely and G. J. Hutchings, *Angew. Chem. Int. Ed. Engl.*, 2012, 51, 5129–33.
21. M. M. J. Treacy and J. B. Higgins, *Collection of Simulated XRD Powder Patterns for Zeolites*, 2007, Elsevier.
22. S. C. Larsen, *J. Phys. Chem. C*, 2007, 111, 18464-18474.
23. M. Zaarour, B. Dong, I. Naydenova, R. Retoux and S. Mintova, *Micro Meso Mater.*, 2014, 189, 11–21.
24. J. Dedecek, V. Balgová, V. Pashkova, P. Klein and B. Wichterlová, *Chem. Mater.*, 2012, 24, 3231–3239.
25. Z. P. Miladinović, J. Zakrzewska, B. T. Kovačević and J. M. Miladinović, *Micro Meso Mater.*, 2014, 195, 131-142.
26. J. Pérez-Ramírez, J. C. Groen, A. Brückner, M. S. Kumar, U. Bentrup, M. N. Debbagh and L. A. Villaescusa, *J. Catal.*, 2005, 232, 318–334.
27. M. S. Kumar, M. Schwidder, W. Grünert and A. Brückner, *J. Catal.*, 2004, 227, 384–397.
28. C. Hammond, I. Hermans and N. Dimitratos, *ChemCatChem*, 2015, 7, 434–440.

29. P. K. Dutta and M. Puri, *J. Phys. Chem.*, 1987, 91, 4329–4333.
30. Y. Yu, G. Xiong, C. Li and F. S. Xiao, *Micro Meso Mater.*, 2001, 46, 23–34.
31. V. R. Choudhary and S. G. Pataskar, *Thermochim. Acta*, 1986, 97, 1–10.
32. A. A. Latimer, A. Kakekhani, A. R. Kulkarni and J. K. Nørskov, *ACS Catal.*, 2018, 8, 6894–6907.
33. R. A. Sheldon, M. Wallau, I. W. C. E. Arends and U. Schuchardt, *Acc. Chem. Res.*, 1998, 31, 485–493.
34. C. Hammond, N. Dimitratos, J. A. Lopez-sanchez, R. L. Jenkins, G. Whiting, S. A. Kondrat, M. Hasbi, M. M. Forde, A. Thetford, H. Hagen, E. E. Stangland, J. M. Moulijn, S. H. Taylor, D. J. Willock and G. J. Hutchings, *ACS Catal.*, 2013, 3, 1835–1844.
35. C. Hammond, R. L. Jenkins, N. Dimitratos, J. A. Lopez-Sanchez, M. H. Ab Rahim, M. M. Forde, A. Thetford, D. M. Murphy, H. Hagen, E. E. Stangland, J. M. Moulijn, S. H. Taylor, D. J. Willock and G. J. Hutchings, *Chem. - A Eur. J.*, 2012, 18, 15735–15745.

Chapter 6. Conclusions and Pertaining Challenges

6.1. Conclusions

At the outset of this PhD thesis, in Chapter 1, the aims of this project were set out to investigate the effect of Fe-ZSM-5 catalyst composition and preparation on the Fe³⁺ speciation within the catalyst and how this impacts partial CH₄ oxidation catalytic performance.

6.1.1. Chapter 3

In Chapter 3, several observations were made regarding the performance Fe-ZSM-5 for catalytic oxidation of CH₄ as a result of the catalyst preparation. Firstly, both Al³⁺ and Fe³⁺ are crucial for catalytic performance; however, Fe-free ZSM-5 was inactive, indicating that Al³⁺ is not involved in the oxidation pathway. Rather, Al³⁺ acts as a structural promoter of Fe³⁺. More specifically, samples were most active at low Fe loadings (0.1 wt %); catalytic activity decreased at Fe loadings greater than 0.25 wt %. It should be noted that these were nominal values, rather than experimentally determined values. Elemental analysis, such as inductively coupled plasma-mass spectrometry (ICP-MS), of the samples should be performed to quantify the actual Fe and Al contents of the catalyst, which may affect the calculated TOF (TOF is defined as (mol product formed)/(mol Fe in catalyst).(time)). If the nominal amount was not incorporated into the framework during the hydrothermal synthesis, then this would not be reflected in the TOF and comparisons might not truly represent the observed catalytic trends.

Through the data given in Chapter 3, it was stipulated that the drop in TOF at higher nominal Fe loadings was due to a higher proportion of clustered spectator Fe-sites, which were observed by DRUV-vis spectroscopy. This meant that a lower percentage of Fe³⁺ species were located in extra framework positions, which have been stipulated to be the active species.^{1,2} It is possible that when Fe loading exceeds a defined quantity, the probability of individual Fe atoms being in proximity increases, which can lead to the formation of Fe³⁺ oligomers and oxide clusters.

Due to the implications of H₂O₂ decomposition on the efficiency of the reaction pathway, studies were performed to investigate the effect of catalyst composition on the rate of H₂O₂. The trends reported for the decomposition of H₂O₂ followed a similar trend to that reported for partial CH₄ oxidation; as the Fe content of the catalyst increased, the TOF decreased. The implication here is that partial CH₄ oxidation is dependent on prior activation of H₂O₂. Prior activation of H₂O₂ has previously been proposed by Hammond *et al.*, where it was suggested

that H₂O₂ is initially activated by the active Fe³⁺ species, to form a reactive Fe⁴⁺-oxo species, which can activate the inert C-H of CH₄.¹ It was not thought that the process was radical mediated, however a radical process could have been ruled out by performing radical scavenging studies. Radical scavenging studies would have provided additional evidence to the reaction mechanism taking place under the reaction conditions. Further, ruling out radical formation in H₂O₂ decomposition experiments performed in Chapter 3, would have provided additional evidence to support existing mechanistic studies.¹

To shorten the preparation of Fe-ZSM-5 for catalytic partial oxidation of CH₄, the effect of each preparation step in the full activation procedure on catalytic performance was investigated at the end of Chapter 3. Using samples with varying SiO₂/Al₂O₃ ratios, the catalysts were tested for CH₄ oxidation activity, as well as being analysed to determine the Fe³⁺ speciation by DRUV-vis and resonance Raman spectroscopy. It was observed that samples with a SiO₂/Al₂O₃ ratio of 42 were active for partial CH₄ oxidation after the OSDA removal step, however, at increasing SiO₂/Al₂O₃ ratios, thus lower Al concentration in the framework, the samples were observed to be relatively inactive following the thermal OSDA removal step. The supporting spectroscopic measurements showed that there were two new maxima at 280 and 320 nm in the DRUV-vis spectra of the active sample, 0.1 wt% Fe-ZSM-5 (42)_{Na}⁺, which were absent in the inactive samples. Previously, maxima at 280 and 320 nm were assigned as extra framework Fe³⁺ species,² which supports the catalytic activity observations made herein. Additionally, resonance Raman was utilised to complement the observations made by DRUV-vis spectroscopy. No new features were observed in either spectra following calcination of the synthesised sample; however a decrease in intensity of the Fe-O-Si vibration at 520 cm⁻¹ was observed in 0.1 wt% Fe-ZSM-5 (42)_{Na}⁺, whereas no major change was observed for 0.1 wt% Fe-ZSM-5 (84)_{Na}⁺. The observed differences in the Fe³⁺ speciation, following the thermal OSDA removal in the different samples, lead to the conclusion that the increased Al concentration within the framework was able to facilitate extraction of inactive, framework Fe³⁺ sites to form active extra framework Fe³⁺ species.

Even though the thermal treatment to remove the OSDA in 0.1 wt% Fe-ZSM-5 (42) results in an increase in catalytic performance, it was not possible to conclude that the heat treatment was necessary to facilitate activation of the catalyst. The presence of the OSDA in the catalyst greatly reduces the micropore volume of the synthesised catalysts, which would prevent reactant diffusion to the active sites located within the zeolite framework. Thus, Chapter 5

looked at the development of an OSDA-free catalyst to discern whether the onset of activity was brought about by changes to the Fe^{3+} speciation.

From the above observations, it can be concluded that Fe-ZSM-5 is most intrinsically active for methane oxidation at low Fe loading (0.1 wt%) and greater Al content ($\text{SiO}_2/\text{Al}_2\text{O}_3 = 42$). Activation of the oxidant is probable, and the above observations imply that reactive hydroxyl species form, leading to the overoxidation of desired reaction products at greater Fe loadings. Furthermore, Fe-ZSM-5 is active for CH_4 oxidation following the thermal OSDA removal step in catalysts with high Al content, and it was assumed ion-exchange and activation were not necessary for catalyst activation. This makes the synthesis of active Fe-ZSM-5 catalysts for oxidation processes more facile and less time-consuming. It will also allow for easier study of the active site speciation by minimising the structural changes that might occur following post-synthetic treatments.

6.1.2. Chapter 4

Another one of the aims of this thesis given in Chapter 1 was to investigate the effect of the catalyst preparation on the catalytic performance of Fe-ZSM-5 for partial CH_4 oxidation. This was started at the end of Chapter 3, where the effect of post-synthetic treatments on the Fe^{3+} speciation and thus, oxidation activity was investigated, with the aim to shorten the overall time it takes to prepare an active material. The hydrothermal synthesis of the as-synthesised form on the catalyst is a long process, which can reduce productivity, which could be a drawback in the uptake of Fe-ZSM-5 for industrial processes, where high productivities are desirable for good economic returns. Therefore, understanding of the kinetic parameters of Fe-ZSM-5 crystallisation can help with reducing synthesis times and therefore improving productivity.

In Chapter 4, it was demonstrated that crystallisation time of 0.1 wt% Fe-ZSM-5 (42) could be reduced from 120 h to 6 h, by increasing the crystallisation temperature to 200 °C, without loss of relative crystallinity, as observed by *p*XRD. Subtle changes in crystallite shape, size and symmetry group of the samples crystallised at shorted crystallisation times were not analysed, thus the effect of particle properties, which can impact catalyst properties, such as size and shape that can affect catalyst performance and accessibility of active sites.³⁻⁵ Moreover, no changes could be observed in the initial Fe^{3+} distribution by DRUV-vis spectra, indicating that the Fe^{3+} had incorporated fully into the MFI framework at the reduced contact time.⁶ At crystallisation times less than 6 h, lower relative crystallinities were observed by *p*XRD, along with the presence of an additional band in the DRUV-vis spectra, indicative of the formation

of oligomeric Fe^{3+} species within the framework. These observations suggested that substitution of the Fe^{3+} precursor into the framework was insufficient at shorter crystallisation times. To further support the conclusion made from the DRUV-vis, inductively coupled plasma (ICP) or X-Ray fluorescence (XRF) studies should be performed to determine the actual Fe content of the synthesised catalysts. If less Fe is present in the crystal post synthesis, then would seem feasible that isomorphous substitution of Fe^{3+} into the T-sites within the MFI framework is a rate limiting factor in Fe-ZSM-5 crystallisation

Further, the crystallisation time could be reduced by changing the crystallisation vessel from stainless-steel autoclaves to stainless-steel tubular reactors. A fully crystalline Fe-ZSM-5 was afforded in 4 h at 175 °C. A reduction in the rate of heat transfer between the heating medium and the gel was thought to reduce the crystallisation time. Moreover, using smaller diameter tubes leads to better heat distribution throughout the gel that evidently resulted in reduced crystallisation times. The crystallisation of Fe-ZSM-5 with lower Al contents resulted in shorter crystallisation periods. For example, 0.1 wt% Fe-silicalite-1 was afforded with 100% crystallinity after 1 h at 175 °C, whereas 0.1 wt% Fe-ZSM-5 (42) required 4 h at 175 °C to afford a fully crystalline material. This indicates that the rate of Fe-ZSM-5 crystallisation is dependent on Al concentration within the initial aluminosilicate gel.

Samples that were shown to be 100% crystalline by *p*XRD were calcined at 550 °C to remove OSDA and subsequently tested for partial CH_4 oxidation. Differences in activity were observed in the calcined samples, along with evident changes in Fe^{3+} speciation in the DRUV-vis and Raman spectra, even though the corresponding spectra of the synthesised samples were comparable. It is possible that changes occur structurally during calcination that affects Fe^{3+} speciation, along with Al^{3+} , which accounts for the observed differences in catalytic activity. Alternatively, the differences in the heat-treated materials may suggest that reduction in crystallisation time affects Al^{3+} and Fe^{3+} siting within the MFI lattice, which was not evident from characterisation of the synthesised materials. The ^{27}Al MAS NMR and DRUV-vis of each sample were comparable, indicating no speciation differences in the parent samples; however, Al^{3+} siting within the structure was not studied here and it has been proposed that Al^{3+} within ZSM-5 frameworks can impact catalytic performance.⁷ If there are differences in Al^{3+} siting within the samples prepared under different crystallisation conditions, then differences in extraction and stabilisation of Fe^{3+} may occur following thermal treatment.⁸

Active oxidation Fe-ZSM-5 catalysts can be synthesised in shorter time frames, yet there are differences in the activated samples that imply that crystallisation mechanism is not analogous. The preliminary results are promising and shows that a continuous regime for the crystallisation of Fe-ZSM-5 could be developed. Continuous processes are seen as an effective way to increase zeolite yields and productivity.⁹

6.1.3. Chapter 5

As alluded to at the end of Chapter 3, thermal removal of the OSDA resulted in an increase in TOF for partial CH₄ oxidation; however, the presence of the OSDA in the synthesised catalyst meant that it was not possible to ascertain whether the lack of reactant diffusion or whether a change in Fe³⁺ speciation brought about by thermal treatment resulted in catalytic activity. To investigate this, a seed-assisted synthesis of Fe-ZSM-5 was developed in Chapter 5. This route employed the use of a seed material, as opposed to the OSDA typically used in zeolite synthesis, to propagate nucleation of the MFI framework.¹⁰ Seeded methods avoided the use of expensive and toxic OSDAs to crystallise the desired zeolite framework and meant that a calcination step is not needed. By developing a seed-assisted method for the synthesis of 0.1 wt% Fe-ZSM-5, it would be possible to rule out diffusion limitations as a reason for inactive as synthesised catalysts. Moreover, *in-situ* spectroscopic observations of the changes of Fe³⁺ speciation in the zeolite lattice would be viable, by minimising interactions and signals that arise from the OSDA.

Based on seeding techniques, where a parent zeolite seed of the desired framework type is added to an aluminosilicate gel prior to crystallisation,¹¹ a novel seed-assisted methodology of preparing 0.1 wt% Fe-ZSM-5 (42) was proposed. To afford a crystalline material, as determined by *p*XRD, the crystallisation temperature was increased along with the crystallisation time, which suggests that seed-assisted crystallisation was slower than OSDA assisted synthesis. The effect of time and temperature on the rate of crystallisation was not fully investigated, and a more comprehensive study of the synthesis parameters should be carried out to determine the kinetics, and better optimise the synthesis. Further, the impact of the crystallite properties of the seed material, such as size and shape, was not related to the crystallite properties of the daughter Fe-ZSM-5 crystals. This should be looked at further, as it has been suggested by Larsen *et al.* that the seed properties can impact the crystallised product.¹¹

Batch reactor testing shows that the synthesised, seed-assisted materials were inactive for CH₄ oxidation and only became active following heat treatment at 550 °C. N₂ physisorption and TGA measurements determined that the pore network of the newly synthesised material was

free of organic material. Thus, it is proposed that the inactivity of the synthesised Fe-ZSM-5 arises from a change in Fe^{3+} speciation, rather than from diffusion limitations of the OSDA-containing Fe-ZSM-5.

It was possible to observe changes to Fe^{3+} speciation in the seed-assisted materials during high-temperature heat-treatments by DRUV-vis and resonance Raman spectroscopy, which could be correlated with observed activity trends. Changes were observed in the DRUV-vis spectra of samples heat-treated at 550 and 700 °C; new maxima were observed at 280 and 320 nm, which are assigned to the LMCT of extra framework Fe^{3+} . In Chapter 3, it was implied that extra framework species are responsible for oxidation activity of Fe-ZSM-5. At temperatures exceeding 900 °C, an increase in absorbance maxima at 450 nm in DRUV-spectra was observed. It was speculated that the increase in proportion of oligomeric and oxidic Fe species resulted in a drop of methanol selectivity. However, this is only a consequential link, and further experimental evidence, along with theoretical modelling studies, should be performed to better understand the evolution of Fe species during thermal treatment.

Herein, it has been demonstrated that hydrothermally synthesised Fe-ZSM-5 is activated by application of elevated temperature, which causes migration of the framework Fe^{3+} species to extra framework positions. Newer, spectator species were observed at greatly elevated temperatures, which was thought to reduce on CH_3OH selectivity and favouring CO_2 and HCOOH formation. Nevertheless, current observations were unable to conclude on the nature of extraction and the structure of the active species that is responsible for CH_4 oxidation. Advanced spectroscopic methods should be used to provide additional evidence for Fe^{3+} speciation within zeolites.

6.2. Pertaining Challenges

6.2.1. Optimisation of Fe-ZSM-5

One of the major questions arising from Chapter 3 pertains to the nature of the active site of Fe-ZSM-5/ H_2O_2 partial CH_4 oxidation. An additional framework Fe^{3+} species was determined from DRUV-vis, yet the true nature of this extra framework was not determined, due to the complexity of the system. Work in the development of the seed-assisted Fe-ZSM-5 (Chapter 5) has allowed the author to explore the active site in more detail, by employing more sophisticated spectroscopic and kinetic methods. However, work is still ongoing in the optimisation and characterisation of seed-assisted Fe-ZSM-5 and will be discussed later in this chapter (Section 6.2.3.).

It was concluded that Al^{3+} was a necessary component of Fe-ZSM-5, though it was shown that it is not implicit in the activation of H_2O_2 and or CH_4 . Thus, it was suggested that Al^{3+} acted as a “structural promoter” of extra framework Fe^{3+} species, providing a stabilising presence for the active Fe species.² However, the mechanism of stabilisation is not well documented. Wichterlova *et al.* previously observed that Al^{3+} siting within a zeolite framework can affect the structural and electronic properties of the zeolite,¹² which implies that Al^{3+} siting could affect the stabilisation of active Fe^{3+} of Fe-ZSM-5. Additionally, there are studies that suggest that the Al^{3+} siting can greatly impact on catalytic performance.¹³ If Al pairs were implicit in the stabilisation of active Fe^{3+} centres, then a good distribution of Al pairs ($\text{Al-O-(Si-O)}_{n=2}\text{-Al}$) within the zeolite would be required for the stabilisation of active site geometry. Therefore, increasing the Al content of the material could increase the probability of forming Al^{3+} pairs in MFI rings that could contribute to the formation of stable, extra framework Fe^{3+} species during calcination of the catalyst. In the current synthesis protocol, it is not known where the Al^{3+} are in the framework. To investigate Al-siting, Co^{2+} titration studies have previously been used along with ^{27}Al MAS-NMR to identify which T-site the Al^{3+} are located within the MFI framework (there are 12 possible T sites in MFI).¹² Understanding of the Al^{3+} siting could be correlated to observations made using Fe-selective spectroscopic techniques, to determine how Al^{3+} siting affects Fe^{3+} speciation. If there is a relationship between Al^{3+} at a given T-site and active Fe^{3+} site, then appropriate crystallisation methods could feasibly be designed that maximise this relationship. Caution must be taken with Fe-zeolites as Fe is paramagnetic and effectively shields the ^{27}Al nuclei from the radiation, thus the signals are dampened.

Furthermore, it is possible that certain CBUs are better at stabilisation of Fe^{3+} centres, thus frameworks with higher CBU density would be more active as the probability of forming the active Fe species is increased.¹⁴ There are 12 crystallographic distinct T-sites in monoclinic MFI, so the data in this thesis does not attribute various Fe^{3+} features with a particular T-site. To harness the catalytic proficiency of this catalyst, it is necessary to understand the effect of T-site location on the formation and stabilisation of active Fe-sites. There are a few ways in which to investigate this. As zeolites are made up of composition building units (CBUs), it might be that T-sites within certain key CBUs are crucial for catalytic activity. For example, Snyder *et al.* compared three different Fe-zeolites for methane hydroxylation in the gas phase (N_2O as the oxidant) and found that zeolites containing a β -6MR motif in the unit cell that were active for methane hydroxylation.¹⁴ It has been proposed that a different Fe^{3+} species is active for the activation and oxidation of CH_4 in the aqueous phase (H_2O_2 as the oxidant), thus a

different CBU may promote the active, extra framework Fe^{3+} species observed for this process. By identifying possible CBUs that can promote oxidation activity, then zeolite catalysts can be chosen that have a higher density of such CBUs within the zeolite lattice.

For context, MFI type zeolites contain four CBUs: *mor* (t-tes), *cas*, *mfi* (t-pen) and *mel* (Figure 1).¹⁵ By synthesising Fe-zeolites that contain the same CBUs and some that do not have any CBUs in common, a link between the role of the framework and the active Fe^{3+} species can be uncovered. For example, the zeolite with framework type MEL (ZSM-11) contains the *mor*, *mfi* and *mel* CBUs but not *cas*, as shown in Figure 1. If Fe-ZSM-11 was active for CH_4 oxidation, then it could be assumed that either the *mor*, *mfi* or *mel* CBU contributed to activity. Moreover, Fe-MOR only contains *mor*, so would provide strong evidence that active Fe-sites correlate strongly with the *mor*. Comparison of the catalytic performance and spectral features of various Fe-zeolites would allow for a logical approach in determining how the active Fe sites in such structures is made and stabilised.

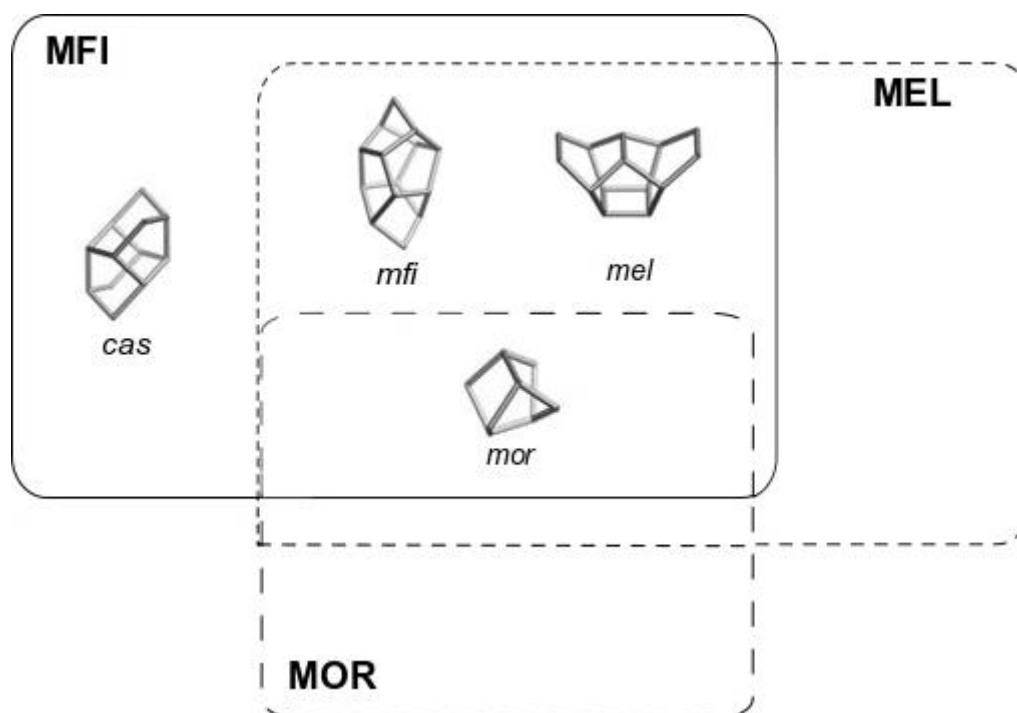


Figure 1 Comparison of the CBUs found in three zeolite topologies that could be used to determine key CBUs required for optimal Al siting for CH_4 oxidation performance.

It was also noted in Chapter 3 that Fe-ZSM-5 was poorly selective to CH_3OH production, and it has been speculated that this is due to the formation of hydroxyl radicals in aqueous solution.¹ Addition of Cu to Fe-ZSM-5 was shown to improve CH_3OH selectivity, whilst maintaining high catalytic activity, by mopping up excess radicals; however, the mechanism of Cu addition

to Fe-ZSM-5 is speculative. Further reaction studies of Cu doped-Fe-ZSM-5, along the lines of the results shown in Chapters 3-5, should be made to determine whether the addition of Cu to Fe-ZSM-5 has an impact on partial CH₄ oxidation and Fe³⁺ speciation. For example, Cu/Fe-ZSM-5 can be prepared by solid-state incorporation of a Cu salt to calcined Fe-ZSM-5 and heat treated to afford Cu/ Fe-ZSM-5. Following the methodologies discussed in Chapter 2, samples should be prepared with varying Cu loadings, to determine the effect of Cu content on catalytic activity and CH₃OH selectivity. If Cu is found to regulate CH₃OH selectivity, then Cu could be incorporated into seed assisted Fe-ZSM-5, that are reported in Chapter 5, to further establish the speciation of Cu within the catalyst.

6.2.2. Optimisation of the synthesis of Fe-ZSM-5

The continuous crystallisation of a variety of zeolites has been recently investigated due to the interest in increased zeolite synthesis productivity for industrial applications.¹⁶⁻¹⁹ One of the limitations of these systems is the formation of a slurry phase during the crystallisation, which results in blockages in the tubular reactors, which prevent further crystallisation of the desired material.¹⁹ Sophisticated engineering solutions will need to be employed to alleviate these limitations; for example, Wakihara *et al.* reported the injection of pressurised and heated water to the gel to prevent the build-up of crystalline material on the reactor walls, without affecting the initial gel composition.¹⁹ Fully crystalline ZSM-5 was afforded in a matter of seconds; however, such small crystallisation times can affect the crystallite properties, such as size and morphology. The effect of TMI incorporation into the framework was not considered, even though this would be important for the synthesis of a range of activity zeolite catalysts.

Considering the past literature, a proof-of-concept crystallisation reactor was built to test whether it was feasible to crystallise Fe-ZSM-5 in a continuous regime, as shown in Figure 3. In this system, the system was filled with H₂O, back-pressure regulated to 15-20 bar and the furnace was heated to 175-200 °C. The templated aluminosilicate gel (prepared using the conventional gel preparation) was then pumped through the reactor once the set temperature had been reached. The solid material was collected at the end of the reactor and characterised to determine crystallinity.

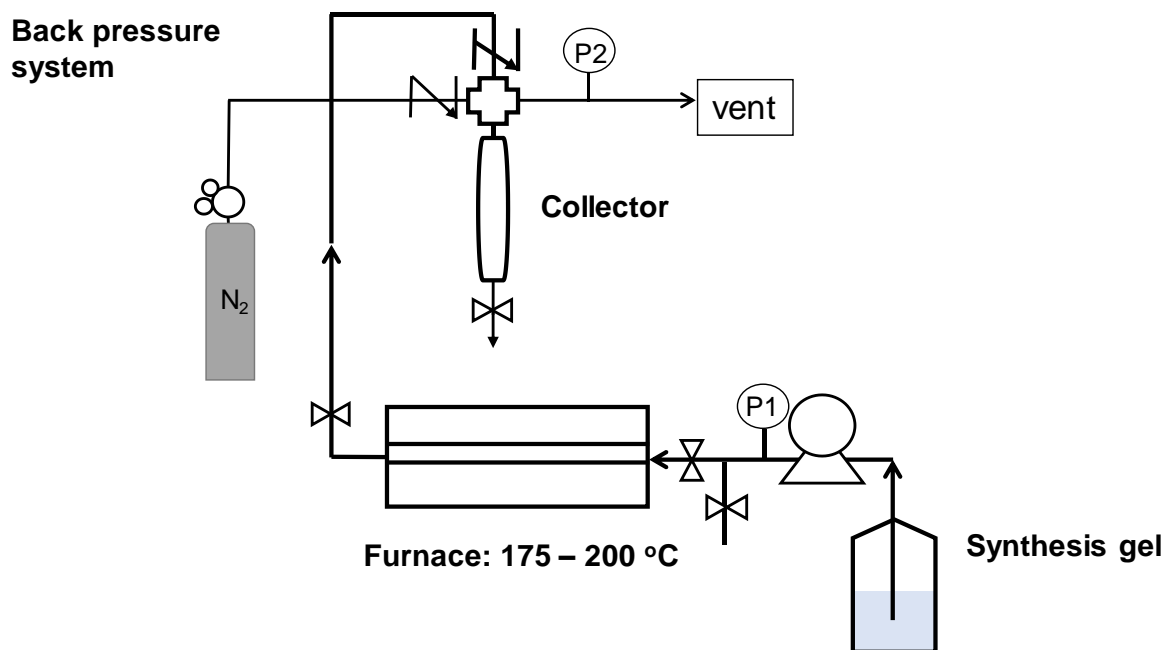


Figure 2 Schematic representation of a semi-continuous reactor for fast crystallisation of Fe-ZSM-5. Arrow heads indicate the direction of flow; thick lines indicate 3/8" SS tubing, and; thin lines indicate 1/8" SS tubing.

The crystallisation time of 4 h of 0.1 wt% Fe-ZSM-5 (42), reported in Chapter 4, is too long for the development of a laboratory-scale continuous feed reactor. To increase crystallisation rate, reactor temperature was increased to 200 °C and the flow rate, F_T , was adjusted to 0.2 mL min^{-1} to reduce crystallisation time to 2 h. Under these conditions, a low yield of solid product was afforded. Solid yield was poor because solid product was depositing on the surface of tubular walls in the heated zone. On removing the heated section of the reactor, the walls were observed to be coated in white solid. Over time, this prevented transport of crystallised products to the collection vessel. To alleviate this, the reactor was redesigned, to exploit gravity to assist with the collection of the crystallised product. Changing the configuration did not improve solid yield. *p*XRD studies showed that the solid recovered from the continuous flow reactor was MFI (Figure 3), as seen by the diffraction peaks at 7-8 ° 2 θ and 22.5-25 ° 2 θ . Relative crystallinity was determined to be 80%, albeit with a degree of amorphous material, and no other crystal phases were detected.

The initial results of a crystalline MFI material being produced is promising; however, much work is needed to resolve the engineering problems that currently hinder this system. An alternative way to solve this problem could be to use microwave heating, utilising coiled tubes sat within the microwave-heated chamber to heat the reactants. Microwave heating has previously been shown to speed up batch zeolite synthesis as it is able to heat the gel internally,

thus eliminating heat-transfer issues related with the use of conventional heating methods.^{20,21} Other methods, such as the use of seeding,²² or the injection of pressurised water should be explored to optimise the continuous process.¹⁹

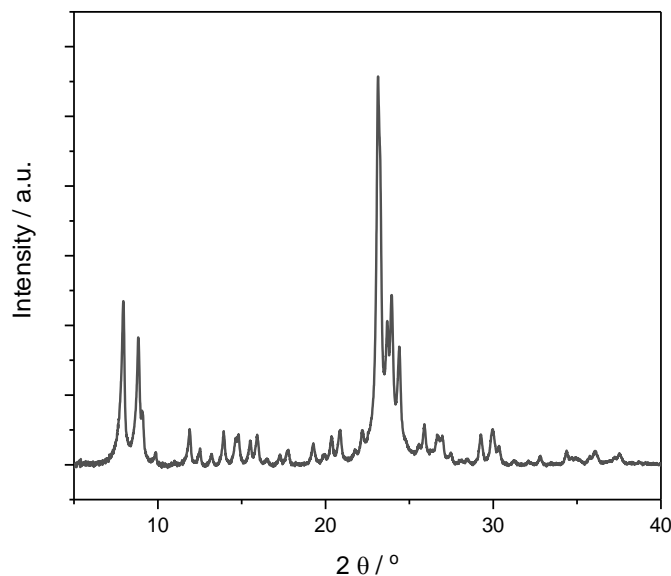


Figure 3 *p*XRD pattern of synthesised 0.1 wt% Fe-ZSM-5 (42)_AS that was collected from the continuous reactor shown in Figure 2.

Another factor to explore is real-time mixing of the starting reagents in-line with the crystallisation process to make the process more “continuous”. In the schematic in Figure 3, the system can only be described as “semi-continuous” as the gel needs to be aged in a batchwise manner. To further increase the productivity of the system, mixing systems could be designed that incorporate the mixing of starting reagents prior to crystallisation. There are some examples of this in the literature for other zeolite types (i.e. zeolite LTA), but the crystallisation of zeolite A is a simpler system. The kinetics of crystallisation during the aging step of Fe-ZSM-5 would need to be explored, and a mixing mechanism proposed, to make continuous mixing more plausible. For example, the effect of temperature on the rate of aging should be explored, whilst the formation of sub-colloidal and colloidal particles should be monitoring to determine the state of the aluminosilicate and Fe-precursors prior to crystallisation, as there is evidence to suggest that this can have a major impact on the outcome of the crystallisation step (crystal phase, morphology, size).¹⁰

In conclusion, continuous crystallisation of Fe-ZSM-5 has shown to be possible, but is currently limited by poor yields, due to incomplete crystallisation in the reactor body. Different

engineering solutions will need to be used to develop an efficient, continuous crystallisation system.

6.2.3. Seed-assisted synthesis of Fe-ZSM-5

Development of Fe-ZSM-5 via seed-assisted methods has allowed for clearer characterisation of the active Fe-centres in the synthesised and heat-treated samples. Even though the synthesis of 0.1 wt% Fe-ZSM-5 (42) was based on already established chemistry, it is also known that the starting gel composition can have an impact on the crystallised product. A more structured approach should be taken in future development work of this material, to better understand the effect of the starting components on the final crystallised product.

It was also observed in Chapter 5 that heat treatment of the synthesised sample is required to elicit changes in Fe³⁺ speciation, though, the nature of these changes is not yet resolved. Further characterisation of the Fe³⁺ centres is needed to gather a more understanding of the oxidation state and coordination geometry of extra framework Fe³⁺. As previously observed, the active Fe³⁺ sites within zeolites can be difficult to identify due to the heterogeneity of the Fe site distribution within the zeolite lattice.¹³ Building on the work presented in Chapter 5, the seed-assisted samples were sent to collaborators at Stanford University for preliminary Mössbauer spectroscopic measurements, to identify changes in Fe³⁺ speciation during heat treatment. Mössbauer spectroscopy can provide information on oxidation state and coordination state of the Fe centres within complex structures.²³ For example, ⁵⁷Fe Mössbauer measurements have been made in the study of Fe-containing enzymes, such as sMMO,^{23–25} and can be applied to the study of Fe-containing zeolites.^{26–28}

Figure 4 presents the Mössbauer spectra of the seed-assisted materials heat-treated at various temperatures (550 – 900 °C) that were recorded at Stanford University. A subtle change can be observed in the splitting pattern of the synthesised samples after heat-treatment. Full quantification of the Mössbauer spectra of heat-treated SA_0.1 wt% Fe-ZSM-5 (42) (crystallised for 168 h) is needed to understand the subtle changes to the distribution of Fe³⁺ species throughout the zeolite lattice. A few observations were made qualitatively for the samples; a doublet, centred at 0 mm s⁻¹, was observed in the as-synthesised material. Which was not observed in samples heat treated with increasing temperature. Furthermore, a new sextet evolves after heat treatment at 550 °C, which correlates with an increase in partial CH₄ oxidation activity, which was reported in Chapter 5. To support these findings, DFT studies should be used to predict the likely conformation for the spectral features that have been

observed throughout this work. Overall, preliminary Mössbauer studies has highlighted the need for further study into the changes in Fe^{3+} speciation in samples prepared by seed-assisted methods.

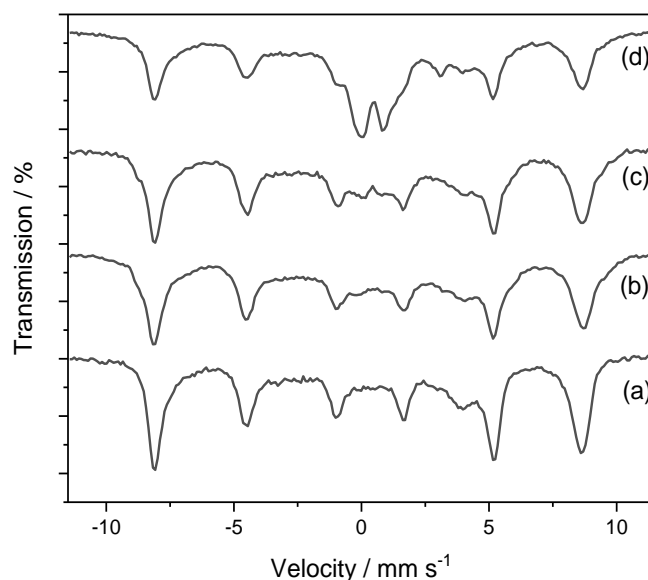


Figure 5 Mossbauer spectra at 4 K of SA_0.1 wt% Fe-ZSM-5 (42) before and after heat treatment. (a) as synthesised; (b) 550 °C; (c) 700 °C, and; (d) 900 °C.

Another area that would benefit from *in-situ* monitoring is the gel aging and subsequent crystallisation step, which would allow for a kinetic determination of the rate of Fe^{3+} substitution into the framework during the crystallisation phase. There are many technicalities related to such a study that would need to be resolved, such as the design of a reactor with a suitable viewing window that does not compromise the pressure integrity of the vessel. The group of Li have designed a modified autoclave reactor which has a high-pressure tolerant viewing window incorporated into the lid of the vessel.²⁹ The modified vessel allowed the group to focus a Raman laser beam into the precursor gel, to monitor the incorporation of Fe^{3+} into the MFI-framework during crystallisation. The formation of bands typical of tetrahedral Fe^{3+} could be observed as the crystallinity of the zeolite increased (crystallinity of the material could be observed by an increase in intensity of the Si-O-Si vibrational stretch at 380 cm^{-1}). The authors suggested, from the data reported, that isomorphous substitution of Fe^{3+} into the MFI framework, was a kinetically controlled process.²⁹ The Raman observations could be supported by time-resolved UV-vis of the crystallisation of Fe-ZSM-5, by using a UV light source with a modified autoclave. *In-situ* UV studies would be feasible, as it was shown in

Chapter 5 that full substitution of tetrahedral Fe³⁺ did not occur in the least crystalline sample (SA_200_24), which indicates other Fe³⁺ species may form.

Alternatively, it may be possible to monitor seed-assisted crystallisation *in-situ* by developing a continuous regime; however, this is a long way from being realised. There are many parameters in the batch synthesis that need to be better understood to enable the design of an optimal crystallisation process. The current crystallisation time for seed-assisted Fe-ZSM-5 is 168 h, though 72 h has been shown to afford a more crystalline sample. For a continuous regime to be feasible, the crystallisation time would need to be substantially reduced. A contact time of 2 h for OSDA-Fe-ZSM-5, was reported in Chapter 4, thus the seed-assisted crystallisation would have to be reduced by 166 h to achieve a feasible contact time. A reduction in crystallisation time of this factor is not unthinkable, and seed-assisted methods are thought to reduce crystallisation times, as the need for nucleation is reduced (the seed materials act as the nucleation site for zeolite crystal growth).^{10,30} Optimisation of crystallisation kinetics could be made by studying the nature of the aluminosilicate gel, which can have an impact on the crystal product. For example, the starting reagents (silica source, aluminium source, sodium source, iron source), the pH of the gel, the molar ratio of the gel, the length of aging and the temperature of the aging step can affect the crystal product and care must be taken to maintain these parameters between each synthesis.

Further, the application of the seed-assisted method to the synthesis of other compositions of Fe-ZSM-5 would allow for a broader study of the material. In the initial synthesis studies, when other SiO₂/Al₂O₃ ratios were synthesised, pure-MFI phase was not observed. At low SiO₂/Al₂O₃ ratios, only amorphous SiO₂ was observed in the *p*XRD pattern, whereas at higher SiO₂/Al₂O₃ (i.e. SiO₂/Al₂O₃ = 84), crystalline MFI diffraction peaks were observed in the diffraction pattern, along with a quartz impurity, with a peak at 26° 2θ. Each of these catalysts were synthesised using the same molar ratio of Na₂O (i.e. 1 SiO₂: x Al₂O₃: 0.067 Na₂O: 0.0147 Fe₂O₃: 39.4 H₂O) and same crystallisation conditions. Evidence suggests that the Al₂O₃/Na₂O ratio is crucial for optimising the correct gel composition that leads to the desired crystal phase.¹¹ By varying the ratio of Al₂O₃/Na₂O in the precursor gel and monitoring the pH throughout the aging process, a seed-assisted approach to the synthesis of a range of Fe-ZSM-5 with varying compositions can be made, thus allowing for an in-depth kinetic and mechanistic study of the active Fe³⁺ species that form in these catalysts.

Seed-assisted methods for the hydrothermal synthesis of Fe-ZSM-5 have recently been developed for CH₄ oxidation and show great potential to study the reaction pathways and active-site speciation in more detail. The work is still in its early stages, and more advanced methods are required to identify the active Fe³⁺ species within these catalysts.

6.3. Final Remarks

Fe-ZSM-5 is an exceptionally active catalyst for CH₄ oxidation, yet care must be taken in the synthesis of the material to optimise the formation of active Fe³⁺ species. Although one of the main aims of this work was to identify the active site, the active Fe³⁺ site is still elusive and work is continuing that can answer this question.

6.4. References

1. C. Hammond, M. M. Forde, M. H. Ab Rahim, A. Thetford, Q. He, R. L. Jenkins, N. Dimitratos, J. a Lopez-Sanchez, N. F. Dummer, D. M. Murphy, A. F. Carley, S. H. Taylor, D. J. Willock, E. E. Stangland, J. Kang, H. Hagen, C. J. Kiely and G. J. Hutchings, *Angew. Chem. Int. Ed.*, 2012, 51, 5129–33.
2. C. Hammond, N. Dimitratos, J. A. Lopez-sanchez, R. L. Jenkins, G. Whiting, S. A. Kondrat, M. Hasbi, M. M. Forde, A. Thetford, H. Hagen, E. E. Stangland, J. M. Moulijn, S. H. Taylor, D. J. Willock and G. J. Hutchings, *ACS Catal.*, 2013, 3, 1835–1844.
3. M. Zaarour, B. Dong, I. Naydenovam R. Retoux and S. Mintova, *Micro Meso Mater.*, 2014, 198, 11-21.
4. K. Zhu and X. Zhou, *Curr. Opin. Chem. Eng.*, 2015, 9, 42-48.
5. M. Shamzhy, M. Opanasenko, P. Concepción and A. Martínez, *Chem. Soc. Rev.*, 2019, 48, 1095-1149.
6. R. V. Prikhod'ko, I. M. Astrelin, M. V. Sychev and E. J. M. Hensen, *Russ. J. Appl. Chem.*, 2006, 79, 1115 – 1121.
7. J. Dedecek, V. Balgová, V. Pashkova, P. Klein and B. Wichterlová, *Chem. Mater.*, 2012, 24, 3231–3239.
8. J. Pérez-Ramírez, J. C. Groen, A. Brückner, M. S. Kumar, U. Bentrup, M. N. Debbagh and L. A. Villaescusa, *J. Catal.*, 2005, 232, 318–334.
9. R. L. Hartman, J. P. McMullen and K. F. Jensen, *Angew. Chemie - Int. Ed.*, 2011, 50, 7502–7519.
10. J. Grand, H. Awala and S. Mintova, *CrysEngComm*, 2016, 18, 650 – 664.

11. M. H. Nada and S. C. Larsen, *Microporous Mesoporous Mater.*, 2017, 239, 444 – 452.
12. J. Dědeček, Z. Sobalík and B. Wichterlová, *Catal. Rev. – Sci. Eng.*, 2012, 54, 135 – 223.
13. B. E. R. Snyder, M. L. Bols, R. A. Schoonheydt, B. F. Sels and E. I. Solomon, *Chem. Rev.*, 2018, 118, 2718 – 2768.
14. B. E. R. Snyder, P. Vanelderen, M. L. Bols, S. D. Hallaert, L. H. Böttger, L. Ungur, K. Pierloor, R. A. Schoonheydt, B. F. Sels and E. I. Solomon, *Nature*, 2016, 536, 317 – 321.
15. International Zeolite Association Structural Database, <https://europe.iza-structure.org>
16. Z. Liu, J. Zhu, T. Wakihara and T. Okubo, *Inorg. Chem. Front.*, 2019, 6, 14 – 31.
17. Z. Liu, T. Wakihara, K. Oshima, D. Nishioka, Y. Hotta, S. P. Elangovan, Y. Yanaba, T. Yoshikawa, W. Chaikittisilp, T. Matsuo, T. Takewaki and T. Okubo, *Angew. Chem. Int. Ed.*, 2015, **54**, 5683 – 5687.
18. Z. Liu, T. Wakihara, C. Anand, S. H. Keoh, D. Nishioka, Y. Hotta, T. Matsuo, T. Takiwaki and T. Okubo, *Micro Meso Mater.*, 2016, 223, 140 – 144.
19. Z. Liu, K. Okabe, C. Anand, Y. Yonezawa, J. Zhu, H. Yamada, A. Endo, Y. Yanaba, T. Yoshikawa, K. Ohara, T. Okubo and T. Wakihara, *Proc. Natl. Acad. Sci.*, 2016, 113, 14267 – 14271.
20. C. Gabriel, S. Gabriel, E. H. Grant, B. S. J. Halstead and M. P. Mingos, *Chem. Soc. Rev.*, 1998, 27, 213 – 223.
21. R. Anuwattana, K. J. Balkus, S. Asavapisit and P. Khummongkol, *Micro Meso Mater.*, 2008, 111, 260 – 266.
22. Z. Liu, T. Wakihara, D. Nishioka, K. Oshima, T. Takewaki and T. Okubo, *ChemComm*, 2014, 50, 2526 – 2528.
23. J. G. DeWitt, K. Hodgson, J. Bentsen, A. C. Rosenzweig, S. J. Lippard, B. Hedman, J. Green, S. Pilkington, H. Dalton and G. C. Papaefthymiou, *J. Am. Chem. Soc.*, 1991, 113, 9219-9235.
24. L. Shu, J. Nesheim, K. Kauffmann, E. Münck, J. D. Lipscomb and L. Que, *Science*, 1997, 275, 515 – 518.
25. M. Martinho, D. Choi, A. DiSpirito, W. Antholine, J. D. Semrau and E. Münck, *J. Am. Chem. Soc.*, 2007, 129, 15783-15785.
26. A. Meagher, V. Nair and R. Szostak, *Zeolites*, 1988, 8, 3-11.
27. K. Lázár, G. Lejeune, R. K. Ahedi, S. S. Shevade and A. N. Kotasthane, *J. Phys. Chem. B*, 1998, 102, 4865-4870.

28. K. A. Dubkov, N. S. Ovanesyan, A. A. Shteinman, E.V. Starokon and G. I. Panov, *J. Catal.*, 2002, 207, 341 – 352.
29. K. Sun, F. Fan, H. Xia, Z. Feng, W-X. Li and C. Li, *J. Phys. Chem. C*, 2008, 112, 16036-16041.
30. K. Iyoki, K. Itabashi and T. Okubo, *Microporous Mesoporous Mater.*, 2014, 189, 22–30.

